Modelling the Effects of Textile Preform Architecture on Permeability

by

Chee Chiew Wong

BEng (Hons)

Thesis submitted to The University of Nottingham

for the degree of Doctor of Philosophy

October 2006

ABSTRACT

Liquid Composite Moulding (LCM) processes are identified as one of the most potentially advantageous manufacturing routes. The challenge currently is to increase their reliability and expand their applicability. To that end, it was perceived that there was a lack of an advanced integrated simulation tool for the manufacture of three-dimensional, multi-layer textile composites. The tools for the analyses of fabric forming and subsequent flow during LCM processes were simple and immature, with the latter suitable to describe flow in thin structures only. Another noted deficiency was that the simulations provided a single answer to any given problem. Industrial experience has shown that during mould filling, due to the nature of statistical variation in the material properties, the filling patterns and arising cycle times are rarely the same between a given set of identical mouldings.

This thesis focuses on permeability prediction of textile reinforcements for LCM processes. The issue of textile variability was also explored through the use of the permeability models' predictive capability. Two novel and efficient numerical approaches were developed to predict textile permeability based on the fabric architecture. The objective was to reduce the complexity of the flow domain and hence provide a faster method to fully characterise the permeability of a textile. Within a wider context, these models were implemented within an integrated modelling framework encompassing draping, compaction and impregnation, based on the TexGen textile schema. TexGen is a generic geometric textile modeller that can be used to create a wide range of textile models. Several validation studies were performed using a range of reinforcements including woven and non-crimp fabrics. A stochastic analysis technique was developed to account for the effect of material variability on permeability. The study based on this technique provided important insights into permeability variations. It was shown that the permeability distribution is a strong function of the textile architecture. The permeability models developed from this work can be used to account for the effects of fabric shear/compaction and statistical variations on permeability. These predicted permeability data can complement experimental data in order to enhance flow simulations at the component scale.

ACKNOWLEDGEMENTS

The work described in this thesis would not have been possible without the help and support of various individuals and organisations. I extend my foremost gratitude to my supervisors, Professor Andy Long, Doctors François Robitaille and Phil Harrison, for sharing their vision and knowledge as well as for their patience with me.

I would also like to thank the Head of the School of Mechanical, Materials and Manufacturing Engineering, Professor Tom Hyde, for the use of the school facilities. The technical support given by Roger Smith and Paul Johns are gratefully thanked. The support of the MultiComp project partners: Ford Motor Company, Dowty Propellers (now under Smith Aerospace), ESI Group and Formax UK Ltd; and the funding support of EPSRC are acknowledged.

Thank you to all my friends and colleagues who made my time here immensely enjoyable and for providing the intelligent discussions, and my housemates through the years for providing excellent companionships and fun laughter (not forgetting the great dinners we shared). Cheers to Yao Li (PhD), Xiao Chen, Seck Jiong (PhD), Gar Nimp, Sophie, Martin, Yang Jing, Zhang He, Xiao Yan, Martin D, Paul, Palanivel, Jon (PhD), Nuno (PhD), Agnes(PhD), Pete (PhD), Rafael (PhD), Angelo, Tom (PhD), Lee, Joul Way, Jo, Kok Hoong, Wout (the ninja), Andreas (PhD), Graham (PhD), Wan Tong, 'K' (Runglawan Somsunan) and countless other friends whom I have not mentioned here – you know who you are in your heart (and so do I).

Last but not least, I dedicate this to Sook Fun, for her love which keeps my sanity in check throughout the years, my parents for being who you are and letting me be who I am, and my brother, for the much needed weekend escapes.

CONTENTS

NOMENCLATURE

a	Aspect ratio	-
a_0	Initial distance between tows (Chapter 6)	m
A	Area	m^2
$[A]$	Finite difference coefficient matrix	-
c	Gebart constant for permeability to flow along the fibres	-
C_1	Gebart constant for permeability to flow transverse to the fibres	-
F	Finite difference pressure coefficient term	-
h	Height or thickness	m
H	Overall height or thickness	m
k	Kozeny constant	-
K	Permeability	m^2
$[K]$	Permeability tensor	m^2
l	Length	m
L	Overall length	m
n	Tow shape power	-
N	Number of experiments	-
P	Pressure	Pa
q	Flow rate per unit height	m^2/s
Q	Volume flow rate	m^3/s
R	Radius	m
R_p	Semi major axis of ellipse (Chapter 6)	m
R_q	Semi minor axis of ellipse (Chapter 6)	m
S_0	Superficial density	g/m^2
u	Superficial velocity	m/s
$\overline{u}$	Average superficial velocity	m/s
u	Superficial velocity tensor	m/s
V_f	Fibre volume fraction	-
W	Width	m

GREEK SYMBOLS

α	Fibre angle	degrees
μ	Fluid viscosity	Pa . s
θ	Angle	degrees

SUBSCRIPTS

0	Initial
1, 2, 3	Principal directions
c	Cell
e	Effective
exp	Experiment
f	Fibre
h	Hydraulic
i, j, k	Cartesian coordinates
n	Normal to mould wall
t	Tangential to mould wall
x, y	In-plane directions
z	Transverse direction
$\parallel$	Parallel to fibres
$\perp$	Transverse to fibres

1 INTRODUCTION

1.1 ADVANCES IN FIBRE REINFORCED COMPOSITES

The aerospace industry has traditionally been the primary driving force in the use of advanced composite materials. Although there are currently many different applications of fibre reinforced composites, advances in aircraft manufacture illustrate the industrial future of composites. The attractiveness of using composite materials over metals in aircrafts is quite obvious: structural efficiency at lower weight, fatigue and corrosion resistance, and lower operating costs due to the weight savings. A prime example of the progress in the use of composite materials is in the manufacture of the horizontal tail plane (HTP) by Airbus. In 1971, Airbus first started to use composite parts on the HTP of the A300 (Viros et al., 2005). This soon progressed to a full composite HTP and finally the new A380, unveiled in January 2005, features a full composite HTP with fuel tanks inside. Overall, 22% in weight of the Airbus A380 components are made using carbon fibre reinforced plastics (CFRP), including part of the rear fuselage, the vertical tail plane (VTP) and rudder, the centre wing-box, flaps, spoilers and ailerons (Airbus online news article, 2005).

Such advances in the use of composite materials are due to improvements made in the constituent materials and particularly advances in manufacturing methods. Liquid composite moulding (LCM) processes, such as Resin Transfer Moulding (RTM), are identified as one of the most potentially advantageous manufacturing routes. Some of the components mentioned above are manufactured using RTM (Viros et al., 2005), a process which consists of the introduction of resin into a closed mould containing a dry preform and results in a near-finished product after curing. RTM technology allows manufacturing of complex parts with outstanding tolerances and surface finishes. Examples of the parts on the A380 manufactured using RTM are the leading edge rib (Figure 1.1) and the trailing edge rib. Perhaps one of the largest components manufactured using vacuum infusion (a variant of RTM) is for off-shore wind turbines, where blades up to 60m in length are produced using glass and carbon fibre reinforcements (LM Glasfiber website, 2005). Another notable application is in the automotive industry, particularly for high performance vehicles, where body panels

which require class-A surface finish are now made from carbon and glass fibre composites using RTM technology.

The use of RTM or any liquid moulding process has many potential advantages as outlined below. However, RTM is still considered a “black art” due to the lack of knowledge about the fundamentals of the process.

Figure 1.1 – HTP leading edge rib manufactured using RTM.
Reproduced from Viros et al. (2005).

1.2 LIQUID COMPOSITE MOULDING PROCESSES

Liquid moulding allows the flexibility of fabricating composites ranging from simple to complex shapes, from low to high performance and from small to large dimensions. Liquid Composite Moulding (LCM) describes a family of closed mould processes whereby the dry reinforcement and the resin are combined within the mould to form the composite component. Highly complex structures can be produced using LCM, thus reducing part-count and off-setting the cost associated with the intermediate assembly stage.

The LCM term is generally used to refer to Resin Transfer Moulding (RTM), the most widely used of the liquid moulding processes. The steps involved in RTM processing are illustrated in Figure 1.2. RTM utilises a pair of matched tools into which a reinforcement preform is placed. Thermosetting resin is injected into the heated tool under positive pressure, usually at 1-10 bar, to impregnate the preform.

The resin is allowed to cure and the composite part is removed. Several variants of the process exist such as Vacuum Assisted Resin Transfer Moulding (VARTM), Resin Film Infusion (RFI) and Structural Reaction Injection Moulding (SRIM), to name a few. The main differences between these variations lie in the injection system and the moulding tools used. Nevertheless, the aim of each of these processes is to provide a reliable and efficient way of manufacturing an integrated composite part.

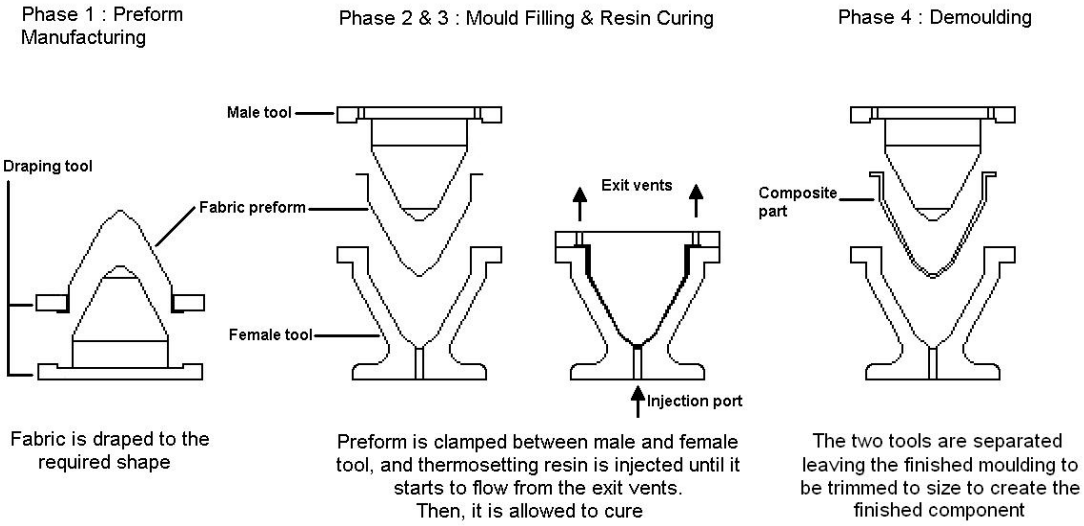

Figure 1.2 – RTM process schematic.

Textile reinforcement

The reinforcements used are made up of individual fibres, typically glass or carbon fibres, which are bundled together to form yarns or tows. These yarns by themselves are not very practical for use as a preform. In order to ease the transportation and handling, reinforcements are usually supplied as random, woven, knitted, stitched or braided mats or fabrics. Due to the wide range of fibre types and the many ways of assembling them, there is a large selection of commercial technical fabrics with different density, strength and draping characteristics. Reinforcements which are easy to handle, able to conform to the mould shape with minimum tailoring, have low crimping properties and offer good structural potential, are the most useful for RTM manufacturing.

Resin system

Some of the common requirements of resin systems for liquid moulding are low viscosity, long gel time and appropriate curing time, and good mechanical and physical characteristics. There are many different types of resin in use in the composites industry, which can be broadly classified under two categories, thermoplastics and thermosets. These two classes differ in the effect of heat on their properties. The selection of the type of resin depends heavily on the class of the component to be produced. The viscosity of the resin and how well it permeates the fabric very much determine the resulting properties of the end product. Almost all RTM parts are made with thermosetting resins, mainly polyesters and epoxies.

Advantages and limitations of RTM

The advantages of RTM can be summarised as the capability to manufacture large, complex, high-performance structures. RTM provides the facility to integrate large numbers of components into one part. Many mainstream applications use RTM to produce sub-assemblies or complete structures with high parts integration. Reduced assembly cost, higher quality and improved functionality are possible advantages if a sufficient degree of integration can be achieved. In order to compete with steel or other materials on a cost basis, a high degree of parts integration using composite materials is required to offset the increased material cost.

A distinct advantage offered by RTM is the ability to pre-place the reinforcement where desired and have it retained in place, which gives increased design flexibility and potential for component optimisation. There is also the flexibility to change the reinforcement type to suit the application without the need to re-engineer the upstream process. The low pressure of the process allows the use of low-tonnage presses in the manufacturing of RTM parts. It provides an inexpensive means of obtaining prototype parts or low production volumes. Being a closed mould process, it has advantages over open mould processes, including low vapour emissions. The increase in the RTM market in the last decade and the acceptance of the process for low-volume applications can be partly attributed to legislative changes regarding styrene emissions. The use of matched moulds means that the resultant components are dimensionally controlled, resulting in minimum hand trimming if tooling is properly designed and the possibility of obtaining a class-A surface finish.

Currently, RTM is limited to low volume production in the range of up to 20,000 components annually. It has found niche markets where high performance predominates such as the aerospace industry, production of top-end cars and sports equipment. There are still problems with filling large parts with high fibre content at low injection pressures, and avoiding resin richness at corners can be difficult. As part integration increases, scrap losses can be costly.

Process simulation

The composites industry has matured considerably in the past decade, with major advancement made in the available resins and reinforcement materials. Computer-aided design (CAD) systems and tooling solutions tailored to the RTM process are becoming increasingly common. The challenge currently is to better understand the fundamental science behind the process in order to increase its reliability and expand its applicability.

In LCM or RTM processes, the reinforcement preforming and resin impregnation phases are the most crucial. Consequently, much effort has been invested in studying them. In an effort to reduce the time spent on "trial-and-error" during manufacturing (hence cost), various draping and flow models have been developed to simulate the physics of these two phases quite accurately. However, in order to generate successful simulations, accurate data for the processing properties of the constituents of the process are needed.

LCM filling simulations depend primarily on accurate permeability data for the reinforcement. Permeability is a measure of the ease of flow through a porous medium, which in this case is the fabric reinforcement. Currently, the most reliable way to obtain accurate permeability values is through experimental measurements. However, experimental permeability characterisation is a time consuming and unproductive process, given the wide range of different types of fabrics available. Also, due to the inherent variable nature of textiles, a single type of fabric reinforcement will exhibit a wide range of permeability values, consequently increasing the number of experiments needed to characterise it properly.

As such, permeability models are an attractive and robust option to obtain accurate permeability data. Their predictive capability would enable one to model the effects of various factors, such as in-plane shear and fibre volume fraction, on the permeability of a textile. Stochastic variations could also be introduced into the model in order to account for the inherent variability of textiles. Permeability data obtained from these models could then be used to complement existing experimental data. Alternatively, permeability models could also be used to enhance the reinforcement design process where one can engineer a fabric to suit a particular application.

1.3 PROJECT FRAMEWORK

The work described in this thesis was performed within the 'Design and Processing of Multi-Layer Structures for Liquid Composite Moulding (MultiComp)' project, which was funded by the EPSRC and several industry partners (Polymer Composites – MultiComp project website, 2005). The aim of the project was to address the issues of obtaining accurate data describing the processing properties of a fabric, specifically formability and permeability. Also, it is known that fabric forming influences the subsequent flow behaviour; therefore the effects of forming on textile structure and hence permeability were studied. Computer simulations based on the fabric architecture were identified as the most viable way to predict these properties. Subsequently, novel analysis techniques which can be applied to three-dimensional, multi-layer textile structures were developed. Within the wider context of the project, these models for processing properties of textile reinforcements were implemented within an integrated modelling framework encompassing draping, compaction and impregnation, based on the TexGen textile schema – which will be described in more detail in Chapter 3 (Polymer Composites – Textile Composites Software website, 2005).

1.4 OVERVIEW OF THESIS

This thesis presents the work done on predicting the permeability of textile structures for liquid composite moulding processes. Two novel and efficient numerical approaches were developed to predict textile permeability based on the fabric architecture. The objective was to reduce the complexity of the flow domain and hence provide a faster method to fully characterise the permeability of a textile. Several validation studies were performed using a range of reinforcements including woven and non-crimp fabrics. A stochastic analysis technique was developed to account for the effect of material variability on permeability. The study based on this technique provided important insights into permeability variations. The permeability models developed from this work can be used to account for the effects of fabric shear/compaction and statistical variations on permeability in order to enhance process simulation. The structure of the thesis is outlined below.

Chapter 2 provides a review of the literature and work that has been done on the subjects of LCM flow simulation and permeability prediction. The fundamental theory relating to flow through porous media and the definition of permeability is analysed. Gaps in the work done on the prediction of textile preform permeability are identified.

Chapter 3 describes the various computational methods that are used in this work and introduces two new approaches to predict permeability, namely the Stream Surface and Grid Average methods. These two approaches were developed based on simplified flow theory to provide fast and efficient methods to predict the permeability of generalised fabric models.

Chapter 4 presents several 2D analyses using the two approaches, which form the initial verification studies. In order to establish the validity of the work, the two simplified approaches are compared to a simple analytical model (for an array of fibres) and an established method in the form of Computational Fluid Dynamics (using porous tow cross sections). This last component of the chapter has been published in part in Wong et al. (2006) as listed in Appendix A.

In Chapter 5, permeability analyses using 3D textile models were performed. The aim of the first section is to demonstrate the capability of the model to simulate the effects of in-plane shear on permeability using a virtual textile model. The second part demonstrates the use of the model to predict the permeability of real textiles. A multi-layer fabric model was generated based on a laminate of a plain weave fabric from which the permeability was calculated. The first section was published in part in Wong et al. (2006).

Chapter 6 discusses the issue of permeability variations within nominally identical textiles. A method to model variability in the textile models is described. This was then used to study the sensitivity of the permeability distribution to changes in tow path variability, computational domain size and fabric structure. This chapter concludes with a discussion of the relationship between macro and mesoscale permeability analyses. This work was submitted in part for publication as Wong and Long (2006).

Chapter 7 contains the overall discussion and conclusions of the work and recommendations for further work.

2 LITERATURE REVIEW

2.1 INTRODUCTION

The resin injection phase in a LCM process is described as flow through a porous medium. Such a simplification is justified from the macroscopic viewpoint, where the fabric layers are compacted into a single permeable preform. However, a textile preform actually has several length scales, starting from the individual fibres making up the fibre bundles, which are woven or stitched together to create the fabric. In effect, a fabric reinforcement exhibits heterogeneous behaviour, whereby the fibre bundles are porous entities with free open spaces between them.

The literature regarding the modelling of flow during the manufacture of textile composites is reviewed in this chapter. Central to the core of LCM flow modelling is the theory of flow in porous media. Originally developed for the geology and construction sectors, the application of particularly Darcy's law, which describes porous flow, to LCM flow is explained. Early studies focussed on macroscopic analyses of the resin injection phase, from which several prominent LCM flow models were developed. Concurrently, fabric permeability measurement techniques were also developed. It is imperative to have accurate permeability data in order to successfully simulate the flow behaviour.

Predictive permeability models offer a potentially accurate and robust alternative to experimental methods. In order to predict fabric permeability, research has advanced into studies at the mesoscopic and microscopic levels. These works focus on understanding the fundamental factors affecting fabric permeability. For simple cases, mathematical models such as the Kozeny-Carman equation relate the permeability to the porosity of the medium with reasonable accuracy. Numerical analysis is another approach adopted to predict permeability based on a description of the micro and macroscopic structure of the fibre preform. A number of such models are reviewed in the following sections.

2.2 LCM FLOW MODELLING

2.2.1 Introduction

Within a textile preform enclosed in a mould, there exists a network of fibres that forms a labyrinth of flow channels, the narrowest of which is several orders of magnitude smaller than the thickness of the mould. As the resin flows through to fill the mould, not only are there shear stresses due to the presence of the fibres and the mould walls, but also capillary effects and surface tension effects which may become significant (Advani et al. 1994).

It would be almost impossible for one to represent the intricate fibre structure of the entire preform geometry, and then solve the equations of fluid motion while accounting for surface tension and capillary effects. Such detailed analysis would both be computationally intensive and inefficient, and may also be unnecessary for the purpose of process design.

In order to simplify matters, resin flow through the fibre preform can be described as fluid flow through a porous continuum. Such an assumption is valid when one considers the macroscopic filling of LCM parts. Practice has thus converged on modelling LCM resin flow using Darcy's law, which describes fluid flow through a porous medium. The fundamental equations for modelling LCM flow are outlined in the next section. This is followed by a review of the methods used to model flow and the various published work on LCM flow models.

2.2.2 Fundamental equations

Flow in porous media was first studied experimentally by Henri-Philibert Darcy in 1856 (Scheidegger, 1974). By observing the flow of water through a bed of sand, he deduced that the volume of water running through the sand is proportional to the pressure loss. The resulting equation is the well known Darcy's law,

$$Q = -K_h A \frac{dP}{dx} \tag{2.1}$$

where Q is the 'total volume of fluid percolating in unit time', A is cross sectional area of the flow, dP/dx is the pressure gradient and K_h is a constant of proportionality known as the hydraulic permeability.

In its original form, Darcy's law is not very useful because the K_h term is dependent on the properties of both the fluid and porous medium. In order to separate the influences of the two constituents, K_h was defined in terms of fluid viscosity μ and permeability K, which is dependent on the structure of the porous medium only,

$$K_h = K/\mu \tag{2.2}$$

This concept was popularised by Wyckoff et al. in 1933 and has since been validated by the various successful determinations of permeability that have been performed using it as a basis (Scheidegger, 1974).

Darcy's law has been studied and tested by many authors, and its validity was confirmed for a wide range of flows. While Darcy's original findings were based on purely heuristic methods, Darcy's law and the notion of permeability has since been proven and derived through theoretical considerations (see Tucker and Dessenberger, 1994). It has also been shown that for liquids at high velocities and for gases at very low and at very high velocities, it becomes invalid (Scheidegger, 1974).

Early developments of Darcy's law were spurred on by studies in hydrology and soil mechanics. The applications normally consisted of particulate beds (sand and rocks) or porous solids, which are considered to be isotropic and homogeneous. Several authors then observed that directional variations of permeability can occur. For a macroscopically homogeneous piece of rock, the permeability is not the same across different cross section faces (see Scheidegger, 1974). In fibre composites engineering, most fibre preforms are heterogeneous material and exhibit anisotropic flow behaviour.

The theory of flow in anisotropic materials was developed particularly by Farrandon in 1948 and Litwiniszyn in 1950, through which the full tensorial form of Darcy's law for anisotropic media was derived,

$$\mathbf{u} = -\frac{[K]}{\mu}\nabla P \tag{2.3}$$

where **u** is the superficial velocity, the velocity one observes on a macroscopic scale, μ is the fluid viscosity, ∇P is the pressure gradient and [K] is the permeability tensor of the porous medium. This model is sufficient to describe the flow of Newtonian fluids in anisotropic, homogeneous porous media provided that inertia and long-range viscous effects are negligible, which are generally considered to be valid assumptions for the LCM flow process (Astrom et al., 1992, Tucker and Dessenberger, 1994).

Most LCM components have shell-like geometry, where the thickness is much smaller than the other dimensions of the part. As such, flow through the thickness can be neglected and flow can be described using a two-dimensional version of Darcy's law. However, it is worthwhile to note that extension to a fully three-dimensional simulation is straightforward and has been done. The only difference is that there is an increase in the number of degrees of freedom. The two-dimensional form of Darcy's law can be written in matrix form as,

$$\begin{pmatrix} u_x \\ u_y \end{pmatrix} = -\frac{1}{\mu}\begin{pmatrix} K_{xx} & K_{xy} \\ K_{yx} & K_{yy} \end{pmatrix}\begin{pmatrix} \dfrac{\partial P}{\partial x} \\ \dfrac{\partial P}{\partial y} \end{pmatrix} \tag{2.4}$$

where the permeability is orthotropic, thus the tensor is symmetric and K_{xy} equals K_{yx}. In order to model flow, one also needs to consider the continuity equation (conservation of mass for an incompressible fluid),

$$\nabla \cdot \mathbf{u} = 0 \tag{2.5}$$

Combining (2.4) and (2.5) yields the fundamental governing equation for pressure during flow through a porous medium, shown in two-dimensional form,

$$\frac{\partial}{\partial x}\left(\frac{K_{xx}}{\mu}\frac{\partial P}{\partial x}\right)+\frac{\partial}{\partial x}\left(\frac{K_{xy}}{\mu}\frac{\partial P}{\partial y}\right)+\frac{\partial}{\partial y}\left(\frac{K_{yx}}{\mu}\frac{\partial P}{\partial x}\right)+\frac{\partial}{\partial y}\left(\frac{K_{yy}}{\mu}\frac{\partial P}{\partial y}\right)=0 \quad (2.6)$$

The solution of (2.6) to model LCM flow is subject to boundary conditions of the applied pressure or flow rate at the inlet gates, zero pressure at the flow front, and zero velocity normal to the solid boundaries of the mould. Tucker and Dessenberger (1994) provide a more thorough review on the governing equations for flow in porous media, including derivation of the momentum equation with inertial effects, and heat transfer and curing reaction considerations during and after flow.

2.2.3 Flow modelling approaches

A number of standard numerical techniques are available to solve the resultant partial differential equation (Equation (2.6)), including the finite difference method (FDM), the boundary element method (BEM) and the finite element method (FEM). Since mould filling is a moving boundary problem, these numerical techniques can be broadly divided into two approaches (Shojaei et al., 2003a) based on either:

i) Moving grid:
The computational domain covers only the resin saturated region in the mould and needs to be remeshed at each time step as the flow front progresses. This scheme provides an accurate representation of the flow front but is very computationally intensive and may encounter problems with multiple flow fronts and injection gates.

ii) Fixed grid:
The computational domain is discretized only once for each simulation. An additional algorithm is needed to simulate the flow front progression, giving a less accurate representation of the flow front compared to a moving grid scheme.

2.2.3.1 Moving grid

The FDM can be implemented relatively easily for 2-dimensional geometries with regular boundaries, but can be problematic for complex geometries. Coulter and Guceri (1989) developed a code called TGIMPG for 2-dimensional resin flow, which utilised boundary fitted finite differences to overcome the difficulties associated with irregular boundaries. A boundary fitted FDM has also been applied by Gauvin and Trochu (1993). While the authors reported good agreement between numerical and experimental results, one difficulty that arose was in modelling of dividing or merging flow fronts. Ultimately, Gauvin and Trochu (1993) concluded that the method is fundamentally flawed by inefficiencies associated with the need for creating a new mesh at each time step.

The BEM reduces the efforts in mesh (re)generation, but can also lead to an effective loss in resin mass within the simulation where the flow front meets the mould wall. Um and Lee (1991) and Yoo and Lee (1996) demonstrated the boundary element method for mould filling simulations of simple geometries and showed that conservation of mass was achieved for these simple problems. Chan and Hwang (1992) described an approach for non-isothermal filling simulation based on the FEM where a new layer of finite elements is added at each time step as the flow front progresses. However, the applications were limited to rectangular moulds.

2.2.3.2 Fixed grid

A finite element fixed grid approach will reduce the time needed for re-meshing and is more suitable for complex geometries. However, additional computation is needed to ensure resin mass conservation across element boundaries.

The control volume with finite element method (CV/FEM) seems to be the most versatile and computationally efficient way to solve mould filling problems (Shojaei et al., 2003a). Bruschke and Advani (1990, 1994) developed a program called LIMS based on the CV/FEM. In this approach, a control volume (CV) is created for each node and a fill factor is assigned to each CV in order to track the flow. The pressure of the filled domain is first calculated using the FEM and then the flow front is advanced using the CV method. Numerous other researchers have successfully

implemented simulations based on the CV/FEM such as Young et al. (1991), Lin et al. (1993), Lim and Lee (2000) and Lin et al. (1998). More recently, Shojaei et al. (2003b) published a study on the difference between using a nodal partial saturation formulation and the conventional method based on a quasi-steady state formulation within a CV/FEM based flow program. While a good agreement was observed by comparing the results of both approaches with analytical solutions for simple cases, the nodal partial saturation scheme was more efficient than the conventional method in terms of CPU time.

The non-conforming finite element method is another interesting approach developed by Gauvin and Trochu (1998) in their code called RTM-FLOT to solve the mould filling problem. In this approach, the fill factor is defined for each element and there is no further need to construct a control volume for each node. This approach also ensures conservation of flow rate across inter-element boundaries. Their code has been commercialised by ESI Software under the name PAM-RTM (ESI Group website, 2006).

2.2.4 Further published work on flow modelling

Most of the above simulations were done in 2D, as most LCM components have thicknesses several orders of magnitude smaller than the largest in-plane dimension, and consequently can be modelled using thin-shell elements. However, as more parts with complex geometries and significant thickness are made with LCM, 3D simulation of the mould filling process will lead to more accurate and realistic results. In addition, non-isothermal simulations are becoming more important as temperature and degree of cure can vary significantly through the thickness for a thick part. This is especially important for optimised processing when resin may begin to gel in the last stages of injection.

Young (1994) developed a non-isothermal computer code to simulate full 3D mould filling problems. Simulations of flow behaviour in simple 3D geometries to study variations of temperature and resin cure rate were described but there was no experimental validation. Bruschke and Advani (1994) have extended the capability of LIMS to include 3D non-isothermal problems. Validation was performed by

comparing the results of LIMS to closed form solutions of simple problems. A case study using a complex 3D part showed a good qualitative agreement between the simulated flow front pattern and experimental results. Lim and Lee (2000) also presented a numerical code for simulating 3D non-isothermal filling processes and have used the code to predict resin flow, temperature distribution and degree of cure for some complicated 3D structures, although experimental validation was performed using a simple cube geometry.

Many authors have used these flow simulations to characterise phenomena such as race-tracking due to poor preform fit at mould edges (Liu et al., 1996, Devillard et al., 2002, Bickerton and Advani, 1999, Diallo et al., 1998), stacking in multi-layer preforms (Gauvin and Trochu, 1998) and dry spots formation (Liu et al., 1996). Gauvin and Trochu (1998) and Diallo et al. (1998) used RTM-FLOT to study flow through multi-layer preforms and edge effects where the resin races along the mould edges due to poor preform fit, and obtained reasonable agreement with experimental observations. Young et al. (1991) attempted to optimize the inlet gate location in the filling simulation of an automotive inner hood by minimising the injection pressure and reducing the number of outlet vents needed. Liu et al. (1996) and Devillard et al. (2002) demonstrated the use of LIMS for gate and vent control in order to prevent dry spot formation, while accounting for race-tracking. Comparison with experimental results shows that simulations can be used effectively to design an optimal injection strategy.

All of the flow models reviewed above used Darcy's law to model resin flow in liquid moulding. The same is true for most of the other published work in this area. Darcy's law is a volume averaged model in which the interaction between the fluid and structure of the porous medium is accounted for through a single variable, the permeability. Accurate permeability characterisation is therefore critical to a successful mould filling simulation.

In the next section, a brief description of permeability is provided followed by a section on the standard techniques used in measuring permeability and the research work done to characterise permeability experimentally. Works on the various factors that affect textile permeability as well as on the variations of permeability values are

also reviewed. This is followed by a discussion of predictive permeability models, the subject of which forms the main scope of the work described in this thesis.

2.3 TEXTILE PREFORM PERMEABILITY

2.3.1 Definition of permeability

Permeability is a measure of the ease of flow of fluid through a porous medium. It arose from Darcy's law where all the detailed microscopic interactions between the fluid and the porous medium were lumped into the permeability value. As such, it is a property of the porous medium, which in this case is the fibre reinforcement and is anisotropic. Its value depends on the porosity of the reinforcement, the dimensions of the capillary passages in various directions in the reinforcement and the tortuosity of these passages (Parnas, 1998). Note that permeability as defined in Darcy's law (2.3) pertains to the steady flow of fluid in a saturated porous medium, whereas the LCM injection process involves unsteady flow of resin into a partly unsaturated preform. Nevertheless, mould filling simulations in current usage rely almost exclusively on solving Darcy's law combined with a numerical approach for flow front advancement.

As seen in equation (2.3), in the general case, permeability is a tensor and its components in three-dimensional space are written as,

$$[K] = \begin{pmatrix} K_{xx} & K_{xy} & K_{xz} \\ K_{yx} & K_{yy} & K_{yz} \\ K_{zx} & K_{zy} & K_{zz} \end{pmatrix} \tag{2.7}$$

For a fibre preform, the permeability tensor is orthotropic where $K_{xy} = K_{yx}$, $K_{xz} = K_{zx}$, $K_{yz} = K_{zy}$, and there exists a principal coordinate system with a principal permeability tensor,

$$[K] = \begin{pmatrix} K_1 & 0 & 0 \\ 0 & K_2 & 0 \\ 0 & 0 & K_3 \end{pmatrix} \tag{2.8}$$

The above holds true when analysing the macroscopic flow through a fibre preform, i.e. flow in production of a composite part. However, one must be aware that the flow behaviour in a fibre preform is markedly different when analysed at the mesoscopic length scale, which concerns the interaction between the fluid and the intricate structure of the fibre bundles.

At the moment, it is sufficient to consider the macroscopic level first as this is more practical for LCM flow simulation. Mesoscopic analyses are useful for looking at localised variations in flow and for permeability prediction, and will be discussed later in this chapter.

2.3.2 Experimental determination of permeability

Experimental measurements remain the most reliable way to determine permeability. Flow experiments on porous materials were originally developed for the geology and construction sectors, as were most of the theories and works on flow in porous media. These experiments and theories were later adapted to fibre reinforced composites engineering to analyse flow in fibre preforms.

In order to fully characterise the fibre reinforcement, it is necessary to measure its three principal permeabilities, K_1, K_2 and K_3. For most LCM parts which are thin shells, the transverse (through-thickness) permeability K_3 is usually neglected and only the in-plane permeabilities K_1 and K_2 need to be evaluated (Parnas, 1998). K_3 values can also be measured (Parnas et al., 1995) and are important for components with large thickness and parts that exhibit significant differences in permeability between layers such as those introduced by using a flow enhancing medium.

The two most widely used techniques for measurement of the in-plane permeability are the rectilinear flow method and the radial flow method. In a rectilinear flow experiment (Figure 2.1a), the reinforcement is usually placed in a rectangular mould and resin is injected from a side gate and allowed to permeate the reinforcement in only one direction. In contrast, in a radial flow experiment (Figure 2.1b), resin is injected through a central circular gate into a square or circular mould containing the reinforcement and proceeds to follow an elliptical flow front. For both techniques,

the fluid can be injected under either constant pressure or constant flow rate. Table 2.1 compares the two experimental methods.

In both experimental methods, a transparent cover is usually used to permit observation of the flow front progression and pressure transducers are placed at various locations inside the mould to measure the pressure field. By measuring the pressure drop and flow rate, one can then use Darcy's law to find the permeability in the flow direction. The solution for radial flow is more complicated whereby the shape of the flow front ellipse has to be resolved into a circle and a series of transformations are performed to calculate the two principal permeabilities. The procedures for both the rectilinear and radial flow experiments for fabrics have been described in detail by Adams, Miller, Rebenfeld and co-workers (Adams et al., 1986, Adams and Rebenfeld, 1987, Hirt et al., 1987 and Adams et al., 1988), Gebart and Lidstrom (1996) and Parnas and Salem (1993) amongst others.

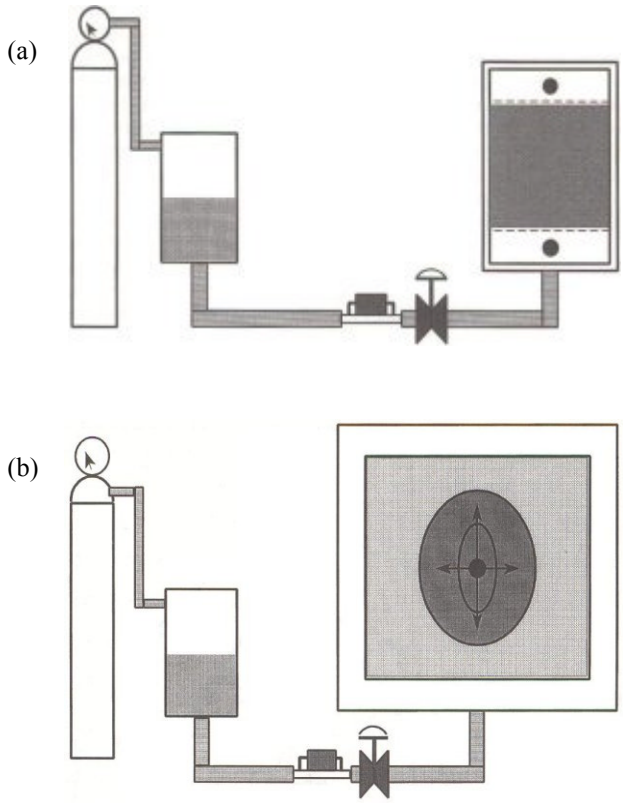

Figure 2.1 – Schematics of the set up for (a) rectilinear flow experiment and (b) radial flow experiment for the measurement of the in-plane permeability of a fibre reinforcement. After Parnas (1998).

Table 2.1 – A comparison between the rectilinear flow method and radial flow method for the determination of in-plane permeabilities of a fibre reinforcement.

Experimental Methods	Features
Rectilinear (Unidirectional) flow method	• Yields permeability along the flow direction only. Employed mainly to characterise isotropic materials. • Permits measurement of saturated and unsaturated permeabilities. • Easy implementation and calculation of permeability. • Prone to edge effects – a preferential flow observed along the mould wall due to a small gap existing between the wall and the preform (usually referred to as 'racetracking').
Radial flow method	• Simultaneous determination of both principal in-plane permeabilities and tensorial orientation. • Measurement of saturated and unsaturated permeabilities. • More complex data processing. • Complicated analytical solution of the permeability values. Error might be induced when determining the equivalent elliptical flow front from the data.

It is generally agreed that both experimental methods give comparable permeability values, although there are researchers who claim otherwise. In an attempt to compare between the two methods and also quantify the repeatability of the permeability measurement experiments, Lundstrom et al. (2000) conducted a series of controlled experiments which included measurements from three parties. Among other findings, they concluded that the rectilinear and radial flow methods will give different permeability measurements. However, they also reported large differences between the permeability values obtained by the different parties involved, up to 50% difference as opposed to 25% difference for the comparison between the two methods. Perhaps the range of permeability values reported is indicative of another major aspect of textile preform permeability, namely its variable nature (see next section).

Heardman et al. (2004) described a radial flow method to measure permeability under transient flow, where neither the pressure nor the flow-rate is considered constant. They obtained good agreement with experiments using the normal constant pressure setup for assemblies of woven fabrics. They also showed that, using error

analysis on the equation used to calculate permeability, the estimated error due to the parameters used to determine permeability (e.g. pressure, viscosity and time) is in the range of 8-16%. However, they did not quantify the range of measured permeability values for their reinforcements and hence did not compare it to the estimated error.

The use of a transparent cover (usually made from Perspex®) limits the range of injection pressures used as it is susceptible to deflection at high pressures. Permeability measurements done at the University of Nottingham were based on a fixed flow-rate injection method (Smith et al., 1997, Robitaille et al., 1998). This method allows a metal cover to be used, as observation of the flow front is unnecessary. The permeability is related to the pressure differences measured using pressure transducers located at various positions in the cavity. This fixed flow-rate approach allows the cavity to be properly reinforced and higher flow rates and pressures to be achieved. More recently, Endruweit et al. (2005) updated the radial flow set-up (using constant pressure injection) at the University of Nottingham with automated data collection and analysis using LabView™. Pressure transducers were used to detect flow front progression, thus negating the need for a transparent cover.

2.3.3 Stochastic variability in textile preform permeability

In practice, permeability measurement is not a trivial task. Large variations in permeability values have been reported in the literature (Rudd et al., 1997, Lundstrom et al., 2000, Luo et al., 2001), most of which are attributed to improper experimental assembly and non-uniform raw material properties.

Pan et al. (2000) and Hoes et al. (2002, 2004) reported a statistical distribution of permeability for both woven and multiaxial warp-knitted (non-crimp) materials. Both groups of researchers tried to analyse the various factors which would affect the permeability data. Pan et al. (2000) performed controlled uni-directional flow experiments for a plain weave and a 0°/90° non-crimp glass fibre fabric, taking 30 measurements per fabric, and found that the permeability of the fabrics was primarily influenced by local changes in fibre orientation and superficial fabric density. Hoes et al. (2002, 2004) measured the distributions of permeability for a plain weave, twill weave and a special PVC-coated layered fabric, using the radial flow method.

Around 90 measurements were taken for each fabric. They used the results for the latter material to suggest that nesting was the major source of the variations in permeability values. Nesting refers to the phenomenon when the textile layers within a stack of reinforcement sit out-of-phase in relation to one another's fibre tow positions, creating a packed reinforcement and perhaps a more homogeneous medium. The permeability data for all the fabrics tested in both studies was found to broadly follow a Normal distribution.

In order to study the influence of fabric structure on the permeability distribution, Endruweit et al. (2005) analysed five fabrics with different architecture and geometrical parameters and measured the permeability using a radial flow set-up with automated data collection and analysis. Between 15 and 20 measurements were taken for each fabric. Variations in the permeability values for each type of fabric were also reported (see Table 2.2). These permeability variations were explained in terms of the structure of the fabrics, and the distributions were related to variations in tow spacing. They concluded that the more homogeneous the structure of the material, the lower is the permeability variation.

2.3.4 Other factors affecting textile preform permeability

Initial studies showed that directional permeability is independent of driving pressure, fluid velocity, fluid viscosity and fibre surface wetting properties (Adams and Rebenfeld, 1987). A linear fluid velocity to pressure gradient relation (Darcy's law) was always observed. However, Martin and Son (1986) and Trevino et al. (1991) observed that the flow behaviour for both saturated and unsaturated porous media deviated significantly from Darcy's law. Martin and Son (1986) further postulated that this behaviour might be due to changes in the fibre orientation with changes in flow rate. Chan et al. (1993) and Lekakou et al. (1996) performed a series of constant flow rate experiments using a different flow rate for each set. They reported that while Darcy's law was obeyed in each set of constant flow rate experiments, the permeability increased with increasing injection flow rate. Chan et al. (1993) explained this observation by the preferential channelling of the liquid through the pore spaces as the pressure gradient goes up.

Table 2.2 – Permeability measured for a series of tests on five different fabrics showing mean and standard deviation of the distribution. From Endruweit et al. (2005)

Material	S_0 g/m^2	N_{exp}	V_f	θ [1]	K_1 / 10^{-10} m^2	K_2 / 10^{-10} m^2	K_1/K_2
Glass random mat	450	20	0.28 ± 0.01 (± 2.9%)	76° ± 50°	11.86 ± 3.48 (± 29.3%)	10.42 ± 2.89 (± 27.7%)	1.14
±45° non-crimp glass fabric	950	20	0.56 ± 0.00 (± 0.8%)	112° ± 43°	0.22 ± 0.05 (± 22.5%)	0.18 ± 0.05 (± 26.1%)	1.19
5-harness satin weave carbon fabric	380	18	0.56 ± 0.01 (± 0.0%)	11° ± 9°	0.33 ± 0.06 (± 17.9%)	0.25 ± 0.03 (± 12.0%)	1.33
5-harness satin weave carbon fabric	290	15	0.61 ± 0.00 (± 0.8%)	91° ± 1°	0.47 ± 0.05 (± 10.0%)	0.21 ± 0.02 (± 9.1%)	2.27
Plain weave glass fabric	912	19	0.53 ± 0.00 (± 0.6%)	95° ± 71°	1.24 ± 0.36 (± 29.2%)	0.65 ± 0.17 (± 25.7%)	1.91

[1] θ refers to the angle between the weft direction of the fabric and the experimentally measured semi-major axis of the flow front ellipse.

In an attempt to show that capillary pressure affects the measured permeability value, Amico and Lekakou (2001) performed a series of constant pressure rectilinear flow experiments for a plain weave glass fibre under low injection pressures (15-90 kPa). They showed that only when capillary pressure is included in the pressure term, will the permeability values calculated from the experiments not change with changing injection pressures. They concluded that the permeability is independent of the injection pressure and that the differences in permeability observed in some studies are due to not accounting for the capillary pressures. Consequently, permeability experiments should be conducted with higher injection pressures (>1 bar) in order to minimise the effect of not accounting for the capillary pressure. Within the same study, they also showed that permeability is independent of the permeating fluid.

Parnas et al. (1996) measured the permeability of a 3D woven fabric proposed as a standard reference material and found no significant changes in the permeability due to changes in injection flow rate. Due to the large variations in reported permeability values and different experiment procedures, a database of standard reference fabrics was developed (Parnas et al., 1995, 1997) to document the various permeability measurement techniques and also systematically list all of the different materials tested. The wide spread of permeability values in the database supports the observation that there are many factors which can affect the validity of permeability measurements. Nevertheless, given the benefit of the doubt, Darcy's law is still widely used to model flow in textile preforms.

Early work by Smith et al. (1997) attempted to relate the permeability of various woven and non-crimp fabrics to the shear angle to represent fibre re-orientation during three dimensional forming. A semi-empirical expression based on the Kozeny-Carman equation (see Section 2.5) and a tensor transformation for relating permeability to the ply angle was found for each of the fabrics studied. They found excellent agreement between the experimental and predicted permeability values over the ply angles tested for four different types of reinforcements – a 0°/90° and ±45° non-crimp fabrics, a plane weave and a 2:2 twill weave. Heardman et al. (2001) applied a similar approach to predict the permeability of a bi-directional fabric as a function of in-plane shear. The bi-directional fabric was considered as two separate unidirectional fabrics, for which the permeability values can be calculated using the Kozeny-Carman equation for known fibre volume fraction, and the permeability was averaged across the layers, taking into account the changes in fibre direction using tensor rotation. Good agreement was found between the measured and predicted values for a 5-harness satin fabric for shear angles below the locking angle.

Using the above approach to determine permeability as a function of the change in fibre volume fraction and fibre re-orientation, Long et al. (1998) combined a draping model with a flow code to simulate resin flow through a draped fabric. The showed that the flow behaviour through a draped reinforcement is dependent on the deformation induced during forming and can be accounted for using the described model. Thus, it is possible to link the draping and flow stages during LCM, given the appropriate permeability data.

2.4 WHY MODEL PERMEABILITY? MULTI-SCALE NATURE OF COMPOSITE TEXTILES

Despite the tremendous amount of permeability data published in the literature, the range of fibre reinforcements available on the market is too large for characterisation based on experiments only. Reliable measurements of permeability are difficult even for a relatively simple flat, undeformed geometry, not to mention trying to measure the permeability of flow at various shear angles. The variable nature of the fabric also means that a large number of measurements (typically 20-100) are needed to characterise just one fabric (for flow at one shear angle). Clearly, such an approach is too time consuming and is not viable in the long term.

As such, there is a need for a predictive permeability model to complement the experimental data because:

a) the fibre volume fraction of the reinforcement measured in the experiment may be different from the one used in the mould;
b) fabric deformation induced during the preforming stage will affect the permeability, and this is hard to characterise experimentally;
c) stochastic variations across the fabric structure will affect the permeability, as evidenced by reported statistical distributions of permeability in the literature; and
d) one may want to predict textile processing properties before materials manufacture.

The key to permeability predictions is the understanding of the architecture of the preform. There are three length scales that exist in textile reinforcements. The microscopic length scale describes the individual strands of fibres which are bundled together to create the fibre tows. These fibre bundles when woven or knitted together create a network of porous tows and open inter-tow spaces, and these form the mesoscopic length scale. Finally, the macroscopic length scale describes the fabric reinforcement as a whole, for example, the preform lay-up at the component level.

By studying the flow at the different length scales individually, one can better understand the interaction between the fluid and the preform. For example, starting with the microscopic flow between the fibres, one can relate the flow behaviour to that in the mesoscopic fibre bundles. At the mesoscopic length scale, resin flows mainly in the spaces between the fibre tows and also within the tows, for which the behaviour is known from the microscopic analysis. Using unit cell analyses, one can then deduce a permeability value which is used in macroscopic simulations to account for the complicated interactions between the fluid and the fabric structure.

Also, variability in textile permeability can be incorporated into the flow simulations for optimised processing by using mesoscopic analyses to deduce a range of permeability values for use in the macroscopic simulations. Essentially, as described above, a fabric is defined by its structure and the interaction between the fibre bundles is the key to the variability of the fabric. Only by looking at the mesoscopic level can one analyse the effect of fabric architecture on variability and address issues such as localised inhomogeneities.

Predictive permeability models can be separated into two general classes, namely analytical and numerical models. Analytical permeability models are closed form equations for calculating permeability, normally relating the permeability to certain characteristics of the porous medium such as the porosity and fibre radius. These are usually derived by analysing the physical aspects of the flow process through the porous medium or based on heuristic equations. Closed form solutions are invariably more suited to describe microscopic flow where it is easier to mathematically describe the arrangement of the fibres.

The numerical approach typically consists of solving flow equations in a unit cell that describes the architecture of the fabric, and using the velocity field to back calculate the effective permeability from Darcy's Law. Such approaches are more adaptable than closed form solutions and can be used to look at the mesoscopic flow through a fabric structure.

2.5 ANALYTICAL PERMEABILITY MODELS

In order to obtain an expression for the permeability as a function of a geometrical property of the porous medium, one generally considers flow through an idealised geometry. One early approach theorized by Kozeny was to represent the porous medium by a collection of channels of various cross-sections but of a specific length. For a cross-section normal to the flow in the porous medium, the Navier-Stokes equations were solved for all the channels. The hydraulic radius concept was then used to express the permeability in terms of the specific surface of the porous medium, which is a measure of the hydraulic radius (Scheidegger, 1974). The most commonly used expression based on the Kozeny theory is the Kozeny-Carman equation, given as (after Gebart, 1992):

$$K = \frac{R_f^{\,2}}{4k} \frac{(1 - V_f)^3}{V_f^{\,2}} \tag{2.9}$$

where K is the permeability, V_f is the fibre volume fraction, R_f is the fibre radius and k is the so called Kozeny constant. Kozeny calculated an approximate value of 2 for k but Carman suggested a value of 5 based on experimental evidence on isotropic beds of granular particles. This illustrates one of the primary issues with the Kozeny theory. One can view k as an experimental fitting parameter and thus acknowledge that the model is not fully predictive.

Being a capillaric model, the Kozeny theory is inherently one-dimensional and works well for isotropic media. A number of researchers have used this model to describe isotropic fibre preforms and some have extended the model to anisotropic preforms (Dave et al., 1987, Gutowski et al., 1987, Lam and Kardos, 1989). For example, Lam and Kardos (1989) measured the permeabilities of a unidirectional carbon fibre bed using water as the permeant and obtained different values of the Kozeny constant for flow along and perpendicular to the fibres by curve fitting, giving k values of 11 and 0.68 respectively.

Strictly speaking, the Kozeny-Carman equation cannot be applied directly to transverse flow through aligned fibre beds. The equation calculates transverse

permeability values greater than zero at the maximum packing density of the fibres, which would otherwise block the transverse flow in unidirectional reinforcements (Gebart, 1992). Experimental results support the observation that it is not suitable to describe flow across fibre beds (Astrom et al., 1992). In order to resolve this problem, Gutowski et al. (1987) proposed a heuristic model,

$$K = \frac{{R_f}^2}{4k} \frac{\left(\sqrt{\frac{V_{fa}}{V_f}} - 1 \right)^3}{\left(\frac{V_{fa}}{V_f} + 1 \right)} \tag{2.10}$$

where V_{fa} is the maximum possible fibre volume fraction. The equation agrees with the Kozeny-Carman equation (2.9) at a maximum theoretical fibre volume fraction V_{fa} of one, but gives a much lower permeability when $V_{fa} < 1$. Nevertheless, due to the dependence of permeability on orientation, different experiments have to be performed to fit the above models to data for an orthotropic reinforcement.

A more realistic approach is to represent the porous medium geometry as an array of aligned cylinders (Advani et al., 1994). By considering the drag resistance across them, the permeability for flow perpendicular to an aligned bed of fibres can be calculated. Early models by Happel (1959) and Kuwabara (1959) made use of a cell model, which assumes that the fibres are spaced far enough apart so that the drag on each fibre is not influenced by the presence of the other fibres. The cell model typically consists of a circular cell with the fibre in the middle, and by considering the drag on the fibre as it moves through the cell, with the appropriate boundary conditions applied, the permeability can be calculated. Such a solution is not dependent on the packing arrangement and is more suitable for high porosities when the fibres are widely spaced (Advani et al., 1994).

At low porosities, the fibres are closely spaced and supercells with multiple fibres and periodic boundary conditions are more suitable models (Ghaddar, 1995). By modelling regular periodic arrays of fibres (quadratic or hexagonal) (Gebart, 1992, Astrom et al., 1992, Bruschke and Advani., 1993), one can use the lubrication theory

to solve for the flow rate/pressure drop relationship analytically and obtain an expression for the permeability. Gebart (1992) used the first principles of Navier-Stokes flow to derive different expressions to fit the permeability to flow along and perpendicular to the fibres arranged in either a quadratic or hexagonal array:

$$K_{||} = \frac{8{R_f}^2}{c}\frac{\left(1-V_f\right)^3}{{V_f}^2} \tag{2.11}$$

$$K_{\perp} = C_1\left(\sqrt{\frac{V_{f\,max}}{V_f}}-1\right)^{5/2}{R_f}^2 \tag{2.12}$$

where $K_{\parallel}$ and $K_{\perp}$ are the permeabilities to flow along and perpendicular to the fibres respectively. C_1 and c are constants and along with $V_{f\max}$ are dependent on the fibre arrangement, the values for which have been determined analytically and are summarised in Table 2.3 for the two types of fibre arrangements mentioned above.

The analytical solution for transverse flow (Eqn. 2.12) differs from the Kozeny-Carman equation (Eqn. 2.9) in that the transverse flow stops when the maximum fibre volume fraction is reached. It is also worth noting that the expression for permeability to flow along the fibres (Eqn. 2.11) is equivalent to the Kozeny-Carman equation (Eqn. 2.9) (the constants are defined differently), thus demonstrating an alternative derivation of this model. A good comparison was obtained between the models and experimental values for a unidirectional reinforcement, although the fibre radius was used as a fitting parameter. Gebart proposed that this may be explained by the fibres being arranged in elliptical bundles with large free channels between them, thus causing the effective fibre radius used in the equations to be larger than the true value.

Bruschke and Advani (1993) presented a hybrid model which tends asymptotically to the lubrication model at low porosities and to an analytical cell model solution at high porosities. A good comparison was obtained between the model and numerical results of flow in arrays of aligned fibres for the full porosity range.

Table 2.3 – Numerical values for the parameters in Eqs. (2.11) and (2.12) as defined by Gebart (1992).

Fibre arrangement	C_1	$V_{f\max}$	c
Quadratic	$16/9\pi\sqrt{2}$	$\pi/4$	57
Hexagonal	$16/9\pi\sqrt{6}$	$\pi/2\sqrt{3}$	53

A limited number of authors have tried to address the effect of random fibre spacing rather than a regular packing arrangement (Yu, C. P. and Soong, 1975, Sangani and Yao, 1988, Neale and Masliyah, 1975). However, the inherent nature of analytical solutions prevents a successful closed form solution from being obtained to account for random fibre arrays.

2.6 NUMERICAL PERMEABILITY MODELS

One major weakness of the analytical models is that they are restricted to a simplified cell geometry consisting of an idealised fibre arrangement. A numerical approach, on the other hand, is free from this drawback and allows for a more complex fibre architecture which is closer to the real fabric structure. The effects of various factors such as porosity, nesting, tow shape, etc. can also be studied and characterised. However, it is important to remember that the results of the numerical models are only as good as the modelled preform geometry and the equations used to solve for flow.

Another major aspect of flow through a fabric reinforcement that needs to be addressed is the heterogeneity of the preform. Most of the experimental and analytical characterisations of permeability have so far assumed an average permeability for the fabric preform, implying that all the fibres are arranged evenly in the preform and the flow behaviour is the same everywhere. In practice, because the preform is actually made up of bundle of fibres woven or stitched together, the flow rate between the tows and within the tows will be different (Advani et al., 1994). The fibre volume fraction will vary across different parts of the preform, and as such, the whole preform cannot be represented by a single value of the permeability.

The common numerical calculation consists of imposing a pressure drop across a prescribed geometric domain, solving the appropriate flow equations, and then from the pressure and velocity fields, using Darcy's law to calculate the permeability. Lekakou and Bader (1998) presented a model to describe flow through the intra and inter tow regions in a textile reinforcement, which incorporated the effects of viscous and capillary forces on the flow. Through a series of computational studies on a woven fabric model, it was shown that at very low injection pressures (<1 bar), capillary flow within the tows would influence the predicted global permeability. However, capillary effects may not be that important as most LCM processes uses injection pressures above 1 bar.

A number of researchers have applied Stokes and Brinkman's equations to model flow in the inter-tow and intra-tow regions respectively (Phelan and Wise, 1996, Spaid and Phelan, 1997, Ngo and Tamma, 2001). Brinkman's equation is a generalization of Darcy's law that facilitates the satisfaction of the continuity of velocity and shear stress boundary conditions at the fluid-tow interface.

Spaid and Phelan (1997) studied steady transverse flow through a square array of elliptical porous cylinders using the Lattice-Bolztman method to solve the respective flow equations. They obtained a good comparison between the numerical model and a semi-analytical lubrication model. Ngo and Tamma (2001) used the finite element method to solve for flow through the 3D unit cell of a plain weave and obtained a good comparison between the predicted permeability values and published data by Adams et al. (1986). However, the model is let down by the fact that the authors relied on geometric data of the fabric published in the literature to construct the model and did not have the fabric in hand. The local permeability of the tows was calculated based on an assumed fibre arrangement and tow fibre volume fraction. Also, they did not demonstrate the predictive capability of their model in accounting for changes to tow spacing, tow shape and fibre volume fraction.

Papathanasiou (1997) studied the effects of intra- and inter-tow porosities on the effective transverse permeability of a square array of permeable tows. He used the boundary element method to solve the Stokes equation for flow in both intra- and inter-tow regions, so as to avoid the difficulty of representing the flow at the fluid-

tow interface. From the results, he suggested a power law function to describe the dependence of the effective permeability of the assembly on the intra- and inter-tow porosities. However, no experimental validation was presented.

Simacek and Advani (1996) proposed a model to calculate the in-plane permeability of a woven fabric based on Stokes flow through the open channels and Darcy flow for flow through the tows. They suggested an extension of the model to include multi-layer preforms. They then calculated the permeability for a simple plain weave fabric for a range of shear angles. However, they did not show any comparison with experimental values. Nedanov and Advani (2002) used the homogenization method to formulate the governing equations for a dual porosity media based on Stokes flow. They solved for flow in a single-ply and three-ply 3D model of a woven fabric. No quantitative agreement with experimental values was obtained for the calculated permeability. They also did not demonstrate the use of the method for predicting the effects of factors such as nesting, fibre volume fraction and tow shape on permeability.

Amico and Lekakou (2004) described a model to predict the permeability of an assembly of unidirectional tows, solving Stokes flow in the spaces between the tows (modelled as channels with rectangular cross sections) and Darcy flow through the elliptical porous tows (capillary pressure included). Transfer of flow from the open channels into the porous tows is accounted for in the model. The predicted advancement of the flow front using the model compared well to that observed in rectilinear flow experiments of unidirectional fabric at low injection pressure. They also showed that at high injection pressures, the difference between the flow fronts in the porous tows and free channels will become negligible, hence demonstrating that capillary effect is negligible at high pressure (> 1 bar).

All of the research works cited above used nominal dimensions within the unit cell to represent the preform weave structure. Most are limited by using an idealized structure of aligned fibre tows. In general, real cross sections of tows are not normally perfect ellipses and tows within a plain weave do not follow a sinusoidal path nor are the fibres within the tows packed in a perfect geometrical structure.

Despite this, such 'ideal' representations of the preform do yield 'average' values for the respective modelled preform.

A more radical and potentially more accurate approach is to determine the preform microstructure via optical methods and directly perform the numerical calculation on the discretized optical image. This approach can accurately represent the preform, and if large sections of the medium are included, the variations and defects in the microstructure will be automatically accounted for in the calculation. However, this approach is time consuming and is probably more tedious to perform than direct experimental measurement of permeability. Nevertheless, a few researchers have studied the use of optical imaging to describe the structure more accurately.

Dunkers et al. (2001) employed a non-destructive technique called optical coherence tomography (OCT) to image the microstructure of a composite and used the Lattice-Boltzman technique to solve for Stokes and Brinkman flow through the discretized image. They obtained excellent agreement with experimental permeability data. However, the predicted permeability values are highly dependent on the image processing method, especially the identification of the tow shape.

Lekakou et al. (2004, 2006) made rigorous digital measurements of the dimensions of the fibre tows, channels between tows and thickness of three types of non-crimp fabrics (NCF) - 0°/90° tricot stitched NCF, ±45° chain stitched and tricot stitched NCFs. Based on these measured values, they used the model from Amico and Lekakou (2004) to predict the permeability which agreed very well with experimental measurements for all three NCFs. However, the discontinuous spaces between the tows in the ±45° NCFs were modelled as continuous channels using the averaged width calculated to give the same area. The described model works extremely well for NCFs but could be difficult to apply directly to woven fabrics, as the model essentially solves for flow along layers of unidirectional tows. In the model, each NCF was modelled as a number of unidirectional layers, for which the permeability for the layer parallel to the flow was calculated using the model and the permeability of the layer transverse to flow was calculated by averaging the transverse permeability of the tows and the free channels. The free channels were assumed to have a transverse permeability equivalent to $h^2/12$, h being the height of

the channel. The total permeability of the NCF was the average of the layer permeabilities. The predicted permeability values were also shown to be very sensitive to the channel size.

Delerue et al. (2003) used 3-dimensional X-ray images of a glass woven laminate to create a representative pore network model of the laminate and calculated the permeability of the reinforcement. The predicted permeability value appears to be in the same order of magnitude as experimental values. Yu et al. (2002) utilised microscopic cross section images of four different types of fabrics to relate to a fractal model representative of the fabrics. They compared the predicted permeabilities with both experimental data and a simplified analytical model for a range of porosities. A good agreement was found for the four types of fabrics studied. However, such imaging methods are generally time consuming and not very productive in analysing a wide range of fabrics.

2.6.1 Variability modelling

All of the models reviewed above attempted to predict a single permeability value for each fabric analysed, or a permeability value for each fibre volume fraction. However, as described earlier in this chapter, textile preform permeability values reported in the literature generally show a broad distribution. In an attempt to model the variations observed experimentally, Endruweit and Long (2005) assumed that the variation in local permeability is primarily caused by stochastic variations in fibre spacing, from which local permeability values can be calculated. Injection simulations at the component level were then simulated for a bi-directional non-crimp fabric for a range of variations in fibre spacing to determine the global permeability variations. A trend was found between relative permeability variations and the maximum frequency of fibre tow waviness, which agreed with the experimental values. In general, the global permeability variation decreased with increasing mould dimensions.

The above attempted to describe the variations at the macroscopic level. It is equally important to address variability at the mesoscopic level. As described earlier in the chapter, a fabric is essentially defined by its structure and only by looking at the

mesoscopic level can one analyse the effect of fabric architecture on variability and address issues such as localised inhomogeneities.

Using optical microscopy and X-ray micro-computed tomography, Desplentere et al. (2005) measured geometrical parameters of the fibre bundles in 3D textiles. Considerable variations were found for these geometrical dimensions. Lundstrom et al. (2004) determined the local permeability of non-crimp fabrics from the dimensions of the flow channels with variable widths between the fibre tows. For a completely random distribution of the local permeability values, the global permeability was found to decrease with increasing maximum variation at the unit cell level, while for a correlated distribution, the permeability can either increase or decrease. To further study the effect of geometry variations on local permeability, Nordlund and Lundstrom (2005) modelled the meso-scopic channels of a non-crimp fabric with variations in width, height and shape of the channels and the effect of the presence of stitches. The study identified the geometric parameters that have the greatest effect on the local permeability. In order to realistically predict flow in a non-crimp fabric (NCF), the effects of the stitching process and statistical variations of the channel dimensions have to be included in the model.

2.6.2 General approach to numerical modelling

One major drawback of all the studies reviewed above is that the models were demonstrated for only one fabric in the study. None has explicitly cited the applicability of the methods to a generic fabric structure with confidence. Perhaps more importantly, none of the models have been shown to be capable of predicting the permeability based on changes in fibre architecture.

A generic approach which can model various types of fabrics and predict the effects on permeability of factors such as nesting, fibre volume fraction and tow shape would be much more useful. Currently, two research groups have demonstrated such a generic model. One is the author's research group where the permeability modelling work described in this thesis is based on the generic approach. The other group is Lomov and co-workers (Lomov et al. 2001, 2004, Belov et al., 2004, Laine 2005).

Lomov et al. (2001) described the development of a textile geometric model called WiseTex, which can be used to construct models for various woven and knitted fabrics. These geometry models can be fed into permeability models and meso-mechanical models to predict permeability and mechanical behaviour respectively. The Lattice Boltzmann method (LB) was used to predict the permeability of fabric models generated using WiseTex (Belov et.al, 2004). They validated the LB approach by predicting the permeability for axial and transverse flow within arrays of parallel fibres and showed a good comparison with analytical calculations. They then proceeded to model a plain weave fabric using WiseTex and obtained a reasonable comparison with experimental values, although the computed values were chosen from a range of permeability values for different configurations in the nesting of the fibre layers. While the LB method can be accurate, it is also very computationally intensive.

2.7 CURRENT DEVELOPMENTS

There is a substantial body of knowledge regarding flow through porous media in the literature. Permeability characterisation either by experiments or computer analysis has come a long way since it was first applied to composites manufacturing around 30 years ago. There is a better understanding now about the various factors affecting the permeability of a fibrous material and how these can be manipulated to successfully manufacture a composite part.

While research interest has continued to grow in numerical simulation and analytical description of the flow process, its application in industry is still limited. The composites industry still depends primarily on experience and expertise. Filling simulations for industrial parts require a large amount of data to describe the permeability, accounting for factors such as local shear, local compaction, multi-layer nesting, ply drop-offs and also the statistical nature of the fabric. Cost considerations dictate that for a successful industrial simulation, the software must be easy to use, cover virtually all types of reinforcements, and be reliable and fast. So far, no model fits all of these criteria.

A significant gap that can be observed is that draping and flow models have always been developed independently of one another, although it is known that the deformation of the fabric during the preforming stage has a profound effect on the permeability distribution across the preform. Only a small number of authors have tried to link the two models, notably as first demonstrated by Long (1994).

Another noted deficiency is that the current simulations provided a single answer to any given problem. Due to the nature of statistical variations in the structure of the textile reinforcements, the filling patterns and cycle times during mould filling are rarely the same between a given set of identical mouldings.

The focus of this work is to develop a generic model which can describe various types of fabrics and account for the effects on permeability of factors such as variations in tow shape, fabric shear and nesting in multi-layer preforms. A model with these capabilities would be able to bridge the gap between the draping and flow simulations across the preform as well as account for the inherent variability of the textile structure. Currently, apart from the author's research team, only one other group have demonstrated such a generic model, i.e. Lomov and co-workers, as described above.

This work proposes two novel and efficient approaches to predict permeability. The aim is to develop fast calculation methods which can accurately describe the permeability of different textiles given a number of variables and perturbations. These permeability modelling approaches are outlined in the next chapter along with an overview of other computation models used in this work. The overall strategy of the generic models is also discussed towards the end of the chapter.

3 NUMERICAL PERMEABILITY MODELS

3.1 INTRODUCTION

As described in Chapter 2, the numerical approach to predict permeability offers much more flexibility than analytical solution in terms of its ability to be adapted to various types of fabrics. A typical numerical prediction of fibre preform permeability begins with the modelling of the structure of the preform, which should closely replicate the real fabric. The flow behaviour of resin through this structure is then simulated using computational methods. Finally, the effective permeability is back calculated from the resultant pressure profile using Darcy's law.

Two simple and efficient numerical approaches to predict permeability based on the textile reinforcement structure, the Stream Surface and Grid Average methods, developed by the author are described in this chapter. Both the approaches make use of the fact that flow in LCM is slow and laminar, allowing simpler equations to be used to characterise the flow. Less complicated calculation means less computational time. The strength of these two approaches lies in their speed. Due to the inherent variability of textiles, a large number of simulations are needed to fully characterise the permeability distribution. As such, a prerequisite of any successful permeability model is efficiency.

Both of these approaches were implemented within an integrated framework encompassing draping, compaction and impregnation, based on the TexGen textile schema. TexGen is a geometric textile modeller that can be used to generate a wide range of textile models. Its in-built functions include in-plane shear deformation and tow variability that can be introduced into the textile model. An overview of TexGen is given at the beginning of this chapter.

Finally, the use of CFD (Computational Fluid Dynamics) as a comparison tool within the context of this work is also reviewed. CFD is the natural choice of computational tool to perform the numerical calculation of the flow. It is a well established approach, and is proven to provide reliable results, certainly for slow, laminar flow, as evident in LCM processes. Several software packages are available commercially.

However, CFD simulations can be computationally expensive as they solve the full set of Navier-Stokes equations of motion. The speed of CFD calculations as well as issues with generating a good mesh of the fabric model can be a deterrent to using this approach to generate large sets of permeability values.

3.2 GEOMETRIC MODELLING OF THE TEXTILE STRUCTURE

One of the critical steps in numerical permeability models is the geometric description of the fabric structure. It is crucial that there exists a modeller which can create realistic textile models and also be flexible enough to be used as a platform to study the effects of textile deformation and variability.

3.2.1 TexGen

The Polymer Composites Research Group in the University of Nottingham has created a textile schema, named TexGen. The prerequisites of this software were to be able to:

i) model various types of textile structures
ii) export the model for use in a general CAE software package

More information about the intricate workings of TexGen can be found in various papers written by Sherburn et al (2004) and Robitaille et al. (1999, 2003). As this is not the author's own work but is a critical prerequisite to the work described in this thesis, a brief description of TexGen is given here.

TexGen begins with vectors describing the path taken by the tows within a textile unit cell (see Figure 3.1). These are then connected to create smoothed path lines (using Bezier curves), for which user-defined cross sections can be assigned individually to each path line to form the tow volumes. Finally, an analysis domain can be defined around the unit cell. Pre-defined types of cross sections available in TexGen include circles, ellipses, shapes produced using the generalised ellipse equation (see Appendix B) and lenticular shapes (the shape of a double-convex lens). It also allows the user to import self-defined tow shapes.

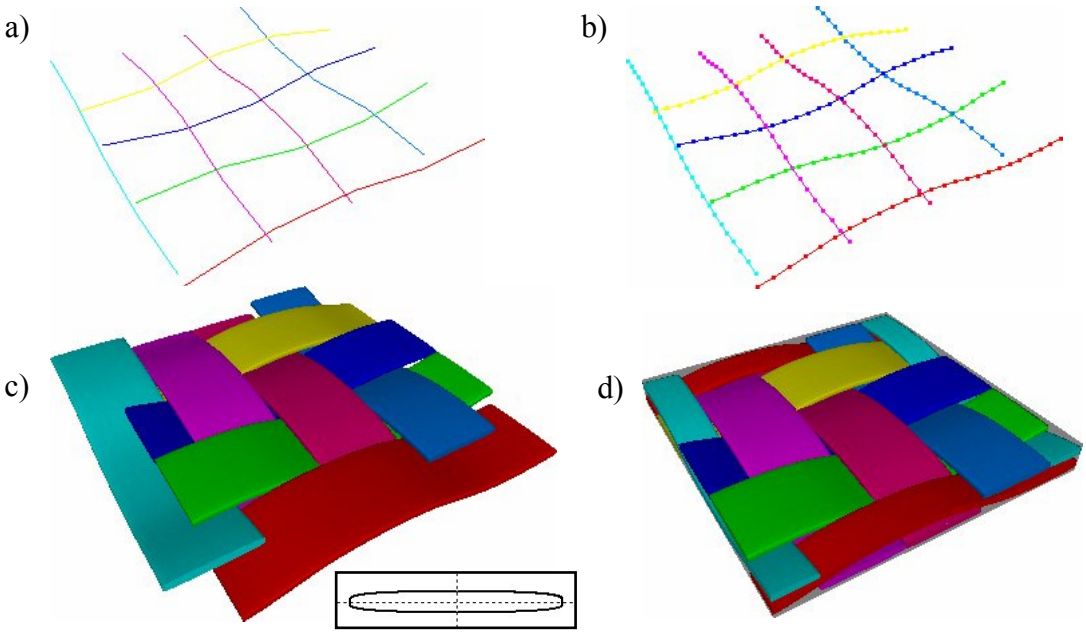

Figure 3.1 – Steps to generate a fabric model in TexGen: (a) Vectors defining the weave pattern. (b) Smoothed path lines from vectors. (c) Cross section (inset) applied to path lines to create tow volumes. (d) Analysis domain of repeatable unit cell.

Some of the built-in functions include tow interference detection and correction algorithms, volume calculation and slice extraction. In-plane shear deformation may also be applied to represent the effects of draping and the tow paths can be randomised with respect to a specified distribution to emulate the variability seen in textiles.

There are a variety of output options. One of these is an ACIS '.sat' file, for import into pre-processors to create a mesh of the model. The ACIS library (Spatial Corporation website, 2006) consists of a set of core functions for creating 3D structures and is the backbone of many CAD packages. TexGen can also write a text-based script file for use with the GAMBIT™ pre-processor which is part of the FLUENT® CFD package (see Section 3.3) to generate the required 3D mesh model. These 3D meshes can be used for both flow and structural analyses.

Tied into TexGen are also the options of generating the data files for the Stream Surface and Grid Average approaches. These are described in Sections 3.3 and 3.4 respectively.

3.3 STREAM SURFACE APPROACH

The Stream Surface approach is based on the assumption that in a textile flow domain, a network of interconnected Stream Surfaces representing the planar movement of the resin can be identified. A requirement of this is that flow is slow and uniformly driven in one direction. This is true within a LCM process, where the resin is normally driven by the pressure difference created by the injection pressure at the inlet and the open outlet vent, and the operating pressure is low, in the range of 1 to 10 bar.

In the Stream Surface approach, the flow domain is first divided into distinct individual free and porous volumes. A bisecting curvilinear plane in the direction of the pressure gradient is identified and discretised for each of the individual volumes. The discretised nodes on each curvilinear plane will have associated local heights and, in the tow regions, local permeability tensors. The nodes on the edges of each plane which lie on the same perpendicular plane are connected by virtue of the conditions that they have the same pressure. These interconnected meshed planes form the Stream Surface mesh. The steps to generate a Stream Surface mesh are illustrated in Figure 3.2.

The Stream Surface represents a collection of individual flow paths through the open and porous regions. These flow paths are coupled at the boundaries where they would either divide or merge into one or several other flow paths. Apart from that, there is no other interaction between the separate Stream Surfaces.

The 3D flow domain has essentially been reduced to 2.5D and the mesh is generated automatically in TexGen. 2.5D in this context means that the Stream Surfaces are 2D curvilinear planes suspended in 3D space. The same Stream Surface principle can be applied to 2D cross section slices through a textile model, which will reduce it to a 1.5D Stream Surface mesh, i.e. 1D curvilinear lines suspended in 2D space (see Figure 3.3). The Stream Surface approach provides a way of representing the flow domain of a textile fabric in a simpler fashion.

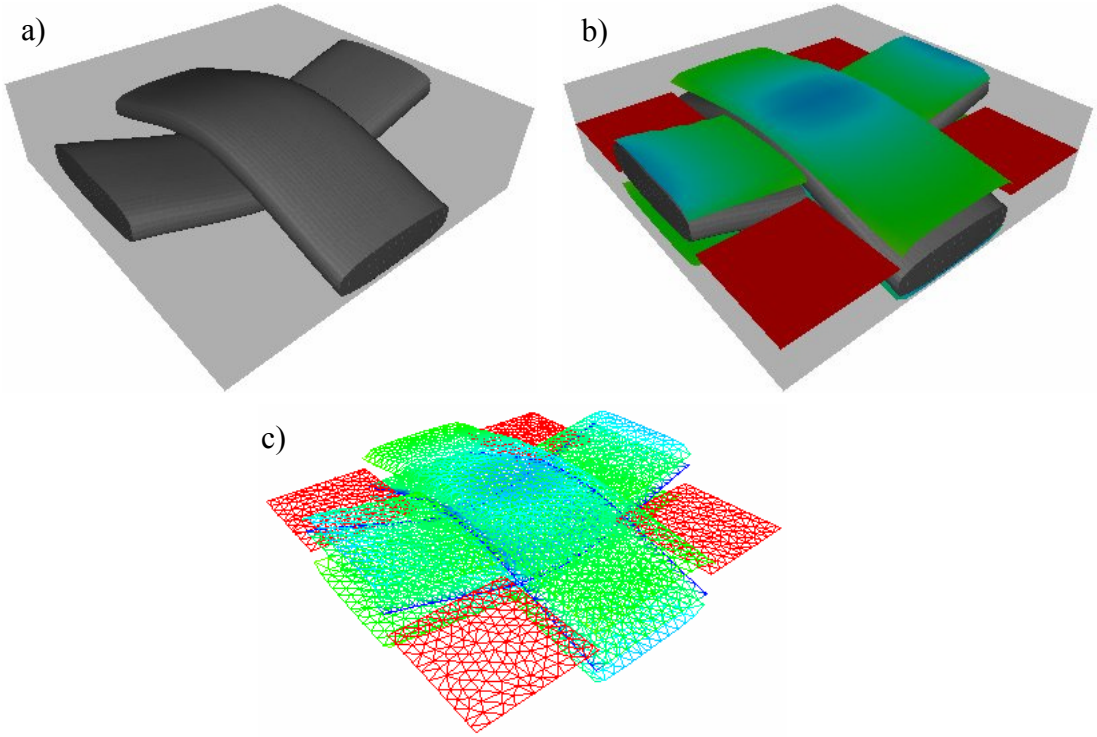

Figure 3.2 – Schematic of the steps to generate a 2.5D Stream Surface mesh: (a) Analysis domain. (b) Bisecting curvilinear planes identified for individual basic porous and open volumes. (c) Resultant 2.5D Stream Surface mesh. Note that there are Stream Surfaces representing the porous tows. The colour of the Stream Surfaces corresponds to the original basic volume height it represents, where the height decreases from red to blue.

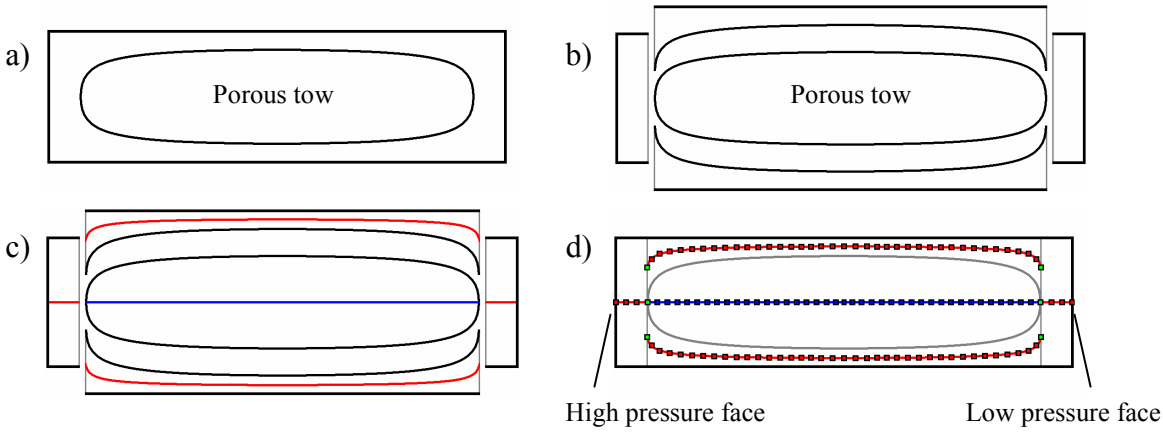

Figure 3.3 – Schematic of the generation of 1.5D Stream Surface mesh for a 2D single tow case. (a) The initial analysis domain. Exploded views showing (b) the identification of basic flow volumes and (c) the identification of the bisecting curves. (d) The final 1.5D Stream Surface mesh.

A main assumption in Stream Surface is that an effective permeability value can be assigned to the free spaces surrounding the tows. Flow through these spaces is approximated to laminar flow between two stationary plates, for which the flow profile can be described mathematically as shown in Appendix C. The mean flow velocity in a channel of height h due to pressure gradient is given as,

$$\bar{u} = -\frac{h^2}{12}\frac{dP}{dx} \tag{3.1}$$

By comparing this to Darcy's law (Eqn. 2.4), the free space permeability can be approximated to $h^2/12$, h being the height of the space measured perpendicular to the flow direction. The tows are modelled as unidirectional fibres locally. The local permeability tensor of the tows is calculated automatically using the Gebart analytical model (see Eqns. 2.11 and 2.12) for a given fibre volume fraction using either a quadratic or hexagonal fibre arrangement.

As each of the nodes on the Stream Surfaces will have an associated permeability value, Darcy flow is solved over the interconnected domain. An existing LCM flow code, LIMS, has been used to solve for flow through the 2.5D Stream Surface. LIMS is a LCM flow solver developed at the University of Delaware, based on the finite element/control volume method to simulate Darcy flow (Gokce and Advani, 2005). The use of LIMS is an attractive option in that it is an established solver and it allows the user to observe the flow behaviour at the mesoscopic level. The input files into LIMS can be generated automatically from TexGen. An added advantage of using third party flow codes is that this can demonstrate the transferability of the Stream Surface approach across different platforms.

However, one minor drawback of using LIMS is that it always models a no-leakage boundary condition at the boundaries of each of the separate stream surfaces. Periodic boundary conditions can only be implemented by modifying the code. Also, in order to interconnect between the Stream Surfaces, the boundaries which lie on the same perpendicular plane are connected using elements that are very thin and have a

high permeability, so that the flow through them will be fast and consequently should not affect the overall flow behaviour.

An in-house solver has been written for the solution of the 1.5D Stream Surface. It is based on finite difference and solves Darcy's equation coupled with the continuity equation. The workings of the solver are described in Section 3.5. The discretisation of the governing equations for the 1.5D Stream Surface is further detailed in Appendix F, which also includes the program listing. Again, the input file is generated automatically using TexGen. The attraction in developing an in-house solver is that it allows a higher degree of control over the solution method. In particular, the inter-connectivity between the Stream Surfaces is hard-coded into the solver (see Appendix F) and, unlike in LIMS, does not require additional elements to connect them.

3.4 GRID AVERAGE APPROACH

The Grid Average concept was born from the need to negate the limitations of meshing as described in Section 3.6.2. It is based on the same principles as Stream Surface, but here the flow domain is simplified further.

In the 2D version of Grid Average, the flow domain is discretised into a regular square grid in the x-y plane, as shown in Figure 3.4a, where flow is solved along either the global x or y axis. The local permeability tensor and fibre volume fraction of each grid element are then calculated as a thickness-weighted average of the properties of the respective layers contained within each element:

$$\overline{K}_{ij} = \frac{1}{H}\sum_{m} h_m K_{ij\,m} \tag{3.2}$$

$$\overline{V}_{f} = \frac{1}{H}\sum_{m} h_m V_{f\,m} \tag{3.3}$$

where H is the domain thickness, and h_m, $K_{ij\,m}$ and $V_{f\,m}$ are the thickness, permeability tensor and fibre volume fraction respectively for each constituent layer in the grid. Again, similar to the Stream Surface approach, a permeability value is assigned to

the free spaces surrounding the tows. This enables the solution of the flow using Darcy's law. The free channel permeability is approximated to $h^2/12$, h being the channel height. The tows are modelled as arrays of unidirectional fibres locally, for which the permeability tensor components are calculated using the Gebart model (Eqns 2.11 and 2.12) for known fibre volume fraction. To account for tow directionality, the tow permeability tensor components in the global axes are calculated using vectors rotation (see Appendix D). Figure 3.4b shows an example of a discretised 2D Grid Average mesh.

Such a concept of averaging permeability is not new, notably described by Scheidegger (1974). Long et al. (1998) approximated a bi-directional fabric to two layers of unidirectional fabric and used the averaging law to calculate the effective permeability. The flow problem in this case has been reduced from a 3D model onto a 2D plane mesh.

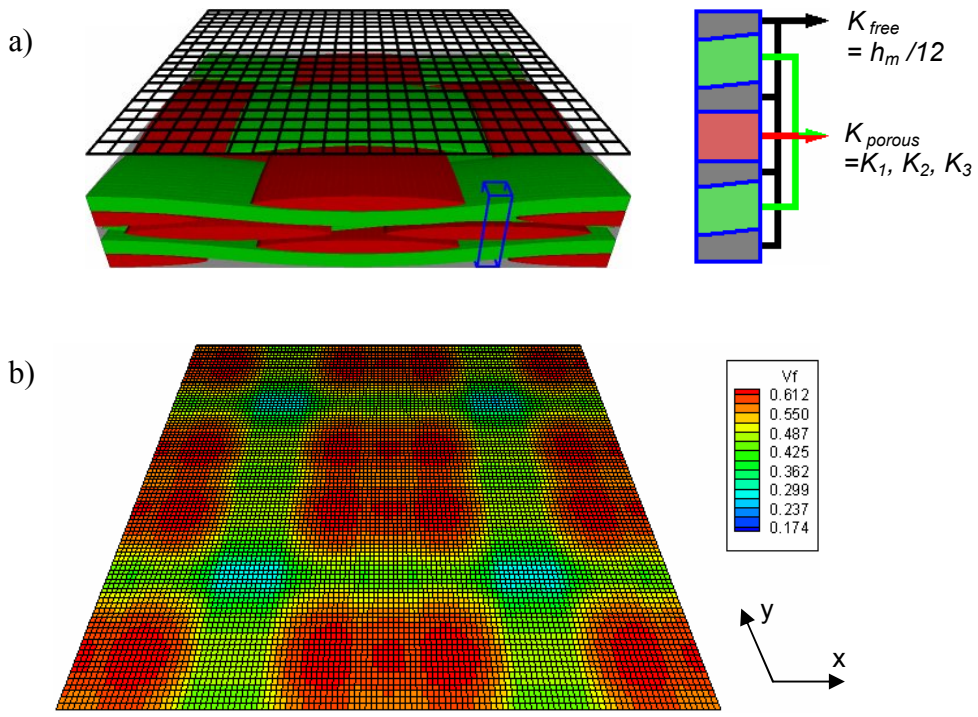

Figure 3.4 – (a) Grid Average method applied to a nested plain weave fabric model. Right: calculation of the effective elemental permeability based on the constituent layers. (b) The model discretised using Grid Average in 2D with 10 divisions/unit showing fibre volume fraction distribution. Flow is solved along either the global x or y axis.

The Grid Average approach can be expanded to a more complex version in 3D space, whereby a number of regularly-sized cube elements are generated through the thickness (see Figure 3.5). As for the 2D method, each of these cube elements will have an associated permeability tensor and fibre volume fraction calculated using Eqns. (3.2) and (3.3) as a thickness-weighted average of the properties of the layers contained in each cube element. An important detail when accounting for the permeability of the open spaces in 3D Grid Average is that the height h used to calculate the free space permeability must be that of the overall open space rather than just the portion contained in the respective cube element.

The 2D Grid Average approach evaluates the flow domain in a very simplified manner, whereby the intricate effects of the textile preform structure are averaged across the thickness, sufficient for determining the permeability of the unit cell. However, in order to visualise resin flow behaviour in a textile preform, the 3D Grid Average method is more useful.

An advantage of the Grid Average approach over the Stream Surface method is that it utilises a regular grid mesh, simplifying the solution of the flow equations and reducing the calculation time. As such, a stand alone flow solver can be used even for relatively complex 3D Grid Average domains with multiple fabric layers. This in-house code is based on finite difference and solves Darcy's equation coupled with the continuity equation. The solution of the governing equations using finite differences is further detailed in Section 3.6 and Appendix E, and the program listing can be found in Appendices G and H. Unlike using LIMS, the boundary conditions can easily be modified to suit the problem (e.g. periodic boundary conditions). The input file (designated .grd) for the solver is generated automatically in TexGen. TexGen divides the flow domain into smaller divisions as specified by the user. It then identifies and outputs the type and height of the constituent layers within each of the divisions. The flow domain dimensions are also provided automatically. Alternatively, LIMS can still be used to simulate and observe the flow behaviour through the Grid Average mesh. The in-house FD solver includes a function to automatically generate Grid Average meshes and property data in LIMS input file format.

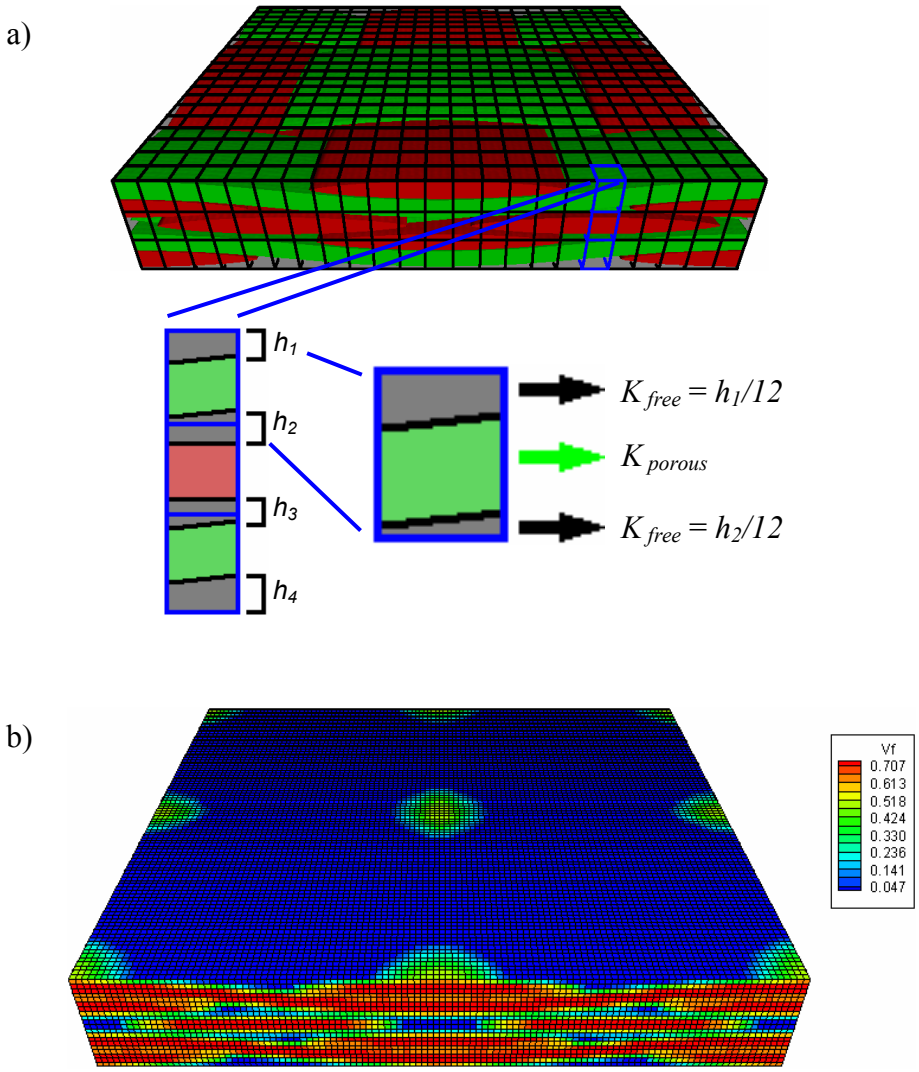

Figure 3.5 – (a) 3D Grid Average method applied to a nested plain weave fabric model. Below: calculation of the effective cube permeability based on the constituent layers. (b) The model discretised using 3D Grid Average with 10 divisions/unit showing fibre volume fraction distribution.

3.5 SOLUTION OF THE PRESSURE FIELD

One of the objectives of this project was to create an efficient, self contained solution procedure. Whilst the permeability modelling methods were developed to be compatible with using third-party software for flow calculations, it is desirable to have a stand-alone code to minimise computation time and to allow full control of material properties and boundary conditions.

3.5.1 Governing equations

As both the approaches described in the previous sections have the proposition that a finite permeability value can be assigned to each individual node, the governing equations for flow are Darcy's law (Eqn. 3.4) coupled with the continuity equation for incompressible flow (Eqn 3.5):

$$\mathbf{u} = -\frac{[K]}{\mu}\nabla P \tag{3.4}$$

$$\nabla \cdot \mathbf{u} = 0 \tag{3.5}$$

Whilst the above two equations are applicable in 3D space, the derivation in 2D space are shown here for brevity. See Appendix E for the full set of equations in 2D and 3D. Eqns. (3.4) and (3.5) are written in matrix form for 2D space as:

$$\begin{pmatrix} u_x \\ u_y \end{pmatrix} = -\frac{1}{\mu}\begin{bmatrix} K_{xx} & K_{xy} \\ K_{yx} & K_{yy} \end{bmatrix}\begin{pmatrix} \frac{\partial P}{\partial x} \\ \frac{\partial P}{\partial y} \end{pmatrix} \tag{3.6}$$

$$\frac{\partial u_x}{\partial x} + \frac{\partial u_y}{\partial y} = 0 \tag{3.7}$$

For flow through a section with changing height h (cross section area), the continuity equation that needs to be solved becomes:

$$\frac{\partial (u_x h)}{\partial x} + \frac{\partial (u_y h)}{\partial y} = 0 \tag{3.8}$$

After substituting the continuity equation into Darcy's law, the governing equation for the pressure distribution becomes:

$$\frac{\partial}{\partial x}\left(F_{xx}\frac{\partial P}{\partial x}\right)+\frac{\partial}{\partial x}\left(F_{xy}\frac{\partial P}{\partial y}\right)+\frac{\partial}{\partial y}\left(F_{yx}\frac{\partial P}{\partial x}\right)+\frac{\partial}{\partial y}\left(F_{yy}\frac{\partial P}{\partial y}\right)=0 \tag{3.9}$$

where either $F_{ab}=\frac{K_{ab}}{\mu}$

or $F_{ab}=\frac{K_{ab}h}{\mu}$ for flow through sections with changing height (see Eqn. 3.8).

3.5.2 Finite difference discretisation and boundary conditions

The finite difference method is applied to the governing equation as detailed in Appendix E. Again for brevity, only the equation in the 2D space is shown here, the derivation in 3D can also be found in Appendix E. The finite difference implementation of Eqn. (3.9) expressed in terms of pressure is (Eqn. E.24 in Appendix E),

$$\begin{aligned}
&P_{i-1,j-1}\left(\frac{F_{xy\,i,j}+F_{yx\,i,j}}{4\Delta x\Delta y}\right)+P_{i,j-1}\left(\frac{F_{yy\,i,j}}{\Delta y^2}\right)+P_{i+1,j-1}\left(-\frac{F_{xy\,i,j}+F_{yx\,i,j}}{4\Delta x\Delta y}\right)\\
&+P_{i-1,j}\left(\frac{F_{xx\,i,j}}{\Delta x^2}\right)\\
&+P_{i,j}\left(-\frac{F_{xx\,i,j}+F_{xx\,i+1,j}}{\Delta x^2}-\frac{F_{xy\,i+1,j}+F_{yx\,i,j+1}-F_{xy\,i,j}-F_{yx\,i,j}}{4\Delta x\Delta y}-\frac{F_{yy\,i,j}+F_{yy\,i,j+1}}{\Delta y^2}\right)\\
&+P_{i+1,j}\left(\frac{F_{xx\,i+1,j}}{\Delta x^2}+\frac{F_{yx\,i,j+1}-F_{yx\,i,j}}{\Delta x\Delta y}\right)\\
&+P_{i-1,j+1}\left(-\frac{F_{xy\,i,j}+F_{yx\,i,j}}{4\Delta x\Delta y}\right)+P_{i,j+1}\left(\frac{F_{xy\,i+1,j}-F_{xy\,i,j}}{\Delta x\Delta y}+\frac{F_{yy\,i,j+1}}{\Delta y^2}\right)+P_{i+1,j+1}\left(\frac{F_{xy\,i,j}+F_{yx\,i,j}}{4\Delta x\Delta y}\right)=0
\end{aligned} \tag{3.10}$$

where $F_{ab}=\frac{K_{ab}}{\mu}$ and i, j are coordinates in Cartesian space.

Periodic boundary conditions are imposed on the x and y limits of the computational domain. At the inlet and outlet faces, this takes the form of a prescribed pressure difference, ΔP, in a direction parallel to either the global x or y axes dependent on the direction of the permeability to be evaluated. Thus, the nodes on the opposing inlet and outlet faces would satisfy

$$P_{inlet} - P_{outlet} = \Delta P \tag{3.11}$$

For the sides parallel to the imposed pressure drop, periodic boundary conditions take the form of equivalent pressure on corresponding nodes on the two opposing faces.

For the 3D Grid Average, an additional assumption is that there is no leakage through the upper and lower mould walls of the domain. The resultant boundary condition requires that the velocity component normal to the upper and lower mould walls is zero at the mould walls, and for an anisotropic medium the following condition holds,

$$\bar{u}_n = -\frac{1}{\mu}\left(K_{nn}\frac{\partial P}{\partial n} + K_{nt}\frac{\partial P}{\partial t} \right) = 0 \tag{3.12}$$

where n denotes the direction normal to the mould walls and t is direction tangential to the mould walls.

The finite difference solution for Stream Surface was implemented in 1.5D space only, which is 1D flow in 2D space. As described for the Stream Surface meshes, the nodes on the edges of the Stream Surfaces which lie on the same perpendicular plane have the same pressure. The solution of pressure for Stream Surface uses Equation (3.8) for mass conservation because the representative height of the Stream Surface elements is changing. See Appendix F for further detail on the finite difference discretisation of the equations for 1.5D Stream Surface flow. The numerical solution procedure to be described in the next section applies equally to the 1.5D Stream Surface, 2D and 3D Grid Average methods.

3.5.3 Numerical solution

The governing equation (Eqn 3.10) with the appropriate boundary conditions applied to a flow domain results in a set of simultaneous equations given in matrix form as:

$$[A]\cdot[P]=[x] \tag{3.13}$$

where [A] is the sparse symmetric matrix of coefficients, [P] is the pressure vector and [x] is the right-hand side vector. This system of equations is solved for the pressure field in the saturated flow domain using a routine for sparse system adapted from *Numerical Recipes in C* (Press et al., 1994) based on the conjugate gradient method.

Once the pressure distribution in the flow domain is known, the averaged velocities across either the inlet and outlet faces are calculated by,

$$\bar{u}=\frac{1}{A_0}\sum_{i=1}^{n}-\frac{K_i A_i}{\mu}\left(\frac{dP}{dx}\right)_i \tag{3.14}$$

where K_i, A_i and $(dP/dx)_i$ are the local permeability, area and pressure gradient of the inlet or outlet node i respectively. A_0 is the total inlet or outlet area. The velocity is then back substituted into Darcy's equation to find the effective permeability of the domain,

$$K_e=-\bar{u}\cdot\mu\frac{\Delta L}{\Delta P} \tag{3.15}$$

L here denotes the length in the direction of the flow. A flow chart for the numerical solution of the pressure field and the calculation of effective cell permeability is shown in Figure 3.6.

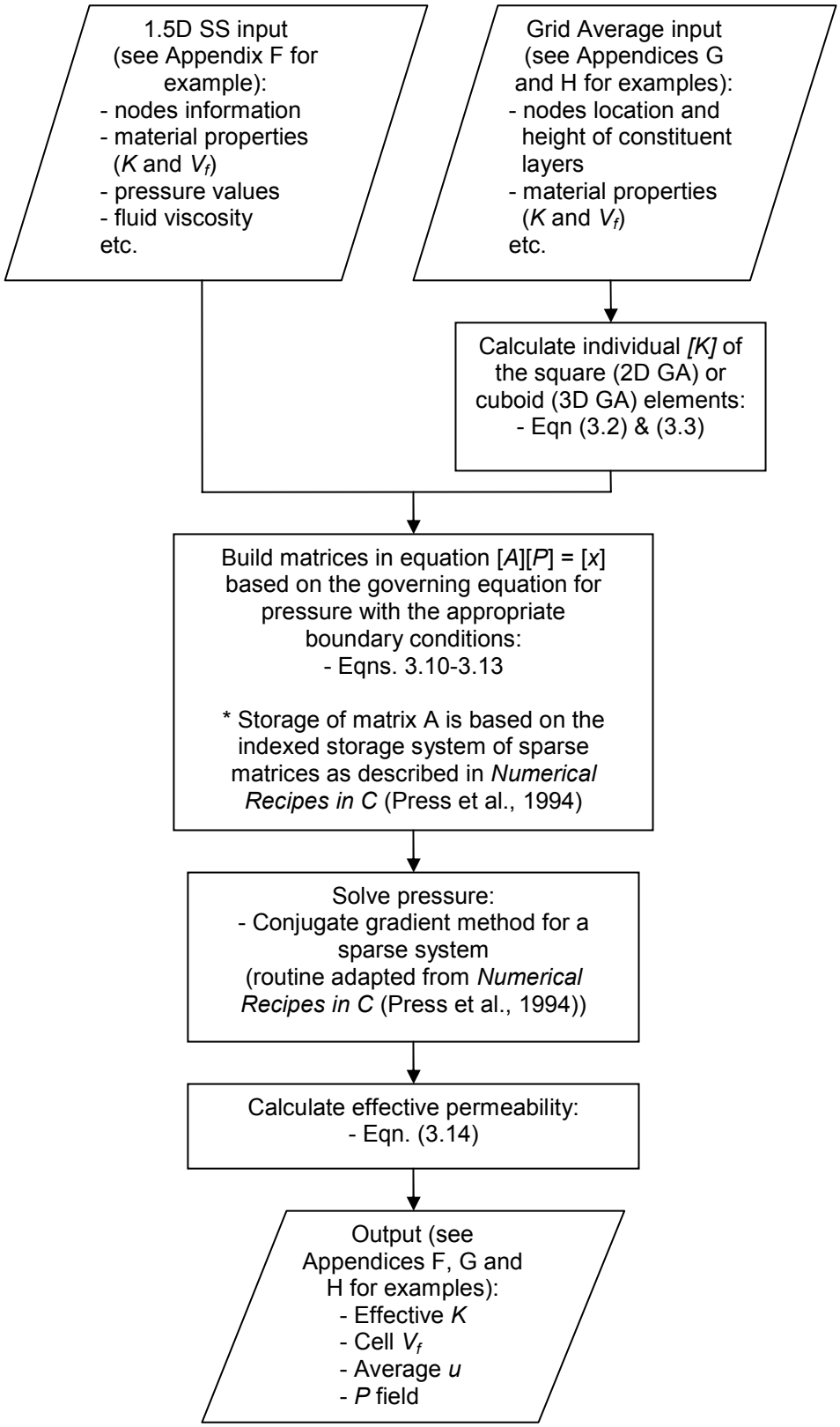

Figure 3.6 – Flow chart of the numerical solution for permeability.

3.6 ON THE USE OF CFD (COMPUTATIONAL FLUID DYNAMICS)

CFD (Computational Fluid Dynamics) provides the most rigorous approach to analyse fluid dynamics problems computationally, solving the full set of equations of motion. This also means that it will require a longer time to obtain the solution compared to the two in-house approaches, Grid Average and Stream Surface. In this project, CFD simulations were used mainly for comparison to the Grid Average and Stream Surface methods. The validity of using CFD results as a benchmark will be discussed further in Chapter 4. A brief description of the CFD software used in this work, FLUENT®, is undertaken here. Details of CFD in general are covered in many textbooks, such as Anderson (1995) and Ferziger and Peric (1999).

3.6.1 FLUENT®

A commercial CFD software package marketed by Fluent Inc. is used in this project. It includes a pre-processor, GAMBIT™, and the CFD solver with the company name which also has advanced post-processing capabilities. FLUENT® solves the Navier-Stokes equations of motion using the finite volume method. It has an extensive range of physical modelling and multiphysics capabilities, including adaptive meshing, turbulence models, heat transfer, and multiphase models.

GAMBIT™ takes either the script (.jou) or the ACIS (.sat) files from TexGen to generate a similar fabric model and meshes it with elements. This is then exported to FLUENT® to simulate the resin flow behaviour. The resin is modelled with a constant viscosity of 0.308 Pa s and density of 1000 kg m^{-3}. The fibrous tows are modelled locally as an array of unidirectional fibres whereby the local tow permeability for a given fibre volume fraction are calculated using the Gebart model (Eqns 2.11 and 2.12). These porous regions are modelled in FLUENT® by the addition of a momentum source term to the standard fluid flow equations. For a simple homogeneous porous media, the source term is,

$$S_i = -\frac{\mu}{K} v_i \tag{3.16}$$

where S_i is the source term for the ith (x, y or z) momentum equation, μ is the fluid viscosity, K is the prescribed permeability value and v_i is the velocity. This momentum sink term is equivalent to the Darcy term. As the physical blockage of the porous medium is not represented in the model, in order to ensure continuity of the velocity vectors across the porous medium interface, FLUENT® by default uses a superficial velocity inside the porous medium, based on the volumetric flow rate.

Various types of boundaries can be prescribed in FLUENT®, such as pressure and flow rate inlets, outlet vent and symmetry. One of the more useful features is periodic boundaries, whereby periodic pressure difference can be applied, which is an essential feature in unit cell modelling. In FLUENT®, the flow at a periodic boundary is treated as though the opposing periodic plane is a direct neighbour to the first periodic boundary. Therefore, when calculating the flow through the periodic boundary, the flow conditions at the cells adjacent to the opposing periodic plane are used.

Laminar flow is modelled in the cases studied here and the default option is used for the solution of the momentum and continuity equations. The governing equations are discretised in the implicit form, where each variable are computed using a relation taking into account both new and old values from neighbouring cells, thus requiring the solution of a set of simultaneous equations.

The segregated solver is used to solve the discretised governing equations. Using this approach, the governing equations are solved sequentially. The solution begins by solving the momentum equations to obtain new values of the velocity components based on the current values of pressure (pressure is initialised at the beginning). The mass continuity equation (pressure correction) is then solved to update the pressure and velocity values, which now satisfy mass continuity but not momentum. The procedure is then repeated until the corrections used to update the pressure and velocity values (referred as residuals) become smaller and are deemed negligible. For the cases studied here, the solution is deemed to have converged when there is a reduction in the residuals of three to four orders of magnitude.

3.6.2 Advantages and disadvantages of CFD

The advantages of using FLUENT® (or any general CFD software) are:

- there is an existing support network (e.g. research papers, benchmark examples etc),
- it has a proven track record of accurately modelling general fluid flow.

The disadvantages are:

- meshing of small gaps (critical in fabric models) is a problem,
- solution can take a long time for a large model (up to days), and
- includes many functionalities which are not needed for LCM flow models.

Whilst CFD should in theory provide the most rigorous and accurate solution, it can be very difficult to generate a good mesh of the textile model. In particular, it is very hard to mesh the narrow and tortuous regions between tows, generating unsatisfactorily skewed elements in most cases.

3.7 SUMMARY

The development of a generic permeability model in this work is part of an integrated modelling strategy, as shown in Figure 3.7. This strategy uses TexGen, a generalised textile geometry model, as the basis to create virtually any type of textile model based on the fabric architecture. Integrated into TexGen is the facility to apply in-plane shear and model tow variability in the textile model. Using the textile model, mechanical properties and permeability characteristics are generated at the unit cell level. These unit cell data would then be used within structural analyses and flow simulations at the component level, providing a fully predictive environment for the design of polymer composite components.

This thesis focuses on the development of permeability models within the framework of the integrated model. One of the aims is to use the models to fully characterise fabric permeability by accounting for the effects of fabric shear and variability. By combining the predicted permeability data with draping simulations, one can perform more accurate simulations of resin flow in a component.

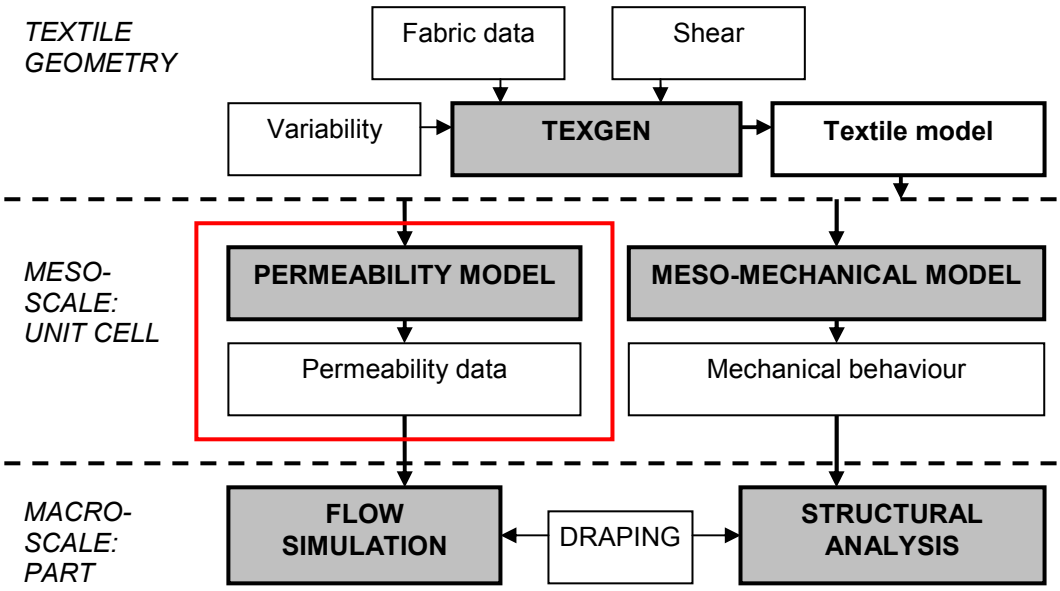

Figure 3.7 – The overall integrated modelling strategy based around TexGen.

The part related to this work is highlighted.

In order to fully characterise the permeability of a textile, a large number of calculations incorporating various factors which affect permeability are needed. Hence, the permeability modelling approach must be robust, accurate and fast if it is to be used for industrial applications. Two simplified and efficient permeability modelling approaches were described in this chapter, the Stream Surface and the Grid Average approaches, along with descriptions of other computational methods used in this work. Figures 3.7 and 3.8 schematically illustrate the two simplified approaches, how they relate to one another and what are the calculation methods used.

The analyses in 2D (Figure 3.8) form the first part of the work, where the initial verification studies are performed and described in Chapter 4. The permeability analyses using 3D textile models (Figure 3.9) are described in Chapter 5, which aims to demonstrate the applicability and capability of the 3D models. While the Stream Surface method has been developed for application in 3D space, due to time constraints, the Stream Surface method in 3D space has not been used to predict any results. Nevertheless, the theoretical basis of the approach is valid and an appropriate solution procedure can be developed in the future. Finally, in Chapter 6, the issue of

variability in fabrics is explored in detail using the Grid Average approach applied to a 3D fabric model. This work highlights the use of the approaches not only for predicting permeability but also to study localised phenomena such as void formation.

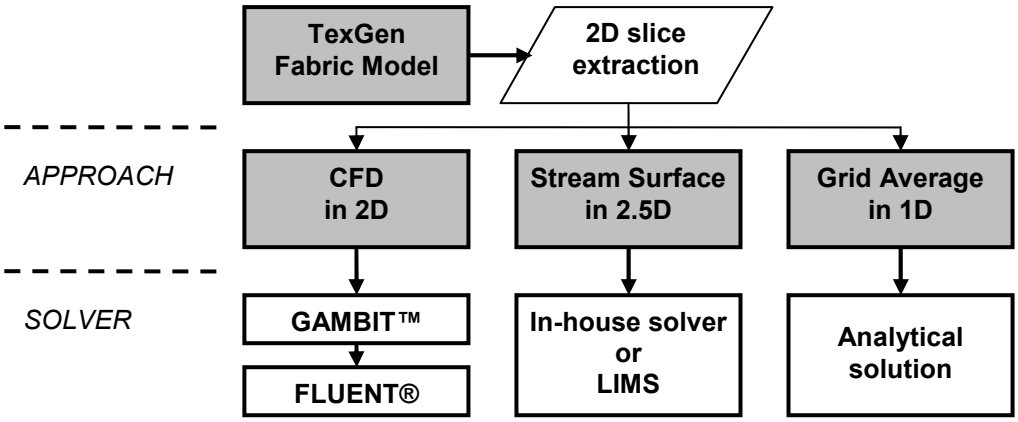

Figure 3.8 – Permeability modelling approaches for 2D slice of a fabric model.

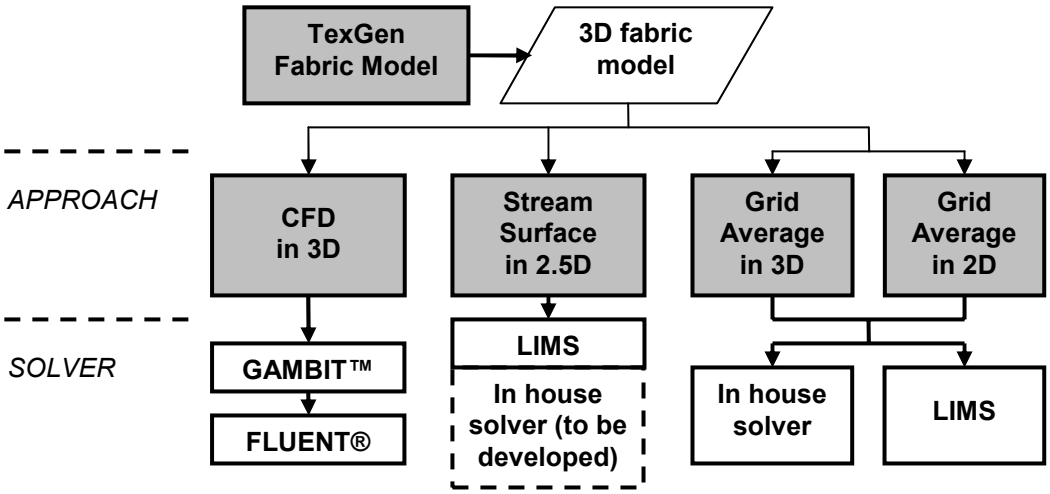

Figure 3.9 – Permeability modelling approaches for 3D fabric model.

4 SYSTEMATIC ANALYSIS OF THE EFFECTS OF TEXTILE GEOMETRIC PARAMETERS ON PERMEABILITY

4.1 INTRODUCTION

In order to build confidence in the two new approaches, Stream Surface and Grid Average, it is useful to compare the results to those generated using Computational Fluid Dynamics (CFD). While CFD would provide a more rigorous simulation of the flow behaviour by calculating the flow based on the full set of momentum equations, it will also be more computationally expensive. This chapter will demonstrate the speed advantage of the Stream Surface and Grid Average methods against CFD even for simple 2D cases. Such efficiency is imperative in LCM permeability models due to the need to generate a large amount of simulations in order to fully characterise the permeability of a fabric.

The chapter begins with an analysis of a square array of unidirectional fibres. The permeability of this fundamental problem has been described accurately by analytical equations, for a range of fibre volume fractions. As such, there are two points of reference, one being analytical solutions and the other CFD simulation. It presents the first milestone for verifying the major inherent assumption of Grid Average and Stream Surface in that flow in the free spaces can be equated to that between two flat plates, consequently giving the permeability of free space as $h^2/12$.

Proceeding from microscopic to mesoscopic level, analyses of cross sections of a single fibrous tow are described next. This introduces another level of intricacy as the permeable boundaries of the fibrous tow challenge the initial assumption of free flow. In addition, this section also provides an insight into the parameters used in constructing a textile model and in particular, how they affect the permeability. To conclude, cross sections of a textile model are evaluated to demonstrate the applicability of these methods to more complex cases.

4.2 MICROSCOPIC ANALYSIS OF A QUADRATIC ARRAY OF UNIDIRECTIONAL FIBRES

Many researchers have tackled the classical problem of an array of unidirectional fibres. Theories include using single fibre geometry, looking at the perturbation of flow around the fibre, to super cell structures, with the fibres arranged in regular geometrical arrays. Various analytical models successfully predict the Darcy permeability of an array of fibres with different fibre packing, based on the fibre radius and fibre volume fraction. Several of these models were reviewed in Section 2.5.

A quadratic array of fibres has been modelled here (see Figure 4.1). CFD, Stream Surface and Grid Average methods were used to estimate the permeability for flow perpendicular and parallel to the fibre direction for a range of fibre volume fractions. The Stream Surface and Grid Average methods within the context of this analysis will result in meshes containing the same type of information. The results generated using CFD and Stream Surface/Grid Average were then compared to those generated using Gebart's analytical model (see Section 2.5 for Equations 2.11 and 2.12).

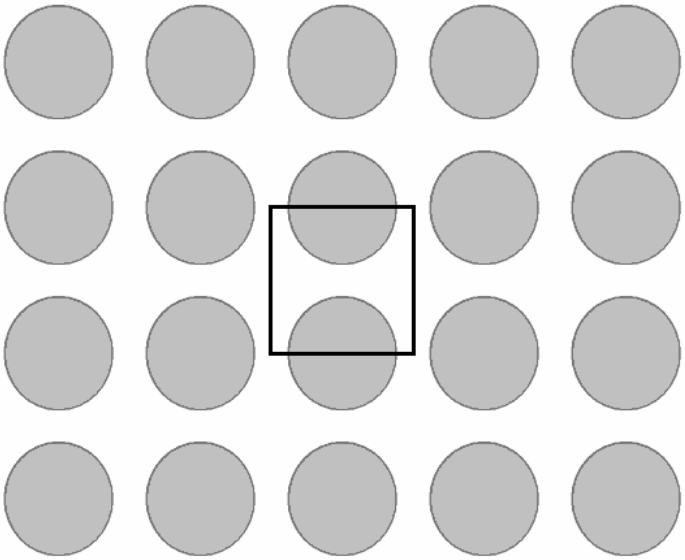

Figure 4.1 – Schematic of fibres arranged in a quadratic array with the repeatable unit cell shown.

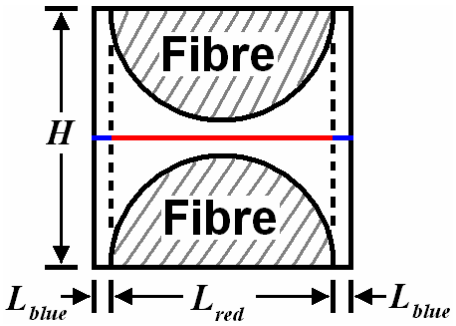

Figure 4.2 – Schematic of repeatable unit cell of a quadratic array of impermeable fibres. The red and blue lines represent the Stream Surface/Grid Average mesh.

4.2.1 Averaging of permeability

For flow perpendicular to the fibres (see Figure 4.2 for the schematic of the unit cell), the solution of the permeability of the unit cell using the Stream Surface and Grid Average methods will simply reduce to a permeability averaging equation, as will be described here. The following derivation follows that of Scheidegger (1974).

Consider first the flow through the gap between the fibres (gap shown red in Figure 4.2) of length L_{red} at a constant flow rate per unit area q. Let the length be divided into n divisions, each with a different length and height. Over the first piece of length L_1, a permeability of K_1 is assumed, over a piece of length L_2, a permeability of K_2, and so on. The pressure at the beginning of L_1 is P_0, at the junction of L_1 and L_2 it is P_1, and so on until the end of piece L_n with P_n. Darcy's law then states that for flow velocity u,

$$u_1 = \frac{K_1}{\mu}\frac{P_1 - P_0}{L_1}, \quad \ldots \quad u_n = \frac{K_n}{\mu}\frac{P_n - P_{n-1}}{L_n} \tag{4.1}$$

The flow rate per unit area q must be constant across the length L, and since the height is changing across the pieces, the flow rate per unit area is given by $q=u_i h_i$. Hence,

$$\frac{L_1 \mu q}{h_1 K_1} = P_1 - P_0, \quad \ldots \quad \frac{L_n \mu q}{h_n K_n} = P_n - P_{n-1} \tag{4.2}$$

Adding all the equations gives,

$$\mu q\left(\frac{L_1}{h_1 K_1}+\ldots+\frac{L_n}{h_n K_n}\right)=P_n-P_0 \tag{4.3}$$

Comparing this to a Darcy's equation with an effective permeability K_e and height H,

$$\frac{q}{H}=\frac{K_e}{\mu}\frac{P_n-P_0}{L_{red}} \tag{4.4}$$

One arrives at,

$$\frac{L_{red}}{HK_e}=\sum_{i=1}^{n}\frac{L_i}{h_i K_i} \tag{4.5}$$

From Appendix C, the permeability of a free gap with height h can be approximated to $h^2/12$, thus,

$$\frac{L_{red}}{HK_e}=\sum_{i=1}^{n}\frac{12L_i}{h_i^{\,3}} \tag{4.6}$$

The effective permeability for transverse flow through the space between the fibres is calculated using Equation (4.6). In order to account for the spaces before and after fibre gap (blue), the same principle of averaging was employed,

$$\frac{L}{HK_e}=\frac{L_{red}}{HK_{red}}+\left(2\times\frac{L_{blue}}{HK_{blue}}\right) \tag{4.7}$$

Since K_{blue} is very large, $L_{blue}/K_{blue}\approx 0$, which gives the effective permeability, K_e, of the unit cell as,

$$K_e=\frac{L\times K_{red}}{L_{red}} \tag{4.8}$$

4.2.2 Flow perpendicular to the fibres

Permeability for flow perpendicular to quadratic array of fibres with fibre radius of 10μm was evaluated for a range of fibre volume fractions by varying the distance between fibres. Each of the CFD meshes had between 14000 and 45000 triangular elements, while the solution for the averaging based on Stream Surface/Grid Average (SS/GA) used 200 divisions for the spacing between the fibres in each case. These optimum mesh densities were determined from preliminary mesh sensitivity studies (see Figures I.1 and I.2 in Appendix I for the results).

The results from the different approaches are compared in Figure 4.3. The predicted permeability values using the three methods are very similar at high fibre volume fraction and start to diverge as the fibre volume fraction drops below 0.4. Although Gebart's analytical model and the SS/GA methods are derived from the same basic principle, the evaluation of Stokes flow, the predicted results differ between the two. On closer examination of Gebart's derivation, an assumption was made that for flow across an array of fibres, pressure gradient changes are most significant for the spaces between the fibres only. Such an assumption will hold at high volume fraction but not at low volume fraction where the gaps between the fibres will influence the pressure distribution in saturated flow. The comparison between the Gebart and SS/GA results confirm this observation.

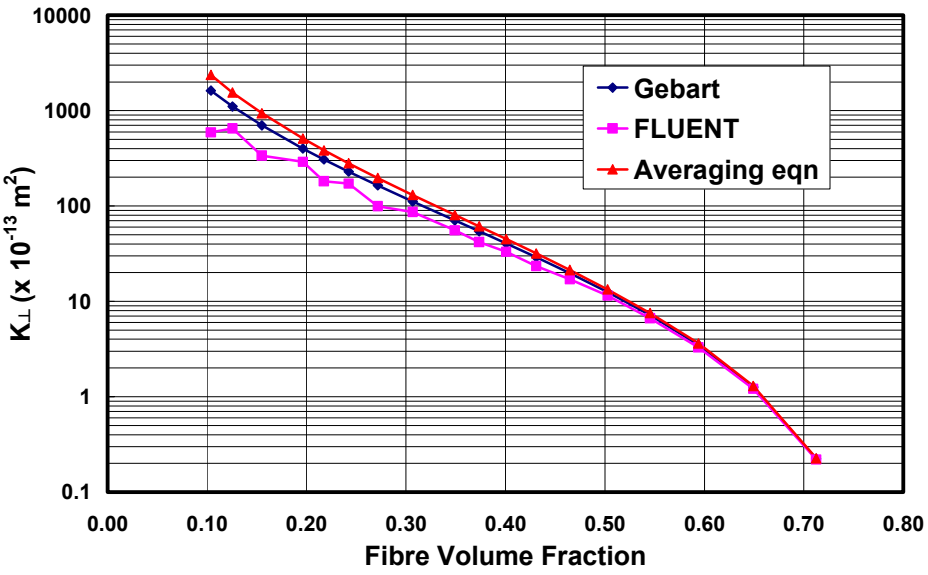

Figure 4.3 – Predicted permeability for flow perpendicular to a quadratic array of impermeable fibres.

4.2.3 Flow parallel to the fibres

The permeability for flow parallel to a quadratic array of fibres was evaluated for the same range of cases as in the above section. 2D Grid Average was used to discretise the problem (the mesh is the same if discretised using 1.5D Stream Surface), and the permeability was calculated using the in-house finite difference solver. Each of the cases has a mesh density of 10251 nodes determined from preliminary mesh sensitivity study (see Figure I.1 in Appendix I – used the same mesh density per unit as that used for flow perpendicular to the fibres). CFD analysis was not performed as the simulation did not converge satisfactorily.

Figure 4.4 compares the results predicted using Stream Surface/Grid Average to that calculated using Gebart's model. The predicted permeability values using the Stream Surface/Grid Average method accounted for flow in the area bounded by the fibres only. This is because the channels outside the boundary of the fibres have a theoretically infinite height. Therefore, if the flow in these channels is taken into account, the unit cell will theoretically have an infinite permeability for flow along the fibres. This is explained in more detail below.

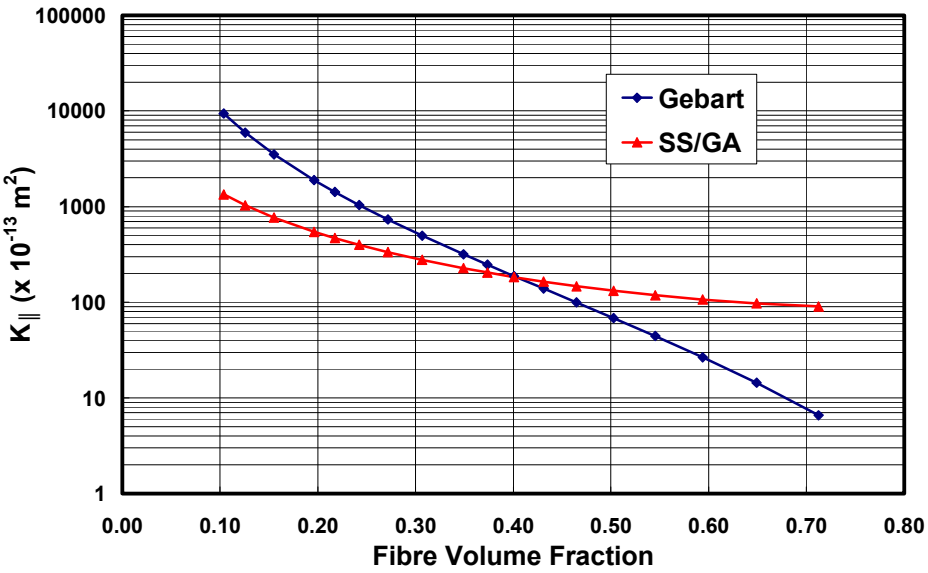

Figure 4.4 – Predicted permeability for flow along a quadratic array of impermeable fibres.

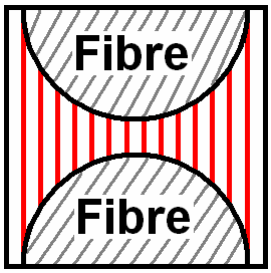

Figure 4.5 – Unit cell divided into individual channels denoted by the red lines.

The solution of flow along the fibres based on Stream Surface/Grid Average can be analysed analytically. The following derivation follows that of Scheidegger (1974). Consider the unit cell in Figure 4.5 where the resin is flowing out of the page. Divide the overall area of flow into individual channels of flow in parallel, all of equal length l. Each of these channels will have an associated permeability K_i (equals $h_i^2/12$) and cross sectional area A_i. The volumetric flow rate Q_i through the ith tube is,

$$Q_i = A_i u_i = A_i \frac{K_i}{\mu} \frac{\Delta P}{l} \tag{4.9}$$

Thus, the total flow Q through all the channels is,

$$Q = \sum Q_i = \sum A_i u_i = \left(\sum A_i K_i\right) \frac{\Delta P}{\mu \cdot l} \tag{4.10}$$

Comparing this to a Darcy's equation with an effective permeability K_e,

$$u = \frac{Q}{A} = \frac{K_e}{\mu} \frac{\Delta P}{l} \tag{4.11}$$

It is seen that the effective permeability of the system is,

$$K_e = \sum \frac{A_i}{A} K_i \tag{4.12}$$

It follows from the analysis above that the Stream Surface/Grid Average approach in this case assumes that the flow along the fibres can be divided into a collection of flows through smaller individual open channels. Such an assumption is valid if one considers flow within a homogenous porous medium, whereby the flow behaviour is roughly the same throughout the medium. However, it is not appropriate here as the flow of resin in one channel will consequently affect the flow behaviour in the adjacent channels. Also, the channels not bounded by the fibres have an infinite theoretical height h. This means that the unit cell effective permeability for flow along the fibres is theoretically infinite.

As can be seen from Figure 4.4, the two sets of results do not compare well. Gebart's approach to calculate the permeability of flow along the fibres is different from the Stream Surface/Grid Average approach. He derived the analytical solution by approximating the flow along the fibres to that in tubes with a specified cross sectional shape. A good agreement was reported between his analytical model and experimental values (Gebart, 1992), although fibre radius was used as a fitting parameter.

The non-conforming results in this section do not mean that the bases of the Stream Surface and Grid Average methods are flawed. This perhaps highlights the applicability limit of these two simple approaches to the analysis of microscopic flow problems. At the mesoscopic level however, there would not be such extreme cases. In a LCM process, the flow of resin will always have a finite boundary and the flow behaviour will be equivalent to porous medium flow.

4.3 MESOSCOPIC ANALYSIS OF PERMEABILITY FOR A 2D CROSS-SECTION OF A FIBROUS TOW

4.3.1 Permeable boundary

The flow of resin through a free channel in textiles (inter-tow gaps) is assumed to be equivalent to viscous laminar flow between two stationary solid boundaries (plane Poiseuille flow - Figure 4.6a). However, this assumption is flawed in the presence of porous tows, whereby one or more of the boundaries surrounding the open channels are permeable. There would be a migration of fluid through the permeable boundaries and the velocity at the interface will not be zero (as opposed to a stationary solid wall) – see Figure 4.6b. This would therefore increase the flow rate of fluid through a free channel bounded by a permeable boundary compared to one bounded by solid walls.

Beavers and Joseph (1967) reported on Poiseuille flow over a naturally permeable material. They obtained an expression to account for the increase in flow rate over the permeable material, based on a slip-flow boundary condition, and showed this to be in good agreement with experimental results. It follows from the paper that the fractional increase in flow rate through a channel with a permeable wall over what it would be if the wall were impermeable is

$$\Phi = \frac{3(\sigma + 2\beta)}{\sigma(1 + \beta\sigma)} \tag{4.13}$$

where $\sigma = \frac{h_i}{\sqrt{K}}$, K is the permeability of the bounding porous material and β is a dimensionless quantity dependant on the structure of the bounding porous material. β is considered to be an empirical parameter. The expression above was used to calculate an effective height for the free channel so that the solution of the flow will allow for this fractional increase in flow rate. From Appendix C, the volumetric flow rate Q in an open channel is,

$$\frac{Q}{W} = -\frac{dP}{dx}\frac{h_e^{\,3}}{12\mu} \tag{4.14}$$

The volumetric flow rate for a channel with a permeable wall is,

$$\frac{Q}{W} = -\frac{dP}{dx}\frac{h_i^{\,3}}{12\mu}\left(1+\frac{3(\sigma+2\beta)}{\sigma(1+\beta\sigma)}\right) \tag{4.15}$$

Equating (4.14) and (4.15) and rearranging gives the equation to calculate the effective height to account for the increase in flow rate,

$$h_e = h_i\left(1+\frac{3}{\sigma}\left(\frac{\sigma+2\beta}{1+\beta\sigma}\right)\right)^{1/3} \text{ with } \sigma = \frac{h_i}{\sqrt{k}} \tag{4.16}$$

where h_e is the effective height and h_i is the original height of the free channel.

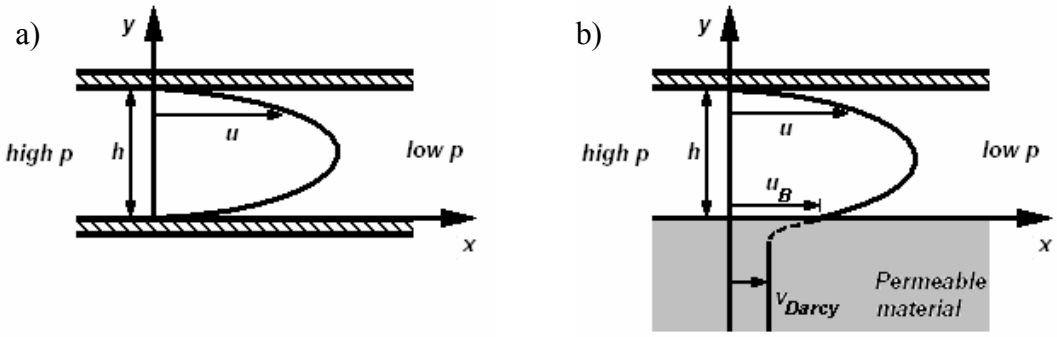

Figure 4.6 – a) The parabolic velocity profile for plane Poiseuille flow. b) Velocity profile for flow in a channel bounded by an upper solid wall and a lower permeable wall as described by Beavers and Joseph (1967). The slip velocity at the permeable boundary will not be zero.

4.3.2 Permeability modelling of a 2D single tow cross section

A schematic of the modelled 2D single tow cross section is shown in Figure 4.7. The shape of the tow is generated using the generalised ellipse equation as described in Appendix B. The use of this equation allows the shape of the tow to be easily manipulated. Calculations for the full 2D domain were conducted using FLUENT®. The mesh was generated using a script file in Gambit™, where each mesh consisted of typically 35000 triangular elements (see Figure 4.8). This was the optimum mesh size taking into account the convergence of the results, determined from mesh sensitivity study as shown in Figure I.4 in Appendix I. A pressure difference of 20 Pa was imposed between the two vertical faces with a no slip boundary condition on the upper and lower limits of the cell. The full set of the Navier-Stokes and continuity equations were solved in FLUENT® for steady, laminar flow in a saturated domain with a resin viscosity of 0.308 Pas. Within the porous tow domain, an additional viscous loss term equivalent to Darcy's law was added to the standard fluid flow equations to model porous media behaviour. The effective directional permeability was then back calculated using Darcy's law from the resultant flow rate.

The corresponding 1.5D Stream Surface mesh is shown in Figure 4.9. The nodes along a Stream Surface were connected to form a finite difference mesh, noting again that nodes at the edge of each Stream Surface that lie on the same vertical line have equivalent pressure. Each 1.5D single tow mesh included typically 3000 nodes (see Figure I.3 in Appendix I for mesh sensitivity study results). For a pressure drop of 20 Pa in the horizontal direction, the pressure field in the Stream Surface was evaluated using an in-house finite difference solver.

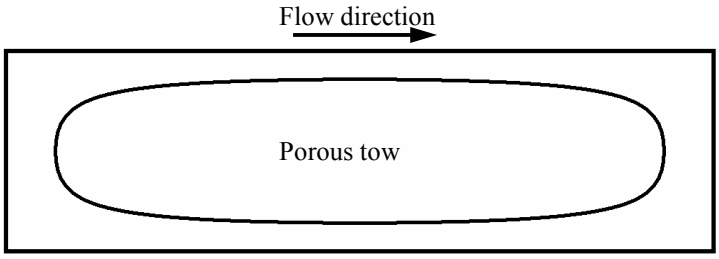

Figure 4.7 – Schematic of the 2D single tow case.

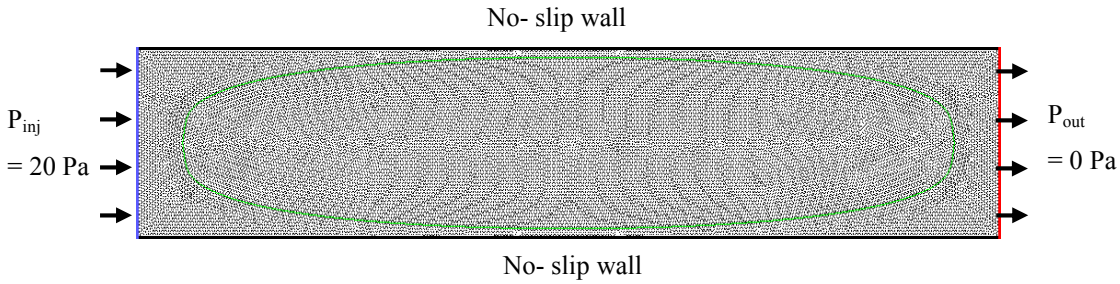

Figure 4.8 – Example of mesh of 2D single tow case 1 as listed in Table 4.2 generated using Gambit™. Boundary conditions for FLUENT® simulation are shown.

The principles of the Grid Average method were also applied here. The domain was first divided into a regular grid (500 divisions were used here), for which the effective permeability of each grid element can be calculated using Equation (3.2). The overall permeability $K_{e\ overall}$ of the corresponding 1D Grid Average case can then be found using the law of harmonic mean formation (Scheidegger, 1974),

$$\frac{1}{K_{e\,overall}} = \sum_{i=0}^{n} \frac{1}{K_{e\,i}} \tag{4.17}$$

where $K_{e\,i}$ is the effective permeability each grid division and n is the total number of divisions. Eqn. (4.17) is similar to Eqn. (4.5) except that the element height and length are constant here.

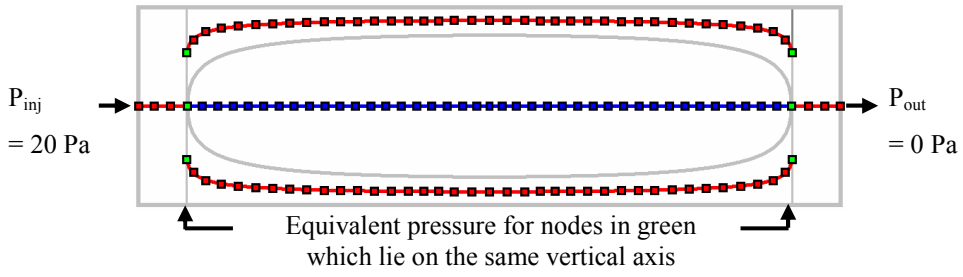

Figure 4.9 – Schematic of the Stream Surface mesh showing the applied boundary conditions. The nodes in red represent the open regions and the nodes in blue represent the porous tow region.

4.3.3 Results and discussion

Four geometric parameters have been identified to highlight their individual effects on the permeability of the single tow domain and these are described in Table 4.1. The tow permeability is calculated using Gebart's model (see Section 2.5, Eqn 2.12) for flow perpendicular to the fibres with quadratic fibre arrangement and fibre diameter of 15.8 μm (8.065×10^{-13} – 2.132×10^{-12} m^2 for tow fibre volume fraction range of 0.416 – 0.500). β has a value of 0.15, chosen to obtain close agreement between the Stream Surface result for nominal case 1 (see Table 4.2) and the CFD calculation. Examples of the pressure distribution and fluid flow profile of nominal case 1 solved using FLUENT® are shown in Figure 4.10.

Table 4.2 lists the 17 combinations of the four parameters with the respective calculated permeability. The predicted permeability values when the effect of the permeable boundary on flow rate is not accounted for are also shown for the Grid Average and Stream Surface methods. Figures 4.11-4.14 compare the predicted effects of parameters P1, P2, P3 and P4 on permeability obtained using the Grid Average, Stream Surface and CFD methods. The numbers next to each point on the graph identify the cases as specified in Table 4.2. Schematics of the geometry of each case are also shown on the figures, with points from the left to the right on the curves corresponding to geometries from the top to the bottom.

In general, when the height of the channel is not corrected to account for the increase in flow rate due to the permeable boundary, the predicted permeability values using Grid Average and Stream Surface are on average about 25% lower than the values calculated using CFD. More importantly however, the three methods predicted the same permeability trends with respect to parameters P1 to P4 (Figures 4.11-4.14) even when the effect of the permeable boundary was not taken into account. After height correction is performed, the predicted permeability values between the three methods are similar.

Table 4.1 – Description of the four geometric parameters varied in the single tow simulations.

No.	Parameter	Description
P1	Tow aspect ratio, a_{tow}	Defined as (width/height) of the tow section, with width along the x-axis and height along the y-axis (Eqn. (B.1)).
P2	Tow shape power, n	The n value defines the shape of the tow: $n = 0.5$ – generates an ellipse, $0 < n < 0.5$ – the ellipse evolves to a more rectangular shape, and $0.5 < n < 1$ – produces a lenticular shape.
P3	Fibre volume fraction of cell, V_{fc}	Given as a percentage of the maximum cell fibre volume fraction, $V_{f\,c,max}$. $V_{f\,c,max}$ occurs when the flow domain has the same width and height as the tow so that the walls are touching the tow.
P4	Cell aspect ratio, a_c	Values for a_c are selected between the maximum and minimum limits corresponding to the cell fibre volume fraction (P3) and tow aspect ratio (P1).

A reduction in permeability with increasing tow aspect ratio is observed in Figure 4.11. This is because the free channels on top and below the tow are becoming narrower and longer, constricting the flow of resin which primarily flows around the tow. Figure 4.12 shows an increase in permeability as the tow shape changes from a rectangular-like shape to an ellipse. Again, the main factor is the change of the resistance in the free channels which open up as the tow becomes more elliptical. Figures 4.13 and 4.14 predict a drastic drop in permeability with increasing cell fibre volume fraction and aspect ratio respectively. Changes in these two parameters have a direct impact on the geometry of the free channels which become very narrow at either a high cell fibre volume fraction or aspect ratio. Importantly, the Grid Average and Stream Surface results agree well with the CFD results, quantitatively and qualitatively. This observation is in direct contradiction to that observed in Section 4.2.3 for flow along an array of unidirectional fibres. The single tow cases studied here are at the mesoscopic length scale and each of the cases has a finite height associated with the flow domain.

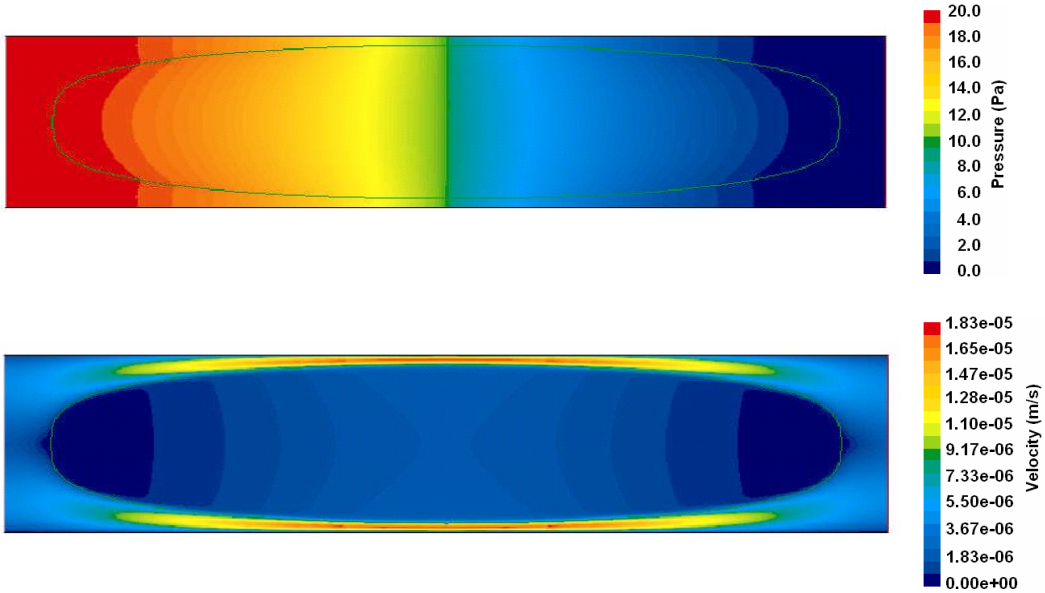

Figure 4.10 – Pressure distribution (top) and velocity flow profile (bottom) of nominal case 1 (see Table 4.2) solved using FLUENT®.

Perhaps more important is the difference between the computational time for CFD and the two more efficient methods, Stream Surface and Grid Average. The time required for mesh generation and simulation for the CFD approach was typically 6 minutes on a standard PC (P4 1.7GHz). The Stream Surface method required about 10 seconds in total for model generation and analysis while the Grid Average method calculation was almost instantaneous (< 1 sec.). When such efficiencies are translated to the simulations of 3D models, this would represent a large savings in time required for the analyses, as will be shown in the following chapters.

Table 4.2 – Parameters and results of the simulations for a single tow model.

Shaded boxes constitute changing parameters with respect to nominal case 1.

Simulation	Parameters				Unit cell dimensions						Results: Permeability (10^{-11} m^2)				
	Tow aspect ratio	Section shape power	Cell fibre vol. fraction	Cell aspect ratio	Tow			Cell			1D Grid Average		1.5D Stream Surface		2D CFD
	a_{tow}	n	V_{fc}	a_c	Width (mm)	Height (mm)	V_f	Width (mm)	Height (mm)	V_f	Height correction		Height correction		
	P1	P2	P3	P4							w/o	with	w/o	with	
1(nominal)	5	0.3	0.80 $V_{fc,max}$	5	5.0000	1.0000	0.460	5.5902	1.1180	0.314	10.14	**12.91**	10.18	**13.16**	**13.29**
2	3	0.3	0.80 $V_{fc,max}$	3	3.8730	1.2910	0.460	4.3301	1.4434	0.314	16.74	**20.41**	16.16	**19.92**	**20.79**
3	4	0.3	0.80 $V_{fc,max}$	4	4.4721	1.1180	0.460	5.0000	1.2500	0.314	12.62	**15.75**	12.60	**15.94**	**16.32**
4	6	0.3	0.80 $V_{fc,max}$	6	5.4772	0.9129	0.460	6.1237	1.0206	0.314	8.49	**10.99**	8.44	**11.11**	**11.46**
5	7	0.3	0.80 $V_{fc,max}$	7	5.9161	0.8452	0.460	6.6144	0.9449	0.314	7.32	**9.61**	7.48	**10.01**	**10.03**
6	5	0.1	0.80 $V_{fc,max}$	5	5.0000	1.0000	0.416	5.5902	1.1180	0.314	6.78	**9.12**	6.71	**8.80**	**8.95**
7	5	0.2	0.80 $V_{fc,max}$	5	5.0000	1.0000	0.439	5.5902	1.1180	0.314	8.66	**11.30**	8.52	**11.16**	**11.53**
8	5	0.4	0.80 $V_{fc,max}$	5	5.0000	1.0000	0.480	5.5902	1.1180	0.314	11.41	**14.20**	11.35	**14.79**	**14.94**
9	5	0.5	0.80 $V_{fc,max}$	5	5.0000	1.0000	0.500	5.5902	1.1180	0.314	12.54	**15.29**	12.40	**16.20**	**16.47**
10	5	0.3	0.70 $V_{fc,max}$	5	5.0000	1.0000	0.460	5.9761	1.1952	0.275	36.34	**42.67**	36.23	**43.41**	**42.92**
11	5	0.3	0.75 $V_{fc,max}$	5	5.0000	1.0000	0.460	5.7735	1.1547	0.295	20.04	**24.36**	19.92	**24.52**	**24.71**
12	5	0.3	0.85 $V_{fc,max}$	5	5.0000	1.0000	0.460	5.4233	1.0847	0.334	4.52	**6.11**	4.34	**6.01**	**6.44**
13	5	0.3	0.90 $V_{fc,max}$	5	5.0000	1.0000	0.460	5.2705	1.0541	0.353	1.70	**2.43**	1.46	**2.24**	**2.68**
14	5	0.3	0.80 $V_{fc,max}$	4.5	5.0000	1.0000	0.460	5.3033	1.1785	0.314	26.00	**30.92**	25.89	**31.17**	**31.64**
15	5	0.3	0.80 $V_{fc,max}$	4.75	5.0000	1.0000	0.460	5.4486	1.1471	0.314	16.75	**20.53**	16.63	**20.65**	**21.16**
16	5	0.3	0.80 $V_{fc,max}$	5.3125	5.0000	1.0000	0.460	5.7622	1.0847	0.314	4.81	**6.49**	4.61	**6.38**	**6.84**
17	5	0.3	0.80 $V_{fc,max}$	5.625	5.0000	1.0000	0.460	5.9293	1.0541	0.314	1.91	**2.74**	1.65	**2.52**	**2.96**

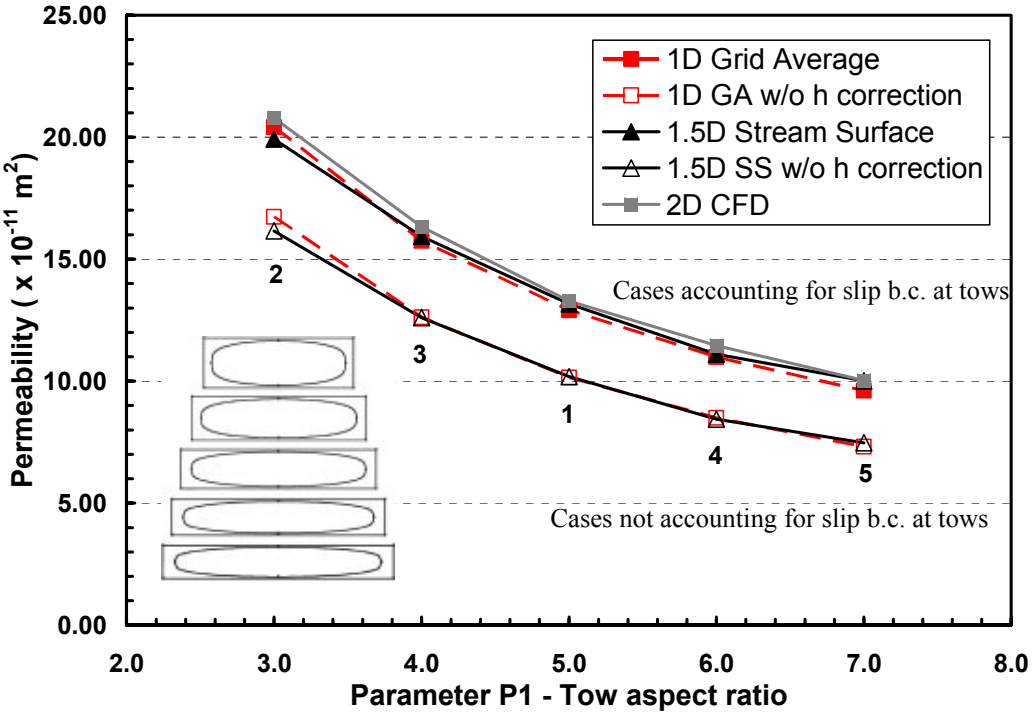

Figure 4.11 – The effect of tow aspect ratio on the cell permeability

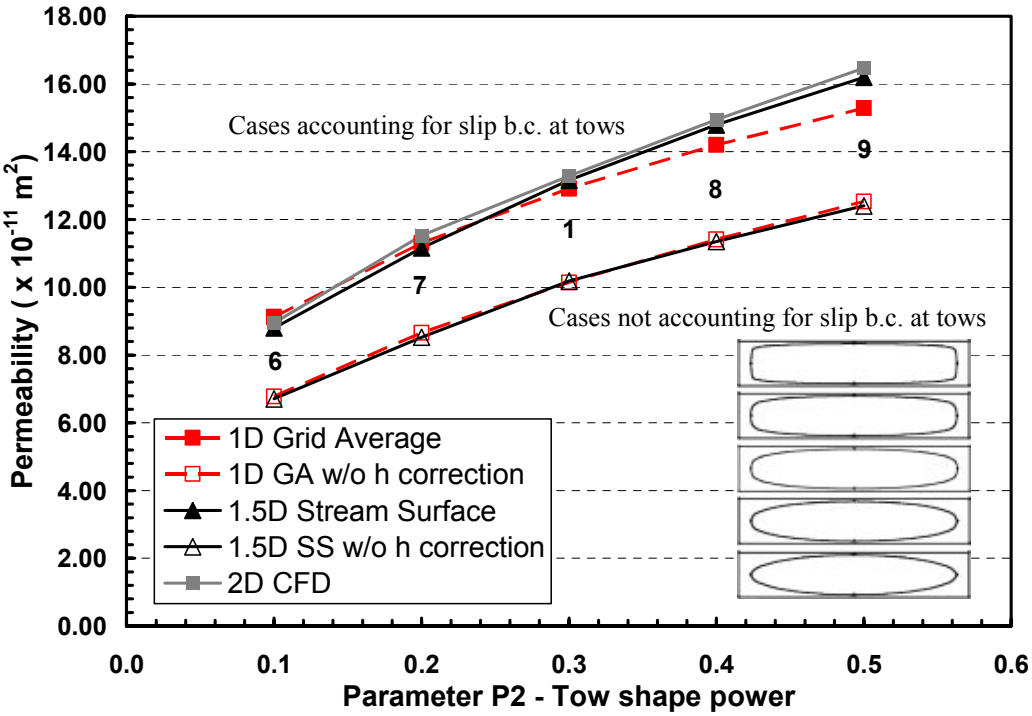

Figure 4.12 – The effect of section shape power on the cell permeability

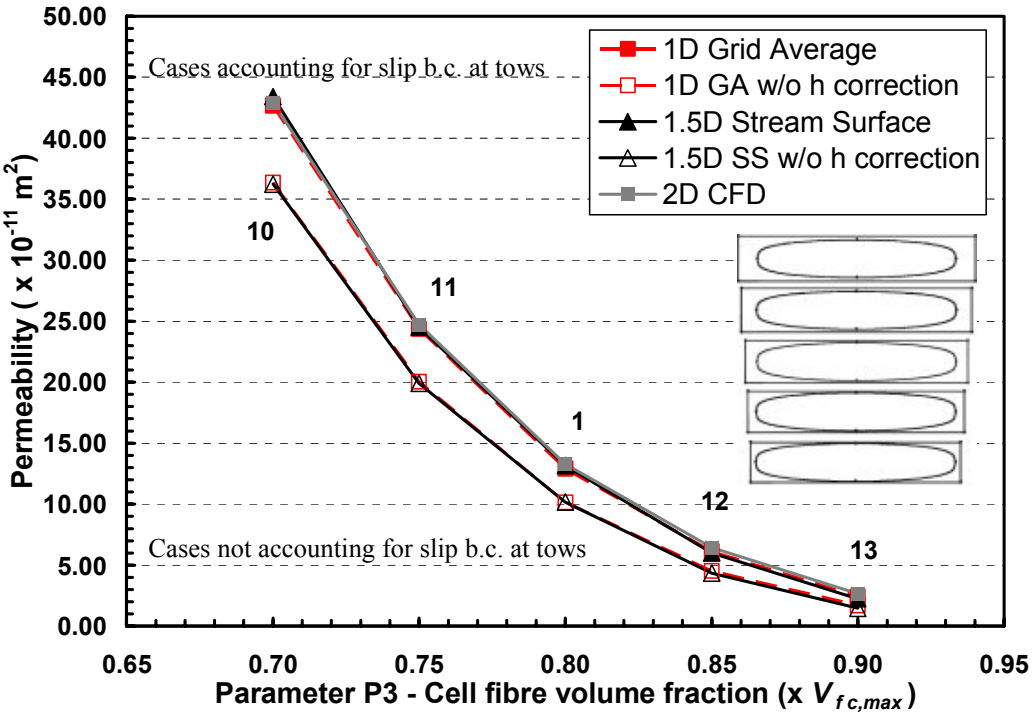

Figure 4.13 – The effects of cell fibre volume fraction on the cell permeability

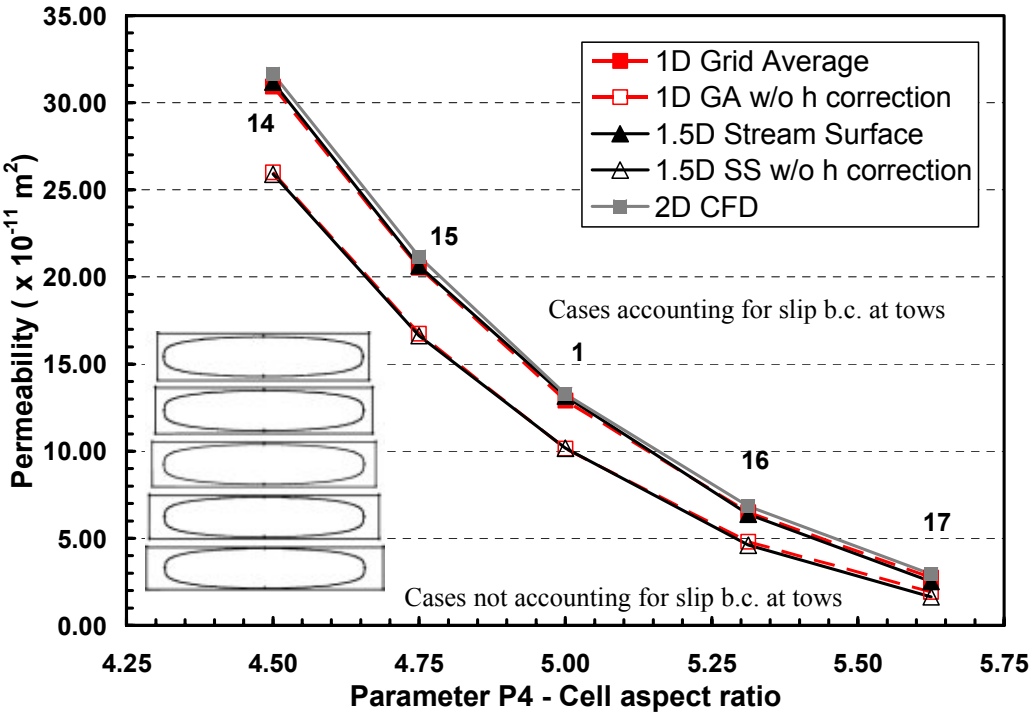

Figure 4.14 – The effect of cell aspect ratio on the cell permeability.

4.4 CROSS-SECTION OF TEXTILE MODEL

4.4.1 Cross-section of a 2:2 twill weave model

A 2:2 twill weave model created using TexGen was analysed to demonstrate the current generic approach for modelling permeability. Figure 4.15a shows the nominal case with tows at ±45° to the direction of flow. The tows have an elliptical cross section with a width of 0.8mm and height of 0.2mm. Fibre volume fraction of the tows is 50%, giving a permeability of 4.38 x 10^{-12} m^2 based on Gebart (1992) (quadratic packing of the fibres and fibre diameter of 15.8 µm – see Eqn. 2.12). Isotropic tow permeability was modelled here so that the results can be compared directly to CFD. The dimensions of the nominal case are 4mm x 4mm x 0.6mm, representing a repeating unit cell of the fabric. The nominal case is sheared by up to 30° in two directions to study its effect on permeability (see Figures 4.15b and 4.15c). 2D cross section slices are taken at the tow crossovers and between the crossovers for two directions, parallel to the x and y-axes. These are evaluated using Grid Average and Stream Surface and compared to CFD calculations. Table 4.3 lists the fibre volume fraction of the cross sections evaluated in this study.

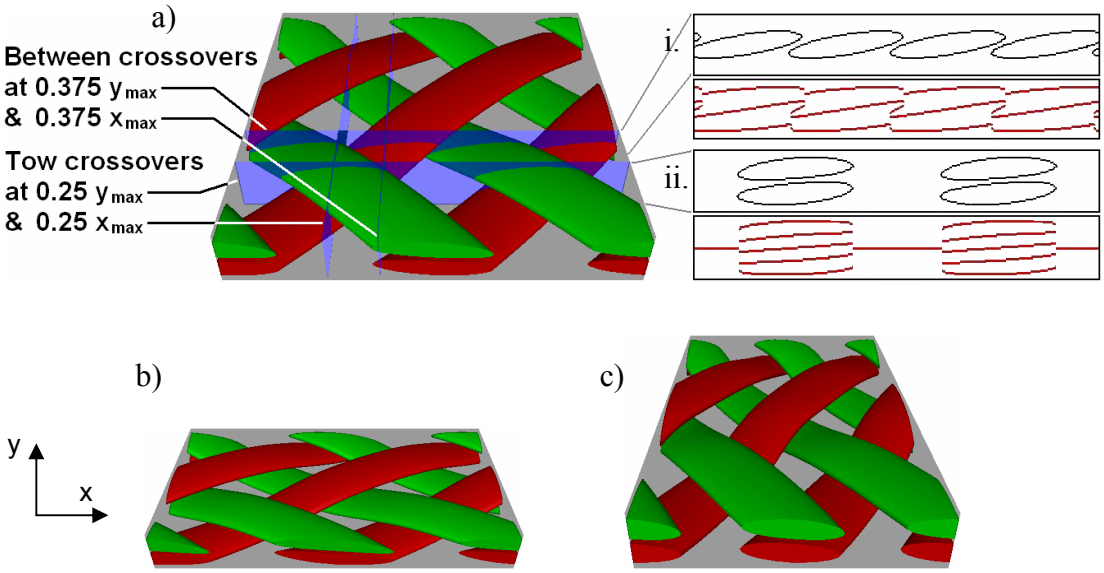

Figure 4.15 – Textile models of a 2:2 twill weave fabric. a) Nominal case with tows at ±45° to the x-axis and dimensions of 4mm x 4mm x0.6mm. The model was sheared to ply angles of (b) ±30° and (c) ±60° with respect to x-axis. Cross sections were taken (i) at the tow crossovers and (ii) between the crossovers and the corresponding Stream Surface meshes are shown for each.

Table 4.3 – Fibre volume fractions of the cross sections of the 2:2 twill weave model.

Cross section V_f (%)	±30°	±45°	±60°
Between tow crossovers	17.13	14.88	16.72
At tow crossovers	16.92	14.62	17.12

Similar to the previous section, the solution using 1D Grid Average reduces to Eqn. (4.17). A mesh density of 100 divisions per unit length (resulting in 401 nodes for the ±45° case) was applied here following a mesh sensitivity study on the cross section at the tow crossovers of the ±45° case for flow along the x-axis (see Figure I.5 in Appendix I). The Stream Surface meshes for the cross sections are created using TexGen, with typically 1500 nodes in each mesh – see Figure I.6 in Appendix I for the mesh sensitivity study results. The 2D cases for FLUENT® are meshed by Gambit™ using script files generated automatically in TexGen. Each CFD mesh consists of about 8000 triangular elements – using the same mesh density inferred from the mesh sensitivity study for the 3D model (see Section 5.3 and Figure I.9 in Appendix I). Saturated flow is simulated for an applied pressure difference of 10^5 Pa from left to right and resin viscosity of 0.308 Pas. The height of the free channels has not been modified to account for permeable boundaries as the fitting method is not sufficiently robust to cover the complicated flow in these cases.

4.4.2 Results

The permeability values predicted using the Grid Average, Stream Surface and CFD methods for flow along the x and y-axes are shown in Table 4.4 and compared in Figure 4.16. Where comparisons can be made, the three approaches showed a relatively good agreement. The 1D Grid Average method generally predicted higher permeability values than the other two methods. This may be due to its inherent simplification of the flow behaviour to calculate permeability.

Looking at the results for the cross sections between the tow crossovers along the x-axis, the permeability is seen at a maximum for the ±45° case, with a large reduction when sheared to ±30° and a smaller reduction when sheared to ±60°. Due to the large inter-tow spaces in the model, changes in permeability are largely affected by geometric changes in these free channels. The resin in the ±30° case has to travel

through longer channels on top and below the tows as opposed to the other two cases (see Figure 4.16a), thus lowering the permeability of the ±30° case. But as the model is sheared to ±60°, even though the channels have shortened, this is counteracted by the tows being much closer together, hence the slight decrease in permeability. For the cross sections at the tow crossovers along the x-axis, the permeability is still at a maximum at ±45°; however there is now a slightly higher reduction in the ±60° case compared to the ±30° case. Similar to the above, the resin has to travel through longer channels in the ±30° case, while the channels, although shorter, are much narrower in the ±60° case, both contributing to the decrease seen. For the cross sections along the y-axis, the predicted trends are just the opposite of the correspondent results along the x-axis.

In general, the cross sections between the tow crossovers have higher permeability than those at the tow crossovers. This can be explained by looking at the predicted pressure field, shown for flow along the x-axis for the ±30° cross section between the tow crossovers in Figure 4.17a and at the tow crossovers in Figure 4.17b. The pressure changes for the former are relatively uniform while the latter exhibits high pressure losses at the tow crossover regions, thus decreasing the overall permeability values.

Table 4.4 – Predicted permeability values of cross sections of 2:2 twill weave model

	K_x (x 10^{-10} m^2)			K_y (x 10^{-10} m^2)		
	±30°	**±45°**	**±60°**	**±30°**	**±45°**	**±60°**
Between tow crossovers						
1D GA	15.86	25.52	22.17	22.96	31.66	17.71
1.5D SS	13.21	21.33	18.47	22.31	28.07	15.25
2D CFD	12.57	21.66	18.89	-	23.30	15.16
At tow crossovers						
1D GA	5.09	5.00	3.32	4.23	5.28	5.79
1.5D SS	3.21	4.55	2.89	4.15	4.09	2.35
2D CFD	4.36	5.60	4.35	4.51	4.68	3.32

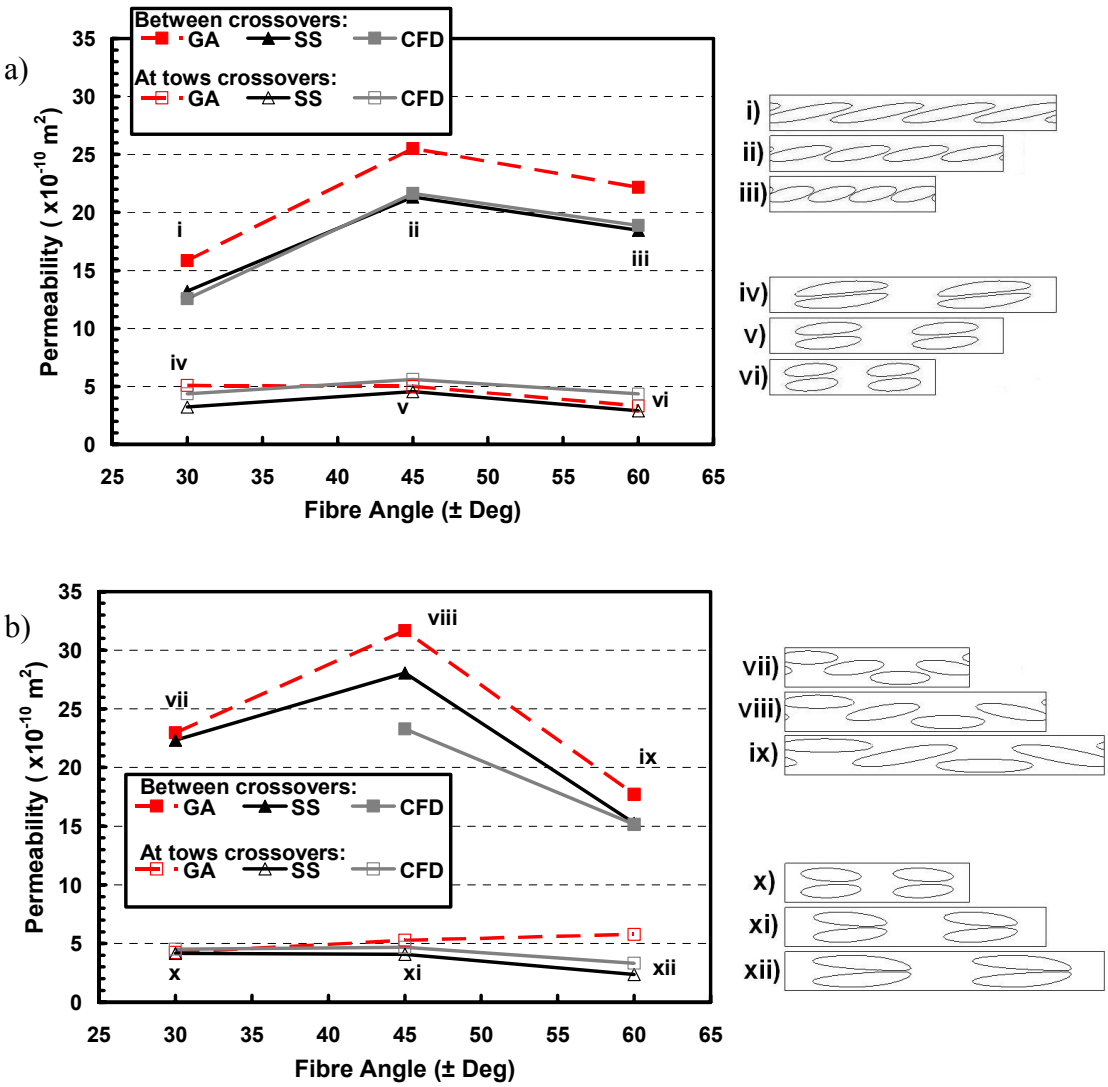

Figure 4.16 – Comparison of predicted permeability values from Stream Surface and CFD methods for flow along (a) x and (b) y-axes. Schematics of the cross section are shown to the right, numbered to the corresponding points on graphs.

Encouragingly, the three methods predicted very similar permeability trends and showed a good agreement, quantitatively and qualitatively (between Stream Surface and CFD), even though the permeable boundary conditions were ignored in Grid Average and Stream Surface. This further strengthens the applicability of the Grid Average and Stream Surface methods for predicting permeability, demonstrating the fact that they can model a more complex case than a single tow. The CFD approach was generally prohibited by difficulties in generating accurate meshes. The overall execution times, including mesh generation and flow simulation, for the Grid Average analyses were almost instantaneous (<1 sec), about 5 seconds each for the Stream Surface analyses whilst those for the CFD analyses were about 30 minutes each, performed on a standard PC (P4 1.7GHz).

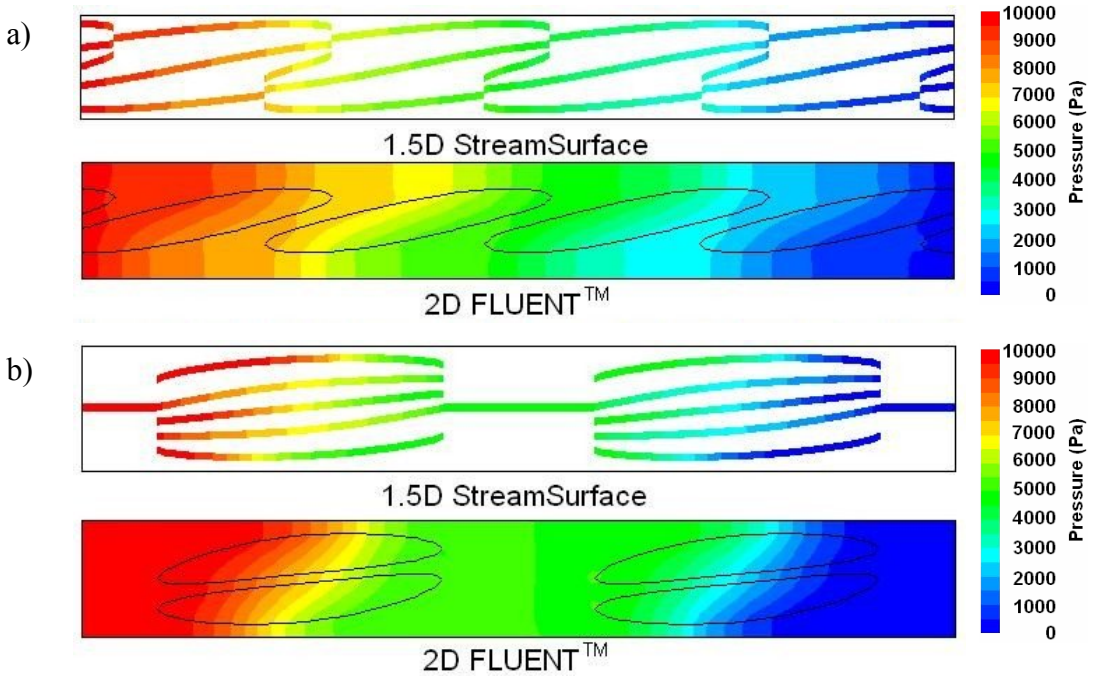

Figure 4.17 – Comparison of predicted pressure fields for cross sections of ±30° twill weave model (a) between the tow crossovers and (b) at the tow crossovers showing results from Stream Surface (top) and CFD (bottom). Resin flow is along the x-axis from left to right

4.5 CONCLUSION

While these 2D calculations are of limited use in predicting the permeability of actual preforms, these studies are an integral part in the development of the Stream Surface and Grid Average approaches. The results have shown that the two simple methods are able to predict permeability values and trends with respect to changes in the tow geometry and in-plane shear which are similar to the results predicted using the more rigorous CFD method.

In the first part, the permeability for flow perpendicular and parallel to a square array of impermeable fibres was evaluated for a range of fibre volume fractions. Both the Grid Average and Stream Surface methods in this case reduce to simple permeability averaging equations. Predicted permeability values for flow perpendicular to the fibres obtained using the equation compared well to CFD and to an analytical model. The predicted results for flow along the fibres using the Grid Average and Stream Surface methods did not agree well with the analytical solution. This highlighted the applicability limit of the two simple approaches for analysing microscopic flow behaviour.

For a domain consisting of fibrous tows, the inter-tow channels are not necessarily bounded only by impermeable walls but also by the permeable boundaries of the tows. The effect of such a boundary condition is explored and accounted for in the evaluation of the permeability of a single tow. Within the study, several tow geometric parameters were also identified to look at their effects on permeability.

It was seen that the permeable boundaries of the fibre bundles do indeed influence the flow and subsequently the permeability. However, this begs another question, what is the priority in developing Stream Surface and Grid Average? The fundamental simplicity of the two methods is underlined here. In order to account for the permeable boundaries, the solution will eventually become very complicated, perhaps reaching the sphere of CFD calculations. This is an antithesis to the idea of Stream Surface and Grid Average, for which efficiency and predictive capability are the primary requirements.

As a demonstration of the generic nature of the proposed methods, more complex cases were studied, being cross sections through a 2:2 twill weave fabric model. The Grid Average and Stream Surface methods generated permeability values and trends with respect to fabric shear in the model which compared really well with CFD results. This is despite not accounting for the effects of permeable boundaries of the fibrous tows on the general flow behaviour. Moreover, the fact that some of the CFD simulations were prohibited by difficulties in generating accurate meshes, as well as long processing time, strengthened the argument of using simpler but more efficient methods such as Stream Surface and Grid Average.

The studies here have highlighted the strengths of the Stream Surface and Grid Average methods when compared to CFD, namely the computational speed advantage of the two efficient methods. For the simple 2D cases shown here, the Stream Surface and Grid Average methods are at least 36 times faster than CFD. Such advantages, when translated to the simulations of 3D cases, will allow large numbers of models to be simulated within acceptable timescales.

This chapter has presented some preliminary studies on the use of Stream Surface and Grid Average for elementary 2-dimensional geometries. Initial results showed the potential of their application. The range of the Grid Average method will be further developed in the following chapters, where it will be applied to 3-dimensional models which approximate the geometry of real fabrics.

5 ANALYSIS OF A 3D TEXTILE MODEL

5.1 INTRODUCTION

One of the core aims of developing a permeability model is to predict the permeability and account for the effects of various factors such as nesting and in-plane shear (representing the effect of draping) on the permeability of an existing fabric. This would complement the measured permeability data and thus enhance the quality of flow simulations involving the fabric in question.

From another viewpoint, designers can utilise the predictive capability of a permeability model to help manufacture fabrics with improved processing properties. Engineers will be able to predict how the fabric will perform under different conditions and modify the configuration to suit the application. This chapter aims to address and demonstrate the use of the Grid Average method from these two perspectives. Stream Surface has not been applied due to time constraints in developing and implementing a robust solver for the solution of Stream Surface in 3D space.

In a numerical permeability model, an accurate description of the fabric structure is critical to a successful prediction. The issues regarding generating such a fabric model are discussed in the first part of the chapter. In the second part, the approach of numerically characterising a fabric is attempted using a fabric model of a 2:2 twill weave with arbitrary but realistic dimensions. The effect of shear on the predicted permeability is studied and compared to published results.

In the third part, a plain weave fabric is analysed with a view to create an equivalent fabric model and then predict its permeability to compare to that determined experimentally. A laminate is manufactured at the same fibre volume fraction as the experiments and cross sections are obtained from the sample. Geometric data such as tow widths, heights and area ratio are then collected from microscopic images of the cross sections. A plain weave model is created based on these data, from which the permeability is predicted and compared to experimental values.

5.2 MESOSCOPIC MODELLING OF TEXTILE

In order to construct a textile model, there are several key parameters which are required. These can be separated into two distinct categories, macro and mesoscopic. The macroscopic parameters are those which can be observed with the naked eye and easily measured. These include:

i) weave type
ii) distance between tows
iii) thickness of the fabric (or mould cavity/laminate)

Mesoscopic parameters define the more intricate or minute detail of the textile, which includes:

i) tow width and height
ii) tow shape
iii) tow fibre volume fraction

If the designer is only interested in constructing a theoretical model, choosing the values of each parameter will be straightforward. However, in creating an accurate textile model which is a replicate of an existing fabric requires a more thorough analysis.

A systematic approach is adopted in this study. First, a laminate of the existing fabric is manufactured using the correct number of layers and mould thickness, from which samples of cross sections are obtained. Microscopic images of the samples are taken and analysed to obtain a statistical distribution of the appropriate mesoscopic parameters. Using these known parameters, a fabric model can then be constructed.

5.3 PERMEABILITY OF A VIRTUAL TEXTILE MODEL – 2:2 TWILL WEAVE

A study on a 2:2 twill weave model was performed to demonstrate the predictive range of the permeability model. The model has been described in Section 4.4.1 and was shown in Figure 4.15.

5.3.1 Effect of in-plane shear

Simulations of the twill weave model for a range of shear angles were performed using the Grid Average and CFD approaches to study its effect on permeability. Five simulations with ply angles ranging from ±30° to ±60° were performed with both the 2D and 3D Grid Average approaches. The height of the free channels was not modified to account for permeable boundaries as the fitting method was not sufficient to cover the complicated flow in these cases. The tows in each of the cases have an elliptical cross section with a width of 0.8mm and height of 0.2mm. Fibre volume fraction of the tows is 50%, giving a permeability of 4.38×10^{-12} m^2 based on Gebart (1992) (quadratic packing of the fibres and fibre diameter of 15.8 μm – see Eqn. 2.12). Isotropic tow permeability was modelled here so that the results can be compared directly to CFD. The dimensions of the nominal ±45° case are 4mm x 4mm x 0.6mm, representing a repeating unit cell of the fabric.

For the 2D Grid Average, each of the case was meshed using a density of 50 divisions per unit resulting in 40,401 nodes for the nominal case (see Figure 5.1). This was the optimum mesh density determined from the mesh sensitivity study (see Figure I.7 in Appendix I for results). Each of the 3D Grid Average simulations was meshed using a density of 32 divisions per unit resulting in 332,830 nodes for the nominal case (see Figure 5.2). Again, from preliminary mesh sensitivity study as shown in Figure I.8 in Appendix I, this was the optimum mesh density taking into account the convergence of the results and an acceptable computational time.

A pressure difference of 10^5 Pa was applied between the two opposing faces in the direction of flow (along the global x-axis) and the boundaries of the cell were modelled to be periodic. The in-house finite difference solvers for 2D and 3D Grid Average were used to calculate the resultant pressure fields. The directional

permeabilities for flow parallel to the x and y axes were then determined using Darcy's law (Eqn. 3.11), as described in Section 3.6.

The corresponding CFD simulations were performed using FLUENT®. The geometric models were meshed using the Gambit™ pre-processor, utilising automated script files generated by TexGen for the twill weave models. Each model typically consisted of approximately 450,000 tetrahedral elements. This was the optimum mesh size which produced a solution within a reasonable time scale (see Figure I.9 in Appendix I). A periodic pressure gradient of 10^5 Pa/m was specified in the direction of flow (along the x axis in Figure 5.3), with no-slip boundary condition for the upper and lower walls and periodic boundary condition on the side walls parallel to the direction of imposed pressure gradient. The CFD simulations were however limited to two ply angles (±30° and ±45°). This was due to difficulty in generating a good mesh, especially for cases which featured small gaps between the tows, an inherent result of tow interference correction. Solutions for many cases like this did not converge, and hence large inter-tow spacings were used which explains the relatively low cell fibre volume fraction (14.7% for the nominal case).

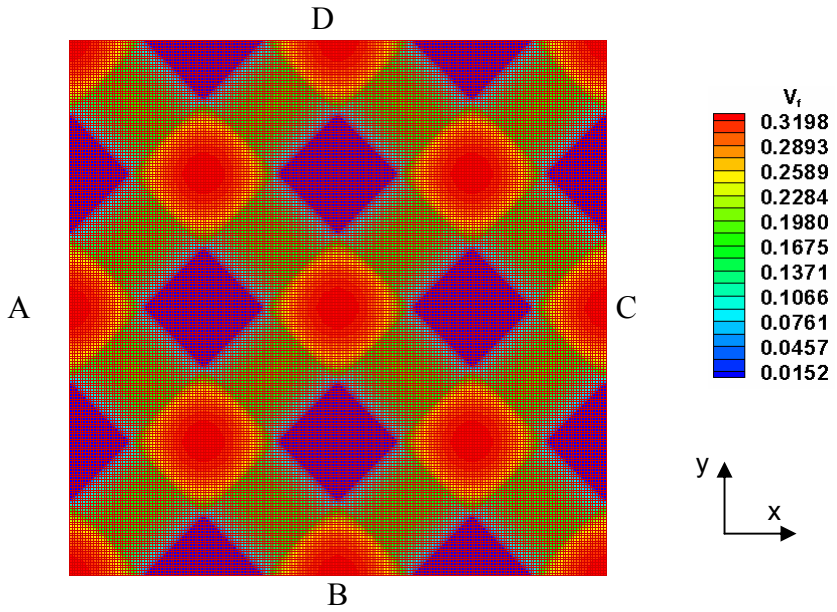

Figure 5.1 – 2D Grid Average mesh of ±45° twill weave model showing fibre volume fraction distribution. Periodic boundary conditions were applied at the boundaries of the mesh, with face A coupled to face C and face B coupled with face D. A pressure difference of 10^5 Pa was applied between faces A and C.

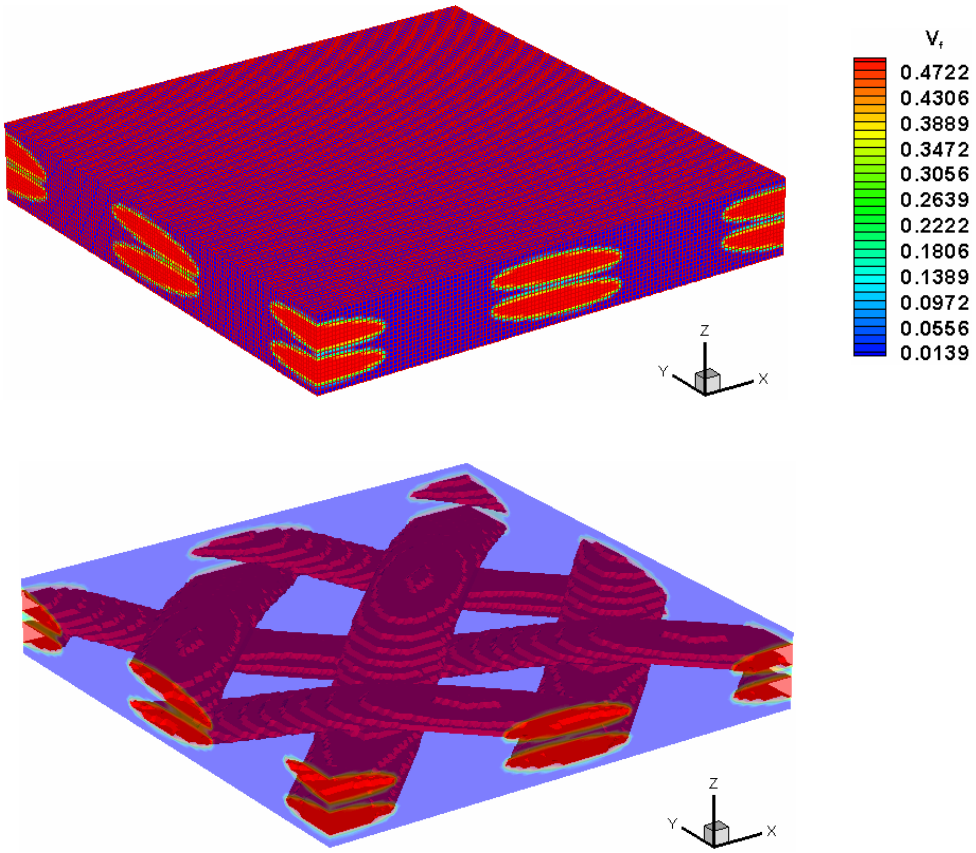

Figure 5.2 – 3D Grid Average mesh of ±45° twill weave model showing fibre volume fraction distribution (top) and showing the tow details (bottom). Periodic boundary conditions were applied to the faces perpendicular to the x and y axes. The faces perpendicular to the z axis were modelled as no leakage walls, i.e. the velocity component normal to them is zero ($u_n = 0$).
A pressure difference of 10^5 Pa was specified in the x axis direction.

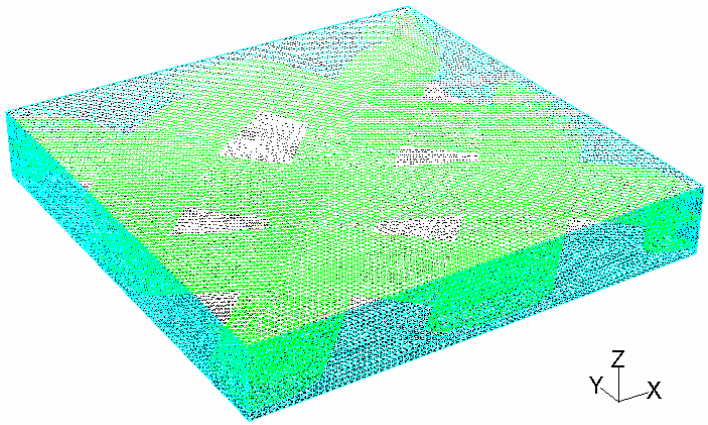

Figure 5.3 – Mesh of ±45° twill weave model generated using Gambit™ for FLUENT®. Periodic boundary conditions were applied to the faces perpendicular to the x and y axes. The faces perpendicular to the z axis were modelled as no-slip walls. A pressure gradient of 10^5 Pa/m was specified in the x axis direction.

5.3.2 Results

The permeability values calculated using CFD and both the 2D and 3D Grid Average approaches are compared in Table 5.1 for flow in the direction of the x-axis. The two sets of permeability values predicted using the Grid Average method were very similar, whereby the 2D Grid Average approach predicted values were 5-9% higher than the values calculated using 3D Grid Average. Where a comparison can be made between the two sets of Grid Average values and the results of the CFD simulations, the calculated permeability values were within 28% of each other. The predicted pressure fields of the nominal case using 2D Grid Average and CFD were also very similar qualitatively (Figure 5.4). These are perhaps encouraging results, given both the simplicity of the Grid Average method, and that the permeable boundary condition at the tow boundary interface was not considered by the Grid Average method.

When a CFD solution was possible, the time required for mesh generation and simulation was about 3 hours on a standard PC (P4 1.7GHz). On the other hand, the 2D Grid Average approach required approximately 2 minutes in total to generate and analyse the model, and the 3D Grid Average approach required about 15 minutes in total. In addition, grid-independence-convergence in the solution was achieved using a relatively small number of nodes for the Grid Average approach, while the mesh sensitivity study for the CFD approach (see Figure I.9 in Appendix I) showed that the solution is still not grid independent even at a prohibitively large mesh size.

Figure 5.5 plots the permeability trend predicted using the 2D Grid Average method for flow parallel to the x-axis. The permeability is seen to be at a maximum at about ±37°, with a slight reduction when sheared to ±30° and a much larger reduction when sheared to ±60°. This is expected as the model thickness is constant and as the fabric is sheared in either direction, the fibre volume fraction will increase.

For ply angles below ±45°, the fibres are re-aligned towards the direction of flow. Increased fibre volume fraction also means that less resin is required for filling, thereby increasing the flow rate, and hence the slight increase in permeability. However, as the ply angle drops below ±37°, the effect of flow restriction due to

increased fibre volume fraction becomes dominant and the permeability decreases. For ply angles above ±45°, the combined effects of increased fibre volume fraction and re-orientation of fibres away from the direction of flow significantly reduce the permeability. This trend matches that observed experimentally by Smith et al. (1997) for a range of bi-directional fabrics (see Figure 5.6).

Table 5.1 – Predicted permeability for flow in the direction of the x-axis (all 10^{-9} m^2 except where indicated).

Fibre angle	**±30°**	**±37.5°**	**±45°**	**±52.5°**	**±60°**
Cell V_f	17.0%	15.2%	14.7%	15.2%	17.0%
2D Grid Average	4.02	4.32	3.91	3.15	2.12
3D Grid Average	3.79	4.13	3.67	2.96	1.94
3D CFD	2.76	-	3.10	-	-

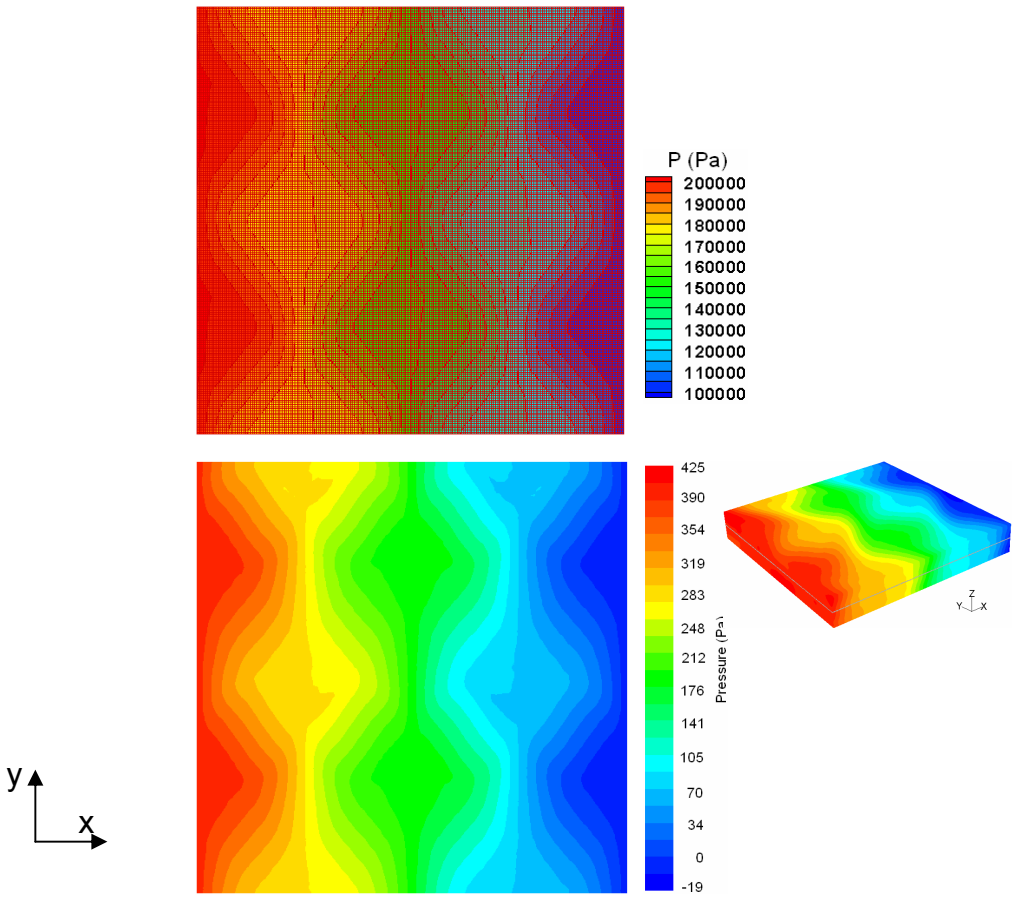

Figure 5.4 – The predicted pressure field for the nominal case obtained using 2D Grid Average (top) and the pressure field extracted from the mid-surface of the CFD 3D model (bottom). For the CFD case, the pressure distribution is reasonably uniform through the thickness.

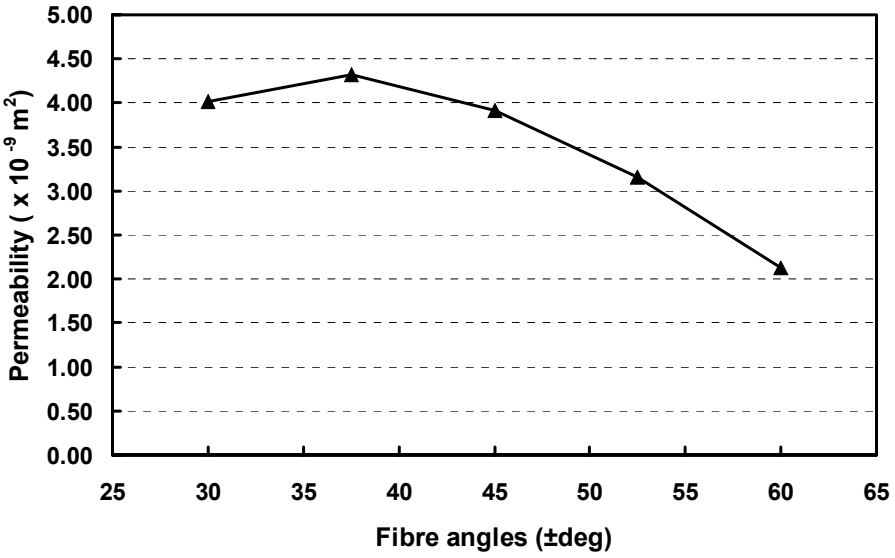

Figure 5.5 – Permeability predictions using the 2D Grid Average approach for flow along the x-axis in 2:2 twill weave sheared to a range of fibre angles.

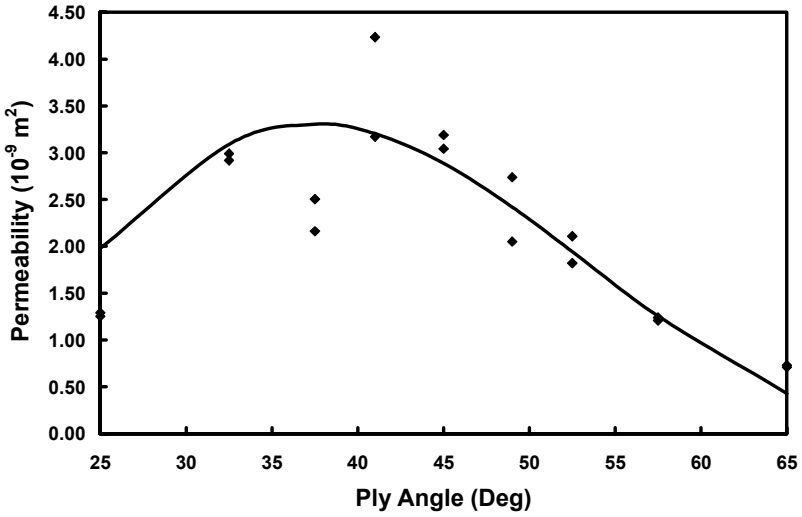

Figure 5.6 – Measured permeability of Chomarat 830S 2:2 twill weave fabric from Smith et al. (1997).

5.4 PERMEABILITY OF A REAL TEXTILE – 900T PLAIN WEAVE

5.4.1 Optical microscopy

The purpose of this exercise is to predict the permeability of a realistic fabric model and compare it to the measured value. The chosen textile is a plain weave fabric, 900T manufactured by Chomarat Composites, for which the permeability has been measured by Endruweit (Endruweit et al., 2005 – see Table 2.2). In order to create a comparable and accurate model of the plain weave, an intricate knowledge of the tow shape and dimensions is required.

A laminate of the plain weave was manufactured using the same configuration as the permeability experiment with three layers of fabric in a 2mm thick cavity (see Table 5.2). The layers were laid up so that the warp and weft fibre directions were aligned. Six specimens were cut from the laminate with the cutting planes perpendicular to the fibre directions, three each for the warp and the weft directions. The specimens had lengths of 20-30mm and widths of about 20mm.

These were put into plastic pots with detachable bases of 40mm in diameter, where they were stood on edge and held in place with a small amount of epoxy based adhesive. Catalyst and accelerator were mixed with a casting resin and the solution poured into the pots. These were allowed to cure over night at room temperature so that the specimens are encased in solid resin.

After the blocks of specimens were removed from the pots, they were cut into thicknesses of about 14mm. The two faces were first coarsely grounded to obtain two parallel faces. Then, the faces to be examined were polished using a Struers DAP-7 machine with an automatic holder (Struers Pedemin-S) at a motor speed of 250 rpm. This was done using waterproof abrasive papers with increasing grit numbers from 240 up to 6000 grit at about 5 minutes each.

The polished specimens were examined under a Zeiss Axiolab optical microscope fitted with a CCD camera which is connected to a PC for image acquisition. A graticule was used for calibration of the measurements. The acquired images were imported into image analysis software, GIMP (GIMP website, 2006), for analysis.

Table 5.2 – Experimental data for 900T fabric laminate.

900T permeability experiment data	
Weave style	*Glass fibre plain weave*
Superficial density	*912 g/m^2*
Domain thickness	*2 mm*
No of layers	*3*
Theoretical V_f	*0.526*

5.4.2 900T plain weave model

Individual tows with reasonable shapes, i.e. non-nested and not distorted, were identified from the images, with a total of 12 samples of warp tows and 15 samples of weft tows selected. An example of a tow cross section is shown in Figure 5.7. For each tow, a bounding rectangle was drawn around the vertical and horizontal limits of the tow to give the tow width and height. In order to characterise the tow shape, a free hand shape was drawn around the edge of the tow, mimicking the tow shape. The covered area, i.e. area of tow, was reported by the software, from which the area ratio of the tow to the bounding rectangle was calculated using Equation (5.1).

$$Tow\ area\ ratio = \frac{Area_{tow}}{Width_{tow} \times Height_{tow}} \tag{5.1}$$

Due to the high level of compaction, the laminate shows a lot of nesting between layers, and many of the tows do not have an easily distinguishable boundary. This has led to only a few measurements being possible for each specimen. Even where the tows have distinct shapes, determining the boundaries is still a challenging task.

The measurements are summarised statistically in Table 5.3. The distances between the tows were obtained by measuring the distance between *n* tows on a fabric layer and dividing it by *n* to get the distance between two adjacent tows. This is repeated several times at different parts of the fabric to get an average value.

Based on the measured values in Table 5.3, two models of the 900T plain weave laminate were created. In the first model, the layers are in phase with one another, i.e. there is no nesting between the layers. Conversely, the layers in the second model are

90° out of phase relative to one another, i.e. maximum nesting between layers. The parameters used to construct the models are listed in Table 5.4. Figures 5.5 and 5.6 show the non-nested and nested model respectively.

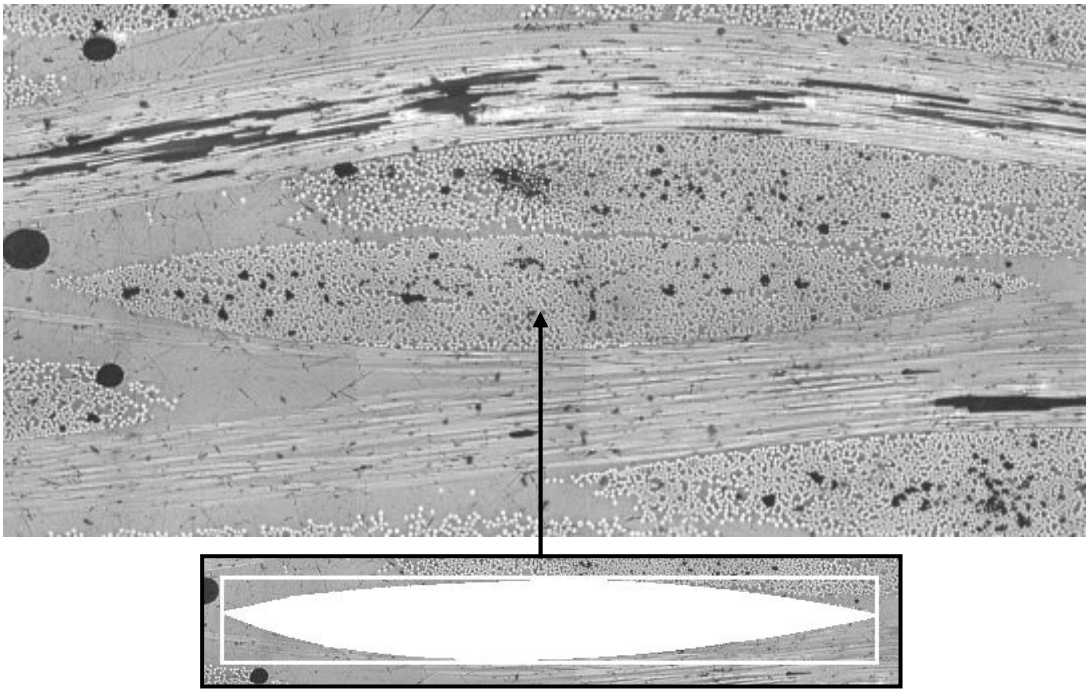

Figure 5.7 – Detail of a tow cross section from the 900T plain weave laminate. Inset showing the drawn bounding rectangle and tow area to characterise the tow geometries.

Table 5.3 – The mean and standard deviation of the measurements from the 900T plain weave laminate. The percentage standard deviation is shown in brackets.

900T plain weave model		Measured values
Unit cell thickness (mm)		2.000
No. of layers		3
Warp	No.of samples	12 tows
	Distance bet. tows (mm)	4.96 ± 0.01 (± 0.29%)
	Width (mm)	4.53 ± 0.17 (± 3.73%)
	Height (mm)	0.49 ± 0.03 (± 6.16%)
	Tow area ratio	0.702 ± 0.032 (± 4.53%)
Weft	No.of samples	15 tows
	Distance bet. tows (mm)	5.80 ± 0.17 (± 0.30%)
	Width (mm)	4.62 ± 0.21 (± 4.62%)
	Height (mm)	0.54 ± 0.07 (± 13.04%)
	Tow area ratio	0.725 ± 0.031 (± 4.23%)

Table 5.4 – Geometrical parameters used to construct the 900T plain weave models.

900T plain weave model		Non nested	Nested
Unit cell thickness (mm)		1.998	1.998
No. of layers		3	3
Warp	Distance bet. tows (mm)	4.96	4.96
	Width (mm)	4.60	4.60
	Height (mm)	0.31	0.38
	Tow shape power, *n*	0.82	0.82
	Tow area ratio	0.703	0.703
Weft	Distance bet. tows (mm)	5.80	5.80
	Width (mm)	4.65	4.65
	Height (mm)	0.31	0.38
	Tow shape power, *n*	0.73	0.73
	Tow area ratio	0.724	0.724

The tow shape power was determined by obtaining the shape which gives a similar tow area ratio as the measured value. The width and the height of the tows are chosen for the optimum configuration of the models, i.e. no interference between tows and maximum packing. Whilst the tow widths still fell within the range of the measured values, the modelled tow heights are 22%-43% less than the measured values. This reflects the many simplifications necessary in the definition of a textile model. A lot of nesting is observed in the laminate specimens and the arrangement of the layers is nowhere near the 'perfect' symmetry of the computer model.

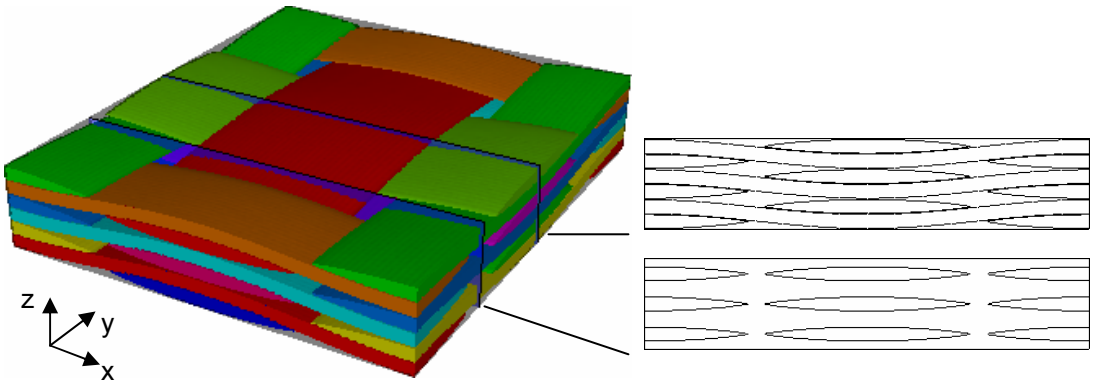

Figure 5.8 – 900T plain weave model with no nesting between layers.

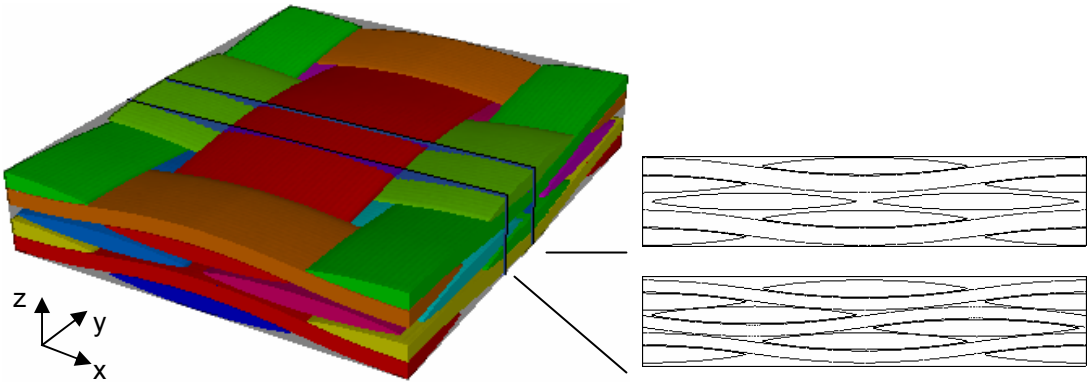

Figure 5.9 – 900T plain weave model with nested layers. Through sections are shown to illustrate the packed geometry.

5.4.3 Results

The dimensions of the domain of the models are 9.92mm x 11.60mm x 1.998mm, representing a repeatable unit cell. Fibre volume fraction of the tows is 75.4%, chosen to give a similar effective cell fibre volume fraction between the nested model and the experimental value. Directional tow permeability was modelled here, calculated using Gebart's model based on hexagonal arrangement of the fibres and a fibre diameter of 15.8 μm, giving local tow permeabilities of 2.49 x 10^{-13} m^2 along the tows and 4.19 x 10^{-14} m^2 perpendicular to the tows.

Simulations were performed for both models using Grid Average (GA) in 2D and 3D. These were compared to the experimentally measured data. The models were discretised using mesh densities of 30 divisions/mm for 2D GA and 20 divisions/mm for 3D GA – resulting in meshes with 104,351 and 1,901,047 nodes respectively. These were chosen based on the mesh sensitivity studies shown Figures I.10 and I.11 in Appendix I respectively, taking into consideration the convergence of the results and the computational time. An in-house finite difference solver was used to calculate the resultant pressure field (an example of the result is shown in Figure 5.10), given a pressure gradient of 10^5 Pa between two opposing faces and periodic boundary conditions. The effective permeability of the cell for flow parallel to the global x and y axes was then back-calculated using Darcy's law (Eqn. 3.11) as described in Section 3.6.

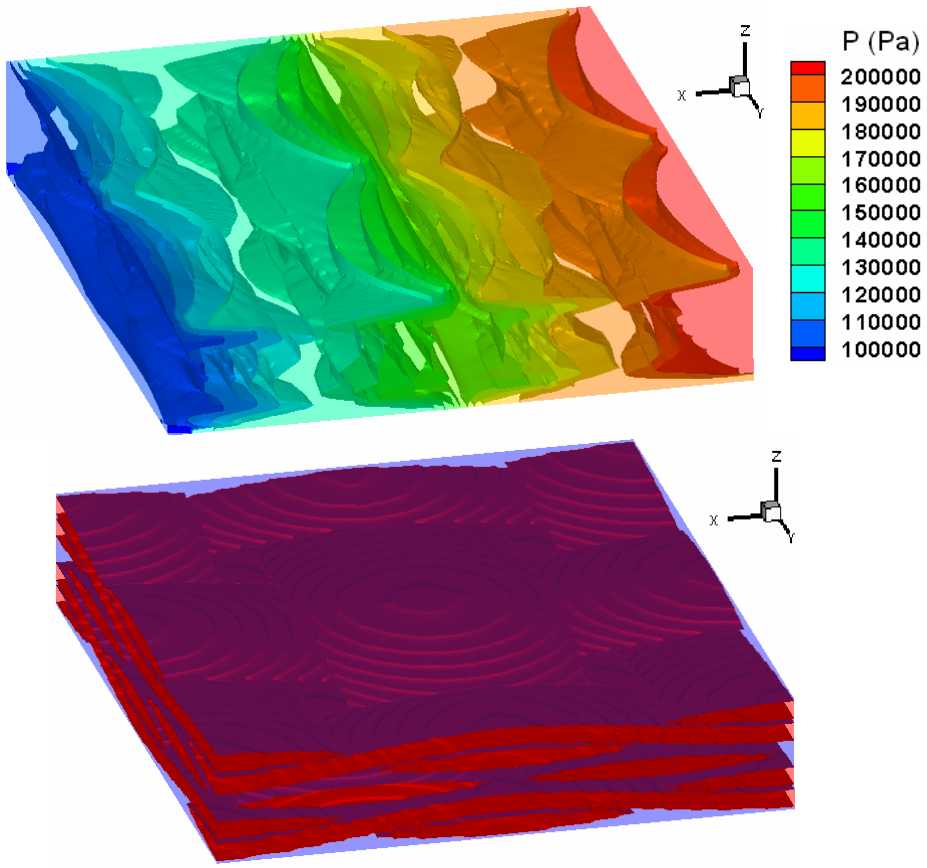

Figure 5.10 – Contour plot of the calculated pressure distribution using 3D Grid Average for the nested 900T plain weave model. The details of the discretised tows are shown below. A pressure difference of 10^5 Pa was applied in the direction of the x-axis.

The permeability values calculated using 2D GA and 3D GA for both the non-nested and nested models are compared to the experimental data in Table 5.5. θ refers to the angle between the weft direction of the fabric and the semi-major axis of the flow front ellipse measured during permeability experiments. In the case of the simulations, the principal axes of permeability are assumed to lie along the weft and warp directions, i.e. the global x and y-axes respectively.

For the non-nested model, the predicted permeability values in all cases do not compare closely with the experimental values. This is reflective of the fact that the cell fibre volume fraction of the model is about 20% less than the experimental value. The instinctive thing to do in this case is to increase the tow fibre volume fraction in order to achieve a higher cell fibre volume fraction. However, as shown in Figure

5.11, increasing the tow fibre volume fraction has a minimal effect on the effective permeability of the cell.

The non-nested model has quite a lot of free spaces between the layers and between the tows. The permeability of these spaces is several orders of magnitude higher than the tow permeability and is the main influence on the permeability of the cell. As such, in order to get a more realistic approximation, it is imperative to increase the volume of the tows within the cell by increasing the level of nesting between the layers.

In the nested model, applying a tow fibre volume fraction of 75.4% gives a cell fibre volume fraction of 52.7% which is similar to the experimental value. The evaluated permeability values using both 2D GA and 3D GA are in the same order of magnitude as that determined experimentally and are much closer to it than the non-nested model – a factor of 5 out as opposed to a factor of 18 out for the non-nested case (for K_x). This is very encouraging given the simple construction of the textile model.

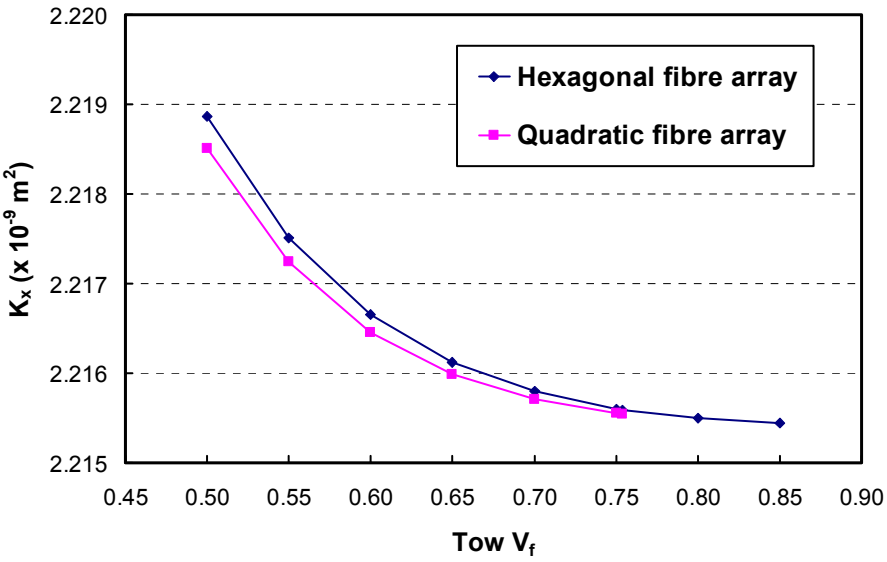

Figure 5.11 – Effect of change in tow fibre volume fraction and fibre arrangement on the permeability for flow along the x-axis of non-nested 900T plain weave model.

However, the predicted values are still about a factor of 5 higher than the measured values. The packing of the tows in the nested model have been maximised, but from Tables 5.3 and 5.4, the modelled tow height is still below the measured values. This means that there is still quite a lot of free space in the model. In order to compensate for this and achieve the experimental cell fibre volume fraction, the tows in the model were given a very high tow fibre volume fraction of 75.4%. From the micrographs, it was also seen that many of the tows interfere with one another and share common boundaries while some of the tows remain at a distance from the others and retain a distinct shape or boundary. It is thought that such a variable level of nesting across the laminate created local pockets of high resistance to flow and thus reduced the global permeability value.

Comparing the 2D GA and 3D GA results, the latter are slightly closer to the experimental data. On the other hand, 3D GA is much more computationally intensive, requiring about 55 hours to compute the solution as opposed to around 5 minutes for 2D GA.

Table 5.5 – Comparison of the measured and predicted permeability of 900T plain weave (± standard deviation).

900T plain weave	**No. of nodes**	**Tow V_f**	**Cell V_f**	**K_x (x10^{-10} m^2)**	**K_y (x10^{-10} m^2)**	**K_x/K_y**	**θ [1]**	**Run time *h:min:sec***
Experimental[2]	-	-	0.53 ± 0.00 (± 0.6%)	1.24 ± 0.36 (± 29.2%)	0.65 ± 0.17 (± 25.7%)	1.91	95° ±71°	-
Non nested model								
2D Grid Average	104351	0.754	0.430	22.16	17.43	1.27	0°	*0:06:19*
3D Grid Average	1901047	0.754	0.429	22.07	-	-	0°	*55:08:21*
Nested model								
2D Grid Average	104351	0.754	0.527	6.99	5.81	1.20	0°	*0:05:26*
3D Grid Average	1901047	0.754	0.526	6.57	4.93	1.33	0°	*54:54:36*

[1] θ refers to the angle between the weft direction of the fabric and the experimentally measured semi-major axis of the flow front ellipse. In the case of the simulations, the principal axes of permeability are assumed to lie along the weft and warp directions.

[2] Values taken from Endruweit et al. (2005) based on 19 experiments (see Table 2.2).

5.5 CONCLUSION

The use of a numerical permeability model can be approached from two opposing points of view. The most obvious approach is to use the model to predict and characterise the permeability of existing textiles. On the other hand, one can use the predictive capability of the model to help configure and manufacture a fabric to suit its application.

In the first part of the chapter, a twill weave model with arbitrary dimensions was analysed to demonstrate the predictive capability of the permeability model. The 2D Grid Average model successfully calculated the permeability values of the textile for a range of applied in-plane shear angles. The predicted permeability trend agreed with published data. Results were similar to those obtained using commercial CFD software, although the latter were far more computationally intensive.

In the second part, a plain weave fabric was modelled to predict its permeability in order to compare to experimental values. An accurate description of the fabric structure is critical to successful permeability prediction using numerical models. A study was subsequently undertaken to characterise the required geometric data for the plain weave laminate as used in the experiments.

Using the laminate data, two models with non-nested and nested geometry were created and their permeabilities evaluated. The predicted permeability of the model with the nested layers was in the same range as the experimental value. This study demonstrated that it is possible to provide a permeability prediction for real preforms in the same order of magnitude as experimental data (factor of about 5 out).

The limitations of the numerical model are also highlighted. Current numerical models assume an idealised shape of the tows and often use idealised tow paths. In reality, there is a lot of mixing of tows between nested layers and often there are no distinct tow boundaries. The current fabric model cannot achieve the same level of nesting as seen in real laminates. This is the main issue which needs to be tackled in subsequent models.

The predictive capability of numerical models will be explored further in the next chapter, with particular emphasis on modelling the variations of textile permeability, which have often been reported in the literature. The sensitivity of the variations will be analysed from the mesoscopic point of view.

6 STOCHASTIC VARIABILITY IN TEXTILES

6.1 INTRODUCTION

In general, textile permeability shows a high variance (Rudd et al., 1997, Lundstrom et al., 2000, Luo et al., 2001), consequently affecting the quality and cycle time of the product. Also, this variability makes it difficult to predict the filling pattern and fill times accurately, thus reducing productivity.

This chapter attempts to address permeability variation by modelling variability in the mesoscopic structure of the fabric itself. In contrast to the works of Lundstrom (2004) and Nordlund and Lundstrom (2005), which are specific to non-crimp fabric, the methodology here is based on the generalised textile modeller, TexGen. Variability is modelled by randomly moving the paths of the fibre bundles according to a statistical distribution and the effective permeability of the randomised flow domain is calculated using the 2D Grid Average method as described in Chapter 3.

The effects of increasing tow variability on permeability variations are first analysed for the unit cell of a non-crimp fabric model. In the second part, the calculation domain size is increased to consider its effect on variation. Finally, a plain weave is compared to a NCF with similar dimensions and fibre volume fraction to analyse the effect of fabric structure.

6.2 MODELLING STOCHASTIC BEHAVIOUR

In TexGen, variability in textile models is generated using the Monte-Carlo method, whereby the tow crossovers points within the fabric are displaced randomly along the global x and y axes independently. This movement will follow a Normal distribution with respect to the original coordinates of the points and a user-specified standard deviation of displacement. Examples of the modelling of tow variations are shown in Figure 6.1. As the tow movement variation is increased, the tows will invariably begin to interfere with one another. In this study, cases with tow interference are discarded. The actual tow position distribution can be easily back calculated for a set of randomised cases.

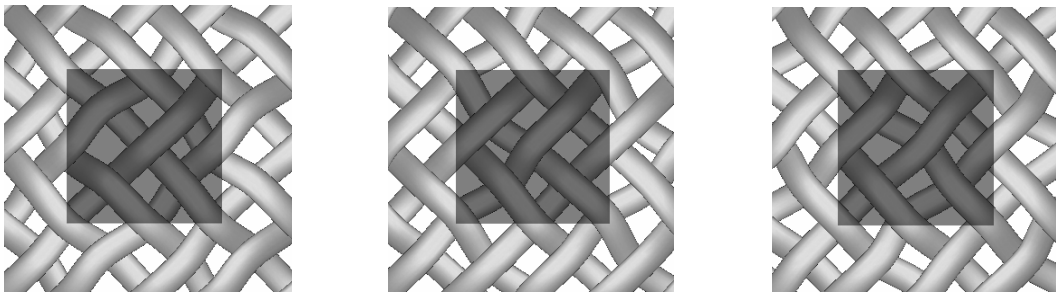

Figure 6.1 – Examples illustrating the effect of statistical variations applied to tow paths in a 2:2 twill weave model. Analysis domain is shaded.

The randomised model is dicretised using the 2D Grid Average method. As periodic boundary conditions are imposed on the four sides of the flow domain in the solution, it is imperative that the model itself exhibits periodicity. This means that within the computational domain of a fabric model, the position and direction of the tows that exit on one side have to correspond to those that enter the opposite side. While this is quite straightforward for a model without distortion, for cases with variability, the number and length of independently variable tows would have to correspond to the size of the analysis domain, as illustrated in Figure 6.2.

For the analysis of a unit cell (Figure 6.2a), only two basic tows representing each layer are needed to ensure periodicity, with lengths equivalent to the diagonal dimension of the domain. A unit cell is defined here as the domain with the minimum dimensions which forms a repeatable representative cell of the fabric. For the analysis with a domain size equivalent to 25 unit cells (Figure 6.2b), ten basic tows are modelled, again with lengths equivalent to the diagonal distance of the domain. While using the basic cell with two tows will also produce periodicity for the enlarged domain, as shown by the black square on Figure 6.2a, the unit cells are replicated 25 times rather than varying independently within the domain as in Figure 6.2b.

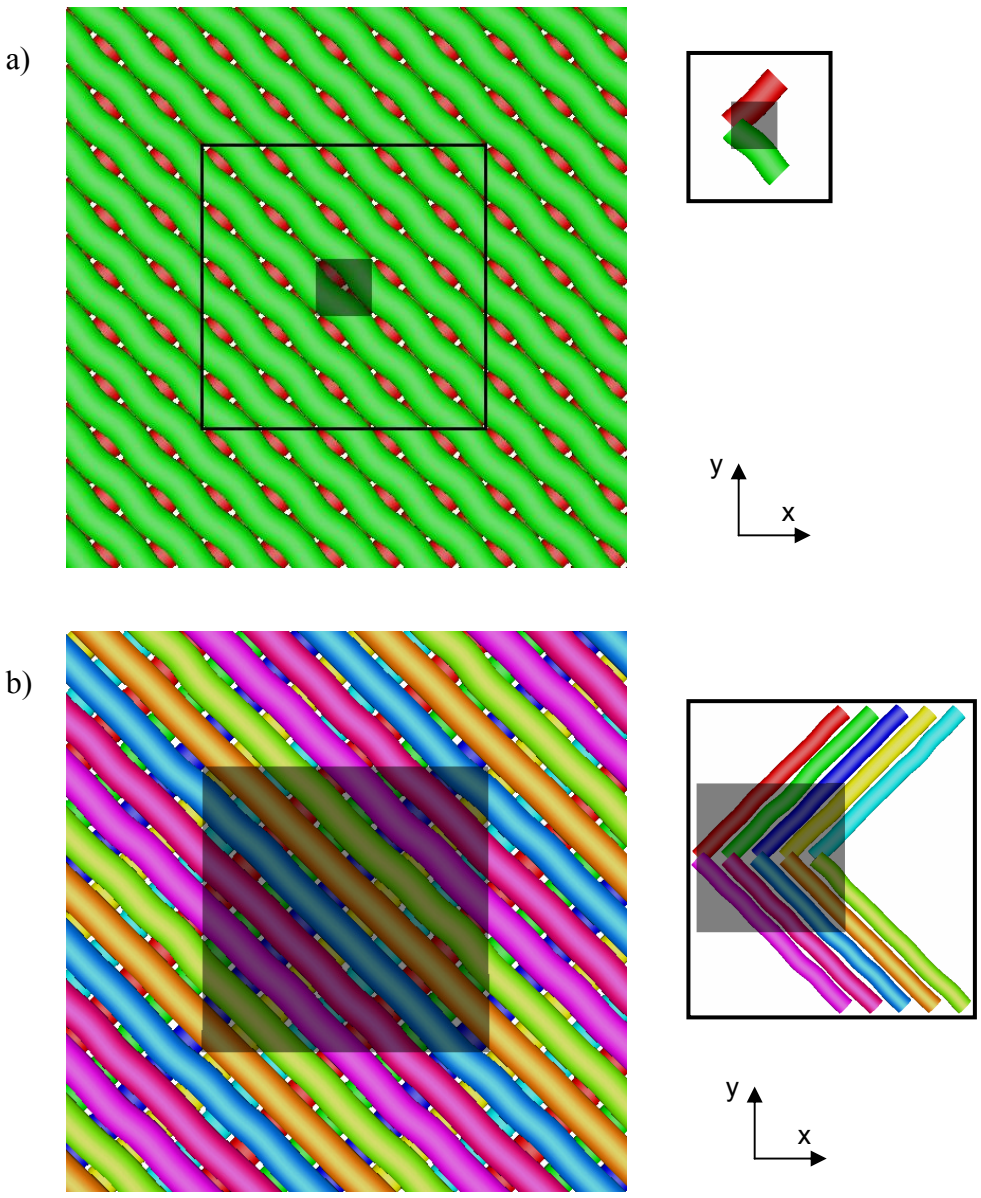

Figure 6.2 – Examples illustrating the relationship between computational domain and number of independent tows required to satisfy periodic boundary conditions. (a) Unit cell analysis with only two tows and (b) analysis with domain size equivalent to 25 unit cells with ten individual tows. The analysis domains are highlighted. The figures to the right shows the model with the basic tows which are repeated across the domain.

6.3 SENSITIVITY OF PERMEABILITY TO VARIABILITY

A ± 45° non-crimp fabric was modelled with the dimensions shown in Figure 6.3. The tows are modelled as elliptical cross sections with semi major axis, R_p, and semi minor axis, R_q, with no stitches present. The upper and lower unidirectional layers are touching giving a domain height of $4R_q$. The tows are separated by a distance a_0, which is also the dimension of the unit cell. The pressure gradient of the analysis domain was set to 10^5 Pa in the direction of the global x axis with a resin viscosity μ of 0.308 Pa s (although the permeability prediction is independent of these values).

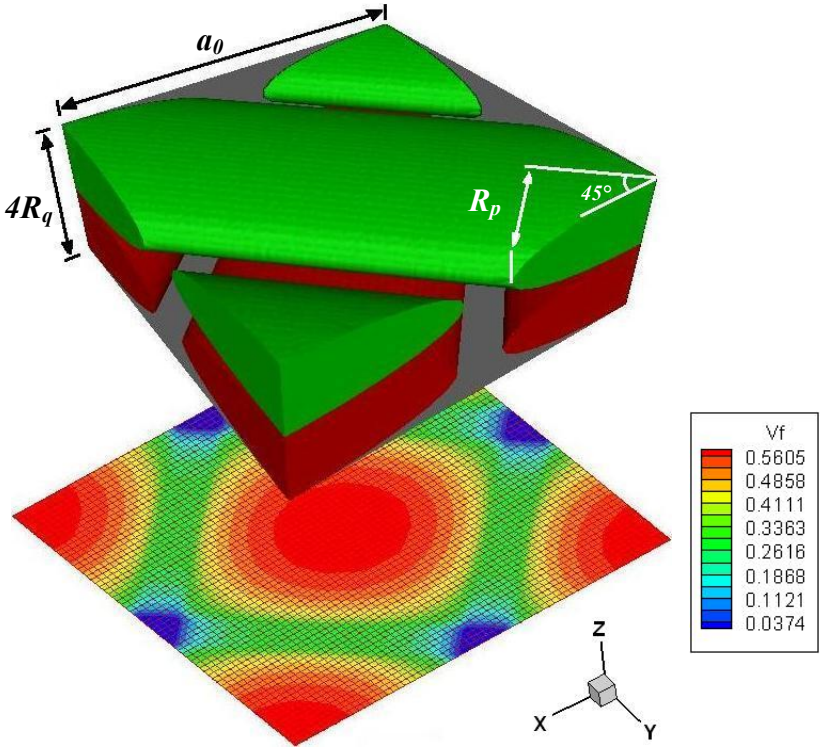

Figure 6.3 – Unit cell of a ± 45° non-crimp fabric model with dimensions as shown (top) and the discretised Grid Average mesh showing fibre volume fraction (bottom), red to blue colours representing high to low fibre volume fraction (tow V_f = 60%).

6.3.1 Degree of tow variability

Two NCF models were created with a_0 values of 2.6mm and 3.6mm respectively, in order to study the effect of distance between tows and hence the relative degree of tow variability on the variation of permeability. Both models have elliptical tow dimensions of R_p = 0.8mm and R_q = 0.25mm. The tow local permeability is calculated for 60% V_f based on the Gebart model (Eqns. 2.11 and 2.12) for a

quadratic array of unidirectional fibres and a fibre diameter of 15.8 μm. This gives local tow permeability values of 1.56 x 10^{-12} m^2 along the tows and 1.97 x 10^{-13} m^2 perpendicular to the tows. Permeability was analysed for unit cell dimensions, which were 2.6 x 2.6 x 1.0 mm and 3.6 x 3.6 x 1.0 mm respectively. As such, the models contain only two independently variable tows in order to satisfy the periodic boundary conditions, as shown in Figure 6.2a. The nominal case cell fibre volume fractions are 40.6% and 29.3% respectively. A Grid Average mesh sensitivity study was performed using the nominal NCF case with a_0 = 2.6mm (see Appendix I). A resolution of 50 divisions per unit length was found to be optimum, resulting in meshes containing 17161 nodes (for a_0 = 2.6mm) and 32761 nodes (for a_0 = 3.6mm).

Randomised cases were generated for both models at three relative degrees of tow variation, where the applied standard deviations of nodal displacement are 14.83%, 29.65% and 59.30% with respect to the spacing between the tows. For each model and different tow variations, a total of 100 randomised cases were simulated and evaluated statistically. The achieved levels of tow variation were also calculated for each set of randomised cases. Table 6.1 lists the absolute and relative values of the standard deviations of tow movement, for both the intended and resultant levels.

For the first two levels, the achieved variations are about a third less than the corresponding applied values. The relative increase between the two levels is consistent for both the applied and achieved values. However when the applied tow movement variation is doubled from 29.65% to 59.30%, the achieved variations less than doubled from 19.89% to 36.34% for the a_0 = 2.6mm model and from 19.78% to 34.53% for the a_0 = 3.6mm model. This is because the models have exceeded the maximum allowable variation without tow interference. Indeed, when generating the randomised cases at this degree of variation, 2 out of 10 cases have to be discarded because of tow interference. As the randomised cases are filtered for tow interference, the geometrical dimension of the fabric is imposing a limit on the variability of the model.

Tables 6.2 and 6.3 show the achieved levels of tow variability and the resultant mean and standard deviations for fibre volume fraction, fibre angle (α) and effective directional permeability (for flow parallel to the x axis in Figure 6.3). The fibre angle,

α, is the angle between the two fibre directions at the crossover points and is calculated from the vectors describing the randomised tow paths. The values in the brackets are the respective coefficients of variation, defined as:

$$\mathbf{CV} = \frac{standard\ deviation}{mean} \tag{7.1}$$

The mean permeability value, in general, decreases with increasing tow position variability, whilst the standard deviation of permeability, as expected, increases with increasing variability. For the model with a_0 = 2.6mm, the CV of permeability for the three degrees of tow variation in increasing magnitudes are 1.39%, 5.14% and 7.64%. The corresponding CV of permeability for the model with a_0 = 3.6mm are 2.36%, 8.29% and 14.48%. These values of relative variation of permeability are reflective of the achieved level of tow variation. Generally as a_0 is increased, the relative variation of permeability is increased. This is because in order to achieve similar relative degrees of tow variation, the absolute values of the variations for the model with larger a_0 are higher than the model with smaller a_0 (see Table 6.1). Interestingly, the distributions of permeability for the model with a_0 = 2.6mm for the three increasing levels of tow position variation, as shown in Figures 6.4 to 6.6 respectively, do not correlate that well with Normal distributions. This observation will be further discussed in the next section.

Table 6.1 – Details of the applied standard deviations of nodal position and the corresponding achieved variation in the randomised cases.

Case	Standard deviation of nodal position			
	Applied		Achieved	
	(mm)	% wrt space between tows	(mm)	% wrt space between tows
NCF model with a_0 = 2.6mm	0.05	14.83	0.035	10.27
	0.10	29.65	0.067	19.89
	0.20	59.30	0.123	36.34
NCF model with a_0 = 3.6mm	0.19825	14.83	0.137	10.27
	0.3965	29.65	0.265	19.78
	0.793	59.30	0.462	34.53

Table 6.2 – Mean and standard deviation values for NCF model with a_0 = 2.6mm

Std. dev. of nodal position as % wrt space between tows		**NCF model with a_0 = 2.6 mm, R_p = 0.8 mm and R_q = 0.25 mm**		
Applied	**Achieved**	**V_f**	**α (deg)**	**K_x (x 10^{-9} m^2)**
0.00	0.00	0.406	90	2.224
14.83	10.27	0.406 ± 0.000 (± 0.04%)	90.01 ± 1.97 (± 0.02%)	2.228 ± 0.031 (± 1.39%)
29.65	19.89	0.406 ± 0.001 (± 0.13%)	89.95 ± 3.73 (± 0.04%)	2.162 ± 0.111 (± 5.14%)
59.30	36.34	0.407 ± 0.001 (± 0.19%)	89.93 ± 5.19 (± 0.06%)	2.070 ± 0.158 (± 7.64%)

Table 6.3 – Mean and standard deviation values for NCF model with a_0 = 3.6mm

Std. dev. of nodal position as % wrt space between tows		**NCF model with a_0 = 3.6 mm, R_p = 0.8 mm and R_q = 0.25 mm**		
Applied	**Achieved**	**V_f**	**α (deg)**	**K_x (x 10^{-9} m^2)**
0.00	0.00	0.293	90	7.623
14.83	10.27	0.294 ± 0.001 (± 0.35%)	90.06 ± 6.41 (± 0.07%)	7.516 ± 0.178 (± 2.36%)
29.65	19.78	0.296 ± 0.003 (± 0.98%)	90.07 ± 11.68 (± 0.13%)	7.211 ± 0.598 (± 8.29%)
59.30	34.53	0.299 ± 0.005 (± 0.55%)	89.83 ± 17.04 (± 0.19%)	6.783 ± 0.982 (± 14.48%)

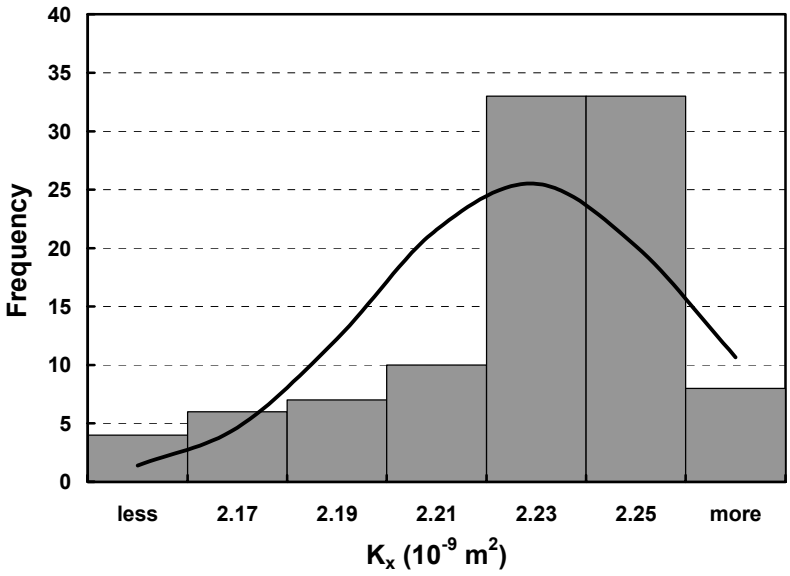

Figure 6.4 – Distribution of predicted K_x for variable NCF model (a_0 = 2.6mm) with applied nodal displacement standard deviation of 14.83% with respect to the spacing between the tows. Corresponding Normal distribution is shown with correlation coefficient of 0.777.

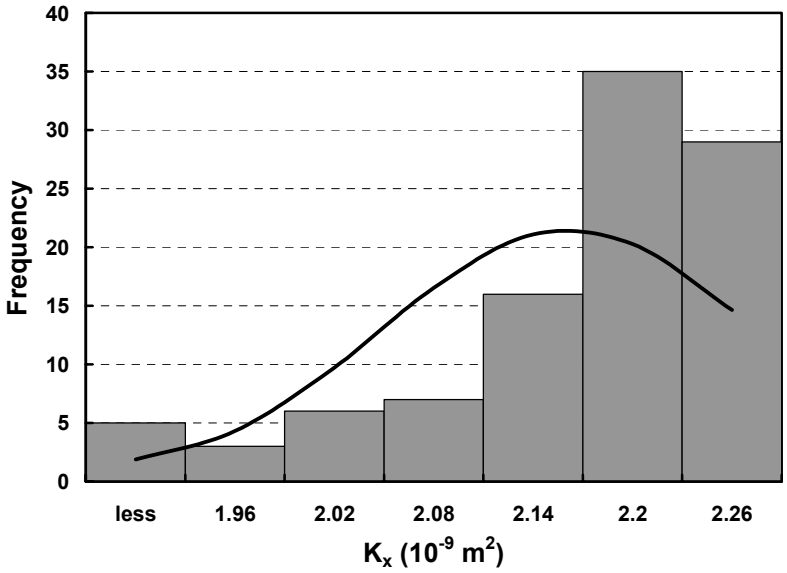

Figure 6.5 – Distribution of predicted K_x for variable NCF model (a_0 = 2.6mm) with applied nodal displacement standard deviation of 29.65% with respect to the spacing between the tows. Corresponding Normal distribution is shown with correlation coefficient of 0.675.

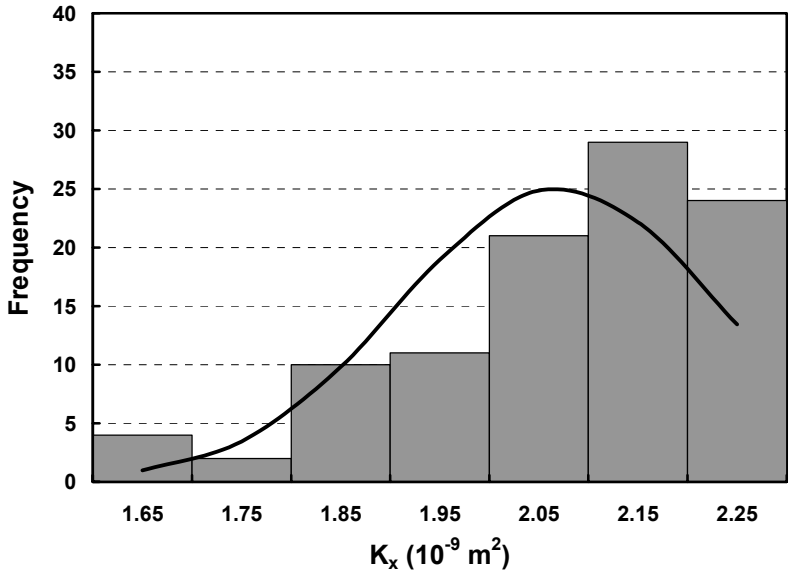

Figure 6.6 – Distribution of predicted K_x for variable NCF model (a_0 = 2.6mm) with applied nodal displacement standard deviation of 59.30% with respect to the spacing between the tows. Corresponding Normal distribution is shown with correlation coefficient of 0.796.

6.3.2 Size of the computational domain

To study the effect of increasing the domain size on variability, the NCF model with a_0 = 2.6mm was modelled with 2, 6 and 10 independently variable tows (see Figure 6.2). This corresponds to domain lengths of 2.6mm, 7.8mm and 13.0mm respectively. The tows retain the same dimensions and parameters as above. Due to the enlarging domain sizes, the models were discretised using 20 divisions per unit, resulting in meshes containing 2809, 24649 and 68121 nodes respectively. This resolution was found to give consistent results from the mesh sensitivity study (see Appendix I). 100 randomised cases were generated for each domain size by applying a tow movement standard deviation of 29.65% with respect to the spacing between the tows. The achieved level of tow variability and the evaluated mean and standard deviations of V_f, α and K_x are listed in Table 6.4.

From the table, the mean values of permeability and fibre volume fraction remained almost unchanged with increasing domain size. However, the standard deviations of K_x and V_f decreased with increasing domain size whilst the fibre angle variations remained almost constant. Figures 6.7 to 6.9 shows that the K_x distribution tends towards a Normal distribution as the domain size increases.

Table 6.4 – Mean and standard deviation values for NCF model with a_0 = 2.6mm. The applied % standard deviation of the nodal position with respect to the spacing between tows is 29.65%.

No. of variable tows	Achieved std. dev. of nodal pos. as % wrt space bet. tows	V_f	α (deg)	K_x (x 10^{-9} m^2) (nominal K_x = 2.204)
2	19.89	0.406 ± 0.001 (± 0.13%)	89.95 ± 3.73 (± 0.04%)	2.094 ± 0.122 (± 5.82%)
6	21.13	0.406 ± 0.000 (± 0.06%)	90.00 ± 4.52 (± 0.05%)	2.060 ± 0.056 (± 2.73%)
10	20.31	0.406 ± 0.000 (± 0.03%)	90.00 ± 4.21 (± 0.05%)	2.075 ± 0.033 (± 1.57%)

The achieved levels of tow variability are similar with increasing domain size, as are the fibre angle variations. The only difference is the combined effect of this variability across the whole analysis domain. In the smallest cases with only 2 variable tows, the effect of the inhomogeneity in that unit cell, whether small or large, is magnified. The pressure distribution of a typical randomised case with 2 variable tows is shown in Figure 6.10a, where a larger region is shown for better comparison. As is evident from the figure, the pressure alternates between distinct regions of steep and gradual drops, as the inhomogeneity present at the unit cell level is duplicated across the enlarged region. This causes the scatter of the K_x and V_f values to be larger.

For the cases with a larger domain size, as they incorporate a higher number of tows that are independently variable, local inhomogeneities will tend to cancel each other out and thus create a balanced domain. Figure 6.10b confirms this, showing a balanced pressure distribution for a typical randomised case with 10 independently variable tows. Each of the randomised cases would be likely to exhibit similar characteristics and the set of K_x and V_f values will narrow, converging onto a Normal distribution. This argument is further supported by Figure 6.11, which compares the permeability of the cases with 2 and 10 tows as a function of fibre volume fraction.

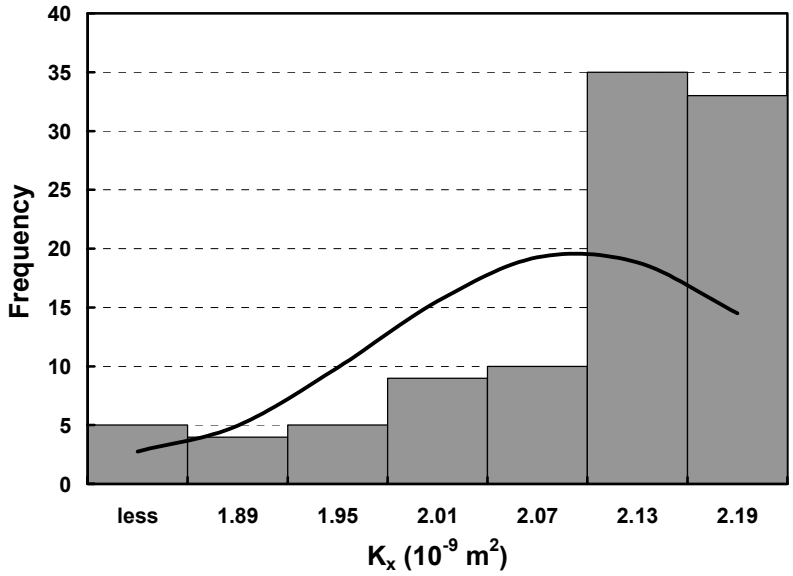

Figure 6.7 – Distribution of predicted K_x for NCF model with 2 independently variable tows and an applied nodal displacement standard deviation of 29.65% with respect to the spacing between the tows. Corresponding Normal distribution is shown with correlation coefficient of 0.593.

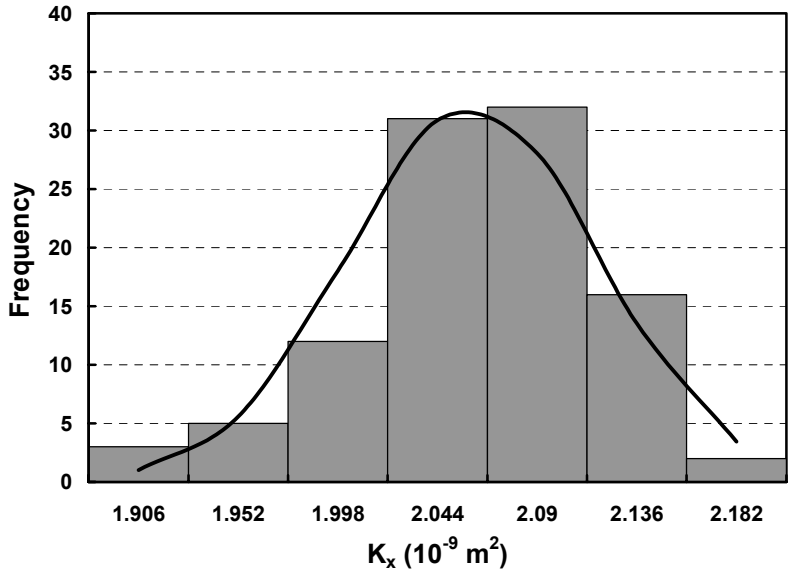

Figure 6.8 – Distribution of predicted K_x for NCF model with 6 independently variable tows and an applied nodal displacement standard deviation of 29.65% with respect to the spacing between the tows. Corresponding Normal distribution is shown with correlation coefficient of 0.966.

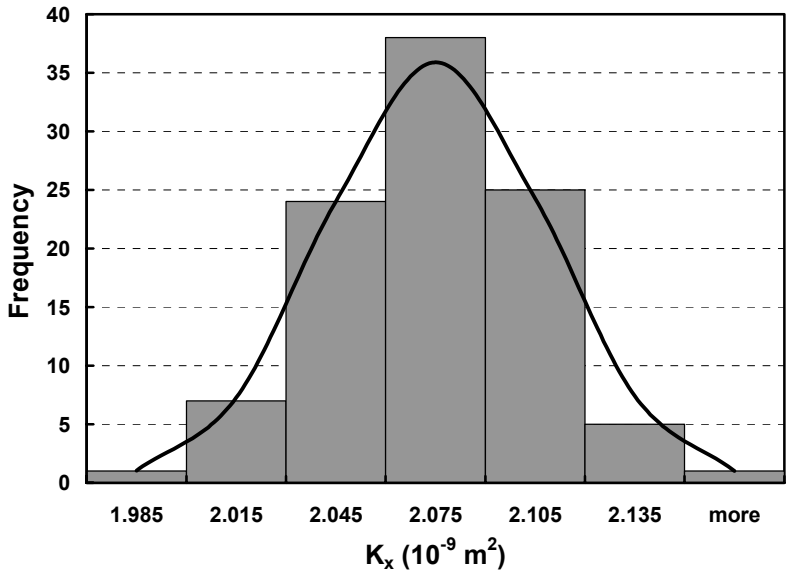

Figure 6.9 – Distribution of predicted K_x for NCF model with 10 independently variable tows and an applied nodal displacement standard deviation of 29.65% with respect to the spacing between the tows. Corresponding Normal distribution is shown with correlation coefficient of 0.998.

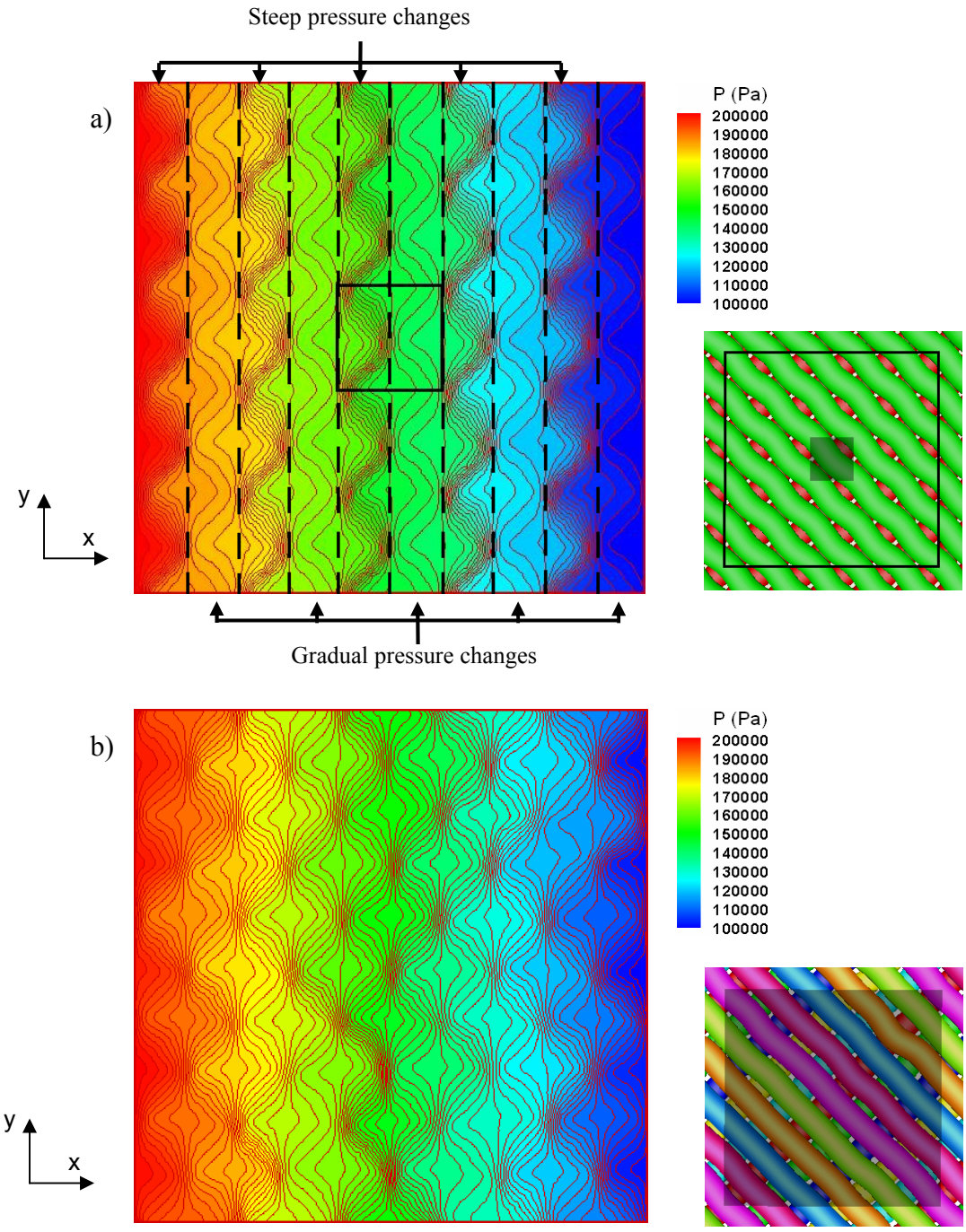

Figure 6.10 – Pressure distribution of a typical randomised NCF model with (a) 2 and (b) 10 independently varying tows. The images to the right show the corresponding shape of the tow paths. For the case with 2 independent tows (a), a larger region is shown for easier comparison and the actual analysis domain size has been highlighted. The effect of a local inhomogeneity on pressure in the case with 2 tows is magnified as it is replicated over the larger region, where the pressure distinctly alternates between regions of steep and gradual drops (a). In the case with 10 tows, local inhomogeneities tend to cancel each other out, leading to a more balanced pressure distribution (b).

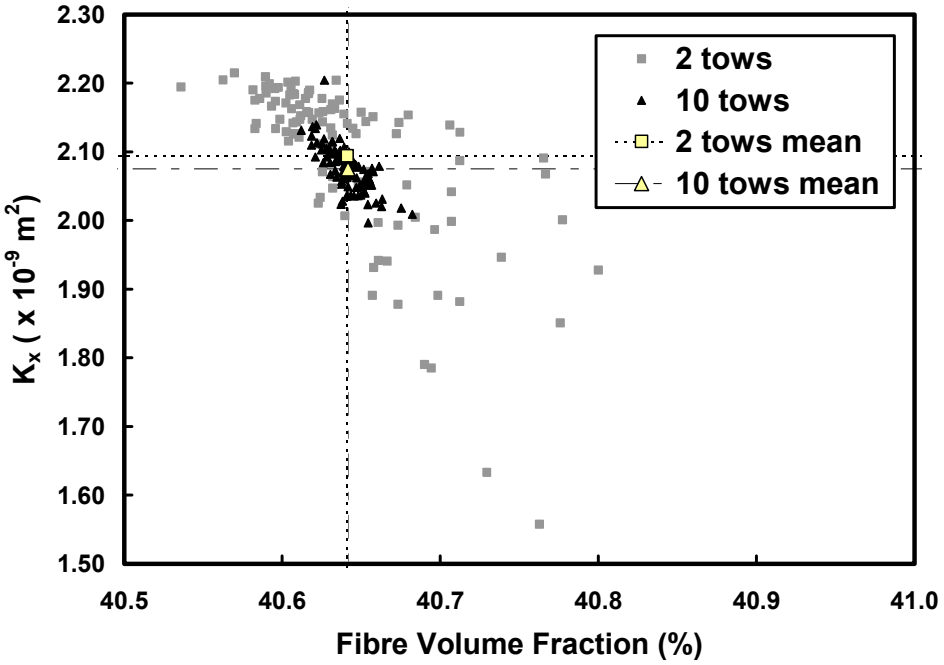

Figure 6.11 – Predicted K_x plotted as a function of fibre volume fraction for the 100 variable cases each of NCF models with 2 and 10 independent tows. The points for the latter congregate towards the mean value.

6.3.3 Fabric structure

Experiments have shown that fabric structure influences the variability of the fabric permeability to a large extent – see Table 2.2 (Endruweit et al., 2005). A plain weave fabric is modelled here and compared to the NCF model (see Figure 6.12). Both the models have elliptical tow cross sections with dimensions a_0 = 2.6mm, R_p = 0.7mm and R_q = 0.175mm. These tows are comparatively smaller than the above studies and the upper and lower layers of these models are not touching, so that tow variations can be introduced in the plain weave without resulting in interference. Consequently, there exists a thin layer of free space between the layers in the corresponding NCF model. The tow local permeability is calculated for 60% V_f based on the Gebart model using parameters listed in Table 2.3 for a quadratic array of fibres and a fibre diameter of 15.8 μm. This gives local tow permeabilities of 1.56 x 10^{-12} m^2 along the tows and 1.97 x 10^{-13} m^2 perpendicular to the tows. The computational domain size is 2.6 x 2.6 x 0.85mm, with nominal cell fibre volume fractions of 29.3% and 30.6% for the NCF and plain weave models respectively. The models are discretised using 50 divisions per unit, resulting in Grid Average meshes containing 17161 nodes.

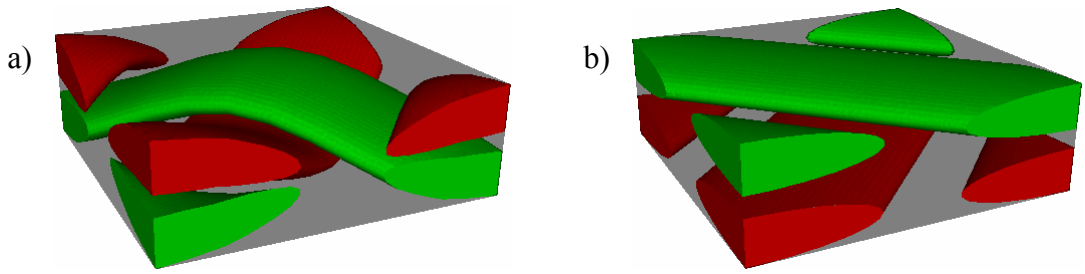

Figure 6.12 – (a) Plain weave model with a_0 = 2.6mm, R_p = 0.7mm and R_q = 0.175mm and (b) corresponding NCF model. Note the gap between the layers in both models.

Randomised cases were generated for the two models by applying two standard deviations of nodal displacement at 14.83% and 29.65% with respect to the spacing between the tows. For each model and different tow variations, a total of 100 randomised cases were simulated and evaluated statistically. The achieved levels of tow variability and resultant mean and standard deviations of V_f, α and K_x are listed in Table 6.5. Generally, the standard deviation of K_x increases with increasing tow variations. Interestingly, the mean value of K_x for the NCF model decreased with increasing variability whilst the mean K_x value for the plain weave increased slightly.

Comparing between the NCF and plain weave models, the mean K_x values of the NCF model are about 3 times that of the plain weave model. This is perhaps reflective of the layer of free space between the two layers of tows in the NCF model. Also, due to the weave style, the plain weave model exhibits a higher V_f than the NCF model. Interestingly, in the experiments conducted by Endruweit et al. (2005), the measured permeability of the NCF is lower than that for the plain weave fabric (see Table 2.2). However, in the experiments, the NCF have a higher V_f than the plain weave fabric and there is no layer of free space between the layers of tows.

The degree of permeability variation is somewhat limited for the plain weave cases. For the NCF model, when the tow position variation is doubled, there is an increase in permeability variations from 1.24% to 4.18%. The plain weave model exhibited an increase of only 11% in permeability variations from 1.73% to 1.93%. Similar observations can be made on the relative increase in the variations of the fibre volume fraction and fibre angle. The standard deviation of the fibre angles for the plain weave is almost the same for the two degrees of tow variation.

Table 6.5 – Mean and standard deviation values for a NCF and a plain weave model with a_0 = 2.6mm, R_p = 0.7mm and R_q = 0.175mm.

Std. dev. of nodal position as % wrt space between tows		V_f	α (deg)	K_x (x 10^{-9} m^2)
Applied	**Achieved**			
Bi-directional NCF				
0.00	0.00	0.293	90	5.485
14.83	10.50	0.293 ± 0.000 (± 0.12%)	89.99 ± 3.90 (± 0.04%)	5.473 ± 0.068 (± 1.24%)
29.65	20.83	0.294 ± 0.001 (± 0.41%)	90.12 ± 6.93 (± 0.08%)	5.347 ± 0.224 (± 4.18%)
Plain weave				
0.00	0.00	0.306	90	1.629
14.83	8.69	0.304 ± 0.000 (± 0.09%)	89.98 ± 3.44 (± 0.04%)	1.665 ± 0.029 (± 1.73%)
29.65	13.12	0.305 ± 0.001 (± 0.21%)	89.98 ± 4.47 (± 0.05%)	1.674 ± 0.032 (± 1.93%)

At applied tow movement variations of 14.83% and 29.65%, the NCF cases achieved variations of 10.50% and 20.83% respectively whilst the plain weave cases achieved 8.69% and 13.12% respectively. The resultant variability levels of the NCF cases were consistently about a third lower than the respective intended level of variability. The same cannot be said about the plain weave cases. Clearly, the plain weave model has reached its structural limit of variation at an applied variation of 29.65%, as evident from the low level of resultant variability of 13.12%. In fact, 7 out of 10 randomised plain weave cases with 29.65% tow variation had to be discarded because of tow interference. The plain weave structure restricts the mobility of the tows more than the NCF does, and this is reflected in the permeability variation.

A secondary effect of the plain weave structure is that its permeability distribution correlates better with a Normal distribution compared to the NCF (see Figures 6.13 and 6.14). The plain weave structure restricts the movement of the tows, particularly at the tow crossover points, where the point of overlap cannot differ too much between randomised cases. As such, most of the randomised cases exhibit a similar pattern of variation, and the predicted pressure distributions will be very close to one

another (see Figure 6.15). Calculated permeability values are hence equally likely to lie on either side of the mean.

On the other hand, the tows in the NCF are less restricted compared to the plain weave. Even with the same level of tow movement variations as the plain weave, the randomised NCF cases have a wider range of possible variation patterns. For the NCF model, in extreme cases, a whole tow can move closer to an adjacent tow, which is not possible for a plain weave. As a result, these cases exhibit distorted and non-uniform pressure distributions, as shown in Figure 6.16. The calculated permeability values of these extreme cases are much lower than the nominal value. Consequently, the inclusion of these smaller permeability values distorts the shape of the permeability distribution of the NCF cases.

The observation in this section on the effect of fabric structure on the shape of the permeability distribution is very interesting. However, published experimental observations (Hoes et al., 2004, Endruweit et al., 2005) suggest that the Normal distribution of permeability is seen for most types of fabrics. One can argue that as the NCF model used here does not include stitches as seen in a real NCF, then the tows are freer to move, creating more variable patterns. The previous section has also shown that it is perhaps more sensible to model a larger domain when variability is involved. In any case, the major implication of the work here is that the structure of a fabric has an important influence on permeability variations at the mesoscopic scale.

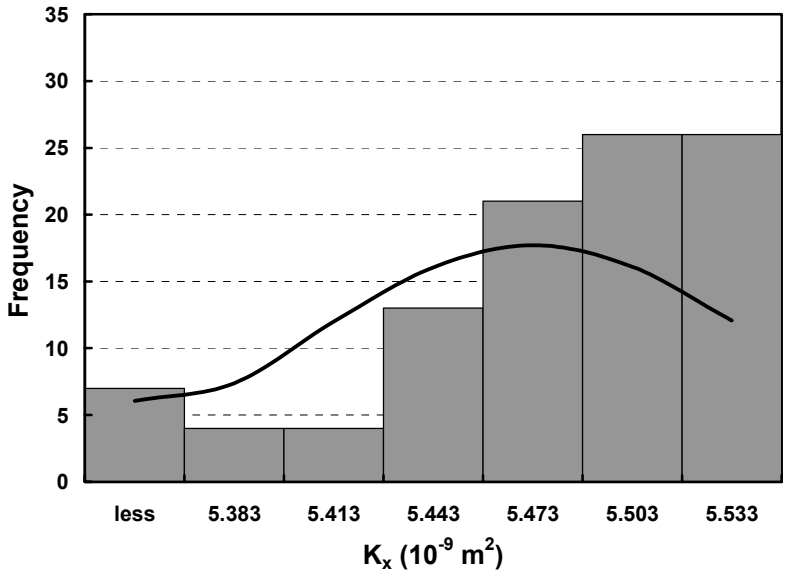

Figure 6.13 – Distribution of predicted K_x for NCF model with R_p = 0.7mm and R_q = 0.175mm, and an applied nodal displacement standard deviation of 14.83% with respect to the spacing between the tows. Corresponding Normal distribution is shown with correlation coefficient of 0.648.

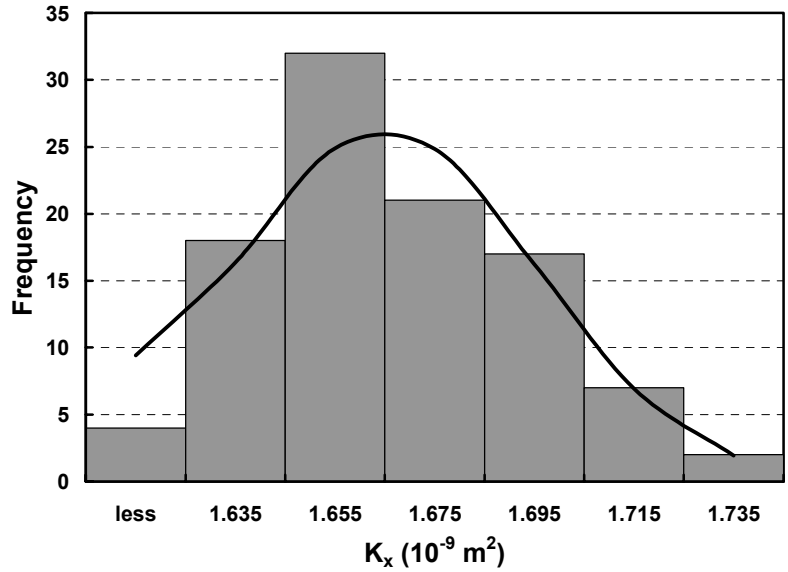

Figure 6.14 – Distribution of predicted K_x for plain weave model with R_p = 0.7mm and R_q = 0.175mm, and an applied nodal displacement standard deviation of 14.83% with respect to the spacing between the tows. Corresponding Normal distribution is shown with correlation coefficient of 0.934.

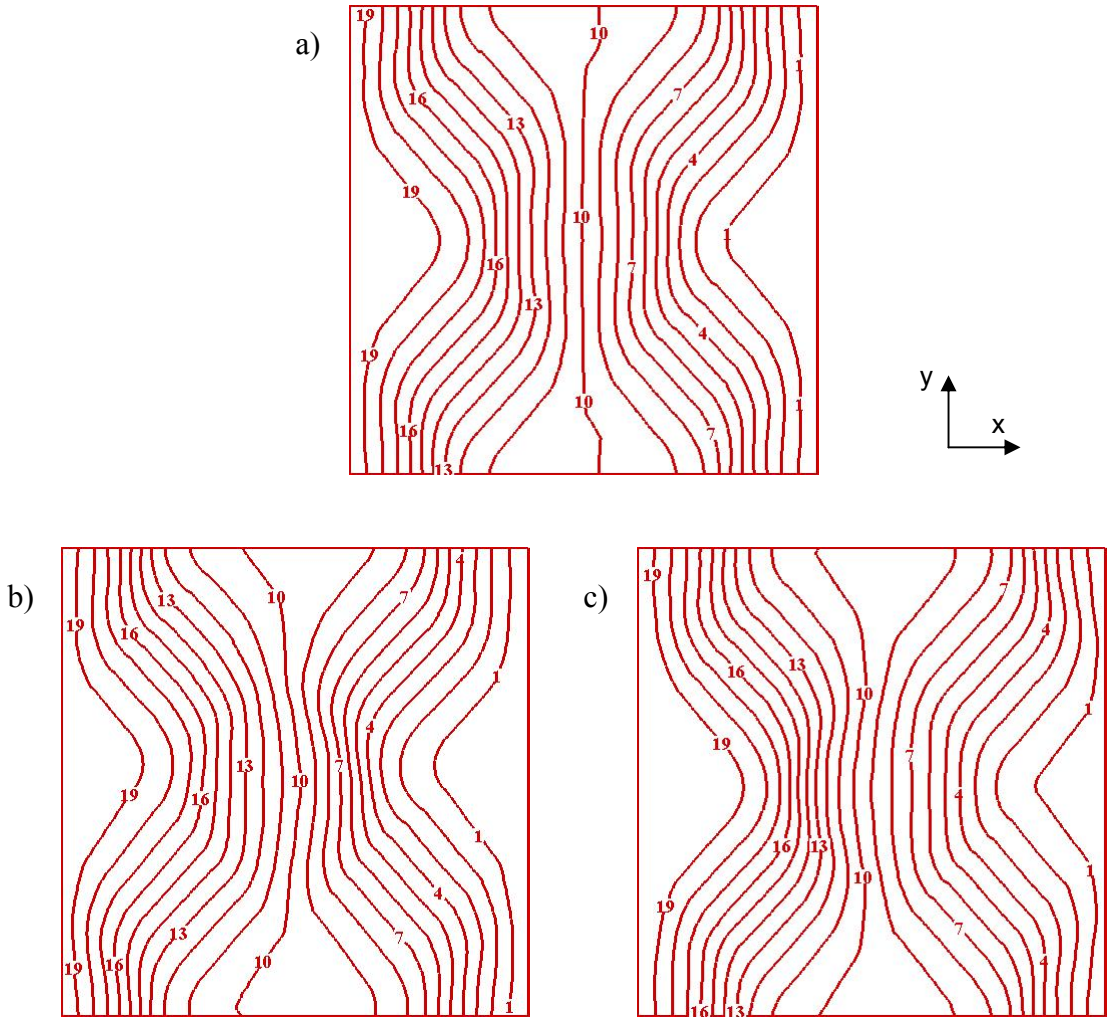

Figure 6.15 – Pressure distributions of (a) the nominal plain weave model with no tow variability and (b & c) typical cases with extreme tow variability. (a) The nominal case exhibits symmetrical pressure contours about the centre line 10. The pressure distributions in (b) and (c) are still quite similar to that of the nominal case (a).

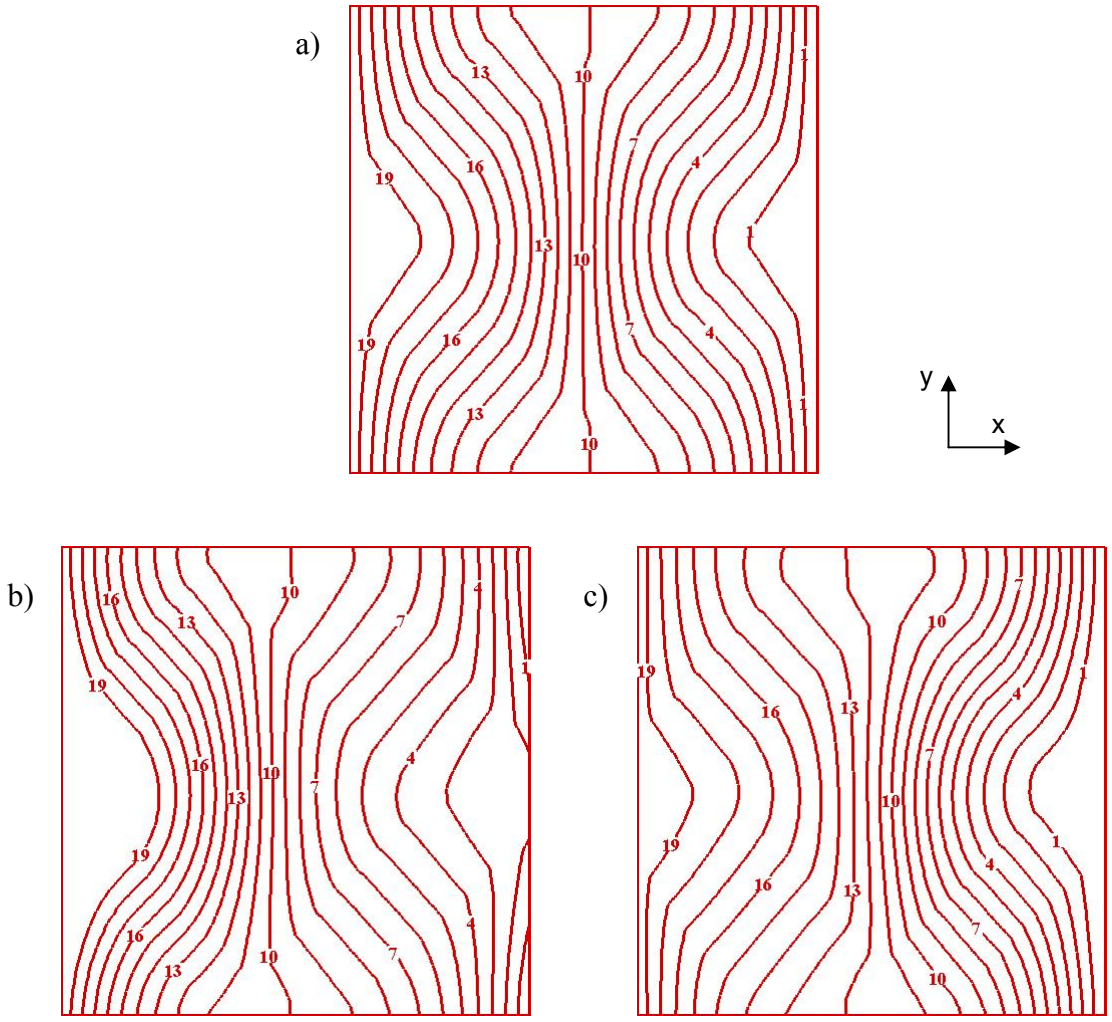

Figure 6.16 – Pressure distributions of (a) the nominal NCF model with no tow variability and (b & c) typical cases with extreme tow variability. (a) The nominal case exhibits symmetrical pressure contours about the centre line 10. In (b), the pressure distribution is distorted compared to (a) whereas in (c), the pressure contours are not symmetrical as line 10 has shifted to the right.

6.3.4 Discussion

The relative variations of permeability predicted in this study are comparatively lower (in the range of 1% to 15%) than some of those reported in the literature. Hoes et al. (2004) reported permeability variations of between 12% and 23% whilst Pan et al (2000) measured variations of 6% to 13%. Endruweit et al. (2005) determined the permeability of five different fabrics and reported permeability variations between 9% and 29% (as shown in Table 2.2). A study was also performed by Endruweit and Long (2005) to model variability on a macroscopic scale which resulted in variations in the range of 7% to 25%.

One can argue that this study is fundamentally different in that it is at the mesoscopic length scale compared to the macroscopic analyses in the reported studies. Endruweit's variability model (Endruweit and Long, 2005) is applicable to a macroscopic flow simulation where the effect of the structure is rather homogenised. The mesoscopic models presented here are based purely on the fabric architecture which is useful to address issues such as localised inhomogeneities. This may allow local phenomena such as a void formation to be studied in detail.

In order to compare between the predicted and measured values, the relative variations of permeability for the NCF data sets with a_0 = 2.6mm, R_p = 0.8mm and R_q = 0.25mm (Tables 6.2 & 6.4) are plotted as a function of the relative variation of cell fibre volume fraction in Figure 6.17. Included on the figure are the measurements reported by Endruweit et al. (2005) for a non-crimp glass fibre fabric (FGE 106 HD) – see Table 2.2. This fabric and the NCF modelled in this paper have a similar geometric characteristic in the ratio R_p/distance between tows: 0.39 for FGE 106 and 0.44 for the NCF model.

A linear function can be deduced for the relationship between relative permeability variation and relative fibre volume fraction variation. Interestingly, this function can be extrapolated from the predicted values, which are in the lower ranges, to the much higher measured values. However, nothing deeper than the face value of Figure 6.17 should or can be deduced. A large gap remains between the predicted and measured values.

One limitation of the present study is that the fabric models have idealised geometries with a low fibre volume fraction, i.e. a lot of free space between the tows. The effective permeability of the domain will be dominated by the free space permeability, which is several orders of magnitude higher than the tow permeability, and thus variations of the tow paths will be less important. Furthermore, the cases with tow interference are filtered out in the study here and hence this limits the modelled variability even further.

Also, experimental measurements are based on several layers of fabric and nesting will affect the variability of permeability as reported by Hoes et al. (2004). The results from the last chapter on the non-nested and nested plain weave models showed that nesting has a significant effect on the predicted permeability. The fabric models used in the present study have only one layer.

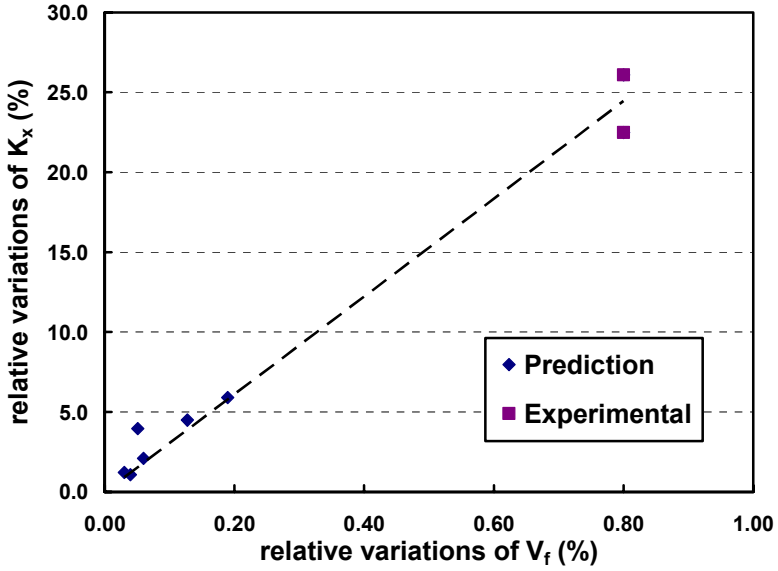

Figure 6.17 – Relative variations of K_x as a function of relative variations of V_f, showing the predicted values for NCF model (a_0 = 2.6mm, R_p = 0.8mm and R_q = 0.25mm) and the measured values from Endruweit et al. (2005) for a non-crimp glass fibre fabric (FGE 106 HD). The model and the fabric have a similar geometric characteristic in the ratio R_p/distance between tows, 0.39 for FGE 106 and 0.44 for the NCF model. However, a large gap remains between the predicted and measured values. The predicted values are based on single layer models with idealised geometries and low V_f, while the measurements are based on several layers of fabric and a higher V_f than the models.

There are also various ways to model variability in the textile models. In this study, the tows are assumed to move randomly at the crossover points according to a Normal distribution, which does not necessarily happen in real life. Non-crimp fabrics have stitches running through them, which would influence the tow alignment. Furthermore, the fibre tows, being long and tortuous, would be less likely to be randomly displaced at each crossover.

Overall, this chapter has highlighted some critical issues to consider when transferring predicted permeability values between meso and macroscopic analyses. In generating local permeability data for a macroscopic analysis using mesoscopic fabric models, it is necessary to relate the element size to the domain size of the fabric model.

Further work that can be done is to model multiple layers in the fabric models, which is expected to have two concurrent effects on variability. On one hand, with an increasing number of fabric layers, the local inhomogeneities in individual layers will be increasingly averaged over the thickness, thus reducing the global permeability variations. On the other hand, the frequency of misalignment of the layers and the magnitude of the effect of nesting in woven fabrics increases with increasing number of layers. These are expected to cause higher variations in the global permeability. Also, different ways of generating variability in the textile models can be studied. The movement of adjacent tow crossovers can be generated so that they are dependent on one another rather than being totally random.

6.4 CONCLUSION

Textile permeability in general shows a high variation. Consequently, researchers have attempted to both measure and model such variability in order to better predict the filling times and flow pattern of LCM processes. This chapter has described a method to model textile variability at the mesoscopic scale based on using a generalised textile modeller. Inhomogeneities were introduced into the textile structure by randomly moving the tow paths at the crossovers according to a given Normal distribution. The effects of various factors on the evaluated permeability distributions were explored.

Two non-crimp fabric (NCF) models with different spacing between the tows (a_0 = 2.6mm and 3.6mm) were analysed for three relative degrees of tow position variation, where the applied standard deviations of nodal displacement applied were 14.83%, 29.65% and 59.30% with respect to the spacing between the tows. 100 randomised cases were simulated for each combination and the permeability data were evaluated statistically. Permeability data were also generated for NCF models (a_0 = 2.6mm) with an increasing number of independently varying tows. Finally, the variations of permeability for a plain weave fabric were compared to a NCF model with a similar cell fibre volume fraction.

As expected, the predicted permeability variations increased with increasing tow position variations and also with increasing a_0. Interestingly, with an increasing domain size and the proportionate increase in number of independently varying tows, the permeability variation decreased while the data tended towards a Normal distribution. This was because the local inhomogeneities tend to cancel one another as the domain size increases, thus creating a much more homogeneous domain for flow.

The architecture of the fabric is also important in that it imposes a limit to the degree of variations of the tow paths. At the highest degree of applied tow movement variation, the NCF cases achieved a much reduced level of variability due to being constrained by the available space between the tows. Consequently, the variation of permeability is limited. From the comparison between two types of fabric, the plain

weave was seen to restrict the movement of the tows more than the NCF. This has two effects: the permeability variation is lower for the plain weave and the permeability distribution correlates better with a Normal distribution.

Comparing between the predicted relative variations of permeability and published measured values, the predicted permeability variations are much smaller than for the measured data. However, it is interesting to note that a linear relationship can be deduced for the relative variations of permeability as a function of the relative variations of fibre volume fraction, which links the predicted and measured values. It should also be noted that a large gap remains between these predicted and measured values. This is attributed to the facts that the fabric models have idealised tow shapes, low fibre volume fraction, and are single layered models, all of which contribute to the low permeability variations seen in the models.

This work has highlighted issues that need to be considered when utilising predicted mesoscopic permeability values in macroscopic analyses. The domain size of the mesoscopic scale model has to be related to the element size of the macroscopic analyses. Future models need to consider multiple layers, which are expected to generate two conflicting effects on permeability variations.

7 DISCUSSION AND CONCLUSIONS

7.1 INTRODUCTION

When the MultiComp project was first proposed, there was a lack of an advanced integrated simulation tool which is capable of describing three-dimensional, multi-layer textile composites. The tools for the analyses of fabric forming and subsequent flow in liquid moulding processes were simple and immature, with the latter suitable to describe flow in thin structures only. Another noted deficiency was that the simulations provided a single answer to any given problem. Industrial experience has shown that during mould filling, due to the nature of statistical variation in the material properties, the filling patterns and arising cycle times are rarely the same between a given set of identical mouldings.

The project addressed the issues of textile formability and permeability from a fundamental viewpoint of using the textile architecture as a basis. Novel modelling techniques developed to predict the process characteristics for textile preforms were implemented within an integrated modelling framework encompassing forming, compaction and impregnation. Stochastic analysis methods were also developed which allowed the effect of material variability to be accounted for in process simulation.

This thesis described the progress made in predicting the permeability of textile reinforcements. The findings and achievements of the work are discussed in this final chapter, from which recommendations for further work are made based on perceived limitations in the proposed techniques. Significant conclusions arising from this work are summarised at the end.

7.2 GENERAL DISCUSSION

The main focus of this work was the development of two novel, simple techniques to discretise the complicated flow structure in a textile model. The first method, Stream Surface, reduces the 3D flow problem into a series of interconnected 2D planes representing the flow in the free channels and porous tows. The second method, Grid Average, discretises the flow problem using a regular square grid and calculates an effective permeability value for each grid element. Both methods were based on the assumption that an effective permeability value can be assigned to the free channels in a textile model. Darcy's law is then solved for flow and the effective cell permeability calculated from the resultant fluid pressure field.

Rigorous validation studies were performed for both the methods using test cases with an increasing degree of complexity, beginning with 2D microscopic analysis of a regular array of fibres, proceeding to 2D cross sections of single and multiple porous tows and finally, 3D models of 2:2 twill weave fabric. The predicted permeability values from the two simplified methods and the more rigorous CFD calculation were within 17% (for 2D models) and 30% (for 3D models) of each other. Comparison was also made between the Grid Average results and experimental measurements. The predicted permeabilities of a plain weave model constructed using experimental data, were of the same order of magnitude. The method was also demonstrated to accurately predict the trend induced by in-plane shear on permeability of the twill weave model.

First and foremost, these studies demonstrated that the simplified methods can predict the permeability of textile models to a certain degree of accuracy (within 17%-30% when compared to CFD). In order to be more accurate, issues such as the effect of permeable boundaries on flow behaviour can be accounted for, as shown for the single porous tow analyses in Chapter 4. However, it was also shown from the same study that the effect of permeable boundaries on the effective cell permeability may not be that important. Moreover, the analyses of the cross sections of a 3D textile incorporating multiple tows in Chapter 4 showed that the permeability trends can still be predicted accurately using the simplified methods without accounting for

permeable boundaries. This observation was reinforced by the subsequent successful analyses involving 3D fabric models in Chapter 5.

The attraction of using the simplified methods to predict permeability lies in their speed. While CFD calculations in theory are the most accurate, the computational times are very long. On average, for the 3D twill weave analysis, the CFD simulation took 3 hours to complete on a standard PC (1.7GHz) compared to 2 minutes using the Grid Average method. There is also the inherent difficulty of generating reasonably accurate meshes for the CFD solutions, particularly for the narrow and tortuous regions between the tows. A large number of simulations are needed in order to generate permeability data which accounts for factors such as local shear, local compaction, multi-layer nesting and also the statistical nature of the fabric. In this respect, the use of simple and quick methods is justified. Such an application was demonstrated in Chapter 6 where hundreds of simulations were performed using the Grid Average method to characterise the effect of fabric variability on permeability.

There is an inherent limitation associated with numerical permeability models: the calculations can only be as accurate as the description of the textile structure. In other words, how accurately can textile models represent real textiles? As was shown in Chapter 5, the reinforcements in real composite parts exhibit high levels of compaction and nesting. Most of the time, there are no distinct boundaries between adjacent tows and the tow shapes vary along the length and between tows. On the other hand, textile models have idealised geometries; the tows are assumed to have a definite volume and boundary and to follow an ideal tow path. As such, there is a lot of free space between the tows. It is thus difficult to get an exact representation of the real textile, as evident from Chapter 5.

Nevertheless, this work has highlighted the importance of evaluating flow and subsequently permeability at the mesoscopic level. Essentially, a fabric is defined by its structure and its permeability is a strong function of the textile architecture. Only by evaluating flow at the mesoscopic level, can one analyse issues such as local tow variability and void formation. This is a key area for future study.

To summarise, the motivation behind the work in this thesis can be best described by a hypothetical scenario. Take a designer who wants to have a full description of the permeability of a particular fabric. In order to account for the effect of shear on permeability, one would measure the permeability at five shear angles. On top of that, one would also ideally conduct 20 measurements per shear angle in order to account for the variability of the permeability. If each permeability measurement experiment takes an optimistic 2 hours, the total time required to fully characterise one fabric is 200 hours (minimum), summarised as below:

	5 shear angles	×	20 measurements per angle	×	2 hours per measurement
=	200 man hours per fabric (minimum)				

However, by using the simple methods such as Stream Surface and Grid Average, one can reduce the time required to generate the permeability data. If one calculates the permeability at ten shear angles, with 100 calculations per angle and each calculation taking only 5 minutes (as shown in Chapter 6), it will only take about 60 computational hours to generate 1000 calculations as opposed to 200 man hours to generate 100 measurements. The computation required here can also be automated and is limited only by the speed of the computer.

	10 shear angles	×	100 calculations per angle	×	5 minutes per calculation
=	1000 computational minutes per fabric		or		60 computational hours per fabric

Whilst the predictive model will not replace the measurement experiments outright, the models can be used to generate additional data to complement the experimental data.

7.3 RECOMMENDATIONS FOR FURTHER WORK

From the discussions of the work done, certain areas have been identified in which further research may be constructive.

- One of the weaker aspects of this work is the lack of comparison to experimentally measured permeability values. Only one comparison was shown in Chapter 5, whereby a fabric model had been generated based on accurate geometrical parameters collected from the analysis of a plain weave laminate. However, it proved to be difficult to match the compaction of the tows as seen in the real laminate, hence the calculated permeability of the model was about 5 times the measured value, as shown in Table 5.5.

  Whilst it is possible to use imaging techniques to create models which are dimensionally similar to real fabrics, this would not utilise the modelling capability of TexGen. One of the aims of this thesis is to explore the use of a generic textile modeller such as TexGen to create fabric models that will replicate the flow behaviour of real textiles.

  As such, any improvements for the prediction of the permeability values will have to stem from improvements to the geometric modeller, TexGen, itself, which in turn will be capable of generating a more accurate fabric model. Such improvements to TexGen would require further extensive experimental characterisation which is beyond the scope of this work.

  Currently, enhancements to the geometric modeller, TexGen, are being implemented by Sherburn et al. (2006). These include improvement to the specification of the tow shapes and orientations as well as the addition of the capability for tow twisting. Following validation of these features using microtomography (Micro-CT) analyses of the textile structures, it will be interesting to see the accuracy of the Stream Surface and Grid Average methods when used to predict the permeability of these dimensionally accurate models generated from the improved TexGen.

- Localised variations of the fabric structure will give rise to inhomogeneities in the flow of resin, which in turn can result in void entrapments. The Grid Average and Stream Surface methods are not only useful for modelling permeability, but can be used to simulate resin flow through the textile model. Void entrapment may be particularly important in 3-dimensional reinforcements whereby it is very hard to visualise the flow behaviour inside the structure. The simplified methods could be utilised to detect instances of void formation during filling simulation of the fabric models.

- The variability study performed in Chapter 6 only accounted for single layer textile models. Multi-layer structures should be modelled and stochastic variations applied to the tows to examine the subsequent effect on permeability variations. The presence of several layers is expected to have two conflicting effects on permeability variation. Local inhomogeneities will be increasingly averaged over the thickness, thus reducing permeability variations. On the other hand, the frequency of misalignment between layers and the magnitude of the effect of nesting increases with the number of layers, thus causing a higher variation in global permeability.

- A different variability model can be studied. The model in Chapter 6 assumes that variability is generated by the random movement of the tows at the crossover points in the fabric. Again, using optical imaging methods, the dimensional data of the fabric structure can be collected. Using the measured mean and the standard deviation of each variable (i.e. tow width, tow height, etc.), models which incorporates variability can then be studied.

Several more technical issues regarding the models themselves which can be taken further are also identified below.

- The Grid Average and Stream Surface methods were created to be flexible in their application. As such, the methods can be modified to account for more complicated flow behaviour, specifically the effect of permeable tow boundaries on the pressure distribution. This issue was tackled briefly in

Chapter 4 and the theory of permeable boundaries can be taken further to enhance the accuracy of the permeability models.

- Further application of the Stream Surface approach in 3-dimensional space was impeded by the lack of a suitable solver for the pressure distribution in the flow. It will be interesting if a solver tailored to Stream Surface specifically is programmed, as it will provide another method to visualise the flow behaviour in textile structures.

- The solution of the Grid Average method can be improved by using grid optimisation. By increasing the mesh density around critical flow areas using intelligent grid optimisation methods one could increase the accuracy of the calculation while maintaining unrestrictive computational times.

- Numerical permeability models are only as accurate as the fabric models. Current textile models can be improved in order to better mimic real textiles, for example by using contacting tows and using variable cross sections along the tows.

7.4 CONCLUSIONS

The conclusions gained from this thesis are summarised below.

- The study of permeability using the mesoscopic structure of textiles is as important as the macroscopic evaluation of permeability. Macroscopic analyses tend to define textile reinforcements as homogenous materials, where the intricate interaction between the fluid and the textile structure is ignored. However, textiles exhibit heterogeneous behaviour in that the fibrous tows are porous entities surrounded by open spaces, and this changes the dynamics of fluid flow through them.

- Flow analyses at the mesoscopic level are important to understand the fundamentals of the flow behaviour and to address issues such as local inhomogeneities and void formation.

- Mesoscopic numerical permeability models are only as accurate as the textile geometric models on which they are based.

- Simple and fast permeability models are crucial for permeability characterisation, if effects such as deformation and statistical variations are to be considered.

- Permeability models based on simplified flow theories can be used to generate a large amount of permeability data in order to complement the experimental data.

  Based on the three points above, one can argue that a very rigorous simulation of the flow behaviour (eg. CFD) is not necessary because it is still limited by the accuracy of the geometric model. Current textile models use idealised geometries to build the tows and cannot entirely mimic the architecture of real laminates. As such, simplified models which can predict accurate permeability trends and also the permeability values up to an acceptable degree of accuracy are more valuable. Hundreds of calculations can be generated quickly using these models, from which the data will complement existing experimental data.

- Since permeability is a strong function of the fabric architecture, the variability of permeability is also strongly dependent on the structure of the fabric. As seen in Chapter 6, the fabric structure will self-impose a limit to the degree of geometric variability, which subsequently restricts the variability in fabric permeability.

- In order to better capture the effect of textile structure variability on permeability, the computational cell used to predict permeability needs to be larger than one unit cell of the fabric. This is due to the effect of inhomogeneity being magnified when only the unit cell is used to predict permeability.

REFERENCES

Airbus Unveil the A380 to the World [online] netcomposites - news article (published: 21/01/2005). Available at: http://www.netcomposites.com/news.asp?2704 (last accessed: 17/01/2006).

ESI Group - Overview [online]. ESI Group. Available at: http://www.esi-group.com/SimulationSoftware/Resin_transfer_molding/ (last accessed: 7/11/2005).

GIMP - The GNU Image Manipulation Program [online]. The GIMP team. Available at: http://www.gimp.org/ (last accessed: 19/01/2006).

LM Glasfiber - In English [online]. LM Glasfiber. Available at: http://www.lmglasfiber.com/ (last accessed: 22/11/2005).

Polymer Composites - MultiComp Project [online]. University of Nottingham. Available at: http://www.nottingham.ac.uk/~eaxccw/ (last accessed: 22/11/2005).

Polymer Composites - Textile Composites Software [online]. University of Nottingham. Available at: http://www.nottingham.ac.uk/~emxmns/texgen.htm (last accessed: 22/11/2005).

Spatial Corporation: 3D software components and services - ACIS Modeller, Interoperability (InterOp) translators [online]. Spatial Corporation. Available at: http://www.spatial.com/ (last accessed: 13/03/2006).

ADAMS, K. L., MILLER, B. and REBENFELD, L. (1986). *Forced in-plane flow of an epoxy resin in fibrous networks*. Polymer Engineering and Science 26(20): 1434-1441.

ADAMS, K. L. and REBENFELD, L. (1987). *In-plane flow of fluids in fabrics: structure/flow characterisation*. Textile Research Journal 57(11): 647.

ADAMS, K. L., RUSSEL, W. B. and REBENFELD, L. (1988). *Radial penetration of a viscous liquid into a planar anisotropic porous medium*. International Journal of Multiphase Flow 14(2): 203.

ADVANI, S. G., BRUSCHKE, M. V. and PARNAS, R. S. (1994). *Resin transfer molding flow phenomena in polymeric composites*, in *Flow and Rheology in Polymer Composites Manufacturing*. Advani, S. G., Ed. Amsterdam, The Netherlands, Elsevier Science B. V. Composite Materials Series, 10: 465-516.

AMICO, S. and LEKAKOU, C. (2001). *An experimental study of the permeability and capillary pressure in resin-transfer moulding*. Composites Science and Technology 61: 1945-1959.

AMICO, S. and LEKAKOU, C. (2004). *Flow through a two-scale porosity, oriented fibre porous medium*. Transport in Porous Media 54: 35-53.

ANDERSON (JR.), J. D. (1995). *Computational Fluid Dynamics: The basics with applications*. Singapore, McGraw Hill, Inc: 547 pages.

ASTROM, B. T., PIPES, R. B. and ADVANI, S. G. (1992). *On flow through aligned fiber beds and its application to composites processing*. Journal of Composite Materials 26(9): 1351-1373.

BEAVERS, G. S. and JOSEPH, D. D. (1967). *Boundary conditions at a naturally permeable wall*. Journal of Fluid Mechanics 30(1): 197-207.

BELOV, E. B., LOMOV, S. V., VERPOEST, I., PETERS, T., ROOSE, D., PARNAS, R. S., HOES, K. and SOL, H. (2004). *Modelling of permeability of textile reinforcements: lattice Boltzmann method*. Composites Science and Technology 64(7-8): 1069-1080.

BICKERTON, S. and ADVANI, S. G. (1999). *Characterization and modeling of racetracking in liquid composite modling processes*. Composites Science and Technology 59(15): 2215-2229.

BRUSCHKE, M. V. and ADVANI, S. G. (1990). *A finite element/control volume approach to mold filling in anisotropic porous media*. Polymer Composites 11(6): 398-405.

BRUSCHKE, M. V. and ADVANI, S. G. (1993). *Flow of generalized Newtonian fluids across a periodic array of cylinders*. Journal of Rheology 37(3): 479-498.

BRUSCHKE, M. V. and ADVANI, S. G. (1994). *A numerical approach to model non-isothermal viscous flow through fibrous media with free surfaces*. International Journal for Numerical Methods in Fluids 19(7): 575-603.

CHAN, A. W. and HWANG, S. T. (1992). *Modeling nonisothermal impregnation of fibrous media with reactive polymer resin*. Polymer Engineering and Science 32(5): 310-318.

CHAN, A. W., LARIVE, D. E. and MORGAN, R. J. (1993). *Anisotropic permeability of fibre preforms: constant flow rate measurement*. Journal of Composite Materials 27(10): 996.

COULTER, J. P. and GUCERI, S. I. (1989). *Resin impregnation during composites manufacturing: theory and experimentation*. Composites Science and Technology 35(4): 317-330.

CROOKSTON, J. J. (2004). *Prediction of elastic behaviour and initial failure of textile composites*. PhD thesis, School of Mechanical, Materials and Manufacturing Engineering, University of Nottingham: 217 pages.

DAVE, R., KARDOS, J. L. and DUDUKOVIC, M. P. (1987). *A model for resin flow during composite processing. part 2: numerical analysis for unidirectional graphite/epoxy laminates*. Polymer Composites 8(2): 123-132.

DELERUE, J.-F., LOMOV, S. V., PARNAS, R. S., VERPOEST, I. and WEVERS, M. (2003). *Pore network modeling of permeability for textile reinforcements*. Polymer Composites 24(3): 344-357.

DESPLENTERE, F., LOMOV, S. V., WOERDEMAN, D. L., VERPOEST, I., WEVERS, M. and BOGDANOVICH, A. (2005). *Micro-CT characterization of variability in 3D textile architecture*. Composites Science and Technology 65(13): 1920-1930.

DEVILLARD, M., GOKCE, A., HSIAO, K.-T. and ADVANI, S. G. (2002). *Addressing flow variations due to imperfect fit between preform edges and the mold walls in resin transfer molding process*. Proceedings of 6th International Conference on Textile Composites (TexComp 6), Sept 11-13 2002, Philadelphia, USA.

DIALLO, M. L., GAUVIN, R. and TROCHU, F. (1998). *Experimental analysis and simulation of flow through multi-layer fiber reinforcements in Liquid Composite Molding*. Polymer Composites 19(3): 246-256.

DING, L., SHIH, C., LIANG, Z., ZHANG, C. and WANG, B. (2003). *In situ measurement and monitoring of whole-field permeability profile of fiber preform for liquid composite molding processes*. Composites: Part A 34(8): 779-789.

DUNKERS, J. P., PHELAN, F. R., ZIMBA, C. G., FLYNN, K. M., SANDERS, D. P., PETERSON, R. C., PARNAS, R. S., LI, X. and FUJIMOTO, J. G. (2001). *The prediction of permeability for an epoxy/E-glass composite using Optical Coherence Tomographic images*. Polymer Composites 22(6): 803-814.

ENDRUWEIT, A. and LONG, A. C. (2005). *Influence of stochastic variations in the fibre spacing on the permeability of bi-directional textile fabrics*. Composites Part A 37(5): 679-694.

ENDRUWEIT, A., MCGREGOR, P., LONG, A. C. and JOHNSON, M. S. (2005). *Influence of the fabric architecture on the variations in experimentally determined in-plane permeability values*. Composites Science and Technology, in press (Available online 13 December 2005).

FERZIGER, J. H. and PERIC, M. (1999). Computational *Methods for Fluid Dynamics*. Springer: 389 pages.

GAUVIN, R. and TROCHU, F. (1993). *Comparison between numerical and experimental results for mold filling in resin transfer molding*. Plastics, Rubber and Composites Processing and Applications 19(3): 151-157.

GAUVIN, R. and TROCHU, F. (1998). *Key issues in numerical simulation for liquid composite molding processes*. Polymer Composites 19(3): 233-240.

GEBART, B. R. (1992). *Permeability of unidirectional reinforcements for RTM*. Journal of Composite Materials 26(8): 1100-1133.

GEBART, B. R. and LIDSTROM, P. (1996). *Measurement of in-plane permeability of anisotropic fiber reinforcements*. Polymer Composites 17(1): 43-51.

GHADDAR, C. K. (1995). *On the permeability of unidirectional fibrous media: A parallel computational approach*. Physics of Fluids 7(11): 2563-2586.

GOKCE, A. and ADVANI, S. G. (2005). *Modeling, optimization and control of resin flow during manufacturing of textile composites with liquid molding*, in *Design and manufacture of textile composites*. Long, A. C., Ed. Cambridge, England, Woodhead Publishing Limited: 242-291.

GUTOWSKI, T. G., CAI, Z., BAUER, S., BOUCHER, D., KINGERY, J. and WINEMAN, S. (1987). *Consolidation experiments for laminate composites*. Journal of Composite Materials 21: 650-669.

HAPPEL, J. (1959). *Viscous flow relative to arrays of cylinders*. American Institute of Chemical Engineers Journal 5(2): 174-177.

HEARDMAN, E., LEKAKOU, C. and BADER, M. G. (2001). *In-plane permeability of sheared fabrics*. Composites Part A 32: 933-940.

HEARDMAN, E., LEKAKOU, C. and BADER, M. G. (2004). *Flow monitoring and permeability measurement under constant and transient flow conditions*. Composites Science and Technology 64: 1239-1249.

HIRT, D. E., ADAMS, K. L., PRUD'HOMME, R. K. and REBENFELD, L. (1987). *In-plane radial fluid flow characterisation of fibrous materials*. Journal of Thermal Insulation 10: 153.

HOES, K., DINESCU, D., SOL, H., PARNAS, R. S. and LOMOV, S. (2004). *Study of nesting induced scatter of permeability values in layered reinforcement fabrics*. Composites Part A 35: 1407-1418.

HOES, K., DINESCU, D., VANHEULE, M., SOL, H., PARNAS, R. S., BELOV, E. and LOMOV, S. (2002). *Statistical distribution of permeability values of different porous materials*. Tenth European Conference on Composite Materials (ECCM-10), Brugge, Belgium.

KUWABARA, S. (1959). *The forces experienced by randomly distributed parallel circular cylinders or spheres in a viscous flow at small Reynolds numbers*. Journal of Physics Society of Japan 14(4): 527-532.

LAINE, B., HIVET, G., BOISSE, P., BOUST, F. and LOMOV, S. V. (2005). *Permeability of the woven fabrics: a parametric study*. Proceedings of 8th ESAFORM Conference, 27-29 April 2005, Cluj-Napoca, Romania, pp. 995-998.

LAM, R. C. and KARDOS, J. L. (1989). *The permeability and compressibility of aligned and cross-plied carbon fiber beds during processing of composites*. Society of Plastics Engineers 47th Annual Technical Conference (SPE-ANTEC '89), May 1-4 1989, New York, USA.

LEKAKOU, C. and BADER, M. G. (1998). *Mathematical modelling of macro- and micro-infiltration in resin transfer moulding (RTM)*. Composites: Part A 29: 29-37.

LEKAKOU, C., EDWARDS, S., BELL, G. and AMICO, S. C. (2004). *Computer modelling for the prediction of the in-plane permeability of non-crimp stitch bonded fabrics*. 7th International Conference on Flow Processes in Composite Materials (FPCM-7), 7-9 Feb 2004, Newark, Delaware, USA: 361-365

LEKAKOU, C., EDWARDS, S., BELL, G. and AMICO, S. C. (2006). *Computer modelling for the prediction of the in-plane permeability of non-crimp stitch bonded fabrics*. Composites Part A 37(6): 820-825.

LEKAKOU, C., JOHARI, M. A. K., NORMAN, D. and BADER, M. G. (1996). *Measurement techniques and effects on in-plane permeability of woven cloths in resin transfer molding*. Composites: Part A 27(5): 401-408.

LIM, S. T. and LEE, W. I. (2000). *An analysis of the three-dimensional resin-transfer mold filling process*. Composites Science and Technology 60(7): 961-975.

LIN, M., HAHN, H. T. and HUH, H. (1998). *A finite element simulation of resin transfer molding based on partial nodal saturation and implicit time integration*. Composites Part A 29(5-6): 541-550.

LIN, R. J., LEE, L. J. and LIOU, M. J. (1993). *Mold filling and curing analysis liquid composite molding*. Polymer Composites 14(1): 71-81.

LIU, B., BICKERTON, S. and ADVANI, S. G. (1996). *Modelling and simulation of resin transfer moulding (RTM) - gate control, venting and dry spot prediction*. Composites Part A 27(2): 135-141.

LOMOV, S. V., HUYSMANS, G., LUO, Y., PARNAS, R. S., PRODROMOU, A., VERPOEST, I. and PHELAN, F. R. (2001). *Textile composites: modelling strategies*. Composites Part A 32(10): 1379-1394.

LOMOV, S.V., PEETERS, T., ROOSE, D. and VERPOEST, I. (2004). *Modelling of permeability of textile reinforcements: lattice Boltzmann method*. Proceedings of 25th SAMPE Europe International Conference, March/April 2004, Paris, France, pp. 387-392.

LONG, A. C. (1994). *Preform design for liquid moulding processes*. PhD thesis, Department of Mechanical Engineering, University of Nottingham: 212 pages.

LONG, A. C., BLANCHARD, P. J., RUDD, C. D. and SMITH, P. (1998). *The development of an integrated process model for liquid composite moulding*. Composites Part A 29A: 847-854.

LUNDSTROM, T. S., FRISHFELDS, V. and JAKOVICS, A. (2004). *A statistical approach to permeability of clustered fibre reinforcements*. Journal of Composite Materials 38(13): 1137-1149.

LUNDSTROM, T. S., STENBERG, R., BERGSTROM, R., PARTANEN, H. and BIRKELAND, P. A. (2000). *In-plane permeability measurements: a nordic round-robin study*. Composites Part A 31(1): 29-43.

LUO, Y., VERPOEST, I., HOES, K., VANHEULE, M., SOL, H. and CARDON, A. (2001). *Permeability measurement of textile reinforcements with several test fluids*. Composites Part A 32(11): 1497-1504.

MARTIN, G. Q. and SON, J. S. (1986). *Fluid Mechanics of Mold Filling For Fiber Reinforced Plastics*. ASM/ESD 2nd Conference on Advanced Composites, Dearborn, Michigan, ASM International.

NEALE, G. and MASLIYAH, J. H. (1975). *Flow perpendicular to mats of randomly arranged cylindrical fibers (Importance of cell models)*. American Institute of Chemical Engineers Journal 21(4): 805-807.

NEDANOV, P. B. and ADVANI, S. G. (2002). *Numerical computation of the fiber preform permeability tensor by the homogenization method*. Polymer Composites 23(5): 758-770.

NGO, N. D. and TAMMA, K. K. (2001). *Microscale permeability predictions of porous fibrous media*. International Journal of Heat and Mass Transfer 44(16): 3135-3145.

NORDLUND, M. and LUNDSTROM, T. S. (2005). *Numerical Study of the Local Permeability of Noncrimp Fabrics*. Journal of Composite Materials 39(10): 929-947.

PAN, R., LIANG, Z., ZHANG, C. and WANG, B. (2000). *Statistical characterizaton of fiber permeability for composite manufacturing*. Polymer Composites 21(6): 996-1006.

PAPATHANASIOU, T. D. (1997). *On the effective permeability of square arrays of permeable fiber tows*. International Journal of Multiphase Flow 23(1): 81-92.

PARNAS, R. S. (1998). *Preform permeability*, in *Resin Transfer Moulding for Aerospace Structures*. Kruckenberg, T. and Paton, R., Eds. Dordecht, The Netherlands, Kluwer Academic Publishings: 177-224.

PARNAS, R. S., FLYNN, K. M. and DAL-FAVERO, M. E. (1997). *A permeability database for composites manufacturing*. Polymer Composites 18(5): 623-633.

PARNAS, R. S., HOWARD, J. G., LUCE, T. L. and ADVANI, S. G. (1995). *Permeability characterization, part 1: a proposed standard reference fabric for permeability*. Polymer Composites 16(6): 429-445.

PARNAS, R. S. and SALEM, A. J. (1993). *A comparison of the unidirectional and radial in-plane flow of fluids through woven composite reinforcements*. Polymer Composites 14(5): 383-394.

PHELAN, F. R. and WISE, G. (1996). *Analysis of transverse flow in aligned fibrous porous media*. Composites Part A 27(1): 25-34.

PRESS, W. H., TEUKOLSKY, S. A., VETTERLING, W. T. and FLANNERY, B. P. (1994). *Numerical Recipes in C, Second Edition*. Cambridge University Press.

ROBITAILLE, F., CLAYTON, B. R., LONG, A. C., SOUTER, B. J. and RUDD, C. D. (1999). *Geometric modelling of industrial preforms: woven and braided textiles*. Proceedings of the Institute of Mechanical Engineers 213(L): 69-83.

ROBITAILLE, F., LONG, A. C., JONES, I. A. and RUDD, C. D. (2003). *Automatically generated geometric descriptions of textile and composite unit cells*. Composites Part A 34(4): 303-312.

ROBITAILLE, F., LONG, A. C., RUDD, C. D. and SOUTER, B. J. (1998). *The measurement of in-plane permeability for sheared preforms*. 6th International Conference on Computer Methods in Composite Materials, CADCOMP 98, Montreal, Canada, Computational Mechanics Publications.

RUDD, C. D., LONG, A. C., KENDALL, K. N. and MANGIN, C. G. E. (1997). *Liquid Moulding Technologies*. Woodhead Publishing Ltd.

RUDD, C. D., LONG, A. C., MCGEEHIN, P. and SMITH, P. (1996). *In-plane permeability determination for simulation of liquid composite molding of complex shapes*. Polymer Composites 17(1): 52-59.

SANGANI, A. S. and YAO, C. (1988). *Transport processes in random arrays of cylinders. II. Viscous flow*. Physics of Fluids 31(9): 2435-2444.

SCHEIDEGGER, A. E. (1974). *The Physics of Flow through Porous Media*. Toronto, Canada, University of Toronto Press.

SHERBURN, M., LONG, A. C., JONES, I. A. and RUDD, C. (2006). *TexGen: Geometric modelling schema for textile composites*. Proceedings of 8th International Conference on Textile Composites, October 2006, Nottingham, U.K.

SHERBURN, M., ROBITAILLE, F., LONG, A. C. and RUDD, C. D. (2004). *Geometric pre-processor for the calculation of physical properties of textiles*. Industrial Simulation Conference, 7-9 June 2004, University of Malaga, Spain, EUROSIS-ETI.

SHOJAEI, A., GHAFFARIAN, S. R. and KARIMIAN, S. M. H. (2003a). *Modeling and simulation approaches in the resin transfer molding process: a review*. Polymer Composites 24(4): 525-544.

SHOJAEI, A., GHAFFARIAN, S. R. and KARIMIAN, S. M. H. (2003b). *Simulation of the three-dimensional non-isothermal mold filling process in resin transfer molding*. Composites Science and Technology 63(7): 1931-1948.

SIMACEK, P. and ADVANI, S. G. (1996). *Permeability model for a woven fabric*. Polymer Composites 17(6): 887-899.

SMITH, P., RUDD, C. D. and LONG, A. C. (1997). *The effect of shear deformation on the processing and mechanical properties of aligned reinforcements*. Composites Science and Technology 57(3): 327-344.

SPAID, M. A. A. and PHELAN, F. R. (1997). *Lattice Boltzmann methods for modeling microscale flow in fibrous porous media*. Physics of Fluids 9(9): 2468-2474.

TREVINO, L., RUPEL, K., YOUNG, W. B., LIOU, M. J. and LEE, L. J. (1991). *Analysis of Resin Injection Molding in Molds with Preplaced Fiber Mats. I: Permeability and Compressibility Measurements*. Polymer Composites 12(1): 20-29.

TUCKER, C. L. and DESSENBERGER, R. B. (1994). *Governing equations for flow and heat transfer in stationary fiber beds*, in *Flow and Rheology in Polymer Composites Manufacturing*. Advani, S. G., Ed. Amsterdam, The Netherlands, Elsevier Science B. V. Composite Materials Series, 10: 257-323.

UM, M. K. and LEE, W. I. (1991). *A study on the mold filling process in resin transfer molding*. Polymer Engineering and Science 31(11): 765-771.

VIROS, D. C., ARCE, D. A. C. and BENAVIDES, F. E. (2005). *The Airbus A380 HTP: the world's largest airborne composite tanker*. JEC Composites: 37-39.

WONG, C. C., LONG, A. C., SHERBURN, M., ROBITAILLE, F., HARRISON, P. and RUDD, C. D. (2006). *Comparisons of novel and efficient approaches for permeability prediction based on the fabric architecture*. Composites Part A 37(6): 847-857.

YOO, Y.-E. and LEE, W. I. (1996). *Numerical simulation of the resin transfer mold filling process using the boundary element method*. Polymer Composites 17(3): 368-374.

YOUNG, W. B. (1994). *Three-dimensional nonisothermal mold filling simulation in resin transfer molding*. Polymer Composites 15(2): 118-127.

YOUNG, W. B., HAN, K., FONG, L. H., LEE, L. J. and LIOU, M. J. (1991). *Flow simulations in moulds with preplaced fibre mats*. Polymer Composites 12(6): 391-403.

YU, B., LEE, L. J. and CAO, H. (2002). *A fractal in-plane permeability model for fabrics*. Polymer Composites 23(2): 201-221.

YU, C. P. and SOONG, T. T. (1975). *A random cell model for pressure drop predictions in fibrous filters*. Journal of Applied Mechanics 22: 301-304.

APPENDIX A PUBLICATIONS

Publications in journals

WONG, C. C., LONG, A. C., SHERBURN, M., ROBITAILLE, F., HARRISON, P. and RUDD, C. D. (2006). *Comparisons of novel and efficient approaches for permeability prediction based on the fabric architecture*. Composites Part A 37(6): 847-857.

WONG, C. C. and LONG, A. C. (2006). *Modelling variations of textile fabric permeability at the meso-scopic scale*. Accepted for publication in Plastics, Rubber and Composites: Macromolecular Engineering. (Accepted on 20 March 2006).

Publications in conference proceedings

ROBITAILLE, F., WONG, C. C., LONG, A. C. and RUDD, C. D. (2003). *Systematic predictive permeability modelling using commercial CFD and dedicated calculation method*. 14th International Conference on Composite Materials (ICCM-14), 14-18 July 2003, July 14-18 2003, San Diego, California, USA.

WONG, C. C., ROBITAILLE, F., LONG, A. C. and RUDD, C. D. (2004). *Prediction of the effects of fibre architecture on permeability using the stream-surface method*. 7th International Conference on Flow Processes in Composite Materials (FPCM-7), 7-9 Feb 2004, Newark, Delaware, USA.

LONG, A. C., WONG, C. C., SHERBURN, M. and ROBITAILLE, F. (2004a). *Modelling the effect of fibre architecture on permeability for multi-layer preforms*. Proceedings of 25th SAMPE Europe International Conference, March/April 2004, Paris, France, pp. 325-330.

LONG, A. C., WONG, C. C., SHERBURN, M. and ROBITAILLE, F. (2004b). *Prediction of permeability distribution for textile reinforcements*. Proceedings of 7th International Conference on Textile Composites (TexComp 7), Sept 2004, Yamagata, Japan, 4 pp.

ENDRUWEIT, A., WONG, C. C., HARRISON, P. and LONG, A. C. (2005). *Dual-scale modelling of flow through non-uniform bi-directional fabrics*. 15th International Conference on Composite Materials (ICCM-15), 27 June - 1 July 2005, Durban, South Africa.

APPENDIX B CHARACTERISATION OF TOW SHAPE AND THE GENERALISED ELLIPSE EQUATION

In order to construct geometric models of textiles, knowledge of the cross-sectional shape of the reinforcement tows is required. A study has been undertaken by Crookston (2004) to characterise fabric geometric parameters such as tow width, aspect ratio and area ratio (ratio of the area of the tow to its bounding rectangle). The data was collected by performing optical microscopy on cross sections of laminates manufactured from a NCF reinforcement (Formax FGE106) at various shear angles.

Figure B.1 shows an example of the laminate cross section. The study indicated that any change in tow shape caused by shearing of the fabric is not significant enough to be clear among the scatter in the measurements. The large variation in the tow geometry suggests that a stochastic approach to modelling, in which the geometric parameters are chosen according to a statistical distribution, may be appropriate. For the purposes of this study, constant tow geometry at all shear angles is assumed, considerably simplifying the work undertaken and reducing the number of variables in a model used to characterise a single material.

A flexible function was required to describe the tow cross section. The following expression, which describes a generalised ellipse, allows the user to control the shape of the tow as well as modify its aspect ratio:

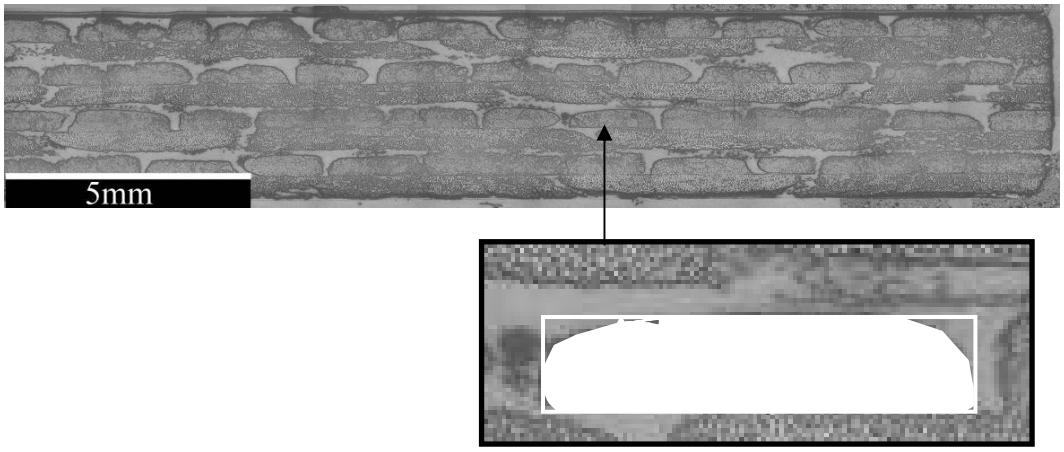

Figure B.1 – A cross section from a ±30° NCF laminate (Formax FGE106). Upper tow layers are perpendicular to the section, i.e. the top layer and alternate layers thereafter. Detail of a tow shape is shown with bounding rectangle and the tow area highlighted. After Crookston (2004).

$$y = \pm \frac{h_{tow}}{2} \left(1 - \frac{x^2}{\left(h_{tow} a_{tow} / 2 \right)^2} \right)^n \tag{B.1}$$

where a_{tow} is the tow aspect ratio, h_{tow} is the tow height, and the power n affects the tow shape. An ellipse is generated using n=0.5 while decreasing n towards zero will cause the shape to become more rectangular. Some examples of the range of tow shapes that can be produced using Equation (B.1) are shown in Figure B.2. The coordinates of the four quadrants are generated independently, permitting asymmetric shapes to be produced, although symmetric tow shapes are used throughout this study.

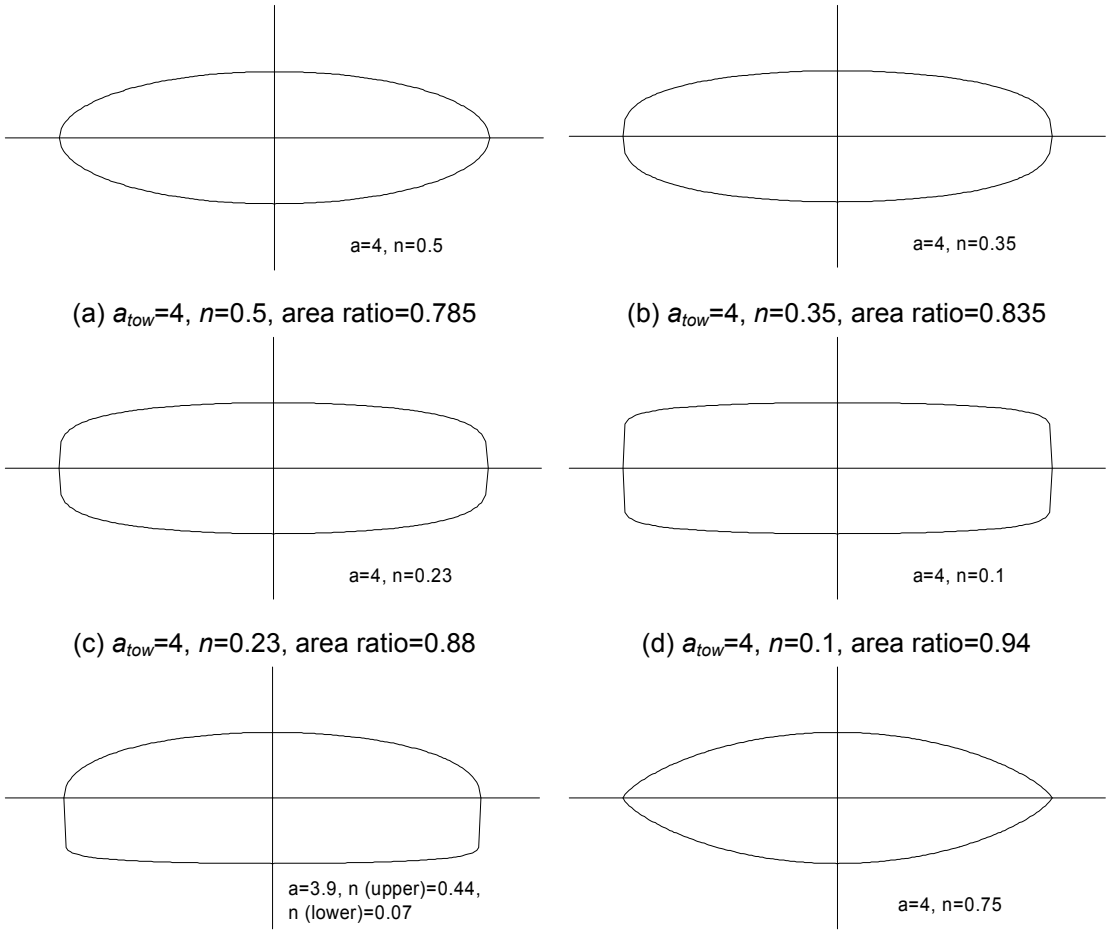

(a) a_{tow}=4, n=0.5, area ratio=0.785

(b) a_{tow}=4, n=0.35, area ratio=0.835

(c) a_{tow}=4, n=0.23, area ratio=0.88

(d) a_{tow}=4, n=0.1, area ratio=0.94

(e) a_{tow}=3.9, n (upper quadrants)=0.44, n (lower quadrants)=0.07, area ratio=0.88.

(f) a_{tow}=4, n=0.75, area ratio=0.72

Figure B.2 – Tow shapes produced using Equation (B.1). (a)-(d) show evolution of tow shape with n; (e) shows the ability to generate asymmetric sections; (f) shows the lenticular shape produced for $0.5<n<1$, such as may be applicable to tows in woven reinforcement.

APPENDIX C LAMINAR FLOW BETWEEN TWO FLAT PLATES

Consider an infinitely deep channel with length l, width h, and pressures at the ends $P(0) = P_1$ and $P(l) = P_2 < P_1$. Let the direction of increasing l be x, and the direction of increasing h be y. The Navier-Stokes x-momentum equation will reduce to,

$$\frac{d^2u}{dy^2} = \frac{1}{\mu}\frac{dP}{dx} \tag{C.1}$$

Integrating (C.1) with respect to y gives,

$$\frac{du}{dy} = \frac{y}{\mu}\frac{dP}{dx} + C_a \tag{C.2}$$

$$u = \frac{y^2}{2\mu}\frac{dP}{dx} + C_a y + C_b \tag{C.3}$$

The constants are found from the no-slip boundary condition at the wall,

At $y = 0$: $$u = 0 = C_b \tag{C.4}$$

At $y = h$: $$u = 0 = \frac{h^2}{2\mu}\frac{dP}{dx} + C_a h$$

$$C_a = -\frac{h}{2\mu}\frac{dP}{dx} \tag{C.5}$$

Substituting back to (C.3) gives the solution for flow in a channel due to pressure gradient,

$$u = -\frac{dP}{dx}\frac{y}{2\mu}(h - y) \tag{C.6}$$

This is also known as Hagen-Poiseuille flow.

The volumetric flow rate, Q, through the channel of cross section area Wh is given by,

$$Q = W\int_0^h u \cdot dy = -\frac{dP}{dx}\frac{W}{2\mu}\int_0^h y(h-y)\cdot dy$$

$$Q = -\frac{dP}{dx}\frac{W}{2\mu}\left[\frac{y^2 h}{2} - \frac{y^3}{3}\right]_0^h$$

therefore,

$$\frac{Q}{W} = -\frac{dP}{dx}\frac{h^3}{12\mu} \tag{C.7}$$

The mean flow velocity through the thickness is given by,

$$\overline{u} = \frac{Q}{Wh} = -\frac{h^2}{12\mu}\frac{dP}{dx} \tag{C.8}$$

Comparing (C.8) to Darcy's law (Eqn. 3.4) gives the effective permeability of a free channel of height h as,

$$K_{free} = \frac{h^2}{12} \tag{C.9}$$

APPENDIX D TENSOR ROTATION

D.1 GENERAL TENSOR ROTATION

Figure D.1 shows a general tensor in 3D space. In order to calculate the components of the tensor in global coordinates, one needs to perform the following mathematical rotation of the tensor.

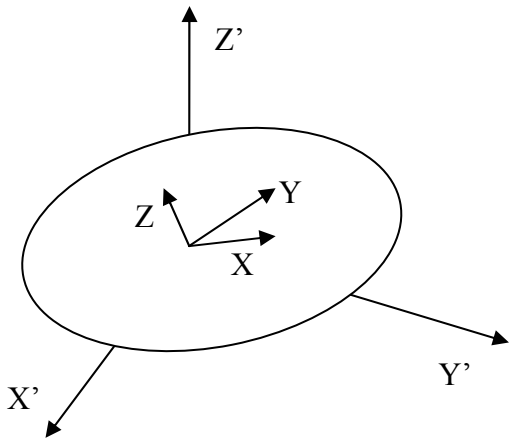

Figure D.1 – Tensor shown in 3D space. X, Y, Z are the local tensor coordinates and X', Y', Z' are the global coordinates

For the rotation about the X axis,

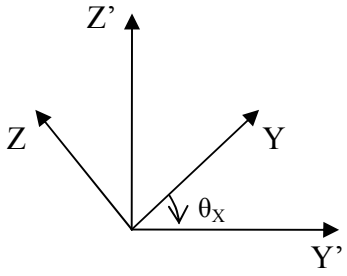

$$\mathbf{K}^{\theta} = \begin{bmatrix} K_{XX'} & K_{XY'} & K_{XZ'} \\ K_{XY'} & K_{YY'} & K_{YZ'} \\ K_{XZ'} & K_{YZ'} & K_{ZZ'} \end{bmatrix} = \begin{bmatrix} 1 & 0 & 0 \\ 0 & \cos\theta_X & \sin\theta_X \\ 0 & -\sin\theta_X & \cos\theta_X \end{bmatrix} \begin{bmatrix} K_{XX} & 0 & 0 \\ 0 & K_{YY} & 0 \\ 0 & 0 & K_{ZZ} \end{bmatrix} \begin{bmatrix} 1 & 0 & 0 \\ 0 & \cos\theta_X & -\sin\theta_X \\ 0 & \sin\theta_X & \cos\theta_X \end{bmatrix}$$

$$= \begin{bmatrix} 1 & 0 & 0 \\ 0 & \cos\theta_X & \sin\theta_X \\ 0 & -\sin\theta_X & \cos\theta_X \end{bmatrix} \begin{bmatrix} K_{XX} & 0 & 0 \\ 0 & K_{YY}\cos\theta_X & -K_{YY}\sin\theta_X \\ 0 & K_{ZZ}\sin\theta_X & K_{ZZ}\cos\theta_X \end{bmatrix}$$

$$= \begin{bmatrix} K_{XX} & 0 & 0 \\ 0 & K_{YY}\cos^2\theta_X + K_{ZZ}\sin^2\theta_X & (-K_{YY} + K_{ZZ})\cos\theta_X \sin\theta_X \\ 0 & (-K_{YY} + K_{ZZ})\sin\theta_X \cos\theta_X & K_{YY}\sin^2\theta_X + K_{ZZ}\cos^2\theta_X \end{bmatrix}$$

For the rotation about the second generation Y axis,

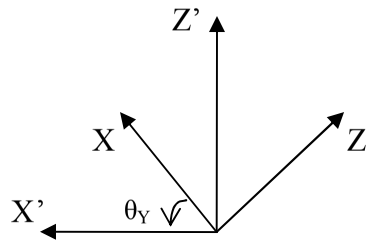

$$\mathbf{K}^{\theta} = \begin{bmatrix} K_{XX'} & K_{XY'} & K_{XZ'} \\ K_{XY'} & K_{YY'} & K_{YZ'} \\ K_{XZ'} & K_{YZ'} & K_{ZZ'} \end{bmatrix} = \begin{bmatrix} \cos\theta_Y & 0 & \sin\theta_Y \\ 0 & 1 & 0 \\ -\sin\theta_Y & 0 & \cos\theta_Y \end{bmatrix} \begin{bmatrix} K_{XX} & 0 & 0 \\ 0 & K_{YY}\cos^2\theta_X + K_{ZZ}\sin^2\theta_X & (-K_{YY}+K_{ZZ})\cos\theta_X\sin\theta_X \\ 0 & (-K_{YY}+K_{ZZ})\sin\theta_X\cos\theta_X & K_{YY}\sin^2\theta_X + K_{ZZ}\cos^2\theta_X \end{bmatrix} \begin{bmatrix} \cos\theta_Y & 0 & -\sin\theta_Y \\ 0 & 1 & 0 \\ \sin\theta_Y & 0 & \cos\theta_Y \end{bmatrix}$$

$$= \begin{bmatrix} \cos\theta_Y & 0 & \sin\theta_Y \\ 0 & 1 & 0 \\ -\sin\theta_Y & 0 & \cos\theta_Y \end{bmatrix} \begin{bmatrix} K_{XX}\cos\theta_Y & 0 & -K_{XX}\sin\theta_Y \\ (-K_{YY}+K_{ZZ})\cos\theta_X\sin\theta_X\sin\theta_Y & K_{YY}\cos^2\theta_X + K_{ZZ}\sin^2\theta_X & (-K_{YY}+K_{ZZ})\cos\theta_X\sin\theta_X \\ K_{YY}\sin^2\theta_X\sin\theta_Y + K_{ZZ}\cos^2\theta_X\sin\theta_Y & (-K_{YY}+K_{ZZ})\sin\theta_X\cos\theta_X & K_{YY}\cos\theta_Y\sin^2\theta_X + K_{ZZ}\cos^2\theta_X\cos\theta_Y \end{bmatrix}$$

$$= \begin{bmatrix} \begin{matrix} K_{XX}\cos^2\theta_Y \\ +K_{YY}\sin^2\theta_X\sin^2\theta_Y \\ +K_{ZZ}\cos^2\theta_X\sin^2\theta_Y \end{matrix} & (-K_{YY}+K_{ZZ})\cos\theta_X\sin\theta_X\sin\theta_Y & \begin{matrix} -K_{XX}\cos\theta_Y\sin\theta_Y \\ +K_{YY}\cos\theta_Y\sin^2\theta_X\sin\theta_Y \\ +K_{ZZ}\cos^2\theta_X\cos\theta_Y\sin^2\theta_Y \end{matrix} \\ (-K_{YY}+K_{ZZ})\cos\theta_X\sin\theta_X\sin\theta_Y & K_{YY}\cos^2\theta_X + K_{ZZ}\sin^2\theta_X & (-K_{YY}+K_{ZZ})\cos\theta_X\cos\theta_Y\sin\theta_X \\ \begin{matrix} -K_{XX}\cos\theta_Y\sin\theta_Y \\ +K_{YY}\sin^2\theta_X\sin\theta_Y\cos\theta_Y \\ +K_{ZZ}\cos^2\theta_X\cos\theta_Y\sin\theta_Y \end{matrix} & (-K_{YY}+K_{ZZ})\cos\theta_X\cos\theta_Y\sin\theta_X & \begin{matrix} K_{XX}\sin^2\theta_Y \\ +K_{YY}\cos^2\theta_Y\sin^2\theta_X \\ +K_{ZZ}\cos^2\theta_X\cos^2\theta_Y \end{matrix} \end{bmatrix}$$

For the rotation about the third generation Z axis,

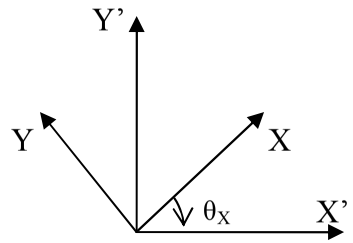

$$\mathbf{K}^{\theta} = \begin{bmatrix} K_{XX'} & K_{XY'} & K_{XZ'} \\ K_{XY'} & K_{YY'} & K_{YZ'} \\ K_{XZ'} & K_{YZ'} & K_{ZZ'} \end{bmatrix}$$

$$= \begin{bmatrix} \cos\theta_Z & \sin\theta_Z & 0 \\ -\sin\theta_Z & \cos\theta_Z & 0 \\ 0 & 0 & 1 \end{bmatrix} \begin{bmatrix} \begin{matrix} K_{XX}\cos^2\theta_Y \\ +K_{YY}\sin^2\theta_X\sin^2\theta_Y \\ +K_{ZZ}\cos^2\theta_X\sin^2\theta_Y \end{matrix} & \left(-K_{YY}+K_{ZZ}\right)\cos\theta_X\sin\theta_X\sin\theta_Y & \begin{matrix} -K_{XX}\cos\theta_Y\sin\theta_Y \\ +K_{YY}\cos\theta_Y\sin^2\theta_X\sin\theta_Y \\ +K_{ZZ}\cos^2\theta_X\cos\theta_Y\sin^2\theta_Y \end{matrix} \\ \left(-K_{YY}+K_{ZZ}\right)\cos\theta_X\sin\theta_X\sin\theta_Y & K_{YY}\cos^2\theta_X+K_{ZZ}\sin^2\theta_X & \left(-K_{YY}+K_{ZZ}\right)\cos\theta_X\cos\theta_Y\sin\theta_X \\ \begin{matrix} -K_{XX}\cos\theta_Y\sin\theta_Y \\ +K_{YY}\sin^2\theta_X\sin\theta_Y\cos\theta_Y \\ +K_{ZZ}\cos^2\theta_X\cos\theta_Y\sin\theta_Y \end{matrix} & \left(-K_{YY}+K_{ZZ}\right)\cos\theta_X\cos\theta_Y\sin\theta_X & \begin{matrix} K_{XX}\sin^2\theta_Y \\ +K_{YY}\cos^2\theta_Y\sin^2\theta_X \\ +K_{ZZ}\cos^2\theta_X\cos^2\theta_Y \end{matrix} \end{bmatrix} \begin{bmatrix} \cos\theta_Z & -\sin\theta_Z & 0 \\ \sin\theta_Z & \cos\theta_Z & 0 \\ 0 & 0 & 1 \end{bmatrix}$$

$$\mathbf{K}^{\theta} = \begin{bmatrix} K_{XX'} & K_{XY'} & K_{XZ'} \\ K_{XY'} & K_{YY'} & K_{YZ'} \\ K_{XZ'} & K_{YZ'} & K_{ZZ'} \end{bmatrix}$$

$$= \begin{bmatrix} \cos\theta_Z & \sin\theta_Z & 0 \\ -\sin\theta_Z & \cos\theta_Z & 0 \\ 0 & 0 & 1 \end{bmatrix} \begin{bmatrix} \begin{array}{l} K_{XX}\cos^2\theta_Y\cos\theta_Z \\ +K_{YY}\left(\cos\theta_Z\sin^2\theta_X\sin^2\theta_Y-\cos\theta_X\sin\theta_X\sin\theta_Y\sin\theta_Z\right) \\ +K_{ZZ}\left(\cos^2\theta_X\cos\theta_Z\sin^2\theta_Y+\cos\theta_X\sin\theta_X\sin\theta_Y\sin\theta_Z\right) \end{array} & \begin{array}{l} -K_{XX}\cos^2\theta_Y\sin\theta_Z \\ +K_{YY}\left(-\sin^2\theta_X\sin^2\theta_Y\sin\theta_Z-\cos\theta_X\cos\theta_Z\sin\theta_X\sin\theta_Y\right) \\ +K_{ZZ}\left(-\cos^2\theta_X\sin^2\theta_Y\sin\theta_Z+\cos\theta_X\cos\theta_Z\sin\theta_X\sin\theta_Y\right) \end{array} & \begin{array}{l} -K_{XX}\cos\theta_Y\sin\theta_Y \\ +K_{YY}\cos\theta_Y\sin^2\theta_X\sin\theta_Y \\ +K_{ZZ}\cos^2\theta_X\cos\theta_Y\sin^2\theta_Y \end{array} \\ \begin{array}{l} K_{YY}\left(-\cos\theta_X\cos\theta_Z\sin\theta_X\sin\theta_Y+\cos^2\theta_X\sin\theta_Z\right) \\ +K_{ZZ}\left(\cos\theta_X\cos\theta_Z\sin\theta_X\sin\theta_Y+\sin^2\theta_X\sin\theta_Z\right) \end{array} & \begin{array}{l} K_{YY}\left(\cos\theta_X\sin\theta_X\sin\theta_Y\sin\theta_Z+\cos^2\theta_X\cos\theta_Z\right) \\ +K_{ZZ}\left(-\cos\theta_X\sin\theta_X\sin\theta_Y\sin\theta_Z+\cos\theta_Z\sin^2\theta_X\right) \end{array} & \left(-K_{YY}+K_{ZZ}\right)\cos\theta_X\cos\theta_Y\sin\theta_X \\ \begin{array}{l} -K_{XX}\cos\theta_Y\cos\theta_Z\sin\theta_Y \\ +K_{YY}\left(\cos\theta_Y\cos\theta_Z\sin^2\theta_X\sin\theta_Y-\cos\theta_X\cos\theta_Y\sin\theta_X\sin\theta_Z\right) \\ +K_{ZZ}\left(\cos^2\theta_X\cos\theta_Y\cos\theta_Z\sin\theta_Y+\cos\theta_X\cos\theta_Y\sin\theta_X\sin\theta_Z\right) \end{array} & \begin{array}{l} K_{XX}\cos\theta_Y\sin\theta_Y\sin\theta_Z \\ +K_{YY}\left(-\sin^2\theta_X\sin\theta_Y\sin\theta_Z\cos\theta_Y-\cos\theta_X\cos\theta_Y\cos\theta_Z\sin\theta_X\right) \\ +K_{ZZ}\left(-\cos^2\theta_X\cos\theta_Y\sin\theta_Y\sin\theta_Z+\cos\theta_X\cos\theta_Y\cos\theta_Z\sin\theta_X\right) \end{array} & \begin{array}{l} K_{XX}\sin^2\theta_Y \\ +K_{YY}\cos^2\theta_Y\sin^2\theta_X \\ +K_{ZZ}\cos^2\theta_X\cos^2\theta_Y \end{array} \end{bmatrix}$$

Therefore, the respective components of the tensor in global coordinates are calculated using the following equations.

$$\begin{aligned} K_{XX'} = & K_{XX}\cos^2\theta_Y\cos^2\theta_Z \\ & + K_{YY}\left(-\cos\theta_Z\sin\theta_X\sin\theta_Y+\cos\theta_X\sin\theta_Z\right)^2 \\ & + K_{ZZ}\left(\cos\theta_X\cos\theta_Z\sin\theta_Y+\sin\theta_X\sin\theta_Z\right)^2 \end{aligned} \tag{D.1}$$

$$\begin{aligned} K_{XY'} = & \\ & - K_{XX}\cos^2\theta_Y\cos\theta_Z\sin\theta_Z \\ & + K_{YY}\left(-\cos\theta_Z\sin^2\theta_X\sin^2\theta_Y\sin\theta_Z+\cos\theta_X\sin\theta_X\sin\theta_Y\sin^2\theta_Z-\cos\theta_X\cos^2\theta_Z\sin\theta_X\sin\theta_Y+\cos^2\theta_X\cos\theta_Z\sin\theta_Z\right) \\ & + K_{ZZ}\left(-\cos^2\theta_X\cos\theta_Z\sin^2\theta_Y\sin\theta_Z-\cos\theta_X\sin\theta_X\sin\theta_Y\sin^2\theta_Z+\cos\theta_X\cos^2\theta_Z\sin\theta_X\sin\theta_Y+\cos\theta_Z\sin^2\theta_X\sin\theta_Z\right) \\ & - K_{XX}\cos^2\theta_Y\cos\theta_Z\sin\theta_Z \\ = & + K_{YY}\left(-\cos\theta_Z\sin\theta_X\sin\theta_Y+\cos\theta_X\sin\theta_Z\right)\left(\cos\theta_X\cos\theta_Z+\sin\theta_X\sin\theta_Y\sin\theta_Z\right) \\ & + K_{ZZ}\left(\cos\theta_X\cos\theta_Z\sin\theta_Y+\sin\theta_X\sin\theta_Z\right)\left(\cos\theta_Z\sin\theta_X-\cos\theta_X\sin\theta_Y\sin\theta_Z\right) \end{aligned} \tag{D.2}$$

$$\begin{aligned} K_{XZ'} = & -K_{XX}\cos\theta_Y\cos\theta_Z\sin\theta_Y \\ & + K_{YY}\cos\theta_Y\sin\theta_X\left(\cos\theta_Z\sin\theta_X\sin\theta_Y-\cos\theta_X\sin\theta_Z\right) \\ & + K_{ZZ}\cos\theta_X\cos\theta_Y\left(\cos\theta_X\cos\theta_Z\sin\theta_Y+\sin\theta_X\sin\theta_Z\right) \end{aligned} \tag{D.3}$$

$$\begin{aligned} K_{YY'} = & K_{XX}\cos^2\theta_Y\sin^2\theta_Z \\ & + K_{YY}\left(\cos\theta_X\cos\theta_Z+\sin\theta_X\sin\theta_Y\sin\theta_Z\right)^2 \\ & + K_{ZZ}\left(\cos\theta_Z\sin\theta_X-\cos\theta_X\sin\theta_Y\sin\theta_Z\right)^2 \end{aligned} \tag{D.4}$$

$$\begin{aligned} K_{YZ'} = & K_{XX}\cos\theta_Y\sin\theta_Y\sin\theta_Z \\ & + K_{YY}\cos\theta_Y\sin\theta_X\left(-\cos\theta_X\cos\theta_Z-\sin\theta_X\sin\theta_Y\sin\theta_Z\right) \\ & + K_{ZZ}\cos\theta_X\cos\theta_Y\left(\cos\theta_Z\sin\theta_X-\cos\theta_X\sin\theta_Y\sin\theta_Z\right) \end{aligned} \tag{D.5}$$

$$K_{ZZ'} = K_{XX}\sin^2\theta_Y + K_{YY}\cos^2\theta_Y\sin^2\theta_X + K_{ZZ}\cos^2\theta_X\cos^2\theta_Y \tag{D.6}$$

D.2 TOW PERMEABILITY TENSOR ROTATION

For a fabric model with the fibrous tow in 3D space, as shown in Figure D.2, the local X axis denotes the axis along the fibrous tows and the local Y and Z axes denote the axes perpendicular to the tows. The local permeability along these local principal axes of the tow can be given as,

$$K_{XX} = K_{\parallel} \tag{D.7}$$

$$K_{YY} = K_{ZZ} = K_{\perp} \tag{D.8}$$

where $K_{\parallel}$ and $K_{\perp}$ are the axial and transverse tow permeabilities respectively, as found using Eqn. (2.11) and (2.12) following Gebart (1992).

For 2D Grid Average, the permeability tensor components of a fibrous tow in the global X'-Y' in-plane are found using Eqns. (D.1), (D.2) and (D.4) and substituting the appropriate terms from Eqns. (D.7) and (D.8).

For 3D Grid Average, the permeability tensor components of a fibrous tow in the global X'-Y'-Z' coordinates are found using Eqns. (D.1)-(D.6) and substituting the appropriate terms from Eqns. (D.7) and (D.8).

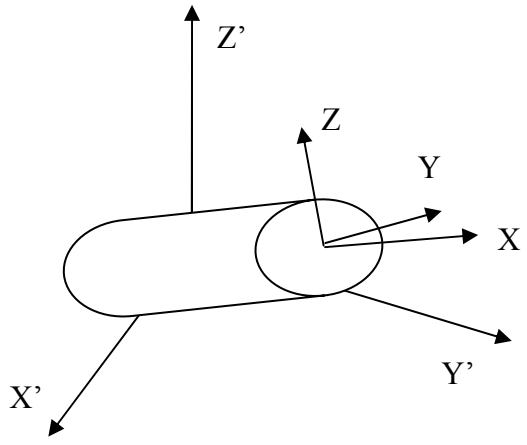

Figure D.2 – Tensor of fibre tow shown in 3D space. X, Y, Z are the local tow coordinates and X', Y', Z' are the global model coordinates

APPENDIX E FINITE DIFFERENCE DISCRETISATION FOR SOLUTION OF PRESSURE FIELD IN POROUS MEDIA FLOW

E.1 INTRODUCTION TO FINITE DIFFERENCES

Most common finite difference representations of derivatives are based on Taylor's series expansions. Consider the following Taylor expansions about the grid points shown in Figure E.1:

$$f_{i+1,j} = f_{i,j} + \Delta x\left(\frac{\partial f}{\partial x}\right)_{i,j} + \frac{(\Delta x)^2}{2}\left(\frac{\partial^2 f}{\partial x^2}\right)_{i,j} + \frac{(\Delta x)^3}{6}\left(\frac{\partial^3 f}{\partial x^3}\right)_{i,j} + \mathrm{O}(\Delta x)^4 \qquad \text{(E.1)}$$

$$f_{i-1,j} = f_{i,j} - \Delta x\left(\frac{\partial f}{\partial x}\right)_{i,j} + \frac{(\Delta x)^2}{2}\left(\frac{\partial^2 f}{\partial x^2}\right)_{i,j} - \frac{(\Delta x)^3}{6}\left(\frac{\partial^3 f}{\partial x^3}\right)_{i,j} + \mathrm{O}(\Delta x)^4 \qquad \text{(E.2)}$$

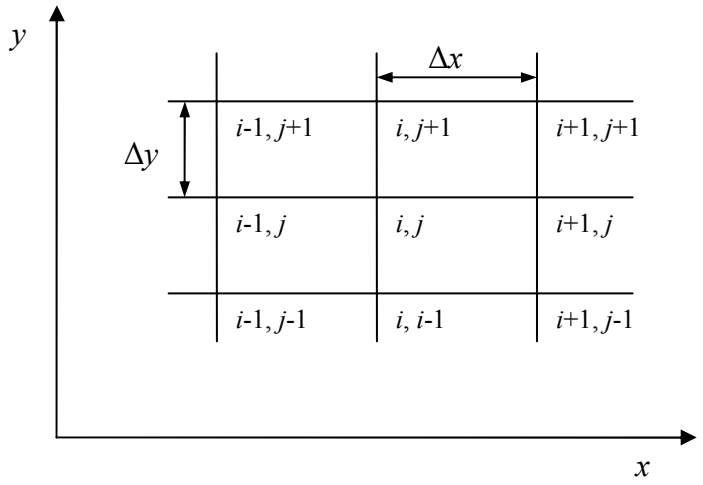

Figure E.1 – Discrete grid points on a structured grid.

From Eqn. (E.1), first order forward difference with respect to x is derived as,

$$\left(\frac{\partial f}{\partial x}\right)_{i,j} = \frac{f_{i+1,j} - f_{i,j}}{\Delta x} + \mathrm{O}(\Delta x) \qquad \text{(E.3)}$$

From Eqn. (E.2), first order rearward difference with respect to x is derived as,

$$\left(\frac{\partial f}{\partial x}\right)_{i,j} = \frac{f_{i,j} - f_{i-1,j}}{\Delta x} + \mathrm{O}(\Delta x) \tag{E.4}$$

Subtracting Eqn. (E.2) from Eqn. (E.1) yields the second order central difference with respect to x,

$$\left(\frac{\partial f}{\partial x}\right)_{i,j} = \frac{f_{i+1,j} - f_{i-1,j}}{2\Delta x} + \mathrm{O}(\Delta x)^2 \tag{E.5}$$

Summing Eqns. (E.1) and (E.2) yields the second order second difference with respect to x,

$$\left(\frac{\partial^2 f}{\partial x^2}\right)_{i,j} = \frac{f_{i+1,j} - 2f_{i,j} + f_{i-1,j}}{(\Delta x)^2} + \mathrm{O}(\Delta x)^2 \tag{E.6}$$

$\mathrm{O}(\Delta x)$, $\mathrm{O}(\Delta x)^2 \ldots \mathrm{O}(\Delta x)^n$ represents the truncation errors in terms of order (Δx), $(\Delta x)^2 \ldots (\Delta x)^n$ respectively. Difference expressions for derivatives with respect to *y* can be obtained in exactly the same fashion, and the results are directly analogous to Eqns. (E.3) to (E.6) for the *x* derivatives.

For the case of mixed derivatives, such as $\partial^2 f / \partial x \partial y$, the finite difference quotients are found as follows. Differentiate Eqns. (E.1) and (E.2) with respect to y,

$$\left(\frac{\partial f}{\partial y}\right)_{i+1,j} = \left(\frac{\partial f}{\partial y}\right)_{i,j} + \Delta x\left(\frac{\partial^2 f}{\partial x \partial y}\right)_{i,j} + \frac{(\Delta x)^2}{2}\left(\frac{\partial^3 f}{\partial x^2 \partial y}\right)_{i,j} + \frac{(\Delta x)^3}{6}\left(\frac{\partial^4 f}{\partial x^3 \partial y}\right)_{i,j} + \mathrm{O}(\Delta x)^4 \tag{E.7}$$

$$\left(\frac{\partial f}{\partial y}\right)_{i-1,j} = \left(\frac{\partial f}{\partial y}\right)_{i,j} - \Delta x\left(\frac{\partial^2 f}{\partial x \partial y}\right)_{i,j} + \frac{(\Delta x)^2}{2}\left(\frac{\partial^3 f}{\partial x^2 \partial y}\right)_{i,j} - \frac{(\Delta x)^3}{6}\left(\frac{\partial^4 f}{\partial x^3 \partial y}\right)_{i,j} + \mathrm{O}(\Delta x)^4 \tag{E.8}$$

Subtract Eqn. (E.8) from (E.7) to give,

$$\left(\frac{\partial^2 f}{\partial x \partial y}\right)_{i,j} = \frac{\left(\partial f/\partial y\right)_{i+1,j} - \left(\partial f/\partial y\right)_{i-1,j}}{2\Delta x} + \mathrm{O}\left(\Delta x\right)^2 \tag{E.9}$$

Referring back to Figure E.1, the two $\partial f/\partial y$ expressions in the first term on the right-hand-side of Eqn. (E.9) can be replaced with a second order central difference as that given by Eqn. (E.5) but using appropriate grid points first centred on (i+1,j) and then on (i-1,j). More specifically,

$$\left(\frac{\partial f}{\partial y}\right)_{i+1,j} = \frac{f_{i+1,j+1} - f_{i+1,j-1}}{2\Delta y} + \mathrm{O}\left(\Delta y\right)^2 \tag{E.10}$$

$$\left(\frac{\partial f}{\partial y}\right)_{i-1,j} = \frac{f_{i-1,j+1} - f_{i-1,j-1}}{2\Delta y} + \mathrm{O}\left(\Delta y\right)^2 \tag{E.11}$$

Substituting Eqns. (E.10) and (E.11) into Eqn. (E.9) yields the second order central difference for the mixed derivative,

$$\left(\frac{\partial^2 f}{\partial x \partial y}\right)_{i,j} = \frac{f_{i+1,j+1} - f_{i+1,j-1} - f_{i-1,j+1} + f_{i-1,j-1}}{4\Delta x \Delta y} + \mathrm{O}\left[\left(\Delta x\right)^2, \left(\Delta y\right)^2\right] \tag{E.12}$$

While the finite difference equations shown above were derived based on a 2D grid with the derivatives with respect to x and y, it can be readily extended to include the z direction. The resulting expressions for derivatives with respect to z are directly analogous to Eqns. (E.3)-(E.6) and (E.12) for derivatives with respect to x and y.

The derivations shown above follow that in Anderson (1995).

E.2 GOVERNING EQUATIONS FOR POROUS MEDIA FLOW

For a two-dimensional problem, Darcy's law and the continuity equation are written in matrix and differential forms respectively,

$$\begin{pmatrix} u_x \\ u_y \end{pmatrix} = -\frac{1}{\mu}\begin{pmatrix} K_{xx} & K_{xy} \\ K_{yx} & K_{yy} \end{pmatrix}\begin{pmatrix} \dfrac{\partial P}{\partial x} \\ \dfrac{\partial P}{\partial y} \end{pmatrix} \tag{E.13}$$

$$\frac{\partial u_x}{\partial x} + \frac{\partial u_y}{\partial y} = 0 \tag{E.14}$$

Combining (E.13) and (E.14) gives the governing equation of the pressure 2D space,

$$\frac{\partial}{\partial x}\left(\frac{K_{xx}}{\mu}\frac{\partial P}{\partial x}\right) + \frac{\partial}{\partial x}\left(\frac{K_{xy}}{\mu}\frac{\partial P}{\partial y}\right) + \frac{\partial}{\partial y}\left(\frac{K_{yx}}{\mu}\frac{\partial P}{\partial x}\right) + \frac{\partial}{\partial y}\left(\frac{K_{yy}}{\mu}\frac{\partial P}{\partial y}\right) = 0 \tag{E.15}$$

Correspondingly, Darcy's law and the continuity equation written in 3D space,

$$\begin{pmatrix} u_x \\ u_y \\ u_z \end{pmatrix} = -\frac{1}{\mu}\begin{pmatrix} K_{xx} & K_{xy} & K_{xz} \\ K_{yx} & K_{yy} & K_{yz} \\ K_{zx} & K_{zy} & K_{zz} \end{pmatrix}\begin{pmatrix} \dfrac{\partial P}{\partial x} \\ \dfrac{\partial P}{\partial y} \\ \dfrac{\partial P}{\partial z} \end{pmatrix} \tag{E.16}$$

$$\frac{\partial u_x}{\partial x} + \frac{\partial u_y}{\partial y} + \frac{\partial u_z}{\partial z} = 0 \tag{E.17}$$

Combining (E.16) and (E.17) gives the governing equation of the pressure in 3D space,

$$\begin{aligned} &\frac{\partial}{\partial x}\left(\frac{K_{xx}}{\mu}\frac{\partial P}{\partial x}\right) + \frac{\partial}{\partial x}\left(\frac{K_{xy}}{\mu}\frac{\partial P}{\partial y}\right) + \frac{\partial}{\partial x}\left(\frac{K_{xz}}{\mu}\frac{\partial P}{\partial z}\right) \\ &+ \frac{\partial}{\partial y}\left(\frac{K_{yx}}{\mu}\frac{\partial P}{\partial x}\right) + \frac{\partial}{\partial y}\left(\frac{K_{yy}}{\mu}\frac{\partial P}{\partial y}\right) + \frac{\partial}{\partial y}\left(\frac{K_{yz}}{\mu}\frac{\partial P}{\partial z}\right) = 0 \\ &+ \frac{\partial}{\partial z}\left(\frac{K_{zx}}{\mu}\frac{\partial P}{\partial x}\right) + \frac{\partial}{\partial z}\left(\frac{K_{zy}}{\mu}\frac{\partial P}{\partial y}\right) + \frac{\partial}{\partial z}\left(\frac{K_{zz}}{\mu}\frac{\partial P}{\partial z}\right) \end{aligned} \tag{E.18}$$

E.2.1 2D finite difference discretisation

Let $F_{ab} = \frac{K_{ab}}{\mu}$ and expanding the 2D governing equation (E.15),

$$\left(\frac{\partial F_{xx}}{\partial x}\frac{\partial P}{\partial x} + F_{xx}\frac{\partial^2 P}{\partial x^2}\right) + \left(\frac{\partial F_{xy}}{\partial x}\frac{\partial P}{\partial y} + F_{xy}\frac{\partial^2 P}{\partial x \partial y}\right) + \left(\frac{\partial F_{yx}}{\partial y}\frac{\partial P}{\partial x} + F_{yx}\frac{\partial^2 P}{\partial y \partial x}\right) + \left(\frac{\partial F_{yy}}{\partial y}\frac{\partial P}{\partial y} + F_{yy}\frac{\partial^2 P}{\partial y^2}\right) = 0 \tag{E.19}$$

Expressing the individual derivatives terms in (E.19) using first order forward finite difference (E.3), second order second difference (E.6) and second order central difference for the mixed derivative (E.12),

$$\left(\frac{\partial F_{xx}}{\partial x}\frac{\partial P}{\partial x} + F_{xx}\frac{\partial^2 P}{\partial x^2}\right) = \left(\frac{F_{xxi+1,j} - F_{xxi,j}}{\Delta x} \cdot \frac{P_{i+1,j} - P_{i,j}}{\Delta x}\right) + \left(F_{xxi,j} \cdot \frac{P_{i+1,j} - 2P_{i,j} + P_{i-1,j}}{\Delta x^2}\right)$$
$$= P_{i-1,j}\left(\frac{F_{xxi,j}}{\Delta x^2}\right) + P_{i,j}\left(-\frac{F_{xxi,j} + F_{xxi+1,j}}{\Delta x^2}\right) + P_{i+1,j}\left(\frac{F_{xxi+1,j}}{\Delta x^2}\right) \tag{E.20}$$

$$\left(\frac{\partial F_{xy}}{\partial x}\frac{\partial P}{\partial y} + F_{xy}\frac{\partial^2 P}{\partial x \partial y}\right) = \left(\frac{F_{xyi+1,j} - F_{xyi,j}}{\Delta x} \cdot \frac{P_{i,j+1} - P_{i,j}}{\Delta y}\right) + \left(F_{xyi,j} \cdot \frac{P_{i+1,j+1} + P_{i-1,j-1} - P_{i-1,j+1} - P_{i+1,j-1}}{4\Delta x \Delta y}\right)$$
$$= P_{i-1,j-1}\left(\frac{F_{xyi,j}}{4\Delta x \Delta y}\right) + P_{i-1,j+1}\left(-\frac{F_{xyi,j}}{4\Delta x \Delta y}\right) + P_{i,j}\left(-\frac{F_{xyi+1,j} - F_{xyi,j}}{\Delta x \Delta y}\right) + P_{i,j+1}\left(\frac{F_{xyi+1,j} - F_{xyi,j}}{\Delta x \Delta y}\right)$$
$$+ P_{i+1,j-1}\left(-\frac{F_{xyi,j}}{4\Delta x \Delta y}\right) + P_{i+1,j+1}\left(\frac{F_{xyi,j}}{4\Delta x \Delta y}\right) \tag{E.21}$$

$$\left(\frac{\partial F_{yx}}{\partial y}\frac{\partial P}{\partial x} + F_{yx}\frac{\partial^2 P}{\partial y \partial x}\right) = \left(\frac{F_{yxi,j+1} - F_{yxi,j}}{\Delta y} \cdot \frac{P_{i+1,j} - P_{i,j}}{\Delta x}\right) + \left(F_{yxi,j} \cdot \frac{P_{i+1,j+1} + P_{i-1,j-1} - P_{i-1,j+1} - P_{i+1,j-1}}{4\Delta x \Delta y}\right)$$
$$= P_{i-1,j-1}\left(\frac{F_{yxi,j}}{4\Delta x \Delta y}\right) + P_{i-1,j+1}\left(-\frac{F_{yxi,j}}{4\Delta x \Delta y}\right) + P_{i,j}\left(-\frac{F_{yxi,j+1} - F_{yxi,j}}{\Delta x \Delta y}\right) + P_{i+1,j-1}\left(-\frac{F_{yxi,j}}{4\Delta x \Delta y}\right)$$
$$+ P_{i+1,j}\left(\frac{F_{yxi+1,j} - F_{yxi,j}}{\Delta x \Delta y}\right) + P_{i+1,j+1}\left(\frac{F_{xyi,j}}{4\Delta x \Delta y}\right) \tag{E.22}$$

$$\left(\frac{\partial F_{yy}}{\partial y}\frac{\partial P}{\partial y}+F_{yy}\frac{\partial^2 P}{\partial y^2}\right)=\left(\frac{F_{yy\,i,j+1}-F_{yy\,i,j}}{\Delta y}\cdot\frac{P_{i,j+1}-P_{i,j}}{\Delta y}\right)+\left(F_{yy\,i,j}\cdot\frac{P_{i,j+1}-2P_{i,j}+P_{i,j-1}}{\Delta y^2}\right)$$
$$=P_{i,j-1}\left(\frac{F_{yy\,i,j}}{\Delta y^2}\right)+P_{i,j}\left(-\frac{F_{yy\,i,j}+F_{yy\,i,j+1}}{\Delta y^2}\right)+P_{i,j+1}\left(\frac{F_{yy\,i,j+1}}{\Delta y^2}\right) \quad \text{(E.23)}$$

Substituting Eqns. (E.20)-(E.23) into (E.19) results in the governing equation expressed in terms of pressure,

$$P_{i-1,j-1}\left(\frac{F_{xy\,i,j}+F_{yx\,i,j}}{4\Delta x\Delta y}\right)+P_{i,j-1}\left(\frac{F_{yy\,i,j}}{\Delta y^2}\right)+P_{i+1,j-1}\left(-\frac{F_{xy\,i,j}+F_{yx\,i,j}}{4\Delta x\Delta y}\right)$$
$$+P_{i-1,j}\left(\frac{F_{xx\,i,j}}{\Delta x^2}\right)$$
$$+P_{i,j}\left(-\frac{F_{xx\,i,j}+F_{xx\,i+1,j}}{\Delta x^2}-\frac{F_{xy\,i+1,j}+F_{yx\,i,j+1}-F_{xy\,i,j}-F_{yx\,i,j}}{4\Delta x\Delta y}-\frac{F_{yy\,i,j}+F_{yy\,i,j+1}}{\Delta y^2}\right)$$
$$+P_{i+1,j}\left(\frac{F_{xx\,i+1,j}}{\Delta x^2}+\frac{F_{yx\,i,j+1}-F_{yx\,i,j}}{\Delta x\Delta y}\right)$$
$$+P_{i-1,j+1}\left(-\frac{F_{xy\,i,j}+F_{yx\,i,j}}{4\Delta x\Delta y}\right)+P_{i,j+1}\left(\frac{F_{xy\,i+1,j}-F_{xy\,i,j}}{\Delta x\Delta y}+\frac{F_{yy\,i,j+1}}{\Delta y^2}\right)+P_{i+1,j+1}\left(\frac{F_{xy\,i,j}+F_{yx\,i,j}}{4\Delta x\Delta y}\right)=0 \quad \text{(E.24)}$$

E.2.2 3D finite difference discretisation

Let $F_{ab} = \dfrac{K_{ab}}{\mu}$ and expanding the 3D governing equation (E.18),

$$\begin{aligned}
&\left(\frac{\partial F_{xx}}{\partial x}\frac{\partial P}{\partial x} + F_{xx}\frac{\partial^2 P}{\partial x^2}\right) + \left(\frac{\partial F_{xy}}{\partial x}\frac{\partial P}{\partial y} + F_{xy}\frac{\partial^2 P}{\partial x \partial y}\right) + \left(\frac{\partial F_{xz}}{\partial x}\frac{\partial P}{\partial z} + F_{xz}\frac{\partial^2 P}{\partial x \partial z}\right) \\
&+ \left(\frac{\partial F_{yx}}{\partial y}\frac{\partial P}{\partial x} + F_{yx}\frac{\partial^2 P}{\partial y \partial x}\right) + \left(\frac{\partial F_{yy}}{\partial y}\frac{\partial P}{\partial y} + F_{yy}\frac{\partial^2 P}{\partial y^2}\right) + \left(\frac{\partial F_{yz}}{\partial y}\frac{\partial P}{\partial z} + F_{yz}\frac{\partial^2 P}{\partial y \partial z}\right) = 0 \\
&+ \left(\frac{\partial F_{zx}}{\partial z}\frac{\partial P}{\partial x} + F_{zx}\frac{\partial^2 P}{\partial z \partial x}\right) + \left(\frac{\partial F_{zy}}{\partial z}\frac{\partial P}{\partial y} + F_{zy}\frac{\partial^2 P}{\partial z \partial y}\right) + \left(\frac{\partial F_{zz}}{\partial z}\frac{\partial P}{\partial z} + F_{zz}\frac{\partial^2 P}{\partial z^2}\right)
\end{aligned} \tag{E.25}$$

Expressing the individual derivatives terms in (E.18) using first order forward finite difference (E.3), second order second difference (E.6) and second order central difference for the mixed derivative (E.9),

$$\begin{aligned}
&\left(\frac{\partial F_{xx}}{\partial x}\frac{\partial P}{\partial x} + F_{xx}\frac{\partial^2 P}{\partial x^2}\right) = \left(\frac{F_{xxi+1,j,k} - F_{xxi,j,k}}{\Delta x} \cdot \frac{P_{i+1,j,k} - P_{i,j,k}}{\Delta x}\right) + \left(F_{xxi,j,k} \cdot \frac{P_{i+1,j,k} - 2P_{i,j,k} + P_{i-1,j,k}}{\Delta x^2}\right) \\
&= P_{i-1,j,k}\left(\frac{F_{xxi,j,k}}{\Delta x^2}\right) + P_{i,j,k}\left(-\frac{F_{xxi,j,k} + F_{xxi+1,j,k}}{\Delta x^2}\right) + P_{i+1,j,k}\left(\frac{F_{xxi+1,j,k}}{\Delta x^2}\right)
\end{aligned} \tag{E.26}$$

$$\begin{aligned}
&\left(\frac{\partial F_{xy}}{\partial x}\frac{\partial P}{\partial y} + F_{xy}\frac{\partial^2 P}{\partial x \partial y}\right) = \left(\frac{F_{xyi+1,j,k} - F_{xyi,j,k}}{\Delta x} \cdot \frac{P_{i,j+1,k} - P_{i,j,k}}{\Delta y}\right) + \left(F_{xyi,j,k} \cdot \frac{P_{i+1,j+1,k} + P_{i-1,j-1,k} - P_{i-1,j+1,k} - P_{i+1,j-1,k}}{4\Delta x \Delta y}\right) \\
&= P_{i-1,j-1,k}\left(\frac{F_{xyi,j,k}}{4\Delta x \Delta y}\right) + P_{i-1,j+1,k}\left(-\frac{F_{xyi,j,k}}{4\Delta x \Delta y}\right) + P_{i,j,k}\left(-\frac{F_{xyi+1,j,k} - F_{xyi,j,k}}{\Delta x \Delta y}\right) + P_{i,j+1,k}\left(\frac{F_{xyi+1,j,k} - F_{xyi,j,k}}{\Delta x \Delta y}\right) \\
&+ P_{i+1,j-1,k}\left(-\frac{F_{xyi,j,k}}{4\Delta x \Delta y}\right) + P_{i+1,j+1,k}\left(\frac{F_{xyi,j,k}}{4\Delta x \Delta y}\right)
\end{aligned} \tag{E.27}$$

$$\begin{aligned}
&\left(\frac{\partial F_{xz}}{\partial x}\frac{\partial P}{\partial z} + F_{xz}\frac{\partial^2 P}{\partial x \partial z}\right) = \left(\frac{F_{xzi+1,j,k} - F_{xzi,j,k}}{\Delta x} \cdot \frac{P_{i,j,k+1} - P_{i,j,k}}{\Delta z}\right) + \left(F_{xzi,j,k} \cdot \frac{P_{i+1,j,k+1} + P_{i-1,j,k-1} - P_{i-1,j,k+1} - P_{i+1,j,k-1}}{4\Delta x \Delta z}\right) \\
&= P_{i-1,j,k-1}\left(\frac{F_{xzi,j,k}}{4\Delta x \Delta z}\right) + P_{i-1,j,k+1}\left(-\frac{F_{xzi,j,k}}{4\Delta x \Delta z}\right) + P_{i,j,k}\left(-\frac{F_{xzi+1,j,k} - F_{xzi,j,k}}{\Delta x \Delta z}\right) + P_{i,j,k+1}\left(\frac{F_{xzi+1,j,k} - F_{xzi,j,k}}{\Delta x \Delta z}\right) \\
&+ P_{i+1,j,k-1}\left(-\frac{F_{xzi,j,k}}{4\Delta x \Delta z}\right) + P_{i+1,j,k+1}\left(\frac{F_{xzi,j,k}}{4\Delta x \Delta z}\right)
\end{aligned} \tag{E.28}$$

$$\left(\frac{\partial F_{yx}}{\partial y}\frac{\partial P}{\partial x}+F_{yx}\frac{\partial^2 P}{\partial y\partial x}\right)=\left(\frac{F_{yx_{i,j+1,k}}-F_{yx_{i,j,k}}}{\Delta y}\cdot\frac{P_{i+1,j,k}-P_{i,j,k}}{\Delta x}\right)+\left(F_{yx_{i,j,k}}\cdot\frac{P_{i+1,j+1,k}+P_{i-1,j-1,k}-P_{i-1,j+1,k}-P_{i+1,j-1,k}}{4\Delta x\Delta y}\right)$$
$$=P_{i-1,j-1,k}\left(\frac{F_{yx_{i,j,k}}}{4\Delta x\Delta y}\right)+P_{i-1,j+1,k}\left(-\frac{F_{yx_{i,j,k}}}{4\Delta x\Delta y}\right)+P_{i,j,k}\left(-\frac{F_{yx_{i,j+1,k}}-F_{yx_{i,j,k}}}{\Delta x\Delta y}\right)+P_{i+1,j-1,k}\left(-\frac{F_{yx_{i,j,k}}}{4\Delta x\Delta y}\right) \quad \text{(E.29)}$$
$$+P_{i+1,j,k}\left(\frac{F_{yx_{i+1,j,k}}-F_{yx_{i,j,k}}}{\Delta x\Delta y}\right)+P_{i+1,j+1,k}\left(\frac{F_{yx_{i,j,k}}}{4\Delta x\Delta y}\right)$$

$$\left(\frac{\partial F_{yy}}{\partial y}\frac{\partial P}{\partial y}+F_{yy}\frac{\partial^2 P}{\partial y^2}\right)=\left(\frac{F_{yy_{i,j+1,k}}-F_{yy_{i,j,k}}}{\Delta y}\cdot\frac{P_{i,j+1,k}-P_{i,j,k}}{\Delta y}\right)+\left(F_{yy_{i,j,k}}\cdot\frac{P_{i,j+1,k}-2P_{i,j,k}+P_{i,j-1,k}}{\Delta y^2}\right)$$
$$=P_{i,j-1,k}\left(\frac{F_{yy_{i,j,k}}}{\Delta y^2}\right)+P_{i,j,k}\left(-\frac{F_{yy_{i,j,k}}+F_{yy_{i,j+1,k}}}{\Delta y^2}\right)+P_{i,j+1,k}\left(\frac{F_{yy_{i,j+1,k}}}{\Delta y^2}\right) \quad \text{(E.30)}$$

$$\left(\frac{\partial F_{yz}}{\partial y}\frac{\partial P}{\partial z}+F_{yz}\frac{\partial^2 P}{\partial y\partial z}\right)=\left(\frac{F_{yz_{i,j+1,k}}-F_{yz_{i,j,k}}}{\Delta y}\cdot\frac{P_{i,j,k+1}-P_{i,j,k}}{\Delta z}\right)+\left(F_{yz_{i,j,k}}\cdot\frac{P_{i,j+1,k+1}+P_{i,j-1,k-1}-P_{i,j-1,k+1}-P_{i,j+1,k-1}}{4\Delta y\Delta z}\right)$$
$$=P_{i,j-1,k-1}\left(\frac{F_{yz_{i,j,k}}}{4\Delta y\Delta z}\right)+P_{i,j-1,k+1}\left(-\frac{F_{yz_{i,j,k}}}{4\Delta y\Delta z}\right)+P_{i,j,k}\left(-\frac{F_{yz_{i,j+1,k}}-F_{yz_{i,j,k}}}{\Delta y\Delta z}\right)+P_{i,j,k+1}\left(\frac{F_{yz_{i,j+1,k}}-F_{yz_{i,j,k}}}{\Delta y\Delta z}\right) \quad \text{(E.31)}$$
$$+P_{i,j+1,k-1}\left(-\frac{F_{yz_{i,j,k}}}{4\Delta y\Delta z}\right)+P_{i,j+1,k+1}\left(\frac{F_{yz_{i,j,k}}}{4\Delta y\Delta z}\right)$$

$$\left(\frac{\partial F_{zx}}{\partial z}\frac{\partial P}{\partial x}+F_{zx}\frac{\partial^2 P}{\partial z\partial x}\right)=\left(\frac{F_{zxi,j,k+1}-F_{zxi,j,k}}{\Delta z}\cdot\frac{P_{i+1,j,k}-P_{i,j,k}}{\Delta x}\right)+\left(F_{zxi,j,k}\cdot\frac{P_{i+1,j,k+1}+P_{i-1,j,k-1}-P_{i-1,j,k+1}-P_{i+1,j,k-1}}{4\Delta x\Delta z}\right)$$
$$=P_{i-1,j,k-1}\left(\frac{F_{zxi,j,k}}{4\Delta x\Delta z}\right)+P_{i-1,j,k+1}\left(-\frac{F_{zxi,j,k}}{4\Delta x\Delta z}\right)+P_{i,j,k}\left(-\frac{F_{zxi,j,k+1}-F_{zxi,j,k}}{\Delta x\Delta z}\right)+P_{i+1,j,k-1}\left(-\frac{F_{zxi,j,k}}{4\Delta x\Delta z}\right) \quad \text{(E.32)}$$
$$+P_{i+1,j,k}\left(\frac{F_{zxi,j,k+1}-F_{zxi,j,k}}{\Delta x\Delta z}\right)+P_{i+1,j,k+1}\left(\frac{F_{zxi,j,k}}{4\Delta x\Delta z}\right)$$

$$\left(\frac{\partial F_{zy}}{\partial z}\frac{\partial P}{\partial y}+F_{zy}\frac{\partial^2 P}{\partial z\partial y}\right)=\left(\frac{F_{zy_{i,j,k+1}}-F_{zy_{i,j,k}}}{\Delta z}\cdot\frac{P_{i,j+1,k}-P_{i,j,k}}{\Delta y}\right)+\left(F_{zy_{i,j,k}}\cdot\frac{P_{i,j+1,k+1}+P_{i,j-1,k-1}-P_{i,j-1,k+1}-P_{i,j+1,k-1}}{4\Delta y\Delta z}\right)$$
$$=P_{i,j-1,k-1}\left(\frac{F_{zy_{i,j,k}}}{4\Delta y\Delta z}\right)+P_{i,j-1,k+1}\left(-\frac{F_{zy_{i,j,k}}}{4\Delta y\Delta z}\right)+P_{i,j,k}\left(-\frac{F_{zy_{i,j,k+1}}-F_{zy_{i,j,k}}}{\Delta y\Delta z}\right)+P_{i,j+1,k-1}\left(-\frac{F_{zy_{i,j,k}}}{4\Delta y\Delta z}\right) \quad \text{(E.33)}$$
$$+P_{i,j+1,k}\left(\frac{F_{zy_{i,j,k+1}}-F_{zy_{i,j,k}}}{\Delta y\Delta z}\right)+P_{i,j+1,k+1}\left(\frac{F_{zy_{i,j,k}}}{4\Delta y\Delta z}\right)$$

$$\left(\frac{\partial F_{zz}}{\partial z}\frac{\partial P}{\partial z}+F_{zz}\frac{\partial^2 P}{\partial z^2}\right)=\left(\frac{F_{zzi,j,k+1}-F_{zzi,j,k}}{\Delta z}\cdot\frac{P_{i,j,k+1}-P_{i,j,k}}{\Delta z}\right)+\left(F_{zzi,j,k}\cdot\frac{P_{i,j,k+1}-2P_{i,j,k}+P_{i,j,k-1}}{\Delta z^2}\right)$$
$$=P_{i,j,k-1}\left(\frac{F_{zzi,j,k}}{\Delta z^2}\right)+P_{i,j,k}\left(-\frac{F_{zzi,j,k}+F_{zzi,j,k+1}}{\Delta z^2}\right)+P_{i,j,k+1}\left(\frac{F_{zzi,j,k+1}}{\Delta z^2}\right) \quad \text{(E.34)}$$

Substituting Eqns. (E.26)-(E.34) into (E.25) results in the governing equation expressed in terms of pressure,

$$
\begin{aligned}
&P_{i,j-1,k-1}\left(\frac{F_{yz\,i,j.k}+F_{zy\,i,j,k}}{4\Delta y\Delta z}\right)+P_{i-1,j,k-1}\left(\frac{F_{xz\,i,j,k}+F_{zx\,i,j,k}}{4\Delta x\Delta z}\right)+P_{i,j,k-1}\left(\frac{F_{zz\,i,j,k}}{\Delta z^2}\right)\\
&+P_{i+1,j,k-1}\left(-\frac{F_{xz\,i,j,k}+F_{zx\,i,j,k}}{4\Delta x\Delta z}\right)+P_{i,j+1,k-1}\left(-\frac{F_{yz\,i,j.k}+F_{zy\,i,j,k}}{4\Delta y\Delta z}\right)\\
&+P_{i-1,j-1,k}\left(\frac{F_{xy\,i,j,k}+F_{yx\,i,j,k}}{4\Delta x\Delta y}\right)+P_{i,j-1,k}\left(\frac{F_{yy\,i,j,k}}{\Delta y^2}\right)+P_{i+1,j-1,k}\left(-\frac{F_{xy\,i,j,k}+F_{yx\,i,j,k}}{4\Delta x\Delta y}\right)\\
&+P_{i-1,j,k}\left(\frac{F_{xx\,i,j,k}}{\Delta x^2}\right)\\
&+P_{i,j,k}\left(\begin{array}{l}
-\dfrac{F_{xx\,i,j,k}+F_{xx\,i+1,j,k}}{\Delta x^2}-\dfrac{F_{yy\,i,j,k}+F_{yy\,i,j+1,k}}{\Delta y^2}-\dfrac{F_{zz\,i,j,k}+F_{zz\,i,j,k+1}}{\Delta z^2}\\
-\dfrac{F_{xy\,i+1,j,k}+F_{yx\,i,j+1,k}-F_{xy\,i,j,k}-F_{yx\,i,j,k}}{\Delta x\Delta y}-\dfrac{F_{xz\,i+1,j,k}+F_{zx\,i,j,k+1}-F_{xz\,i,j,k}-F_{zx\,i,j,k}}{\Delta x\Delta z}\\
-\dfrac{F_{yz\,i,j+1,k}+F_{zy\,i,j,k+1}-F_{yz\,i,j,k}-F_{zy\,i,j,k}}{\Delta y\Delta z}
\end{array}\right)\\
&+P_{i+1,j,k}\left(\frac{F_{xx\,i+1,j,k}}{\Delta x^2}+\frac{F_{yx\,i,j+1,k}-F_{yx\,i,j,k}}{\Delta x\Delta y}+\frac{F_{zx\,i,j,k+1}-F_{zx\,i,j,k}}{\Delta x\Delta z}\right)\\
&+P_{i-1,j+1,k}\left(-\frac{F_{xy\,i,j,k}+F_{yx\,i,j,k}}{4\Delta x\Delta y}\right)+P_{i,j+1,k}\left(\frac{F_{yy\,i,j+1,k}}{\Delta y^2}+\frac{F_{xy\,i+1,j,k}-F_{xy\,i,j,k}}{\Delta x\Delta y}+\frac{F_{zy\,i,j,k+1}-F_{zy\,i,j,k}}{\Delta y\Delta z}\right)\\
&+P_{i+1,j+1,k}\left(\frac{F_{xy\,i,j,k}+F_{yx\,i,j,k}}{4\Delta x\Delta y}\right)\\
&P_{i,j-1,k+1}\left(-\frac{F_{yz\,i,j.k}+F_{zy\,i,j,k}}{4\Delta y\Delta z}\right)+P_{i-1,j,k+1}\left(-\frac{F_{xz\,i,j,k}+F_{zx\,i,j,k}}{4\Delta x\Delta z}\right)\\
&+P_{i,j,k+1}\left(\frac{F_{zz\,i,j,k+1}}{\Delta z^2}+\frac{F_{xz\,i+1,j,k}-F_{xz\,i,j,k}}{\Delta x\Delta z}+\frac{F_{yz\,i,j+1,k}-F_{yz\,i,j,k}}{\Delta y\Delta z}\right)\\
&+P_{i+1,j,k+1}\left(\frac{F_{xz\,i,j,k}+F_{zx\,i,j,k}}{4\Delta x\Delta z}\right)+P_{i,j+1,k+1}\left(\frac{F_{yz\,i,j.k}+F_{zy\,i,j,k}}{4\Delta y\Delta z}\right)=0
\end{aligned}
\tag{E.35}
$$

where $F_{ab}=K_{ab}/\mu$.

APPENDIX F 1.5D STREAM SURFACE FINITE DIFFERENCE SOLVER

F.1 GOVERNING EQUATIONS AND FD DISCRETISATION

1.5D Stream Surface is essentially 1D flow in 2D space. Darcy's law for 1D flow,

$$u_x = -\frac{K}{\mu}\frac{\partial P}{\partial x} \tag{F.1}$$

As the height of the Stream Surfaces will vary, the mass conservation equation to be solved is,

$$\frac{\partial(u_x h)}{\partial x} = 0 \tag{F.2}$$

Combining (F.1) and (F.2) gives the governing equation of the pressure,

$$\frac{\partial}{\partial x}\left(\frac{K}{\mu}h\frac{\partial P}{\partial x}\right) = 0 \tag{F.3}$$

Let $G = \frac{K}{\mu}h$ and expanding the 1D governing equation (F.3),

$$\left(\frac{\partial G}{\partial x}\cdot\frac{\partial P}{\partial x}\right) + \left(G\cdot\frac{\partial^2 P}{\partial x^2}\right) = 0 \tag{F.4}$$

The standard finite difference requires a uniform grid for calculation. In order to apply finite differences to a non-uniform grid, the grid must be transformed to a uniform computational grid. For a non-uniform, curvilinear grid with one varying dimension x (physical domain), it needs to be related to a uniform, linear grid, represented by the variable ξ (computational domain). The governing equation must be transformed from x to ξ,

$$\frac{\partial}{\partial x} = \left(\frac{\partial}{\partial \xi}\right)\left(\frac{\partial \xi}{\partial x}\right) \tag{F.5}$$

$$\frac{\partial^2}{\partial x^2} = \left(\frac{\partial}{\partial \xi}\right)\left(\frac{\partial^2 \xi}{\partial x^2}\right) + \left(\frac{\partial^2}{\partial \xi^2}\right)\left(\frac{\partial \xi}{\partial x}\right)^2 \tag{F.6}$$

Applying (F.5) and (F.6) to the terms in (F.4),

$$\frac{\partial G}{\partial x} = \frac{\partial G}{\partial \xi} \cdot \frac{\partial \xi}{\partial x} \tag{F.7}$$

$$\frac{\partial P}{\partial x} = \frac{\partial P}{\partial \xi} \cdot \frac{\partial \xi}{\partial x} \tag{F.8}$$

$$\frac{\partial^2 P}{\partial x_2} = \frac{\partial P}{\partial \xi} \cdot \frac{\partial^2 \xi}{\partial x^2} + \frac{\partial^2 P}{\partial \xi^2} \cdot \left(\frac{\partial \xi}{\partial x} \right)^2 \tag{F.9}$$

where $\frac{\partial^2 \xi}{\partial x^2} = -\left(\frac{\partial x}{\partial \xi} \right)^{-3} \left(\frac{\partial^2 x}{\partial \xi^2} \right)$. Substituting (F.7)-(F.9) into (F.4) gives the governing equation with grid transformation,

$$\left(\frac{\partial G}{\partial \xi} \cdot \frac{\partial P}{\partial \xi} \right) \cdot \left(\frac{\partial x}{\partial \xi} \right)^{-2} + G \left(-\left(\frac{\partial P}{\partial \xi} \right) \cdot \left(\frac{\partial^2 x}{\partial \xi^2} \right) \cdot \left(\frac{\partial x}{\partial \xi} \right)^{-3} + \left(\frac{\partial^2 P}{\partial \xi^2} \right) \cdot \left(\frac{\partial x}{\partial \xi} \right)^{-2} \right) = 0 \tag{F.10}$$

Expressing the individual derivatives terms in (F.10) using first order forward finite difference (F.3) and second order central difference (F.5),

$$\begin{aligned} &\left(\frac{G_{i+1} - G_i}{\Delta \xi} \right) \cdot \left(\frac{P_{i+1} - P_i}{\Delta \xi} \right) \cdot \left(\frac{x_{i+1} - x_i}{\Delta \xi} \right)^{-2} \\ &+ G_i \left(-\left(\frac{P_{i+1} - P_i}{\Delta \xi} \right) \cdot \left(\frac{x_{i+1} - 2x_i + x_{i-1}}{\Delta \xi^2} \right) \cdot \left(\frac{x_{i+1} - x_i}{\Delta \xi} \right)^{-3} + \left(\frac{P_{i+1} - 2P_i + P_{i-1}}{\Delta \xi^2} \right) \cdot \left(\frac{x_{i+1} - x_i}{\Delta \xi} \right)^{-2} \right) = 0 \end{aligned} \tag{F.11}$$

Rearranging the terms gives the governing equation for a non-uniform 1D grid expressed in terms of pressure,

$$\begin{aligned} &P_{i-1} \left(\frac{G_i}{(x_{i+1} - x_i)^2} \right) + P_i \left(-\frac{G_{i+1} + G_i}{(x_{i+1} - x_i)^2} + \frac{G_i (x_{i+1} - 2x_i + x_{i-1})}{(x_{i+1} - x_i)^3} \right) \\ &+ P_{i+1} \left(\frac{G_{i+1}}{(x_{i+1} - x_i)^2} - \frac{G_i (x_{i+1} - 2x_i + x_{i-1})}{(x_{i+1} - x_i)^3} \right) = 0 \end{aligned} \tag{F.12}$$

where $G_i = \frac{K_i h_i}{\mu}$.

F.2 SPECIAL CONSIDERATION FOR STREAM SURFACE

F.2.1 Finite difference revisited

Consider again the second order second difference with respect to x (Eqn. F.5) which can be represented as,

$$\left.\frac{\partial^2 f}{\partial x^2}\right|_i = \frac{\partial}{\partial x}\left(\left.\frac{\partial f}{\partial x}\right|_i\right) = \left.\frac{\partial A}{\partial x}\right|_i \tag{F.13}$$

Applying forward difference,

$$\left.\frac{\partial^2 f}{\partial x^2}\right|_i = \left.\frac{\partial A}{\partial x}\right|_i = \frac{A_{i+1} - A_i}{\Delta x} \tag{F.14}$$

where $A_i = \left.\frac{\partial f}{\partial x}\right|_i$ and $A_{i+1} = \left.\frac{\partial f}{\partial x}\right|_{i+1}$

Applying rearward difference,

$$\left.\frac{\partial^2 f}{\partial x^2}\right|_i = \frac{\frac{f_{i+1} - f_i}{\Delta x} - \frac{f_i - f_{i-1}}{\Delta x}}{\Delta x}$$

$$\left.\frac{\partial^2 f}{\partial x^2}\right|_i = \frac{f_{i+1} - 2f_i + f_{i-1}}{\Delta x^2} \tag{F.15}$$

Eqn. (F.15) is the same as Eqn. (E.6), demonstrating a different approach to derive the second order second difference term.

F.2.2 Branching of Stream Surfaces

Consider the flow through three 1D Stream Surfaces,

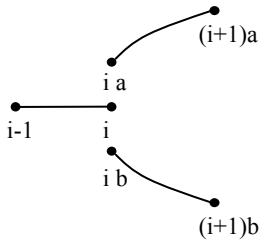

If the resin is flowing from left to right, the flow is dividing into two paths and the Stream Surfaces are connected by virtue of the three coinciding i-nodes having the same pressure. The problem can be re-represented as,

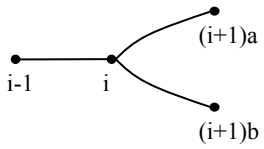

The standard finite difference terms are not sufficient to describe the dividing flow. Instead, the governing equation at node i needs to be derived based on the method described in Section (F.2.1).

First applying forward difference to the mass conservation equation (F.5) at node i,

$$\frac{\partial(uh)}{\partial x} = \frac{(uh)_{(i+1)a} + (uh)_{(i+1)b} - (uh)_i}{\Delta x} = 0 \tag{F.16}$$

Applying rearward difference to evaluate each *u*,

$$u_{(i+1)a} = -\left(\frac{K}{\mu}\frac{\partial P}{\partial x}\right)_{(i+1)a} = -\left(\frac{K}{\mu}\right)_{(i+1)a}\frac{P_{(i+1)a} - P_i}{\Delta x} \tag{F.17}$$

$$u_{(i+1)b} = -\left(\frac{K}{\mu}\frac{\partial P}{\partial x}\right)_{(i+1)b} = -\left(\frac{K}{\mu}\right)_{(i+1)b}\frac{P_{(i+1)b} - P_i}{\Delta x} \tag{F.18}$$

$$u_i = -\left(\frac{K}{\mu}\frac{\partial P}{\partial x}\right)_i = -\left(\frac{K}{\mu}\right)_i\frac{P_i - P_{i-1}}{\Delta x} \tag{F.19}$$

Substituting (F.17)-(F.19) into (F.16) results in the governing equation for the branching node i expressed in terms of pressure,

$$P_{i-1}\left(\frac{G_i}{\Delta x^2}\right)-P_i\left(\frac{G_i+G_{(i+1)a}+G_{(i+1)b}}{\Delta x^2}\right)+P_{(i+1)a}\left(\frac{G_{(i+1)a}}{\Delta x^2}\right)+P_{(i+1)b}\left(\frac{G_{(i+1)b}}{\Delta x^2}\right)=0 \qquad \text{(F.20)}$$

where $G_i=\dfrac{K_i h_i}{\mu}$

Generally, for n branches,

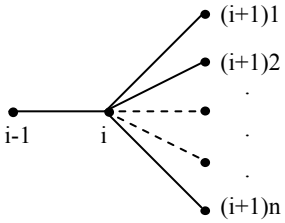

$$P_{i-1}\left(\frac{G_i}{\Delta x^2}\right)-P_i\left(\frac{G_i+G_{(i+1)1}+\ldots+G_{(i+1)n}}{\Delta x^2}\right)+P_{(i+1)1}\left(\frac{G_{(i+1)1}}{\Delta x^2}\right)+\ldots+P_{(i+1)n}\left(\frac{G_{(i+1)n}}{\Delta x^2}\right)=0 \qquad \text{(F.21)}$$

F.2.3 Merging of Stream Surfaces

Now, consider the case where the flow is merging,

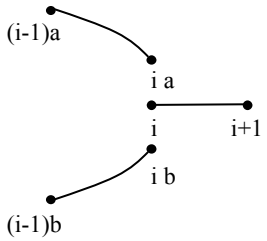

which can be re-represented as,

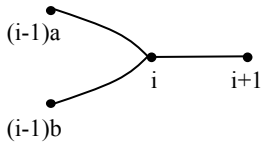

Applying forward difference to the mass conservation equation (F.5) at node i,

$$\frac{\partial(uh\phi)}{\partial x} = \frac{(uh\phi)_{i+1} - (uh\phi)_i}{\Delta x} = 0 \tag{F.22}$$

Applying rearward difference to evaluate each *u*,

$$u_{i+1} = -\left(\frac{K}{\mu}\frac{\partial P}{\partial x}\right)_{i+1} = -\left(\frac{K}{\mu}\right)_{i+1}\frac{P_{i+1} - P_i}{\Delta x} \tag{F.23}$$

$$u_i = -\left(\frac{K}{\mu}\frac{\partial P}{\partial x}\right)_i = -\left(\frac{K}{\mu}\right)_i\left(\frac{P_i - P_{(i-1)a}}{\Delta x} + \frac{P_i - P_{(i-1)b}}{\Delta x}\right) \tag{F.24}$$

Substituting (F.23) and (F.24) into (F.22) results in the governing equation for the merging node i expressed in terms of pressure,

$$P_{(i-1)a}\left(\frac{G_i}{\Delta x^2}\right) + P_{(i-1)b}\left(\frac{G_i}{\Delta x^2}\right) - P_i\left(\frac{2G_i + G_{i+1}}{\Delta x^2}\right) + P_{i+1}\left(\frac{G_{i+1}}{\Delta x^2}\right) = 0 \tag{F.25}$$

where $G_i = \dfrac{K_i h_i}{\mu}$

Generally, for n branches,

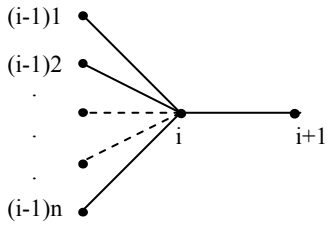

$$P_{(i-1)1}\left(\frac{G_i}{\Delta x^2}\right) + \ldots + P_{(i-1)n}\left(\frac{G_i}{\Delta x^2}\right) + P_i\left(\frac{-nG_i - G_{i+1}}{\Delta x^2}\right) + P_{i+1}\left(\frac{G_{i+1}}{\Delta x^2}\right) = 0 \tag{F.26}$$

F.2.4 General Stream Surface node

For a node with n merging paths and branching into m paths,

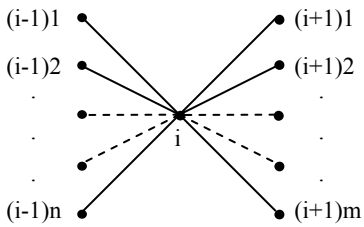

the generalised governing equation can be shown to be,

$$P_{(i-1)1}\left(\frac{G_i}{\Delta x^2}\right)+\ldots+P_{(i-1)n}\left(\frac{G_i}{\Delta x^2}\right)+P_i\left(\frac{-nG_i-G_{(i+1)1}-\ldots-G_{(i+1)m}}{\Delta x^2}\right)$$
$$+P_{(i+1)1}\left(\frac{G_{(i+1)1}}{\Delta x^2}\right)+\ldots+P_{(i+1)m}\left(\frac{G_{(i+1)m}}{\Delta x^2}\right)=0 \qquad \text{(F.27)}$$

where $G_i=\dfrac{K_i h_i}{\mu}$

F.3 1.5D STREAM SURFACE FD SOLVER INPUT AND OUTPUT

F.3.1 Input file format

```
Number of nodes = #
Index X     Y     h     material
(Lists the coordinates, height and material type of the nodes.
Material type corresponds to the material numbers below.)
#     #     #     #     #
Connectivity
(Lists the connections between the nodes.
The node numbers correspond to the index above.)
node(i-1)   nodei node(i+1)
#           #     #
Number of materials = #
Viscosity = #
Index FP    Permeability      Porosity
(Lists the properties of the materials of the nodes. FP indicates
either it is a free region (1) or porous material (2))
#     #     #     #
Number of inlets = #
Inlet Node  Inlet Pressure
(Lists the inlets node numbers and pressure value)
#           #
Number of outlets = #
Outlet Node Outlet Pressure
(Lists the outlets node numbers and pressure value)
#           #
Number of multi-paths nodes = #
n     m     dx    nodei node(i-1)   node(i+1)
(Lists the nodes at the branching or merging of the Stream Surfaces.
n is the number of nodes before the branching/merging node and m is
the number of nodes after.)
#     #     #     #     #           #
```

Input file example:

```
Number of nodes = 3190
Index X                 Y                 h                 material
1     0.00000000000     0.00055901700     0.00111803400     1
2     0.00000491669     0.00055901700     0.00111803400     1
...
3189  0.00558525331     0.00055901700     0.00111803400     1
3190  0.00559017000     0.00055901700     0.00111803400     1
Connectivity
node(i-1)   nodei node(i+1)
0     1     2
1     2     3
...
3188  3189  3190
3189  3190  0
Number of materials = 2
Viscosity = 0.308000
Index FP    Permeability      Porosity
1     1     1                 1
2     2     1.30264E-12       0.540135
Number of inlets = 1
Inlet Node        Inlet Pressure
1                 20
```

```
Number of outlets = 1
Outlet Node       Outlet Pressure
3190              0
Number of multi-paths nodes = 2
n     m     dx          nodei       node(i-1)                node(i+1)
1     3     0.000005    62          61    63    1095         2097
3     1     0.000005    3129        1094  2096  3128         3130
```

F.3.2 Output file format

```
Execution time =  # s   (Computation time)
Viscosity =       # Pas (Fluid viscosity)
Overall dP =      # Pa  (Applied pressure difference)
Length =          # m   (Flow length)
Average inlet velocity =      # m/s (Calculated average   )
Inlet permeability =          # m^2 (velocities and       )
Average outlet velocity =     # m/s (permeabilities at the)
Outlet permeability =         # m^2 (inlets and outlets   )
Node  X(m)              Y(m)              h(m)
      dxfwd             dxrwd             f or p      K(m^2)
      Pressure    Velocity
(Lists the coordinates and height of the nodes, distances to nodes
before and after, free or porous region nodes, the individual
permeability, pressure and velocity of flow.)
#     #     #     #     #     #     #     #     #     #
```

Output file example

```
Execution t =     2.000000          s
Viscosity =       3.080000e-01      Pas
Overall dP =      -2.000000e+01     Pa
Length =          5.590170e-03      m
Average inlet velocity =      1.210048e-06      m/s
Inlet permeability =          -1.041714e-10     m^2
Average outlet velocity =     1.155450e-06      m/s
Outlet permeability =         -9.947107e-11     m^2
Node  X(m)              Y(m)              h(m)
      dxfwd             dxrwd             f or p      K(m^2)
      Pressure    Velocity
1     0.000000e+00      5.590170e-04      1.118034e-03
      4.916690e-06      0.000000e+00      free        1.041667e-07
      2.000000e+01      1.210048e-06
2     4.916690e-06      5.590170e-04      1.118034e-03
      4.916700e-06      4.916690e-06      free        1.041667e-07
      1.999998e+01      1.210048e-06
...
3189  5.585253e-03      5.590170e-04      1.118034e-03
      4.916690e-06      4.916700e-06      free        1.041667e-07
      1.679755e-05      1.155450e-06
3190  5.590170e-03      5.590170e-04      1.118034e-03
      0.000000e+00      4.916690e-06      free        1.041667e-07
      0.000000e+00      1.155450e-06
```

F.4 1.5D STREAM SURFACE FINITE DIFFERENCE SOLVER CODE IN C – HEADER

```
/* 1.5D Stream Surface Finite Difference Solver                    */
/* Program to calculate pressure distribution using finite         */
/* difference for 1.5D Stream Surface meshes.                      */
/*                                                                 */
/* Chee Chiew Wong February 2004                                   */

#include <math.h>
#include <stddef.h>
#include <stdio.h>
#include <stdlib.h>
#include <time.h>

#define MAXNODE 10000    // maximum number of nodes permitted
#define NMAX 40000       // maximum array for sa and ija for storing
                         // of sparse matrix A
#define MAXMAT 10        // maximum type of materials
#define MAXINOUT 100     // maximum number of inlets and outlets
#define MAXBRMR 10       // maximum branching and merging nodes
#define MAXSTR 1000      // string size
#define THRESHOLD 1e-15 // threshold for evaluating non-zero
                         // components in 'sprsin' function
#define ITOL 1           // type of iterative option
#define TOL 1e-16        // iterative tolerance
#define ITMAX 10000      // maximum number of iteration
#define NR_END 1         // Numerical Recipes in C constant
#define FREE_ARG char*   // Numerical Recipes in C constant
#define EPS 1.0e-14      // Numerical Recipes in C constant

/* Functions declaration */
void    ReadInput(void);            // Reads and stores input data
void    MatrixBuildAndCalc(void);
   // Matrix build function and solves [a][p]=[b] for pressure.
   // Calculates effective permeability

// The following functions were adapted from Numerical Recipes in C
double  **dmatrix(long nrl, long nrh, long ncl, long nch);
   // Allocates a double matrix with subscript range
   // m[nrl..nrh][ncl..nch]
int     **imatrix(long nrl, long nrh, long ncl, long nch);
   // Allocates a int matrix with subscript range
   // m[nrl..nrh][ncl..nch]
double  *dvector(long nl, long nh);
   // Allocates a double vector with subscript range v[nl..nh]
unsigned long  *lvector(long nl, long nh);
   // Allocates an unsigned long vector with subscript range
   // v[nl..nh]
void    free_dmatrix(double **m, long nrl, long nrh, long ncl, long
nch);
   // Frees a double matrix allocated by dmatrix()
void    free_dvector(double *v, long nl, long nh);
   // Frees a double vector allocated with dvector()
void    sprsin(double **a, unsigned long n, float thresh, unsigned
long    nmax, double *sa, unsigned long *ija);
   // Stores a double matrix a in sparse index storage system
void    linbcg(double *sa, unsigned long *ija, unsigned long n,
double  *b, double *x, int itol, double tol, int itmax, int *iter,
double  *err);
```

```
   // Solves the system of equations [a][p]=[b] using the conjugate
   // gradient method where [a] is stored in a sparse index storage
   // system using sprsin
void    nrerror(char error_text[]);
   // Numerical Recipes in C standard error handler

// The following were used to check through arrays
int rangebm (unsigned long nrl, unsigned long nrh, unsigned long ncl,
        unsigned long *nch1, unsigned long *nch2, int **a, int b);
int rangebm2 (unsigned long nrl, unsigned long nrh, unsigned long
        ncl, unsigned long *nch, int **a, unsigned long b);
int rangebm3 (unsigned long nrl, unsigned long nrh, unsigned long
        *ncl, unsigned long *nch, int **a, unsigned long b);
int rangebm4 (unsigned long nrl, unsigned long nrh, int **a, int  b);

char    in_name[MAXSTR],            // Input file name
        out_name[MAXSTR];           // Output file name

double  *X, *Y,                     // Node coordinates
        *h, hio=0,                  // Height
        *perm, perm_i,              // Permeability
        *poro,                      // Porosity
        visc,                       // Fluid viscosity
        *pres,                      // Pressure
        *inpres, *outpres,          // Inlet and outlet pressure
        dP,                         // Pressure difference
        *dx, *dxfwd, *dxrwd,        // Distance between nodes
        *F,                         // Matrix coefficient term
        *velo,                      // Velocity
        veloin, veloout, vh=0,      // Calculated velocity
        kin, kout;                  // Calculated permeability

unsigned long   totnode,                    // Total nodes
                totmat,                     // Total materials
                totnodein, totnodeout,      // Total input and
                                            // outlet nodes
                totnodebm,                  // Total branching and
                                            // merging nodes
                *mat, matredun,             // Material type
                *fp,                        // Node type
                *nodein, *nodeout,          // Inlet and outlet node
                *nodea, *nodeb, noderedun,  // Nodes connectivity
                *npath, *mpath;             // Branching and merging
                                            // paths

int     **nodebm,                   // Branching and merging nodes
        cond;                       // Condition

time_t  t1, t2;                     // time counters

main()
{   int i,j;                        // counters

    /************************/
    /* INPUT & OUTPUT FILES */
    /************************/
    FILE *fpout, *tecout;           // file pointers
    printf ("Enter name of input file with extension > ");
    scanf ("%s", in_name);          // Get name of input file
    printf ("\nEnter name of output file with extension\n");
    printf ("WARNING: this will overwrite previous copies > ");
```

```
scanf ("%s", out_name);          // Get name of output file
fpout = fopen(out_name, "w");
tecout = fopen("tecout.tec", "w");

/*****************************************/
/* Reads and stores data from input file */
/*****************************************/
ReadInput();

/*************************************************************/
/* Builds matrix and stores in sparse index storage format  */
/* using sprsin(). Calls linbcg() to solve for pressure     */
/* iteratively using conjugate gradient method.             */
/* Calculates effective permeability of domain.             */
/*************************************************************/
MatrixBuildAndCalc();

/*****************/
/*    Output     */
/*****************/

/* Tecplot Output */
int path=0, tecnode, tecelem;
for (i=1; i<=totnodebm; i++)    path += mpath[i];
tecnode = (totnode - totnodebm) * 2;
tecelem = totnode - path - totnodebm - totnodeout;
fprintf (tecout, "Title = \"%s\"\n", in_name);
fprintf (tecout, "Variables = \"x\", \"y\", \"z\", \"p\",
          \"velocity\"\n");
fprintf (tecout, "Zone N = %d, E = %d, F = FEPOINT,
          ET = QUADRILATERAL\n", tecnode, tecelem);
for (i=1; i<=totnode; i++){
    if((cond=rangebm4(1,totnodebm,nodebm,i)))
        printf("cond tec %lu\n", i);
    else if((cond=rangebm4(1,totnodebm,nodebm,nodea[i]))) {
        fprintf (tecout, "%le\t%le\t0\t%le\t%le\n",
                  X[i],Y[i],pres[i],velo[i]);
        fprintf (tecout, "%le\t%le\t1e-5\t%le\t%le\n",
                  X[i],Y[i],pres[i],velo[i]);
    } else {
        fprintf (tecout, "%le\t%le\t0\t%le\t%le\n",
                  X[i],Y[i],pres[i],velo[i]);
        fprintf (tecout, "%le\t%le\t1e-5\t%le\t%le\n",
                  X[i],Y[i],pres[i],velo[i]);
    }
}
int count=0, z;
for (i=1; i<=totnode; i++) {
    if ((cond=rangebm4(1,totnodebm,nodebm,i))) {
        count++; printf("%lu cond tec conc %lu\n", i,count);
    } else if((cond=rangebm4(1,totnodebm,nodebm,nodeb[i])))
        printf("%lu cond tec conc %lu\n", i,count);
    else if (nodeb[i]==0)
        printf("%lu cond tec conc %lu\n", i,count);
    else {
        j = i-count; z = nodeb[i]-count;
        fprintf (tecout, "%d\t%d\t%d\t%d\n",(j-1)*2+1,
                  (z-1)*2+1,(z-1)*2+2,(j-1)*2+2);
    }
}
```

```
    /* Results Output */
    fprintf (fpout, "Execution t = \t %f\t s\n", difftime(t2, t1));
    fprintf (fpout, "viscosity =\t%le\tPas\n", visc);
    fprintf (fpout, "overall dP =\t%le\tPa\n",
              (pres[nodeout[1]]-pres[nodein[1]]));
    fprintf (fpout, "length  =\t%le\tm\n",
              (X[nodeout[1]]-X[nodein[1]]));
    fprintf (fpout, "Average inlet velocity =\t%le\tm/s\n", veloin);
    fprintf (fpout, "Inlet permeability =\t%le\tm^2\n", kin);
    fprintf (fpout, "Average outlet velocity =\t%le\tm/s\n",
              veloout);
    fprintf (fpout, "Outlet permeability =\t%le\tm^2\n", kout);
    fprintf (fpout, "Node\tX(m)\tY(m)\th(m)\tdxfwd\tdxrwd
              \tf or p\tK(m^2)\tPressure\tVelocity\n");
    for (i=1; i<=totnode; i++) {
        fprintf (fpout, "%d\t%le\t%le\t%le\t%le\t%le\t",
                  i,X[i],Y[i],h[i],dxfwd[i],dxrwd[i]);
        if (fp[mat[i]]==1)
            fprintf (fpout, "free\t");
        else
            fprintf (fpout, "porous\t");
        perm_i = (fp[mat[i]] == 1) ? (h[i] * h[i])/12 : perm[mat[i]];
        fprintf (fpout, "%le\t%le\t%le\n", perm_i, pres[i], velo[i]);
    }

    printf("Execution time was %f s\n", difftime(t2, t1));

    /* Closes output file */
    fclose (fpout);

    free_dvector(X, 1, MAXNODE);
    free_dvector(Y, 1, MAXNODE);
    free_dvector(h, 1, MAXNODE);
    free_dvector(F, 1, MAXNODE);

    /********************/
    /* END OF MAIN BODY */
    /********************/
    return 0;
}
```

[589 lines of code follow]

APPENDIX G 2D GRID AVERAGE FINITE DIFFERENCE SOLVER

G.1 2D GRID AVERAGE FD SOLVER INPUT AND OUTPUT

The 2D GA solver first reads in the batch file, which contains the list of TexGen generated grid files to be evaluated as well as the operating conditions. It then proceeds to evaluate the grid files in the list. The grid file is generated automatically using TexGen and contains information pertaining to the textile model, such as domain size, grid divisions and the properties at each grid point.

G.1.1 Input file format

Grid Average 2D batch file format:

```
Batch results output filename
#
Number of analysis
#
The following lines will be repeated for each input file:
Grid Average input filename (.grd file)
#
Output filename (without file extension)
#
Analysis flow direction (0=x-axis, 1=y-axis)
#
Number of types of tows
#
Number of tows
#
Types of tow in the following format - repeated for the total number
of types of tows:
Vf, number of tows with current type, tow numbers (cf. .grd file)
#     #     # (total tow numbers equals the preceding total)
The following numbers are for LIMS output:
Additional rows at beginning and end of analysis domain
Additional rows parallel to X & Y axes
#     #     #     #
```

Input batch file example:

```
45_cross_ms.xls
8
45_cross_x_010.grd
45_cross_x_010
0 1 2
0.5 2 1 2
0 0 0 0
...
45_cross_x_100.grd
45_cross_x_100
0 1 2
0.5 2 1 2
0 0 0 0
```

Grid Average .grd input file example (self explanatory):

```
** GRID SIZE: MinX, MinY, MinZ, MaxX, MaxY, MaxZ
-1.325,     -1.325,     -0.25,      1.325,      1.325,      0.75
** DIVISIONS: X, Y
53,   53
** GRID POINTS: NUMVOLUMES { VOLUME NUMBER, BOTTOM Z, TOP Z,
DIRECTION (X, Y, Z) }
5
0,    -0.25,      -0.248519,  0,    0,    0
1,    -0.248519,  0.248519,   0.707107,   0.707107,   0
0,    0.248519,   0.251481,   0,    0,    0
2,    0.251481,   0.748519,   0.707107,   -0.707107,  0
0,    0.748519,   0.75, 0,    0,    0
5
0,    -0.25,      -0.247824,  0,    0,    0
1,    -0.247824,  0.247824,   0.707107,   0.707107,   0
0,    0.247824,   0.252176,   0,    0,    0
2,    0.252176,   0.747824,   0.707107,   -0.707107,  0
0,    0.747824,   0.75, 0,    0,    0
...
5
0,    -0.25,      -0.248519,  0,    0,    0
1,    -0.248519,  0.248519,   0.707107,   0.707107,   0
0,    0.248519,   0.251481,   0,    0,    0
2,    0.251481,   0.748519,   0.707107,   -0.707107,  0
0,    0.748519,   0.75, 0,    0,    0
```

G.1.2 Output file example (self explanatory)

```
Cell dimensions: 0.002600 x 0.002600 x 0.001000
Grid size: 53 x 53
No. of nodes = 2809
Flow parallel to x-axis.
Tow Type 1:
Tow Vf = 0.600000
Tow K1 = 1.557208e-012, K2 = 1.968939e-013
Viscosity = 3.080000e-001 Pas
dP = 1.000000e+005 Pa

Cell Vf = 0.406342
Inlet K = 2.204383e-009 m^2
Outlet K = 2.204383e-009 m^2
Average inlet Ux = 2.752726e-001 m/s
Average outlet Ux = 2.752726e-001 m/s
Execution time = 2.000000 s
Also possible to output the coordinates of the nodes and the
corresponding permeability, pressure and velocity of flow.
```

G.2 2D GRID AVERAGE FD SOLVER CODE IN C – HEADER AND MAIN LISTING

```
/* Program to read Grid Average file from TexGen,  */
/* write 2D input and script files for LIMS,       */
/* or calculate pressure field for 2D GA using     */
/* finite differences. Then calculate the          */
/* effective permeability.                         */
/*                                                 */
/* Chee Chiew Wong                                 */
/* Last modified 24th June 2005                    */

#include <stdio.h>
#include <stdlib.h>
#include <string.h>
#include <math.h>
#include <time.h>

#define ITOL    1               // Type of iterative option
#define TOL     1e-18           // Iterative tolerance
#define ITMAX   100000          // Maximum number of iteration
#define NR_END  1               // Numerical Recipes in C constant
#define FREE_ARG char*          // Numerical Recipes in C constant
#define EPS     1.0e-14         // Numerical Recipes in C constant
#define PI 0.31415926535897932e+01

// Function prototypes
void    Body(void);             // Operation body called from main
void    ReadGRD(void);          // Processes TexGen .grd file
void    CreateLIMS(void);       // Write 2D LIMS .dmp file
void    CreateLIMStube(void);   // Write 2D LIMS .dmp file in
                                // cyclical format
void    WriteK(void);           // Dumps the calculated Ks for
                                // elements into a file
void    WriteK2(void);          // Same as WriteK with calculation
                                // of average K for row
void    WriteLB(void);          // Writes LIMS .lb script file
void    WriteLB2(void);

void    CalcP1(void);           // Calculates pressure distribution
void    CalcP2(void);           // for flow along x- and y-axes
                                // respectively using Pin and Pout -
                                // not periodic inlet and outlet

void    CalcP3(void);           // Calculates pressure distribution
void    CalcP4(void);           // for flow along x- and y-axes
                                // respectively using dP -
                                // periodic inlet and outlet

void    WriteTec(unsigned long *ija, double *p, double *Ux, double
*Uy);                           // Writes .tec Tecplot output file
                                // for post-processing
void    GebartKmodel(void);     // Calculates tow K based on
                                // Gebart's model
float   **CreateGrid(int iWidth, int iHeight);
        // Function to create space for 2D array
void    DeleteGrid(float **pCubeGrid, int iWidth, int iHeight);
        // Function to free 2D array space
```

```
// The following functions were adapted from Numerical Recipes in C
void    linbcg(double *sa, unsigned long *ija, unsigned long n,
               double  *b, double *x, int itol, double tol, int
               itmax, int *iter, double  *err);
    // solves the system of equations [a][p]=[b] using the conjugate
       gradient method where [a] is stored in a sparse index storage
       system
double  *dvector(long nl, long nh);
    // allocate a double vector with subscript range v[nl..nh]
void    free_dvector(double *v, long nl, long nh);
    // free a double vector allocated with dvector()
void    nrerror(char error_text[]);
    // Numerical Recipes in C standard error handler

char    InFileName[80],          // Input file name
        OutFileName[80],         // Output file name
        DMPFName[80],LBFName[80];   // .dmp and .lb output filenames
float   TowVf,                   // Tow fibre volume fraction
        TowK1, TowK2,            // Tow principal permeabilities
                                    (1=fibre direction, 2=transverse)
        *TowVfT, *TowK1T, *TowK2T,
        Viscosity,               // Resin viscosity
        InjFlowrate,             // Injection volumetric flow rate
        MinX, MinY, MinZ,
        MaxX, MaxY, MaxZ,        // Grid size
        GeomFact,                // Scale factor for geometry
        CellH,                   // Unit cell thickness
        CellXd, CellYd,          // Unit cell x & y dimensions
        CellAvgVf,               // Average cell Vf
        CellAvgK,                // Average permeability
        **CellKxx, **CellKxy,    // K tensor and Vf
        **CellKyy, **CellVf,     // for each grid element
        FR;                      // Fibre radius
double  Kcellfinal, Ucellfinal, errfinal; // K and U cell values
int     XDiv, YDiv,              // Number of elements in grid
        AddRows, AddRowsf,       // Additional rows of elements along
                                 // flow dirn
        Addxf, Addyf,            // Additional rows in front
        Addx,Addy,               // Additional rows in x & y dirns
        AddElemsX, AddElemsY,    // Additional elements specified in
                                 // grd file
        Iterfinal,
        FlowDirn,                // Flow direction (0=parallel to x,
                                 // 1=parallel to y)
        FArrayType,              // Fibre array type
                                 // (0=Quadratic, 1=Hexagonal)
        KType,                   // Tow permeability type
                                 // (0 = isotropic, 1 = vectorial)
        NTowType,                // No of types of tow
        *TowType,                // Tow type
        OutputType;              // Output type (0=LIMS, 1=P solver)
time_t  t1, t2;                  // time counters

int main()
{   /*******************************************************/
    /* Reads the batch file to obtain grid filename and ****/
    /* operating parameters, then calls body() to begin*****/
    /* evaluation. Repeats procedure for each input file. **/
    /*******************************************************/
    FILE    *infile, *outfile;  // Input file identifier
    char    BatchFileName[80],  // Input file name
```

```
            BatResultsFileName[80];
    int     NoofFile,
            NTotTow, NTow, dummy,
            count1, count2, count3;
    // Open batch file
    printf("Input batch filename: ");
    scanf("%s", BatchFileName);
    infile=fopen(BatchFileName, "r");
    if (infile==NULL) {
        printf("Error - file does not exist!\n");
        exit(1); // Abort if file does not exist
    }
    // Starts reading batch file
    fscanf(infile,"%s",&BatResultsFileName);
    fscanf(infile,"%d",&NoofFile);
    outfile=fopen(BatResultsFileName, "w");
    // Opens batch file output
    if (outfile==NULL) {
        printf("Error - file cannot be opened!\n");
        exit(1); // Abort if file cannot be opened
    }
    fprintf(outfile,"No.\tXDiv\tYDiv\tCell Vf\tCell K
            \tInlet U\tIterations\terror\ttime\n");
    for (count1=1; count1<=NoofFile; count1++) {
        // Scans input and output file name
        fscanf(infile,"%s",InFileName);
        fscanf(infile,"%s",OutFileName);
        fscanf(infile,"%d",&FlowDirn);
        fscanf(infile,"%d",&NTowType);
        TowVfT = new float [NTowType+1];
        TowK1T = new float [NTowType+1];
        TowK2T = new float [NTowType+1];
        fscanf(infile,"%d",&NTotTow);
        TowType = new int [NTotTow+1];
        for (count2=1; count2<=NTowType; count2++) {
            fscanf(infile,"%f",&TowVfT[count2]);
            fscanf(infile,"%d",&NTow);
            for (count3=1; count3<=NTow;count3++) {
                fscanf(infile,"%d",&dummy);
                TowType[dummy]=count2;
            }
        }
        fscanf(infile,"%d %d %d %d",
               &AddRowsf,&AddRows,&AddElemsX,&AddElemsY);
        /************************************/
        /* Calls Body() to begin evaluation */
        /************************************/
        Body();

        fprintf(outfile,"%d\t%d\t%d\t%f\t%e\t%e\t%d\t%e\t%f\n",
                count1,XDiv,YDiv,CellAvgVf,Kcellfinal,Ucellfinal,
                Iterfinal,errfinal,difftime(t2,t1));
        delete [] TowVfT;
        delete [] TowK1T;
        delete [] TowK2T;
        delete [] TowType;
    }
    fclose(infile);
    fclose(outfile);
    return 0;           /* End of main body */
}
```

```
void Body(void)
{   int count;
    char dummy[80];
    // Sets flow conditions and parameters
    OutputType=2;   // Output type (0=LIMS, 1=P solver, 2=1DGA)
    FArrayType=0;   // Fibre array type (0=Quadratic, 1=Hexagonal)
    KType=0;        // Tow permeability (0=isotropic, 1=vectorial)
    FR = 7.9e-6;    // Fibre radius
    Viscosity=(float) 0.308;    // Pa.s
    // InjPressure=(float)1e5;  // Pa.s
    InjFlowrate=(float) 0.001;  // m^3/s
    GeomFact=(float) .001;   // Conversion for geometric units to m

    if (KType==0) {             // Isotropic K
        for (count=1; count<=NTowType; count++) {
            TowVf=TowVfT[count];
            GebartKmodel();
            TowK1T[count]=TowK1;
            TowK2T[count]=TowK1;
        }
    } else if (KType==1) {      // Vectorial K
        for (count=1; count<=NTowType; count++) {
            TowVf=TowVfT[count];
            GebartKmodel();
            TowK1T[count]=TowK1;
            TowK2T[count]=TowK2;
        }
    } else {
        nrerror("define either 0 or 1 for OutputType in main()");
    }
    time(&t1);      // execution time begins
    /*********************************************************/
    /* Calls function to read grid file from TexGen and      */
    /* generate average fibre volume fractions and plugflow */
    /* averaged permeabilities for each grid element.        */
    /*********************************************************/
    ReadGRD();

    printf("Grid size : %d x %d\n\n",XDiv, YDiv);
    printf("Flow dirn (0 = x-axis, 1 = y-axis) : %d\n", FlowDirn);

    /*********************************************************/
    /* Calls the appropriate functions to evaluate the       */
    /* problem according to type of output needed.           */
    /*********************************************************/
    /***************/
    /* LIMS output */
    /***************/
    if (OutputType==0) {
        printf("No. of additional rows of elements in front of flow
                direction : %d\n",AddRowsf);
        printf("No. of additional rows of elements at the back of
                flow direction : %d\n",AddRows);
        // Note: additional rows of isotropic elements are added to
        // avoid edge effects, eg. fluid hitting solid boundary at
        // outlet, and also to simulate unit cell behaviour.
        // Usually choose XDiv/2 or YDiv/2, depending on flow dir.
        printf("No. of additional elements along x-axis used in grd
                file : %d\n",AddElemsX);
        printf("No. of additional elements along y-axis used in grd
                file : %d\n",AddElemsY);
```

```
        if (FlowDirn==1) {
            Addx=0;         Addy=AddRows;
            Addxf=0;        Addyf=AddRowsf;
        } else {
            Addx=AddRows;   Addy=0;
            Addxf=AddRowsf; Addyf=0;
        }

        time(&t2);      // execution time ends
        CreateLIMS();   // Create .dmp input file for LIMS
        WriteLB2();     // Write .lb library files for LIMS
        WriteK();       // Dump permeability values to file
    /******************/
    /* 2DGA FD solver */
    /******************/
    } else if (OutputType==1) {
        // Calculates pressure distribution
        if (FlowDirn == 0)              // Flow along x-axis
            CalcP3();
        else if (FlowDirn == 1)         // Flow along y-axis
            CalcP4();
        WriteTec(ija, p, Ux, Uy);
        DeleteGrid(CellKxx, XDiv, YDiv);
        DeleteGrid(CellKxy, XDiv, YDiv);
        DeleteGrid(CellKyy, XDiv, YDiv);
        DeleteGrid(CellVf, XDiv, YDiv);
    /********************/
    /* 1DGA calculation */
    /********************/
    } else if (OutputType==2) {
        time(&t2);
        WriteK2();
    } else {
        nrerror("define either 0 or 1 for OutputType in main()");
    }

    // Displays summary on screen
    printf("\nBounding box\n  bottom left : %f, %f, %f\n
            top right   : %f, %f, %f\n\n",
            MinX, MinY, MinZ, MaxX, MaxY, MaxZ);
    printf("Grid size : %d x %d\n\n",XDiv, YDiv);
    printf("%d additional rows of gap elements in front of flow-
            direction\n",AddRowsf);
    printf("%d additional rows of gap elements at the back of flow-
            direction\n",AddRows);
    printf("Average cell fibre volume fraction = %f\n\n",CellAvgVf);
    for (count=1; count<=NTowType; count++) {
        printf("Tow Type %d:\n",count);
        printf("Tow Vf = %f\n",TowVfT[count]);
        printf("Tow K1 = %e, K2 = %e\n", TowK1T[count],
                TowK2T[count]);
    }
    printf("Approximate permeability = %e m^2\n\n",CellAvgK);
    printf("Execution time = %f s\n\n", difftime(t2, t1));

}
```

[1256 lines of code follow]

APPENDIX H 3D GRID AVERAGE FINITE DIFFERENCE SOLVER

H.1 3D GRID AVERAGE FD SOLVER INPUT AND OUTPUT

Similar to the 2D GA solver, the 3D GA solver reads a batch file which contains the list of TexGen generated grid files to be evaluated as well as the operating conditions. It then proceeds to evaluate the grid files in the list. The grid files used by the 3D GA solver are similar to that used by the 2D GA solver.

H.1.1 Input file format

Grid Average 3D batch file format:

```
Batch results output filename
#
Number of analysis
#
The following lines will be repeated for each input file:
Grid Average input filename (.grd file)
#
Output filename (without file extension)
#
Analysis flow direction (0=x-axis, 1=y-axis)
#
Type of tow permeability (0=isotropic, 1=vectorial)
#
Number of types of tows
#
Number of tows
#
Types of tow in the following format - repeated for the total number
of types of tows:
Vf, number of tows with current type, tow numbers (cf. .grd file)
#     #     # (total tow numbers equals the preceding total)
The following numbers are for LIMS output:
Additional rows at beginning and end of analysis domain
#     #
```

Input batch file example:

```
900T_3D_results.xls
16
900T_non_010.grd
900T_non_010
0 1 2 12
0.754 6 3 4 7 8 11 12
0.754 6 1 2 5 6 9 10
0 0   ...
900T_nested_025.grd
900T_nested_025
1 1 2 12
0.754 6 3 4 7 8 11 12
0.754 6 1 2 5 6 9 10
0 0
```

Grid Average .grd input file example (self explanatory):

```
** GRID SIZE: MinX, MinY, MinZ, MaxX, MaxY, MaxZ
-5.0101,    -5.85,      0,    5.0101,     5.85, 1.998
** DIVISIONS: X, Y
100,  117
** GRID POINTS: NUMVOLUMES { VOLUME NUMBER, BOTTOM Z, TOP Z,
DIRECTION (X, Y, Z) }
9
0,    0,    0.0152953,  0,    0,    0
1,    0.0152953,  0.394705,   1,    0,    0
0,    0.394705,   0.425174,   0,    0,    0
4,    0.425174,   0.804826,   0,    1,    0
0,    0.804826,   1.1933,     0,    0,    0
9,    1.1933,     1.5727,     1,    0,    0
0,    1.5727,     1.60317,    0,    0,    0
12,   1.60317,    1.98283,    0,    1,    0
0,    1.98283,    1.998,      0,    0,    0
...
9
0,    0,    0.0152953,  0,    0,    0
1,    0.0152953,  0.394705,   1,    0,    0
0,    0.394705,   0.425174,   0,    0,    0
4,    0.425174,   0.804826,   0,    1,    0
0,    0.804826,   1.1933,     0,    0,    0
9,    1.1933,     1.5727,     1,    0,    0
0,    1.5727,     1.60317,    0,    0,    0
12,   1.60317,    1.98283,    0,    1,    0
0,    1.98283,    1.998,      0,    0,    0
```

H.1.2 Output file example (self explanatory)

```
Cell dimensions: 9.919998e-003 x 1.160000e-002 x 1.998000e-003
Grid size : 100 x 117 x 21
No. of nodes =    245700
Flow parallel to x-axis.
Tow Type 1:
Tow Vf = 0.754000
Tow K1 = 2.466783e-013, K2 = 4.194165e-014
Tow Type 2:
Tow Vf = 0.754000
Tow K1 = 2.466783e-013, K2 = 4.194165e-014
Viscosity =  3.080000e-001    Pas
dP =   1.000000e+005    Pa

Cell Vf =    0.526218
Inlet K =    7.136275e-010    m^2
Outlet K =   7.136275e-010    m^2
Average inlet Ux =       2.335658e-002    m/s
Average outlet Ux =      2.335658e-002    m/s
Execution time =   2952.000000       s
Also possible to output the coordinates of the nodes and the
corresponding permeability, pressure and velocity of flow.
```

H.2 3D GRID AVERAGE FD SOLVER CODE IN C – HEADER AND MAIN LISTING

```
/* Program to read Grid Average file from TexGen,      */
/* calculate pressure field for 3D Grid Average using  */
/* finite differences and then calculate               */
/* the effective permeability.                         */
/*                                                     */
/* Chee Chiew Wong                                     */
/* Last modified 5th July 2005                         */

#include <stdio.h>
#include <stdlib.h>
#include <string.h>
#include <math.h>
#include <time.h>

#define TOLERANCE   1.0e-9      // Tolerance for testing equality of
                                // floating point values
#define ITOL    1               // Type of iterative option
#define TOL     1.0e-18         // Iterative tolerance
#define ITMAX   100000          // Maximum number of iteration
#define NR_END  1               // Numerical Recipes in C constant
#define FREE_ARG char*          // Numerical Recipes in C constant
#define EPS     1.0e-14         // Numerical Recipes in C constant
#define PI      0.31415926535897932e+01

// Function prototypes
void    Body(void);             // Operation body called from main
void    ReadGRD3D(void);        // Processes .grd file and outputs
                                // in 3D format
void    CreateLIMS(void);       // Writes .dmp file for LIMS
void    WriteLB(void);          // Writes .lb for LIMS

void    CalcP3Dx(void);         // Calculates pressure distribution
void    CalcP3Dy(void);         // for flow along x-, y- and z-axes
void    CalcP3Dz(void);         // respectively using dP in 3D

void    WriteTec(unsigned long *ija, double *x, double *Ux, double
*Uy, double *Uz);               // Writes .tec Tecplot output file
                                // for post-processing
void    WriteK(void);           // Writes permeability values to
                                // file **for information only**
void    GebartKmodel(void);     // Calculates tow K based on
                                // Gebart's model
int     round(float xx);        // Rounds up floating point value
float   ***CreateGrid(int iWidth, int iHeight, int iDepth);
                // Function to create space for 3D array

void    DeleteGrid(float ***pCubeGrid, int iWidth, int iHeight, int
iDepth);        // Function to free 3D array space


// The following functions were adapted from Numerical Recipes in C
void    linbcg(double *sa, unsigned long *ija, unsigned long n,
                double *b, double *x, int itol, double tol, int
                itmax, int *iter, double *err);
    // solves the system of equations [a][p]=[b] using the conjugate
    // gradient method where [a] is stored in a sparse index storage
    // system
```

```
double  *dvector(long nl, long nh);
    // allocate a double vector with subscript range v[nl..nh]
void    free_dvector(double *v, long nl, long nh);
    // free a double vector allocated with dvector()
void    nrerror(char error_text[]);
    // Numerical Recipes in C standard error handler

char    InFileName[80],         // Input file name
        OutFileName[80],        // Output file name (stub)
        DMPFName[80],LBFName[80];   // .dmp and .lb output filenames
float   Viscosity,              // Resin viscosity
        InjFlowrate,            // Injection volumetric flow rate
        MinX, MinY, MinZ,
        MaxX, MaxY, MaxZ,       // Grid size
        GeomFact,               // Scale factor for geometry
        CellH,                  // Unit cell thickness
        CellMinZ, CellMaxZ,     // Max/min Z dimensions of cell
        CellXd, CellYd,         // Unit cell x & y dimensions
        CellAvgVf,              // Average cell Vf
        CellAvgK,               // Average permeability
        ***EKxx, ***EKyy, ***EKzz,
        ***EKxy, ***EKxz, ***EKyz, // K tensor for each grid element
        ***EVf,                    // Vf for each grid element
        TowVf,                  // Tow fibre volume fraction
        TowK1, TowK2,           // Tow principal permeabilities
                                   (1=fibre direction, 2=transverse)
        *TowVfT, *TowK1T, *TowK2T,
        FR;                     // Fibre radius
double  Kcellfinal, Ucellfinal, errfinal; // K and U cell values
int     XDiv, YDiv, ZDiv, ZDivN, // Number of elements in grid
        AddRows, AddRowsf,      // Additional rows of elements
                                // along flow dirn
        Addxf, Addyf,           // Additional rows in front
        Addx,Addy,              // Additional rows in x & y dirns
        Iterfinal,
        FlowDirn,               // Flow direction (0=parallel to x,
                                // 1=parallel to y)
        FArrayType,             // Fibre array type
                                // (0=Quadratic, 1=Hexagonal)
        KType,                  // Tow permeability type
                                // (0=isotropic, 1=vectorial)
        NTowType,               // No of types of tow
        NTotTow,                // No of tows
        *TowType,               // Tow type
        OutputType;             // Output type (0=LIMS, 1=P solver)
time_t  t1, t2;                 // time counters

int main()
{   /*******************************************************/
    /* Reads the batch file to obtain grid filename and ****/
    /* operating parameters, then calls body() to begin*****/
    /* evaluation. Repeats procedure for each input file. **/
    /*******************************************************/
    FILE    *infile, *outfile;  // Input file identifier
    char    BatchFileName[80],  // Input file name
            BatResultsFileName[80];
    int     NoofFile,
            NTow, dummy,
            count1, count2, count3;
```

```
    // Open batch file
    printf("Input batch filename: ");
    scanf("%s", BatchFileName);
    infile=fopen(BatchFileName, "r");
    if (infile==NULL) {
        printf("Error - file does not exist!\n");
        exit(1); // Abort if file does not exist
    }
    // Starts reading batch file
    fscanf(infile,"%s",&BatResultsFileName);
    fscanf(infile,"%d",&NoofFile);
    // Open batch file output
    outfile=fopen(BatResultsFileName, "w");
    if (outfile==NULL) {
        printf("Error - file cannot be opened!\n");
        exit(1); // Abort if file cannot be opened
    }
    fprintf(outfile,"No.\tXDiv\tYDiv\tZDiv\tCell Vf\tCell K
            \tInlet U\tIterations\terror\ttime\n");

    for (count1=1; count1<=NoofFile; count1++) {
        // Scans input and output file name
        fscanf(infile,"%s",InFileName);
        fscanf(infile,"%s",OutFileName);
        fscanf(infile,"%d",&FlowDirn);
        fscanf(infile,"%d",&KType);
                // Tow permeability (0=isotropic, 1=vectorial)
        fscanf(infile,"%d",&NTowType);
        TowVfT = new float [NTowType+1];
        TowK1T = new float [NTowType+1];
        TowK2T = new float [NTowType+1];
        fscanf(infile,"%d",&NTotTow);
        TowType = new int [NTotTow+1];
        for (count2=1; count2<=NTowType; count2++) {
            fscanf(infile,"%f",&TowVfT[count2]);
            fscanf(infile,"%d",&NTow);
            for (count3=1; count3<=NTow;count3++) {
                fscanf(infile,"%d",&dummy);
                TowType[dummy]=count2;
            }
        }
        fscanf(infile,"%d %d",&AddRowsf,&AddRows);
        /***********************************/
        /* Calls Body() to begin evaluation */
        /***********************************/
        Body();

        fprintf(outfile,"%d\t%d\t%d\t%d\t%f\t%e\t%e\t%d\t%e\t%f\n",
                count1,XDiv,YDiv,ZDivN,CellAvgVf,Kcellfinal,
                Ucellfinal,Iterfinal,errfinal,difftime(t2,t1));
        delete [] TowVfT;
        delete [] TowK1T;
        delete [] TowK2T;
        delete [] TowType;
        TowVfT = NULL;
        TowK1T = NULL;
        TowK2T = NULL;
        TowType= NULL;
    }
    return 0; /* End of main body */
}
```

```
void Body(void)
{
    int count;
    // Set flow conditions and parameters
    OutputType=1;   // Output type (0=LIMS, 1=P solver)
    FArrayType=1;   // Fibre array type (0=Quadratic, 1=Hexagonal)
    FR = 7.9e-6;    // Fibre radius
    Viscosity=(float) 0.308;    // Pa.s
    InjFlowrate=(float) 0.002;  // m^3/s
    GeomFact=(float) .001;   // Conversion for geometric units to m

    if (KType==0) {             // Isotropic K
        for (count=1; count<=NTowType; count++) {
            TowVf=TowVfT[count];
            GebartKmodel();
            TowK1T[count]=TowK1;
            TowK2T[count]=TowK1;
        }
    } else if (KType==1) {      // Vectorial K
        for (count=1; count<=NTowType; count++) {
            TowVf=TowVfT[count];
            GebartKmodel();
            TowK1T[count]=TowK1;
            TowK2T[count]=TowK2;
        }
    } else {
        nrerror("define either 0 or 1 for KType in main()");
    }
    time(&t1);      // execution time begins
    /*********************************************************/
    /* Calls function to read grid file from TexGen and      */
    /* generate average fibre volume fractions and plugflow */
    /* averaged permeabilities for each cuboid element.      */
    /*********************************************************/
    ReadGRD3D();
    printf("Grid size : %d x %d\n\n",XDiv, YDiv);
    printf("Flow dirn (0 = x-axis, 1 = y-axis) : %d\n", FlowDirn);

    /*********************************************************/
    /* Calls the appropriate functions to evaluate the       */
    /* problem according to type of output needed.           */
    /*********************************************************/
    /***************/
    /* LIMS output */
    /***************/
    if (OutputType==0) {
        printf("No. of additional rows of elements in front of flow
direction : %d\n", AddRowsf);
        printf("No. of additional rows of elements at the back of
flow direction : %d\n", AddRows);
        // Note: additional rows of isotropic elements are added to
        // avoid edge effects, eg. fluid hitting solid boundary at
        // outlet, and also to simulate unit cell behaviour.
        // Usually choose XDiv/2 or YDiv/2, depending on flow dir.
        if (FlowDirn==1) {
            Addx=0;         Addy=AddRows;
            Addxf=0;        Addyf=AddRowsf;
        } else {
            Addx=AddRows;   Addy=0;
            Addxf=AddRowsf; Addyf=0;
        }
```

```
        time(&t2);      // execution time ends
        CreateLIMS();   // Create .dmp input file for LIMS
        WriteLB();      // Write .lb library files for LIMS
    /******************/
    /* 3DGA FD solver */
    /******************/
    } else if (OutputType==1) {
        // Calculate pressure distribution
        if (FlowDirn == 0)              // Flow along x-axis
            CalcP3Dx();
        else if (FlowDirn == 1)         // Flow along y-axis
            CalcP3Dy();
        time(&t2);

    } else {
        nrerror("define either 0 or 1 for OutputType in main()");
    }

    // Displays summary on screen
    printf("\nBounding box\n  bottom left : %f, %f, %f\n
            top right   : %f, %f, %f\n\n",
            MinX, MinY, MinZ, MaxX, MaxY, MaxZ);
    printf("Grid size : %d x %d\n\n",XDiv, YDiv);
    printf("%d additional rows of gap elements in front of flow-
            direction\n",AddRowsf);
    printf("%d additional rows of gap elements at the back of flow-
            direction\n",AddRows);
    printf("Average cell fibre volume fraction = %f\n\n",CellAvgVf);
    for (count=1; count<=NTowType; count++) {
        printf("Tow Type %d:\n",count);
        printf("Tow Vf = %f\n",TowVfT[count]);
        printf("Tow K1 = %e, K2 = %e\n", TowK1T[count],
                TowK2T[count]);
    }
    printf("Approximate permeability = %e m^2\n\n",CellAvgK);
    printf("Execution time = %f s\n\n", difftime(t2, t1));

    DeleteGrid(EKxx, XDiv, YDiv, ZDivN);
    DeleteGrid(EKxy, XDiv, YDiv, ZDivN);
    DeleteGrid(EKyy, XDiv, YDiv, ZDivN);
    DeleteGrid(EKzz, XDiv, YDiv, ZDivN);
    DeleteGrid(EKxz, XDiv, YDiv, ZDivN);
    DeleteGrid(EKyz, XDiv, YDiv, ZDivN);
    DeleteGrid(EVf, XDiv, YDiv, ZDivN);

}
```

[2310 lines of code follow]

APPENDIX I MESH SENSITIVITY STUDIES

I.1 QUADRATIC ARRAY OF FIBRES

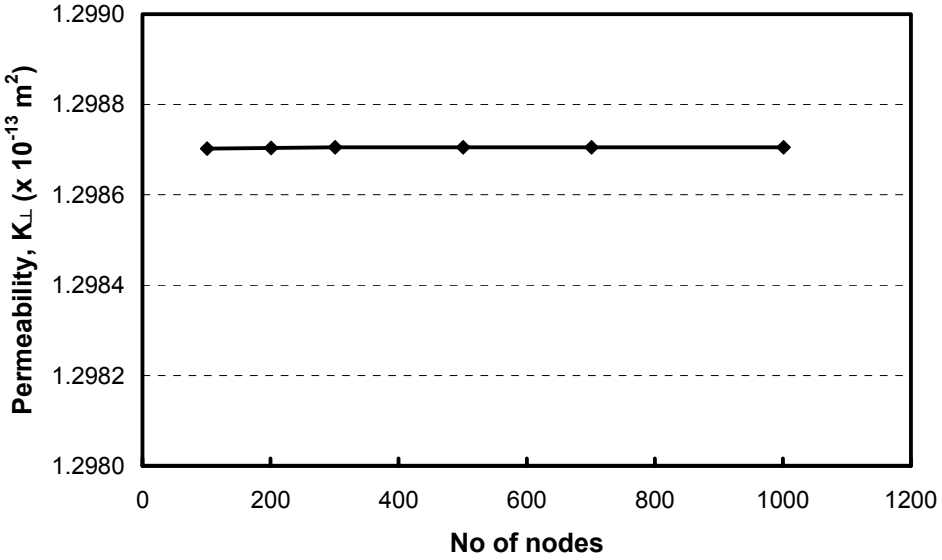

Figure I.1 – Averaging equation mesh sensitivity study for flow transverse to a quadratic array of fibres with $V_f = 0.65$.

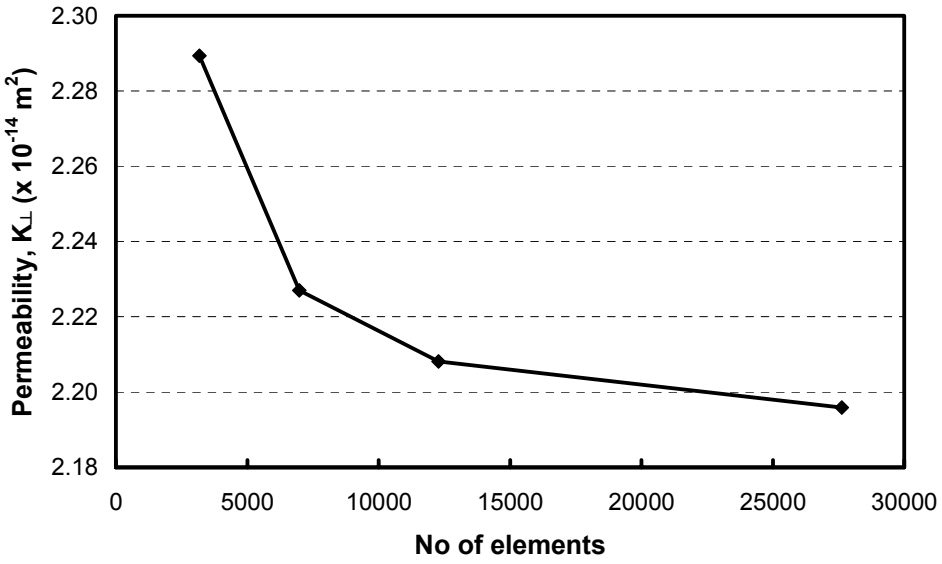

Figure I.2 – 2D CFD mesh sensitivity study for flow transverse to a quadratic array of fibres with $V_f = 0.71$.

I.2 2D CROSS SECTION OF A FIBROUS TOW

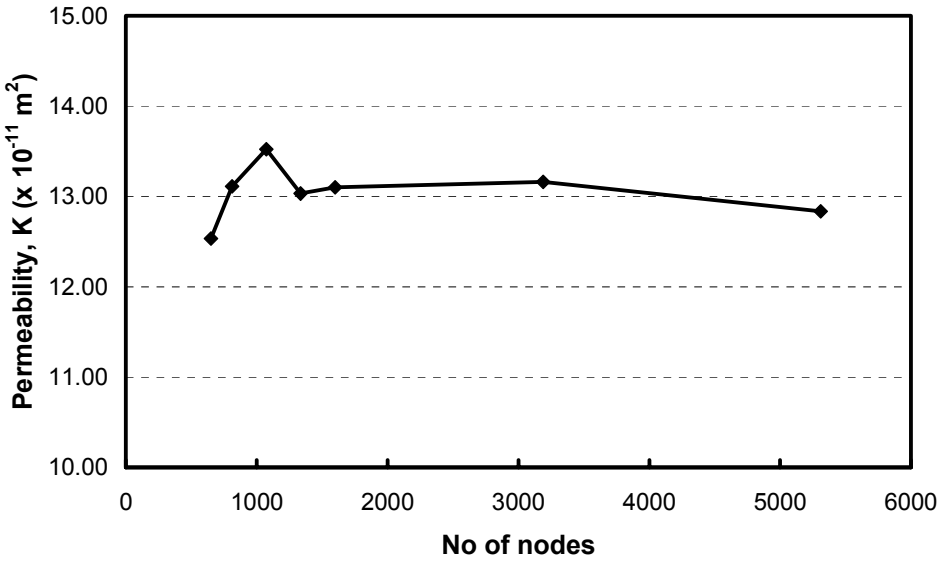

Figure I.3 – 1.5D Stream Surface mesh sensitivity study for the nominal case 1 of a cross section of a porous tow.

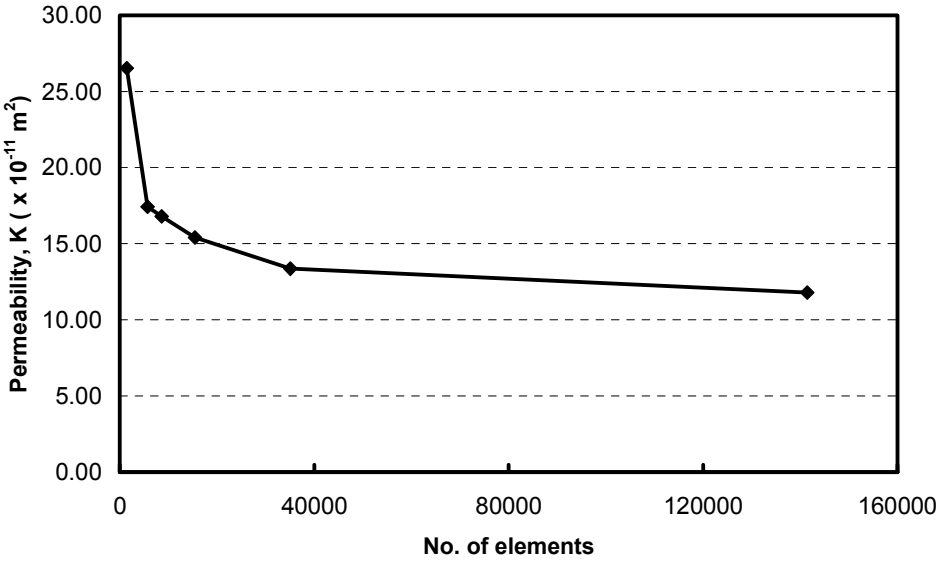

Figure I.4 – 2D CFD mesh sensitivity study for the nominal case 1 of a 2D cross section of a porous tow.

I.3 2:2 TWILL WEAVE MODEL

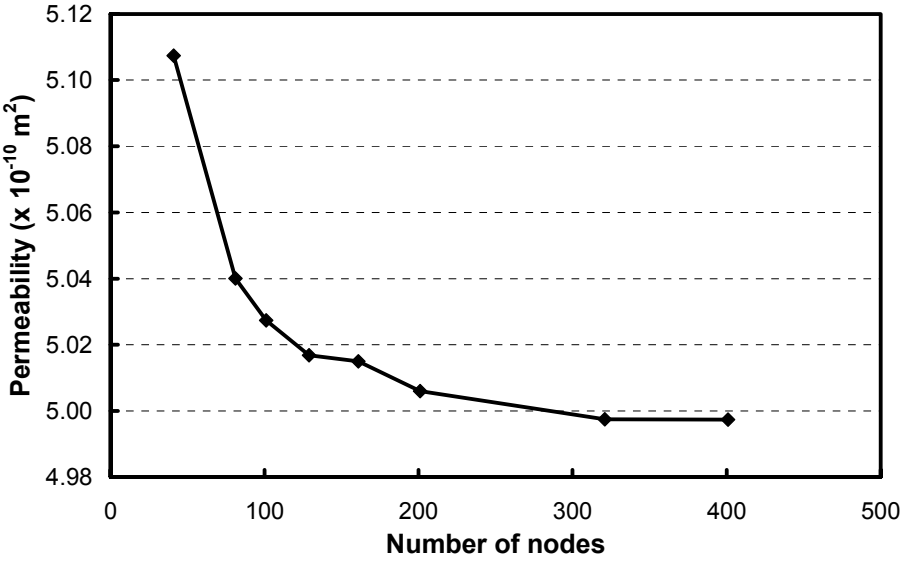

Figure I.5 – 1D Grid Average mesh sensitivity study of the cross section at the tow crossovers of the ±45° 2:2 twill weave model for flow along the x axis

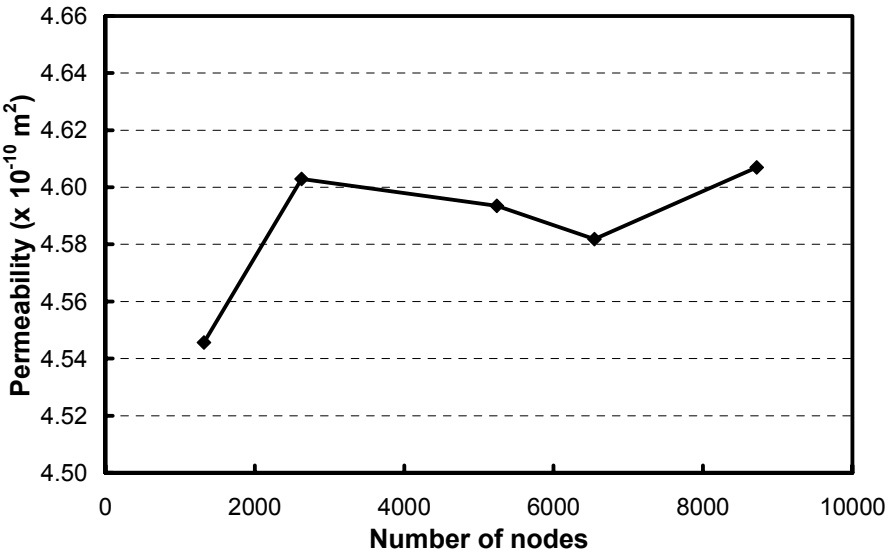

Figure I.6 – 1.5D Stream Surface mesh sensitivity study of the cross section at the tow crossovers of the ±45° 2:2 twill weave model for flow along the x axis

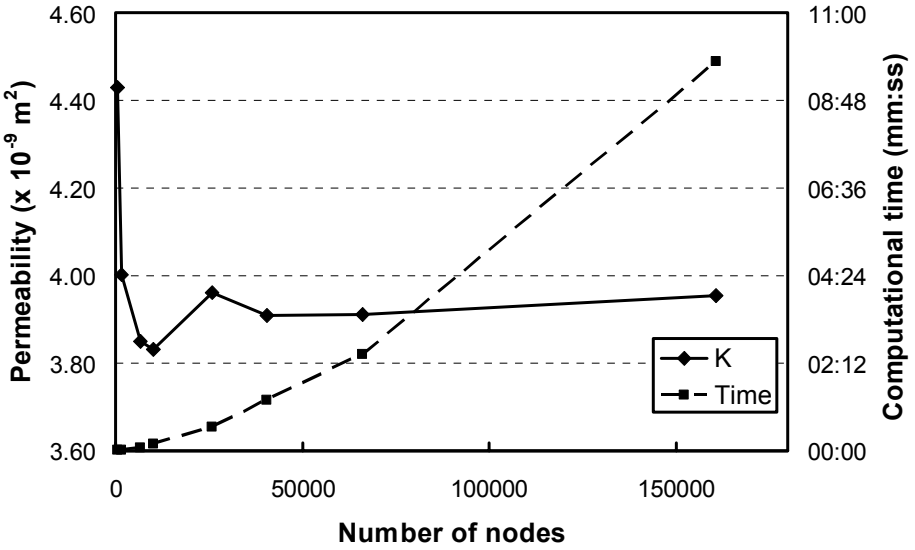

Figure I.7 – 2D Grid Average mesh sensitivity study of ±45° 2:2 twill weave model for flow along the x axis.

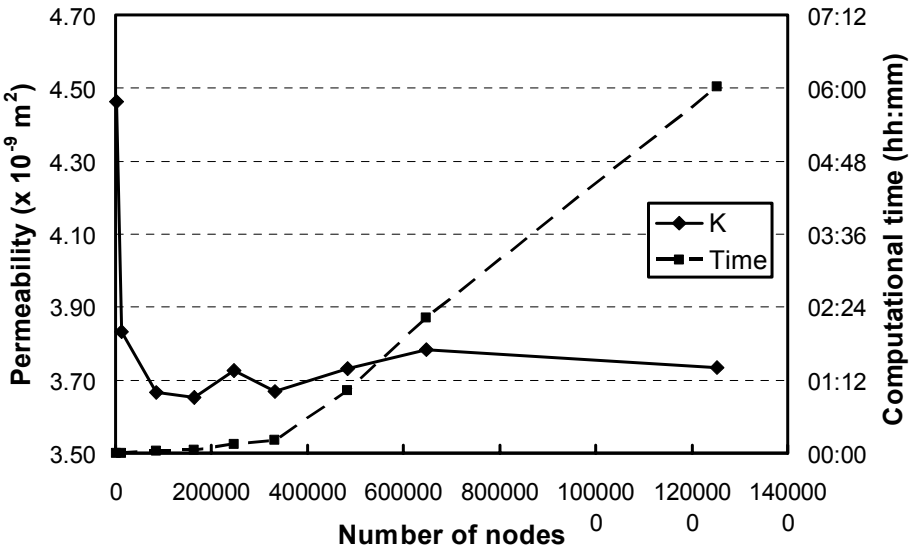

Figure I.8 – 3D Grid Average mesh sensitivity study for ±45° 2:2 twill weave model for flow along the x axis.

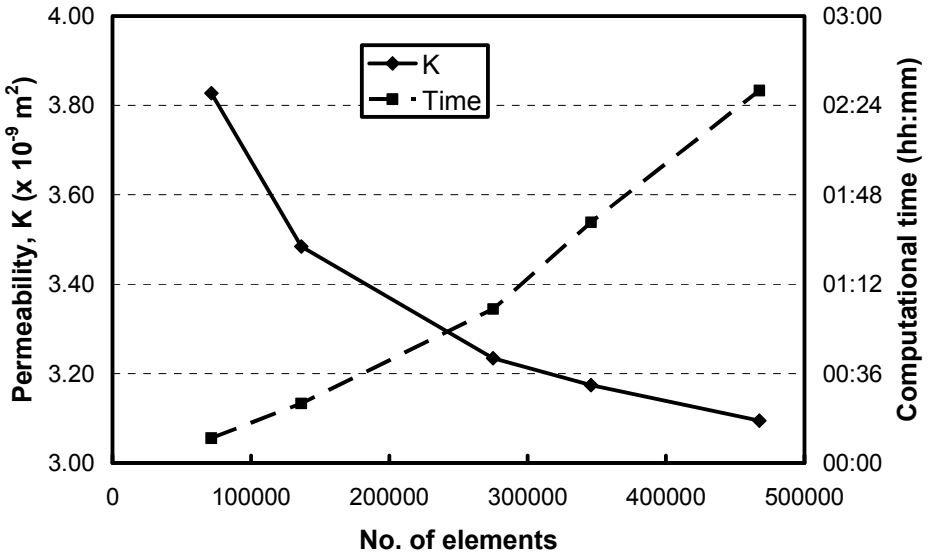

Figure I.9 – 3D CFD mesh sensitivity study of ±45° 2:2 twill weave model for flow along the x axis.

I.4 900T PLAIN WEAVE

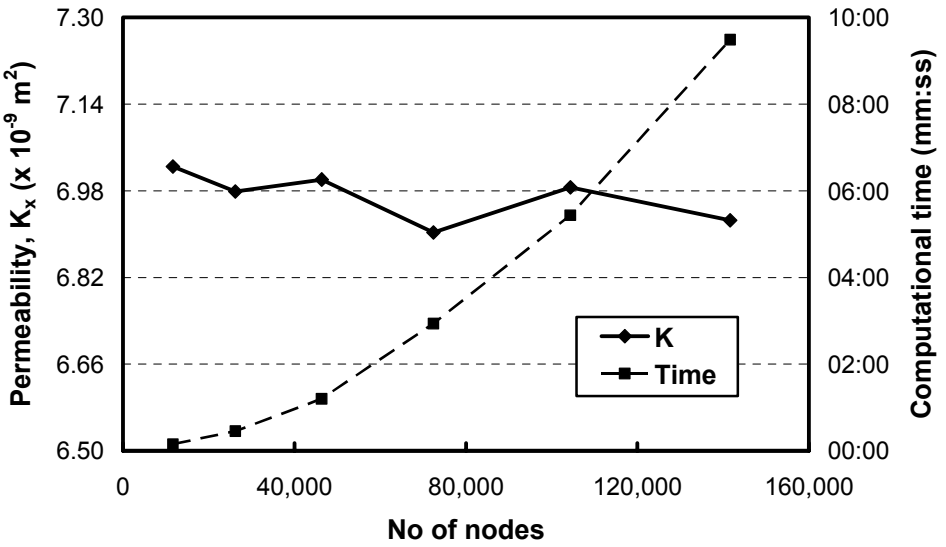

Figure I.10 – 2D Grid Average mesh sensitivity study for 900T plain weave nested model for flow along the x axis.

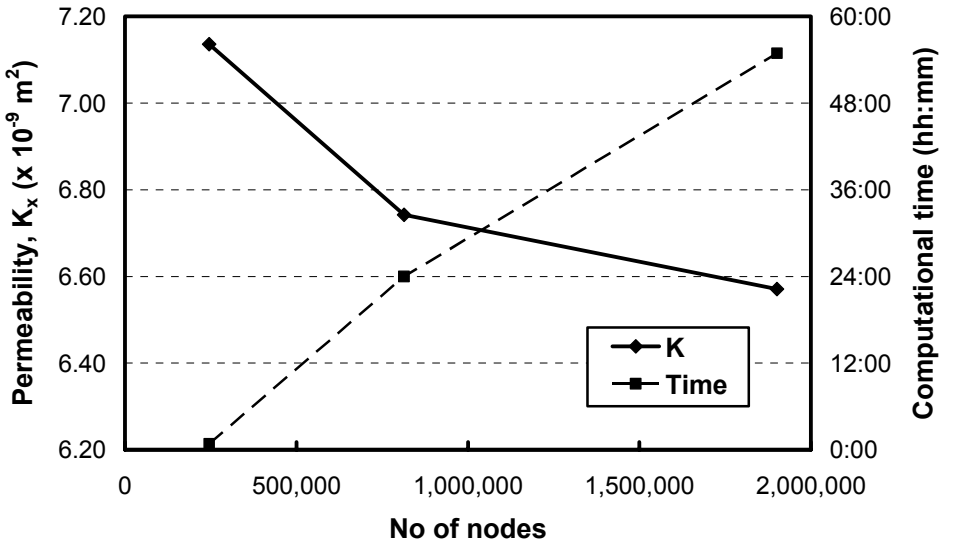

Figure I.11 – 3D Grid Average mesh sensitivity study for 900T plain weave nested model for flow along the x axis.

I.5 ±45° BI-DIRECTIONAL NON-CRIMP FABRIC

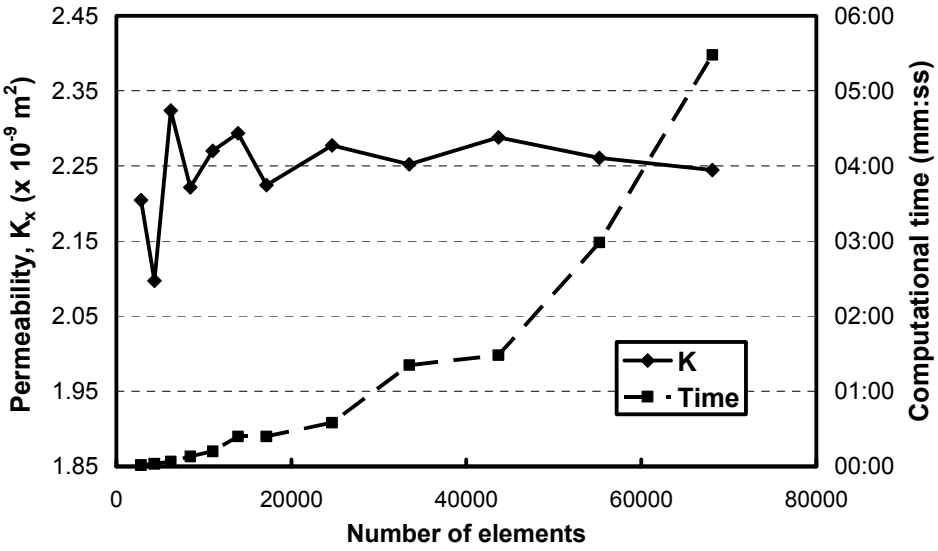

Figure I.12 – 2D Grid Average mesh sensitivity study for ±45° non-crimp fabric model with a_0 = 2.6mm.